
Development of fluorescent biosensors probing RNA function

**Dissertation
der Fakultät für Biologie
der Ludwig-Maximilians-Universität
München**

**vorgelegt von
Martina Schifferer-Waritschlager**

München, den 15.09.2011

Betreuer:

Dr. Oliver Griesbeck

Erstgutachter:

Prof. Dr. Alexander Borst

Zweitgutachter:

Prof. Dr. Charles David

Tag der mündlichen Prüfung:

08.12.2011

“Hier treffen wir nun auf die eigene Schwierigkeit, die nicht immer klar ins Bewusstsein tritt, dass zwischen Idee und Erfahrung eine gewisse Kluft befestigt scheint, die zu überschreiten unsere ganze Kraft sich vergeblich bemüht. Demohngeachtet bleibt unser ewiges Bestreben, diesen Hiatus mit Vernunft, Verstand, Einbildungskraft, Glauben, Gefühl, Wahn und, wenn wir sonst nichts vermögen, mit Albernheit zu überwinden.“

J.W. Goethe

Bedenken und Ergebung (1823)

Contents

Contents.....	4
Table of figures	9
Abbreviations.....	12
Abstract.....	14
1. Introduction	16
1.1. RNA characteristics	16
1.1.1 RNA structure.....	16
1.1.2 RNA classification.....	16
1.2. mRNA fate in eukaryotic cells	17
1.2.1 mRNA transcription and processing	17
1.2.2 mRNA subcellular localization	19
1.2.3 mRNA turnover	27
1.3. viral RNA-protein interactions	30
1.3.1 Arginine-rich motif (ARM) peptides.....	30
1.3.2 HIV RRE aptamer.....	31
1.3.3 Rsg1.2 –RRE interaction.....	33
1.4. Fluorescence imaging	34
1.4.1 Fluorescent proteins	34
1.4.2 Genetically encoded fluorescent biosensors.....	36
1.5. RNA imaging.....	40
1.5.1 Chemical RNA dyes	40
1.5.2 Molecular beacons.....	42
1.5.3 Genetically encoded FP-based RNA labels	42

1.5.4 Recent advances in imaging technology.....	47
1.6 Project goal	49
2. Materials and Methods.....	52
2.1. DNA molecular biology	52
2.1.1 Polymerase Chain Reaction (PCR).....	52
2.1.2 Error-prone PCR.....	53
2.1.3 Site-directed mutagenesis via PCR	54
2.1.4 DNA purification.....	56
2.1.5 Restriction digest of DNA.....	56
2.1.6 Dephosphorylation of vector DNA.....	57
2.1.7 Ligation of DNA fragments.....	58
2.1.8 Preparation of chemically-competent <i>E. coli</i>	58
2.1.9 Transformation of chemically-competent <i>E. coli</i>	59
2.1.10 Bacterial DNA purification	59
2.2. RNA molecular biology.....	59
2.2.1 <i>In vitro</i> transcription	60
2.2.2 Reverse transcription (RT)	61
2.2.3 Systematic Evolution of Ligands by Exponential Enrichment (SELEX)	62
2.3 Protein Biochemistry.....	64
2.3.1 Protein expression using the <i>E. coli</i> BL21 strain	64
2.3.2 Affinity purification of recombinantly expressed proteins.....	65
2.3.3 Size exclusion chromatography of recombinantly expressed proteins.....	65
2.3.4 ATPase assay	66
2.4 Spectroscopy.....	66
2.4.1 Testing for <i>in vitro</i> ratio change of FRET RNA sensors.....	66

2.4.2 Spectroscopic determination of K_D -value	67
2.4.3 pH titration.....	67
2.4.4 <i>In vitro</i> transcription assay.....	67
2.4.5 Spectroscopic REFlex FRET assay	67
2.5 Bacterial screening.....	68
2.5.1 Sensor library generation	68
2.5.2 Bacterial colony selection	68
2.6 Cellular biology.....	70
2.6.1 Preparation of dissociated hippocampal neuronal culture	70
2.6.2 Immunocytochemistry	72
2.6.3 Fluorescence in situ hybridization (FISH).....	73
2.6.4 Isolation of DNA and RNA from cell lysates.....	74
2.6.5 Transfection methods.....	75
2.6.6 Cellular assays and imaging	77
2.7 Materials	79
2.7.1 Instruments.....	79
2.7.2 Consumables.....	79
2.7.3 Buffers, solutions and media	80
2.7.4 Chemicals	82
2.7.5. Plasmids, bacterial strains, cell-lines and flies.....	84
3. Results.....	86
3.1 Application of genetically encodable RNA labels for imaging of neuronal RNAs.....	86
3.1.1. Dual RNA imaging in neurons	86
3.1.2. NMDAR1 splicing reporter	88
3.2. RNA imaging using an on-off chemical dye	90

3.2.1 <i>In vitro</i> development of the on-off dye – aptamer pair	91
3.2.2 On-off dye performance in mammalian cell lines	92
3.3. Development of a genetically encodable dynamic single fluorophore RNA sensor	94
3.3.1 FP emission change upon direct aptamer interaction.....	94
3.3.2 Aptamer-dependent emission change in a FP-peptide hybrid.....	96
3.4 Engineering of the FRET-based RNA biosensor VAmPIRe	99
3.4.1 Aptamer-peptide pair selection for the FRET biosensor	99
3.4.2 Rational engineering of FR-Rsg1.2	102
3.4.3 Development of a functional screen for FRET sensor performance in bacteria ..	107
3.4.4 VAmPIRe <i>in vitro</i> characterization	111
3.4.5 Aptamer engineering	114
3.4.6 Cellular RNA imaging using VAmPIRe	116
3.5. Development of the EJC FRET sensor REFlex.....	120
3.5.1 eIF4AIII FRET biosensor design and incorporation into the EJC	120
3.5.2 ATP and RNA are necessary for REFlex FRET change.	121
3.5.3 PYM or Imp13 binding to MAGO-Y14 results in EJC disassembly.	122
3.5.4 Monitoring RNA binding to eIF4AIII by FRET	124
4. Discussion.....	125
4.1 Evaluation of dual FP-based RNA labeling using MS2 and λ N22.....	126
4.2 Imaging cellular RNAs by synthetic on-off ASR dyes	127
4.3 Performance and potential of single fluorophore RNA sensors.....	128
4.3.1 Aptamer-induced FP emission	129
4.3.2 RNA binding peptide-EGFP hybrid	131
4.3.3 Design of novel single fluorophore sensor	133
4.4 VAmPIRe sensor performance	133

4.4.1 VAmPIRe <i>in vitro</i> performance	133
4.4.2 FRET RNA sensor engineering	135
4.4.3 Cellular performance	144
4.4.4 Screening for FRET sensor performance.....	154
4.5 REFlex sensor performance	159
4.5.1 REFlex assay <i>in vitro</i> application	159
4.5.2 REFlex application for cellular imaging.....	160
4.6 Conclusion.....	163
References	165
Acknowledgements.....	190
Curriculum Vitae	192
Versicherung	194

Table of figures

Figure 1 RNA structure and processing.....	19
Figure 2 Subcellular localization of mRNAs.....	20
Figure 3 Regulation of neuronal functions by localized mRNAs.....	24
Figure 4 Dendritic CaMKII α mRNA.....	25
Figure 5 NMDAR1 exon 21 splicing.....	27
Figure 6 Structure and function of the EJC.....	29
Figure 7 Structure of aptamer-ARM peptide complexes.....	30
Figure 8 Structure and function of the HIV RRE RNA.....	32
Figure 9 Comparison of the RRE RNA interaction with Rev and Rsg 1.2.....	33
Figure 10 Fluorescent proteins.....	36
Figure 11 FRET principle.....	38
Figure 12 FRET biosensor strategies.....	39
Figure 13 Orbital energy diagram for fluorescent PET sensors before and after cation binding.....	41
Figure 14 Functional principle of FP-mediated RNA labeling.....	43
Figure 15 Dynamics of mRNA molecules in the cytoplasm of mammalian cells.....	45
Figure 16 Functional principle of split YFP mediated RNA visualization.....	46
Figure 17 Strategies for RNA labeling and dynamic RNA reporters.....	50
Figure 18 Workflow for biosensor engineering.....	51
Figure 19 Concepts of visualizing RNA-mediated processes.....	51
Figure 20 SELEX procedure for the selection of a trGFP binding RNA aptamer.....	64
Figure 21 Bacterial colony screening procedure.....	70
Figure 22 Hippocampal dissection.....	72
Figure 23 MS2 and λ N22 labeling in rat hippocampal neurons.....	87
Figure 24 NMDAR1 splicing reporter strategy.....	88
Figure 25 NMDAR1 splice reporter granule characterization.....	89
Figure 26 NMDAR1 exon21 alternative splice variant imaging in hippocampal neurons.....	90
Figure 27 Principle of aptamer-induced fluorescence of a chemical compound.....	91
Figure 28 Chemical compound approach performance in HeLa cells.....	92
Figure 29 Staining of HeLa cells with a tat-conjugated on-off RNA dye.....	93
Figure 30 Design principles of dynamic single-FP RNA sensors.....	94
Figure 31 Strategy for engineering aptamer-induced protein fluorescence.....	95
Figure 32 λ N22 peptide insertion into EGFP.....	97

Figure 33 Aptamer-dependent fluorescence of a cpEGFP-viral peptid hybrid.....	98
Figure 34 FRET RNA biosensor principle.....	99
Table 1: Ratio change in FRET biosensor constructs using selected ARM peptides as sensing moiety.	100
Figure 35 FRET YFP/CFP measurements in the cuvette.....	101
Figure 36 FR-Rsg1.2 RNA aptamer specificity.....	102
Figure 37 Peptide multiplication and rational linker design.....	103
Figure 38 Ratio change of a spectrally shifted RNA FRET sensor.....	105
Figure 39 Rsg1.2 peptide Proline 12 mutagenesis.....	106
Figure 40 FR-Rsg1.2 ph-sensitivity engineering by Arginine substitution.....	107
Figure 41 FR-Rsg1.2 7A8Q performance in bacteria.....	108
Figure 42 Screening for aptamer-induced FRET ratio change in bacteria.....	110
Figure 43 Performance of selected sensor variants.....	111
Figure 44 VAmPIRe FRET characteristics.....	112
Figure 45 VAmPIRe <i>in vitro</i> properties.....	113
Figure 46 Dynamic and reversible imaging of RNA transcription and decay <i>in vitro</i>	114
Figure 47 RRE aptamer multimerization.....	115
Figure 48 VAmPIRe performance in living mammalian cells.....	116
Figure 49 Imaging temporal RNA dynamics.....	117
Figure 50 Intracellular RNA localization in fibroblasts.....	118
Figure 51 Stress granule formation in fibroblasts.....	119
Figure 52 REFlex engineering and performance.....	121
Figure 53 REFlex FRET change reports assembly of the EJC and requires ATP and RNA.....	122
Figure 54 REFlex reports EJC disassembly by PYM and Imp13.....	124
Figure 55 REFlex sensitivity for different RNA targets.....	125
Figure 56 Two-plasmid KAN antitermination assay.....	130
Figure 57 Single fluorophore RNA sensor strategies.....	132
Figure 58 Design of novel RNA biosensors.....	133
Figure 59 Aptamer linker design.....	136
Figure 60 RRE aptamer mutants.....	137
Figure 61 Rsg1.2 peptide functional assignment of amino acids.....	138
Figure 62 FRET efficiency for linked donor-acceptor pairs distributed in three dimensions.....	139
Figure 63 Charge effect on the interaction of vampire components.....	140
Figure 65 FRET pair dimer interface engineering.....	143

Figure 66 FRET efficiency in dependence of distance.....	144
Table 2 Comparison of vampire with the MS2/ λ N22 systems.	148
Figure 67 Design of novel RNA biosensors.	148
Figure 68 Rev sensor strategy.....	150
Table 3 Comparison of VAmPIRe to the Rev sensor.	150
Figure 69 Comparison of confocal and STED microscopy in spines.....	152
Figure 70 Ectopic spine targeting by Lifeact..	153
Figure 71 RNA induction in bacteria using the TetON system.....	155
Figure 72 The effect of acrAB efflux pumps on RNA induction by TC.....	156
Figure 73 Workflow for the cellular screening of FRET sensors.	158
Figure 74 Oskar mRNA and the EJC in <i>Drosophila</i> oogenesis.	161
Figure 75 eIF4AIII in neurons.	162

Abbreviations

aa	amino acid
APS	ammonium persulfate
Arc	activity-regulated cytoskeleton-associated protein
ASR	fluorescently quenched sulforhodamine dye
ATP	adenosine 5'-triphosphate
BDNF	brain-derived neurotrophic factor
BFP	blue mutant of GFP
bp	base pairs
BIV	bovine immunodeficiency virus
BSA	bovine serum albumin
Btz	Barentsz
CaMKII α	Calcium/Calmodulin-dependent Protein Kinase II
CCD	charge-coupled device
CFP	cyan fluorescent protein
CMV	cytomegalovirus
CP	circularly permuted
Da	Dalton
DIV	days in vitro
DMEM	Dulbecco's Modified Eagle Medium
DMSO	dimethylsulfoxid
DNA	desoxyribonucleic acid
dNTP	deoxyribonucleotid-triphosphate
E18	embryonic day 18
EDTA	ethylenediamine tetraacetic acid
eGFP	Enhanced green fluorescent protein
EJC	exon junction complex
eIF4AIII	eukaryotic initiation factor 4AIII
Eppi	eppendorf 1.5 / 2 ml vial
ESPT	excited state proton transfer
FCS	fetal calf serum
FISH	fluorescence in vitro hybridization
FMRP	fragile X mental retardation protein
FP	fluorescent protein
FRET	fluorescence or förster resonance energy transfer
GFP	green fluorescent protein
HBSS	Hanks' balanced salt solution
HEK	human embryonic kidney
HeLa	Henrietta Lacks
HIV	human immunodeficiency virus
Imp13	Importin 13
IPTG	isopropyl- β -D-thiogalactopyranoside
K _d	dissociation constant
λ N22	Lambda-N22 protein
LB	Luria-Bertani broth
M	molar
MB	molecular beacon
miRNA	micro RNA
mKO2	monomeric Kusabira Orange2

MOPS	3-(N-morpholino)propanesulfonic acid
mRNA	messenger RNA
mTFP	monomeric teal fluorescent protein
MTRIP	multiply labeled tetravalent <i>RNA imaging probes</i>
MW	molecular weight
ncRNA	noncoding RNA
NLS	nuclear localization signal
NMDA(R)	<i>N</i> -methyl <i>D</i> -aspartate (receptor)
nt	nucleotides
NTA	nitriloacetic acid
OD _x	optical density at <i>x nm</i>
ORF	open reading frame
PAGE	polyacrylamide gel electrophoresis
PALM	photoactivated localization microscopy
PBS	phosphate-buffered saline
PCR	polymerase chain reaction
PET	photoinduced electron transfer
pH	reverse logarithmic representation of relative H ⁺ concentration
PMSF	phenylmethylsulfonylfluoride
R	ratio, fluorescence intensity of acceptor emission over donor emission
ΔR	difference of ratio R
REFlex	reporter of eIF4AIII flexure
Rev	regulator of virion expression
RBP	RNA binding protein
RNA	ribonucleic acid
RNAi	RNA interference
RNP	ribonucleoprotein
ROI	region of interest
RRE	Rev responsive element
RT	room temperature
SDS	sodium dodecyl sulfate
SELEX	systematic evolution of ligands by exponential enrichment
SFV	semliki forest virus
STED	stimulated emission depletion
TAE	tris-acetate-EDTA electrophoresis buffer
TE	tris-EDTA buffer
TEMED	<i>N,N,N',N'</i> -Tetramethyl-ethylendiamine
tRNA	transfer RNA
YFP	yellow fluorescent protein
WT	wildtype
ZBP1	zipcode binding protein 1

Abstract

Live cell imaging of RNA or their protein binding partners is crucial to obtain an authentic picture of RNA transcription, processing and trafficking. The development of methods for tracking of specific target RNAs in diverse cellular systems has been approached by different strategies including synthetic dyes, molecular beacons and genetically encoded RNA labels. In this work, we challenged current fluorescent protein RNA labeling methods by testing their performance for RNA visualization in neurons. Lack of dynamic behavior revealed the limitations of these current approaches and subsequently the need for novel on-off RNA reporters. Consequently, we designed synthetic and genetically encodable RNA biosensors with an RNA-dependent signal output and established tests suitable for analyzing their performance *in vitro*, in bacterial and eukaryotic systems. Application of synthetic on-off RNA dyes was hampered by impermeability or low specificity within the cellular environment.

We engineered genetically encoded FRET RNA reporters based on the interaction of viral or synthetic RNA-peptide binding partners. Intramolecular FRET between two fluorescent proteins occurs only if the interspaced peptide undergoes a conformational change upon high-affine RNA aptamer binding. One of the identified sensors based on the Rsg1.2 peptide and the HIV Rev Responsive Element (RRE) RNA aptamer was called VAmPIRe (**V**iral **A**ptamer binding **P**eptide based **I**ndicator for **R**NA detection). Its dynamic range was improved by engineering both the RNA aptamer tag and the fusion protein by random linker insertion and targeted mutagenesis. We demonstrate that the system is quantitative, reversible and can be used to tag RNAs of interest with high specificity *in vitro* and in living bacteria and mammalian cells.

Besides tracking of specific RNAs, biosensors studying the function of RNA binding proteins like RNA helicases can provide further insights into RNA-based processes. Particularly interesting, the RNA helicase eIF4AIII is situated at the core of the Exon Junction Complex (EJC), a multi-protein complex involved in splicing, translation and RNA quality surveillance. We have designed the FRET-based fluorescent biosensor REFlex (**R**eporter of **eIF4AIII** **F**lexure) that monitors the conformational change of eIF4AIII underlying its transition from the open to the closed state. Generally, *in vitro* FRET monitoring using REFlex can be applied to reveal components that modulate EJC complex stability. More specifically, we have

identified Importin 13 as a novel protein that is necessary and sufficient for EJC complex disassembly. Furthermore, REFlex can be used to analyze the specificity of eIF4AIII for different RNAs. This genetically encodable FRET sensor enables *in vitro* biochemical and biophysical studies of eIF4AIII-related factors and can potentially be applied for functional live-cell imaging.

Assisting general sensor engineering, we established the first method for functional screening for FRET performance in bacterial colonies. The prokaryotic system combines simple generation and testing of large libraries with the functionality of a living organism. Bacterial screening was applied to improve VAmPIRe performance and provides a powerful tool for the engineering of many kinds of genetically encoded biosensors.

1. Introduction

1.1. RNA characteristics

According to the RNA (ribonucleic acid) world hypothesis (Gilbert 1986), pre-cellular life was based on RNA. RNA is both able to encode and store genetic information and to catalyze reactions comparable to proteins.

1.1.1 RNA structure

The polymer consists of four different nucleotides adenine, cytosine, guanine and uracil (instead of thymidine for DNA) composed of a ribose sugar, a phosphate group and a nucleobase. Genetic information encoded by the RNA nucleotide sequence serves either as a mobile messenger RNA (mRNA) or replaces DNA in some viral genomes.

Inter- and intra-molecular Watson-Crick pairing (A with U and C with G) as well as non-canonical base pairing allows the formation of discrete structural motifs. The single-stranded RNA helix displays a stable A-type configuration (Salazar et al. 1993) with a narrow major and a shallow minor groove due to constraints originating from the ribose 2'-OH. Base stacking by van der Waals interactions further contributes to a high enthalpy. While RNAs, especially RNA modules and motifs, are thermodynamically stable, chemical stability is low compared to DNA as the ribose 2'-OH can attack the phosphodiester bond to cleave the backbone.

The interaction of secondary structural elements like hairpin loops and bulges leads to the formation of a unique tertiary structure (Figure 1). The characteristic folding with its flexibility permit RNA-based molecular recognition (Hermann and Patel 2000) as well as catalytic activities.

1.1.2 RNA classification

Only 3% of eukaryotic RNAs are mRNAs while the majority does not code for proteins. Unexpectedly, the repertoire of RNAs found in living cells is exceedingly complex, with large regions of the genome being transcribed into non-coding RNAs (ncRNA) that are involved in

gene expression. During protein translation, transfer RNAs (tRNA) act as adaptors linking the respective amino acid with its nucleotide coding sequence. Fine-tuning and networking functions in gene expression have been assigned to small ncRNAs including micro RNAs (miRNAs), small interfering RNAs (siRNAs) and Piwi-interacting RNAs (piRNA). In a mechanism called RNA silencing, these short RNAs bind to their complementary target RNA thereby blocking translation and inducing its degradation (Wu and Belasco 2008).

RNA folding into intricate secondary and tertiary structures adds another important facet. Short RNA strands called aptamers (“aptus” = to fit) are recognized and bound with high affinity by specific ligands including peptides. Systematic evolution of ligands by exponential enrichment (SELEX) (Tuerk and Gold 1990) (Ellington and Szostak 1990) has been used to screen for aptamers from randomized RNA pools. So-called ribozymes are even able to catalyze specific chemical reactions (Kruger et al. 1982). Similarly, ribosomal RNAs (rRNA) constitute the catalytic component of the ribosome. Another RNA class called riboswitches undergoes regulated conformational change after recognition of a certain metabolite leading to altered RNA processing (N. Sudarsan et al. 2008).

1.2. mRNA fate in eukaryotic cells

The richness of mRNA dynamics is evident in the exquisitely timed and tightly controlled processes by which mRNAs from different genes are produced and degraded, in their export from the nucleus to the cytoplasm, and in their sorting and localization into different regions of the cytoplasm.

1.2.1 mRNA transcription and processing

Transcription relies on RNA synthesis on the DNA template and is the first and most highly regulated step in gene expression. Eukaryotic mRNAs are transcribed in the nucleus by RNA polymerase II. The mRNA coding region consists of exons that are interrupted by noncoding introns. Pre-mRNAs contain untranslated regions (UTR) at both ends of the coding region (Figure 1). Both UTRs determine translational efficiency and mediate the interaction with

ribonucleases. The 3'UTR contains transport signals and can be bound by miRNAs that regulate translation and degradation of the mRNA.

In most eukaryotic organisms the synthesized pre-mRNA transcripts undergo a series of processing reactions required to produce a functional RNA (Figure 1). Eukaryotic mRNA processing takes place before the transport from the nucleus to the cytoplasm, where protein synthesis occurs.

The 5' end of pre-mRNAs is stabilized by the addition of a 7-methylguanosine cap that protects the transcript from exonuclease attack, facilitates RNA splicing and transport from the nucleus to the cytoplasm. The 3' end of most eukaryotic mRNAs is defined by cleavage of the primary transcript and addition of a poly-A tail during polyadenylation. Poly(A) polymerase recognizes an AAUAAA sequence and subsequently adds about 200 adenylate (AMP) residues to the 3' end of mRNA. The poly(A) tail facilitates mRNA transport to the cytoplasm as well as translation. mRNA molecules form circular structures due to an interaction between the cap binding complex and poly(A)-binding protein. Circularization is thought to promote recycling of ribosomes on the same message leading to efficient translation.

During a multi-step reaction called splicing introns are precisely excised from the mature mRNA by an RNA-protein complex called spliceosome. Mutually exclusive inclusion of different exons is called alternative splicing and allows the production of different mRNAs from the same pre-mRNA. The RNA processing event, called RNA editing, occurs in some mRNAs and alters the protein-coding sequences.

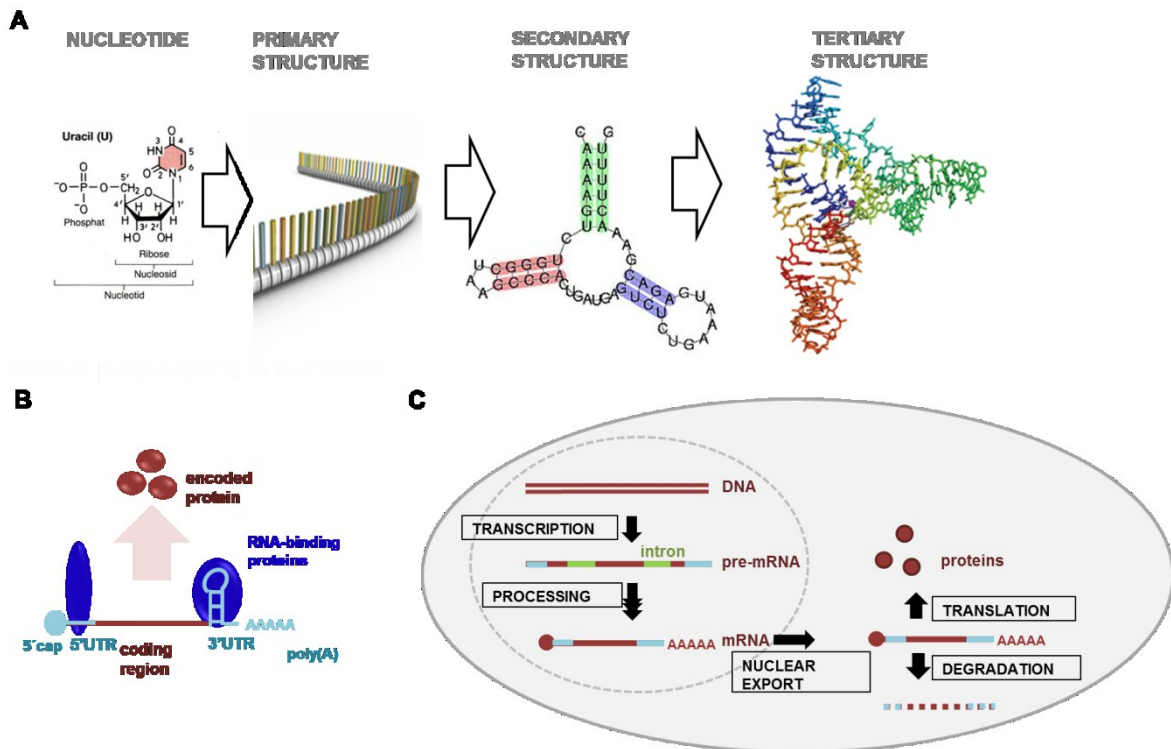


Figure 1 RNA structure and processing. (A) RNA structure principle including nucleotide building blocks, primary, secondary and tertiary structure. (B) mRNA functional parts: 5'cap, 5'UTR, coding region, 3'UTR and poly(A) tail. RNA binding proteins contact conserved regions mainly within the UTRs. (C) mRNA processing starting from transcription, processing including splicing, nuclear export, transport, translation and degradation.

1.2.2 mRNA subcellular localization

1.2.2.1 mRNAs local translation

As eukaryotic transcription and translation is compartmentally separated, eukaryotic processed mRNA has to be transported to the cytoplasm. Transport is also required for mRNA targeting to free-floating or ER-associated ribosomes assuring appropriate protein distribution within the cell. Beyond that, transport to and translation at specific subcellular locations allows autonomous spatio-temporal control of gene expression and saves energy in cellular transport (Nasmyth and RP Jansen 1997) (BASSELL et al. 1999).

Local translation is particularly important for cells with complex architectures or pronounced polarization (Figure 2A). A locally specific mRNA repertoire is needed for

patterning of the *Drosophila* embryo by establishing polarity of morphogenetic gradients in oocytes (Ferrandon, Elphick, Nüsslein-Volhard, et al. 1994). Both *bicoid* and *oskar* mRNAs are specifically transported to the anterior or posterior pole, respectively (Kim-Ha et al. 1991). A similar system of cell fate determination through asymmetric cell division has been observed in budding yeast, where Ash1 protein, the determinant for mating type is localized to the daughter cell (Sil and Herskowitz 1996).

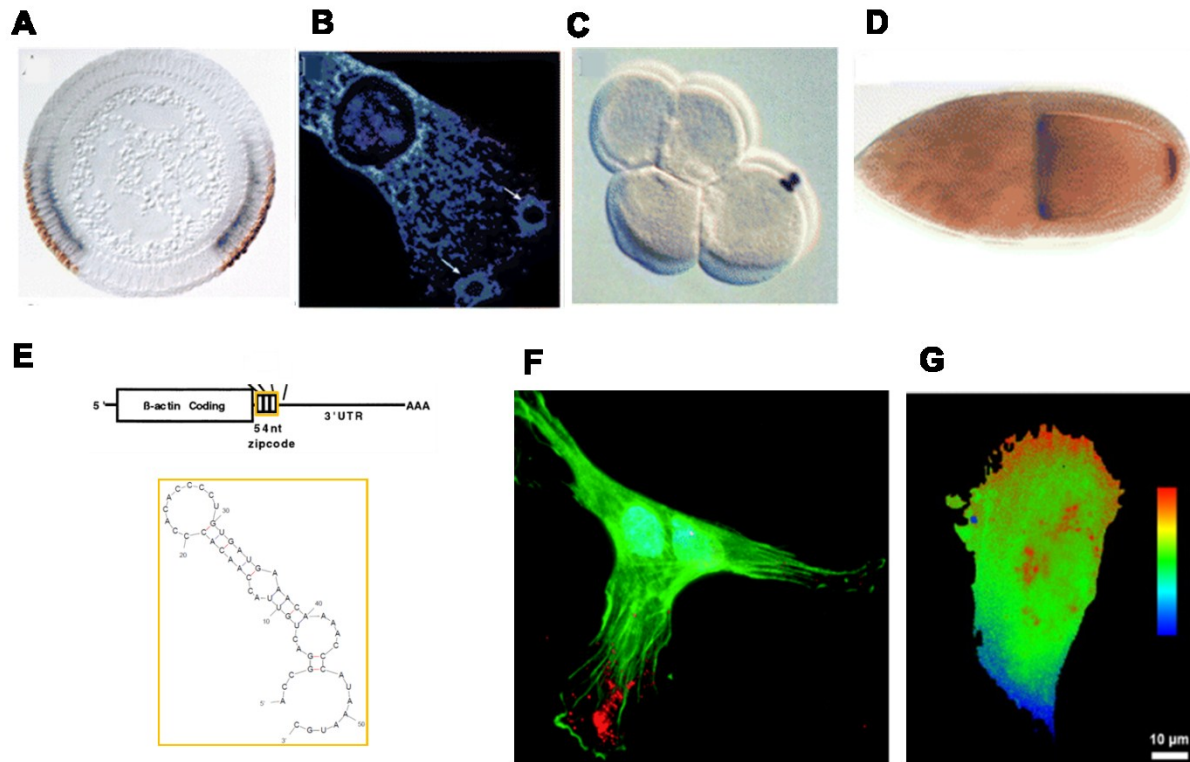


Figure 2 Subcellular localization of mRNAs. (A-D, F) Examples of localized mRNAs. (A) *brinker* mRNA (blue) localizes basally in the *Drosophila* blastoderm embryo, whereas short gastrulation mRNA (brown) is concentrated apically (first) (Jazwinska et al. 1999). (B) recruitment of total RNA (blue) to focal adhesion complexes after cell binding to extracellular matrix-coated beads (arrows) (Chicurel et al. 1998). (C) localization of HrZF-1 mRNA to the posterior-vegetal cytoplasm in a 8-cell embryo of the ascidian *Halocynthia roretzi* (Sasakura et al. 2000). (D) *bicoid* (black) and *oskar* (red) mRNAs localize to the anterior and posterior poles of the *Drosophila* oocyte (upper left) (Isabel M. Palacios and Johnston 2001). (E-G) The β -actin mRNA contains a subcellular targeting sequence called zipcode. (E) β -actin mRNA yielding the 54 nt zipcode sequence; zipcode secondary structure (yellow box). (F) Migrating fibroblasts showing β -actin protein (green) and mRNA (red) accumulation at the leading edge (BASSELL et al. 1999). (G) ReAsH labeling in C2C12 cells reveals the sites of β -actin translation. A reporter construct for newly translated β -actin protein pulse-labeled by ReAsH, pseudocolored ratio image. β -actin synthesized during the chase period is localized to the perinuclear region and the leading edge of the cell. (Rodriguez, Shailesh M. Shenoy, et al. 2006e)

1.2.2.2 Mechanism of mRNA transport

Mature mRNAs are exported through the nuclear pore after nuclear processing. *Cis*-acting elements on the mRNA contain zip-codes that specify RNA targeting to a specific subcellular location. These codes are recognized by proteins called *trans*-acting factors that bind the zip-codes and act as adaptors in the assembly of larger ribonucleoprotein particles (RNPs). Long- and short-range transport tracks are formed by microtubules and microfilaments, respectively. Some mRNAs seem to require both microfilament- and microtubule-dependent transport routes (Bassell and Singer, 1997). The actual movement along the cytoskeleton is mediated by molecular motors that have affinity for both the cargo and the tract. Dynein and kinesin mediate the movement of RNPs along microtubules and myosin along actin filaments (Muslimov et al. 2002) (Gary J Bassell and Kelic 2004). During transport, mRNAs are translationally dormant until this inhibition is released at their final destination. Once transported, mRNA is anchored to either the tubulin or the actin cytoskeleton for translation (Kislauskis *et al.* 1994, Latham *et al.* 1994, Morris *et al.* 2000, Shestakova *et al.* 2001).

1.2.2.3 β -actin mRNA transport

β -actin mRNA serves as well-studied model for local translation. On-site actin polymerization is important for the extension of lamellipodia, filopodia or pseudopodia in moving cells (Rafelski and Theriot 2004). Initiated by local cues, subcellular actin translation not only facilitates autonomous fine-tuning but also circumvents energy-consuming transport of β -actin protein. Transport and local β -actin protein synthesis are conserved mechanisms in moving chicken embryonic fibroblasts (JB Lawrence and R H Singer 1986), growth cones of chicken neurons (Q Zhang, Kazuo Harada, et al. 2001k) and dendrites of hippocampal neurons (Taesun Eom et al. 2003) (Figure 2E-G).

A 54 nucleotide (nt) zipcode within the 3'UTR is essential for β -actin mRNA sorting to the leading edge (Kislauskis, Zhu, and R H Singer 1994a). Zipcode binding protein (ZBP1) interacts with that RNA motif within the nucleus and initiates subcellular transport. Both translational silencing of β -actin mRNA and its incorporation into RNPs is mediated by ZBP1. PDGF has been shown to induce the transport of β -actin mRNA to the fibroblast lamellae

(Latham *et al.* 1994), and cAMP-PKA pathway has been suggested to be involved in regulating the localization of the β -actin mRNA in cultured neurons (Bassell *et al.* 1998).

1.2.2.4 Local translation of neuronal mRNAs

As neurons are unique among cells regarding their extreme functional and morphological polarity, decentralization of gene expression control has proven particularly important. The ability of each synaptic terminal to change strength of their connection with experience is known as the cellular mechanism underlying learning and memory (Bliss and Collingridge 1993). The long-lasting form of synaptic plasticity is dependent on protein synthesis (JB Flexner *et al.* 1963). Therefore, it was hypothesized that mRNA transport and local translation could function as a “synaptic tag” that dynamically and specifically responds to stimulation driving the establishment and/or the maintenance of synaptic connections (Uwe Frey and Morris 1997). Further indication for dendritic protein expression came from the detection of components of the translation machinery and several mRNAs in post-synaptic compartments of vertebrate and invertebrate neurons (O Steward and Levy 1982) (Feig and Lipton 1993). The first direct functional link was shown with the requirement of dendritic protein synthesis for the rapid enhancement of synaptic transmission induced by brain derived neurotrophic factor (BDNF) in hippocampal Schaeffer collateral synapses (Kang and Schuman 1996). In line with activity-induced changes in spine morphology, proteins encoded by activity-regulated mRNAs alter actin dynamics or spine size including ARC, actin and LIMK1 (Oswald Steward and Worley 2001) (Schratt *et al.* 2006). Other dendritically localized mRNAs play a role in receptor trafficking and regulation as well as extracellular secretion.

Activity can alter both mRNA transport and dendritic translation. Specific mRNAs including ARC and CaMKII α are labeled for transport via their dendritic targeting elements (DTEs) within the 3'UTR (W Link *et al.* 1995) (Mori *et al.* 2000) (S Miller, Yasuda, Coats, Y Jones, Martone, and Mayford 2002a). RNA-binding proteins like Staufen, ZBP1 and fragile X mental retardation protein (FMRP) recognize these elements and form RNA protein particles (RNPs) that are sent to the dendrite (Köhrmann *et al.* 1999) (HL Zhang *et al.* 2001) (JC Darnell *et al.* 2001). Neuronal RNPs are transported by the kinesin KIF5 along microtubules and finally are

translocated into spines by the actin-based motor myosin Va (Kanai et al. 2004) (Yoshimura et al. 2006).

Translation at the synapse is regulated by diverse mechanisms that either target all RNAs present or a certain subset of transcripts. General regulators including translation initiation or elongation factors and the synthesis of ribosomal proteins are controlled via the same pathway. Both FMRP and CPEB1 bind to certain 3'UTRs, recruit a protein complex and transiently inhibit the target RNA translation until activity-dependent phosphorylation (Mendez and Richter 2001) (Garber et al. 2006). Even more specific inhibition is mediated by local miRNAs including BDNF-induced silencing of LIMK1 mRNA by miR134 (Schratt et al. 2006).

Despite recent success in determining identity and function of dendritic mRNAs very little is known about how the molecular identity of individual synapses is set up or maintained. Another unresolved question includes the mechanisms for mRNA recruitment to and anchoring at the activated synapse which determines spatial specificity. Insights into molecular mechanisms will allow the examination of the popular molecular model for memory formation which involves a master protein that is highly regulated on the mRNA level (Kang and Schuman 1996).

Similarly to local dendritic translation, presynaptic protein synthesis plays a role in the navigation of axonal growth cones in developing neurons, during regeneration of injured axons and in specific classes of vertebrate and invertebrate neurons (X-hui Zhang and Poo 2002) (Brittis et al. 2002) (Ming, Wong, Henley, et al. 2002).

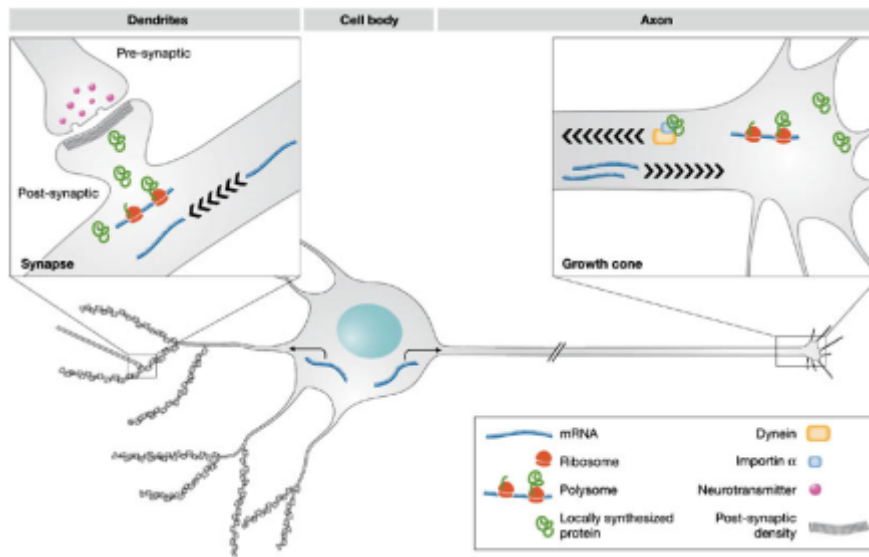


Figure 3 Regulation of neuronal functions by localized mRNAs. Schematic of a polarized neuron. For dendrites, translationally active mRNAs (polysomes) are concentrated at the base of the dendritic spines. Post-synaptic protein synthesis is regulated by trans-synaptic stimuli where the locally synthesized proteins contribute to synaptic components of the dendritic spine, translational machinery and cytoskeleton. Activity also selectively targets some dendritic mRNAs to activated synapses. For axons, ribosomes appear uniquely concentrated in growth cones. Axonal protein synthesis is regulated by guidance cues in growing axons and by injury in mature axons. Guidance cues also modulate anterograde transport of axonal mRNAs. (Gary J Bassell and Twiss 2006)

1.2.2.4.1 CaMKII α mRNA dendritic targeting

Ca²⁺/calmodulin-dependent protein kinases II (CaMKII) are serine/threonine-specific protein kinases that are regulated by the Ca²⁺/calmodulin complex. CaMKII is involved in many signaling cascades and is considered an important mediator of learning and memory (Yamauchi 2005). One of the major isoforms, CaMKII α , has been found to play a critical role in the induction and maintenance of LTP (Soderling 2000). Both, CaMKII α mRNA dendritic targeting and translation are activity-dependent processes and locally synthesized CaMKII α protein is thought to be incorporated into synapses that are being modified, altering their signaling capabilities (Ouyang et al. 1999) (Figure 4).

The 3'UTR is necessary and sufficient to mediate dendritic CaMKII α localization (Mayford et al. 1996). Dendritically translated CaMKII α protein has proven essential for late phase LTP and memory consolidation (S Miller, Yasuda, Coats, Y Jones, Martone, and Mayford 2002b).

Movement of RNA granules containing CaMKII α mRNA were monitored by RNA imaging using the MS2 system (see 1.5.3.2) (Rook et al. 2000) (Figure 4C). This study revealed the transition of CaMKII α mRNA from an oscillatory granule to an anterograde motile pool upon depolarization.

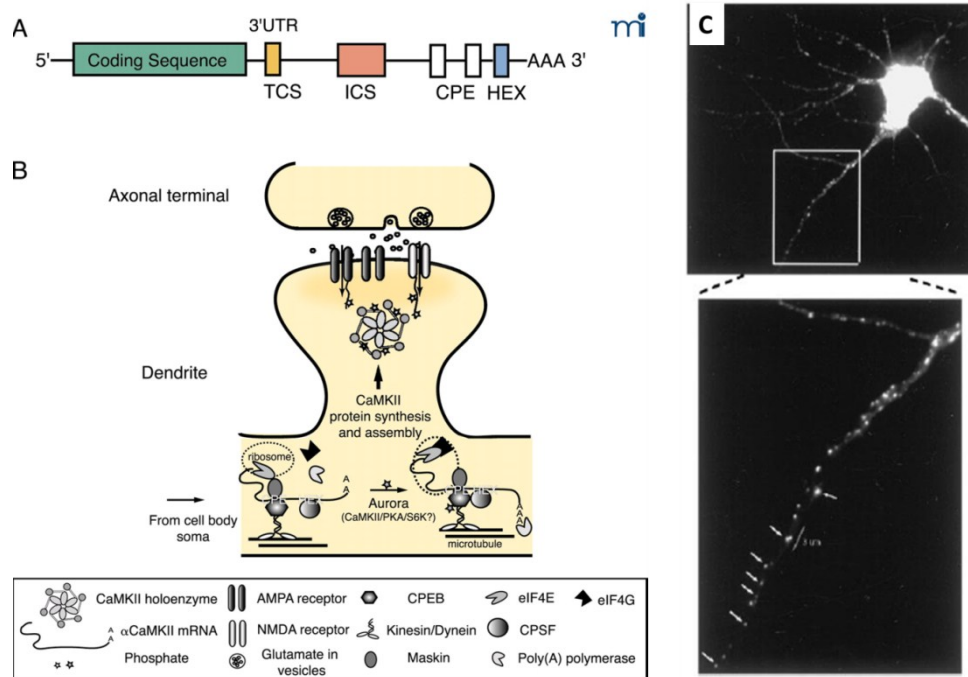


Figure 4 Dendritic CaMKII α mRNA. (A) Structure of CaMKII α mRNA including coding sequence and 3'UTR with different dendritic targeting elements: the Targeting Cis-Sequence (TCS), Inhibitory Cis-Sequence (ICS), two Cytoplasmic Polyadenylation Elements (CPEs) and the hexanucleotide polyadenylation signal (HEX) **(B)** Regulation of dendritic targeting and translation of CaMKII α mRNA. Dendritically targeted CaMKII α mRNA interacts with CPE and CPEB and is shuttled to dendrites by motor proteins (kinesin or dynein). Maskin binds CPEB and thereby inhibits translation until sustained synaptic activity activates a kinase (Aurora) to phosphorylate and activate CPEB (Griffith et al. 2003). **(C)** Imaging of MS2-tagged CaMKII α mRNA by MS2-GFP in rat hippocampal neurons. Arrows highlight CaMKII α at the base of spines. (Rook et al. 2000)

1.2.2.4.2 NMDAR1 splice variants

NMDA (*N*-methyl *D*-aspartate) selectively binds to its specific ionotropic glutamate receptor. NMDAR activation results in the opening of an ion channel that is nonselective to cations. A unique property of the NMDA receptor is its voltage-dependent activation, a result of ion channel block by extracellular Mg²⁺ ions. This renders the flow of Na⁺ and small amounts of

Ca²⁺ ions into the cell and K⁺ out of the cell voltage-dependent (Cull-Candy et al. 2001). Calcium flux through NMDARs plays a critical role in synaptic plasticity.

The NMDAR forms a heterotetramer between two NMDAR1 and two NMDAR2 subunits. The modular composition of NMDAR1 includes an extracellular agonist binding domain, a transmembrane and a cytoplasmic domain containing a phosphorylation and protein interaction sites.

NMDAR1 splicing is a well-studied example for the link between splicing and synaptic plasticity. NMDAR1 mRNA contains 3 alternatively spliced exons 5, 21 and 22 which results in at least seven mRNA isoforms that differ in their physiological properties or subcellular distribution (Zukin and Bennett 1995).

Exon 21 encodes for the cytoplasmic C1 peptide cassette that is important for NMDAR1 membrane trafficking, phosphorylation by protein kinases C and A, protein interaction and NMDAR1-induced gene expression (Bradley, Carter, et al. 2006b) (Ehlers et al. 1998) (S Okabe et al. 1999) (Scott et al. 2001) (Tingley et al. 1993) (Standley et al. 2000). Exon 21 inclusion is favored after KCl-induced polarization in several neuronal cell types (J-A Lee et al. 2007). Highly dynamically regulated splicing is mediated by 3 KCl-responsive elements within exon 21. Two elements are responsive to CaMKIV and one constitutes a binding site for the splicing repressor heterogeneous nuclear ribonucleoprotein A1 (hnRNP A1) (An and Grabowski 2007). Further regulators include NOVA1 and 2, hnRNP H and NAPOR with binding sites located within the intron between exons 21 and 22 (L ZHANG et al. 1999) (J Han 2005)(J Ule et al. 2005) (W ZHANG et al. 2002) (YYL Yang et al. 1998).

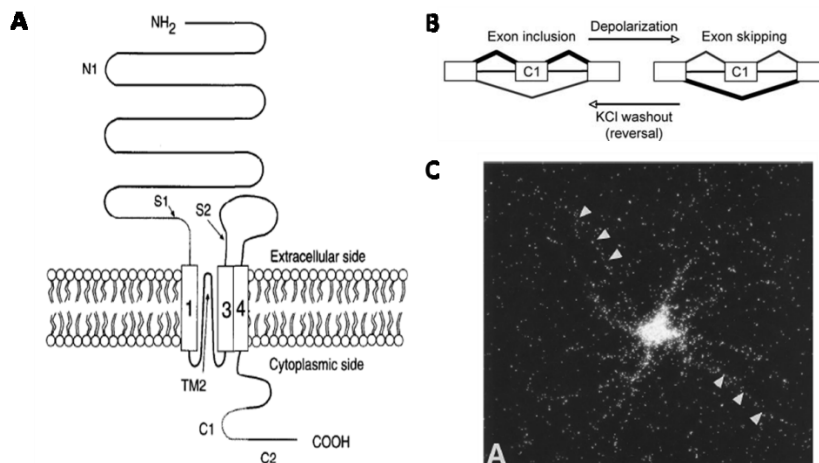


Figure 5 NMDAR1 exon 21 splicing. (A) NMDAR1 protein domains (Zukin and Bennett 1995) (B) and depolarization-dependent splicing of NMDAR1 exon 21 (C1 protein domain) in neurons (An and Grabowski 2007). (C) NMDAR1 in situ hybridization revealing somatic and dendritic (arrowheads) localization in rat hippocampal neurons. (Gazzaley et al. 1997)

1.2.3 mRNA turnover

mRNA turnover is determined by the rate of transcription versus degradation and varies in a range of minutes to days among different mRNAs. The shorter the lifetime the more flexible is the cellular protein expression to altering needs.

1.2.3.1 Balancing translation and mRNA degradation

Both ends of actively translated transcripts are bound by ribosomes, the eukaryotic initiation factors eIF-4E and eIF-4G, and poly(A)-binding protein. Thereby, it is protected from 5' end decapping by DCP2 and exonuclease digestion of the 3' end. Poly(A) tail removal would disrupt the circular structure, destabilize the cap binding complex leading to the degradation by the exosome or the decapping complex. mRNA degradation can furthermore be initiated by RNA interference (RNAi) including the binding to siRNAs and miRNAs as well as by internal AU-rich sequences. Processing bodies (P-bodies) are cytoplasmic foci for target mRNA storage before degradation or translation. These subcellular RNP granules contain proteins involved in decapping, storage and miRNA repression (Parker and Sheth 2007).

1.2.3.2 Nonsense mediated decay and the exon junction complex

Eukaryotic messages are subjected to surveillance by nonsense mediated decay (NMD). NMD is a mechanism to remove transcripts with premature termination codons (PTCs) in the message. PTCs can arise via incomplete splicing, transcription errors or leaky scanning by the ribosome causing a frame shift. Detection of a PTC triggers mRNA degradation by 5' decapping, 3' poly(A) tail removal, or endonucleolytic cleavage (Isken and Maquat 2007).

As normal stop codons lie downstream of any splice site, aberrant stop codons are identified by an upstream proximity to splice sites. Molecular recognition of NMD targets is mediated by the exon junction complex (EJC). The EJC is deposited at each splice site during splicing in the nucleus. Eukaryotic initiation factor 4AIII eIF4AIII is the first EJC component that binds to mRNAs in a sequence-independent but position-specific way, 20 nt upstream of an exon-exon junction (Gehring, Lamprinaki, Hentze, and Kulozik 2009a) (Herve Le Hir, Izaurralde, et al. 2000i) (Tange, Nott, et al. 2004j). Recruitment of MAGO (Boswell et al. 1991) and Y14 (Hachet and Ephrussi 2001d) stabilizes eIF4AIII binding by inhibiting its ATPase activity. Thus, MAGO-Y14 keeps eIF4AIII associated to the spliced mRNA during nuclear export (Reichert, *Genes Dev*, 2002). In the cytoplasm, Barentsz (or MNL15) completes the EJC core (Degot et al. 2004), (Van Eeden, I.M. Palacios, Petronczki, Weston, et al. 2001c) that constitutes a platform for the binding of different other RNA-binding proteins involved in diverse RNA processing steps (Hervé Le Hir and Séraphin 2008). The EJC is eventually released during ribosome scanning during the pioneer round of translation (Dostie and Dreyfuss 2002) by the ribosome-associated protein PYM (Bono, Ebert, Unterholzner, Güttler, et al. 2004a) (Nielsen et al. 2009) (Bono et al. 2006) (Gehring, Lamprinaki, Kulozik, and Hentze 2009b). Sharing the same binding site on MAGO-Y14, the nuclear import factor Importin 13 (Imp13) replaces PYM (Bono, AG Cook, Grünwald, Ebert, and Conti 2010a) and reimports MAGO-Y14 into the nucleus (Mingot et al. 2001).

As soon as the translational machinery reaches a PTC, UPF1 is recruited to the site. Interaction of UPF1 with a downstream EJC leads to the dissociation from the ribosome and the rapid degradation of the mRNA.

The DEAD-box helicase eIF4AIII is mainly localized in the nucleus. Proteins of this superfamily use the energy of ATP binding and hydrolysis for the unwinding of RNA duplexes and the remodeling of RNA-protein complexes. DEAD-box proteins belong to the largest

subfamily of RNA helicases called DExD/H-box proteins that possess eight conserved motifs (Cordin et al. 2006).

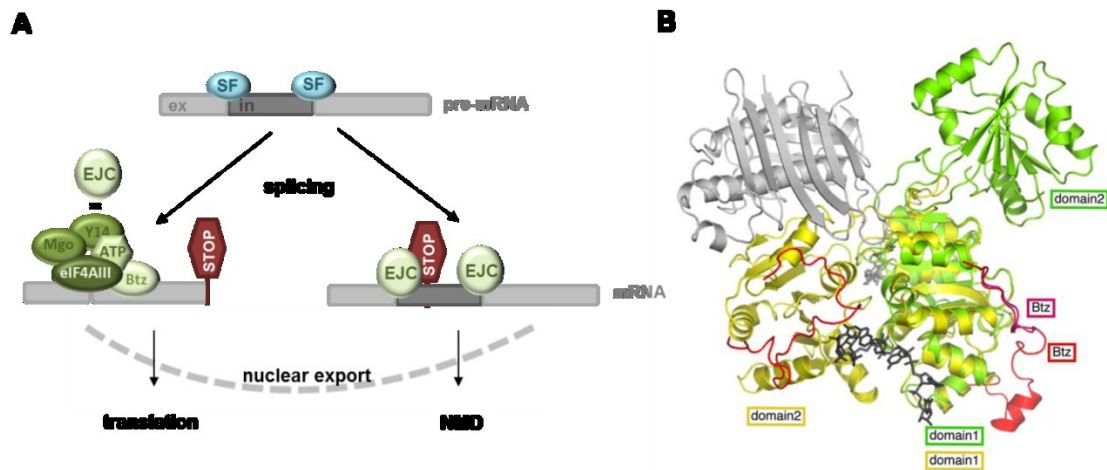


Figure 6 Structure and function of the EJC. (A) Upon splicing of nuclear pre-mRNAs splice factors are replaced by EJC that label exon-exon junctions. Transcripts with premature stop codons are targeted for NMD. exon (ex), intron (in), splice factors (SF), stopcodon (STOP) **(B)** Crystal structure of EJC-bound eIF4AIII (yellow) and free eIF4AIII (green), Barentsz (Btz) (red), MagoY14, ATP and RNA (grey). (Bono et al. 2006)

The crystal structure of the EJC has been solved (Bono et al. 2006). The eIF4AIII dumbbell-like shape originates from two RecA-like domains that are linked by a 10 amino acid cleft-forming linker. The conserved helicase motifs are carried by loop regions at the ends of the RecA β -strands. Free eIF4AIII undergoes a large conformational change upon incorporation into the EJC with the pivotal point for the 160° fold residing within the linker region (CBF Andersen et al. 2006). The induced close proximity of the RecA domains is crucial for the formation of an ATP- and RNA-binding site formed by the helicase motifs. This “on-” state is characteristic for all DEAD-box family members (Tanner and Linder 2001). Both Barentsz and MAGO-Y14 inhibit the eIF4AIII ATPase activity and thereby stabilize the ATP bound “on”-state.

1.3. viral RNA-protein interactions

1.3.1 Arginine-rich motif (ARM) peptides

Regulation and assembly of RNP complexes relies on protein-RNA recognition mediated by conserved sequence motifs. Proteins bearing an Arginine-rich motif (ARM) constitute a prevalent class of RNA binding proteins (Weiss and Narayana 1998) (C A Smith et al. 2000). All proteins share high Arginine prevalence but possess a diverse structural repertoire including β -hairpin, α -helix, and helix-bend-helix. ARM peptides bind their target RNAs with nanomolar affinity. The ARM-RNA interaction is characterized by adaptive conformational transitions (BAYER et al. 2005). The RNA aptamer binding partners contain non-canonical elements such as purine-purine mismatches, base triples, and flipped bases which enlarge and extend the RNA major groove to create specific peptide-binding pocket.

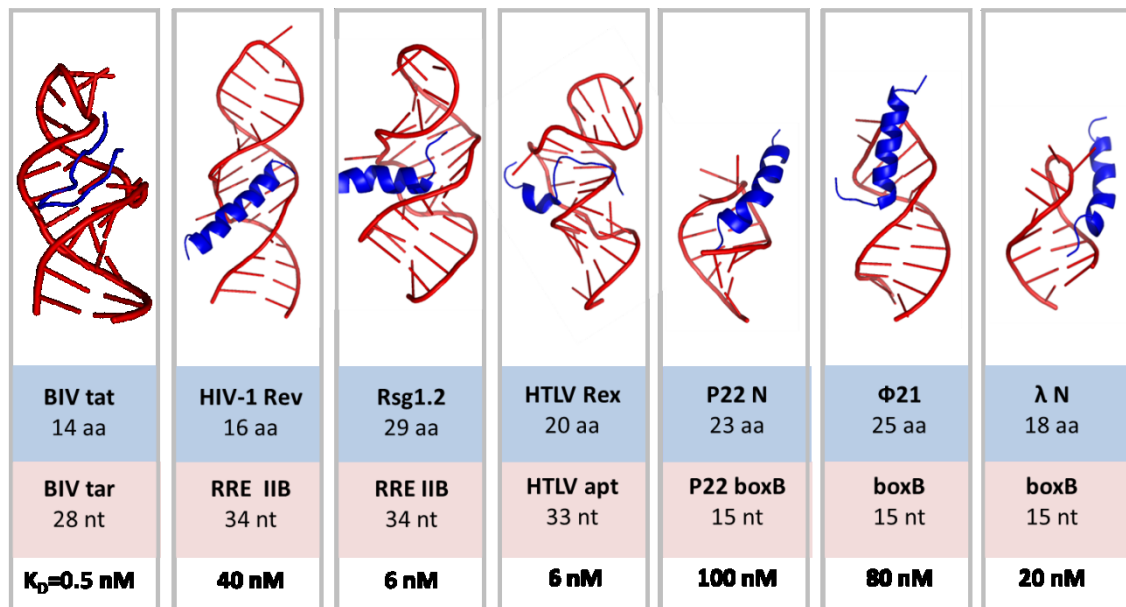


Figure 7 Structure of aptamer-ARM peptide complexes. The RNA aptamers are shown in red and the corresponding peptides in blue. Names, amino acid or nucleotide lengths are indicated below. (PDB ID 1MNB, 1ETF, 1G70, 1EXY, 1A4T, 1NYB, 1QFQ). The affinity of interaction is indicated for each peptide-aptamer pair.

1.3.2 HIV RRE aptamer

Human immunodeficiency virus (HIV) kills human T-cells by taking over cellular processes to make new viruses. Upon attachment to the cell, the virus inserts its RNA genome (Figure 8A) and uses the host machinery to produce genomic copies that are incorporated into new virus particles. The viral Rev protein prevents nuclear trapping of unspliced viral RNA and initiates its nuclear export. The ARM-containing Rev peptide functions through binding to a highly structured segment of HIV RNA called the Rev response element (RRE) (Daly et al. 1989). The minimal RRE is a 234-nucleotide RNA sequence within the *env*-coding region (Malim et al. 1990); more recent studies have suggested that an elongated 351-nucleotide RRE provides optimal Rev function by allowing binding of more Rev molecules (Mann et al. 1994) (Figure 8B). The α -helical Rev peptide binding site is located within the 34-nucleotide stem-loop IIB (Battiste, H Mao, et al. 1996a). Two non-canonical purine-purine pairs within the internal bulge of stem-loop IIB widen the major groove of the A-form RNA double helix and cause an S-shaped fold. Increased accessibility for the Arginine-rich, positively-charged Rev peptide allows contacts to the phosphate backbone and with purine residues (Bartel et al. 1991) (JL Battiste, H Mao, et al. 1996a).

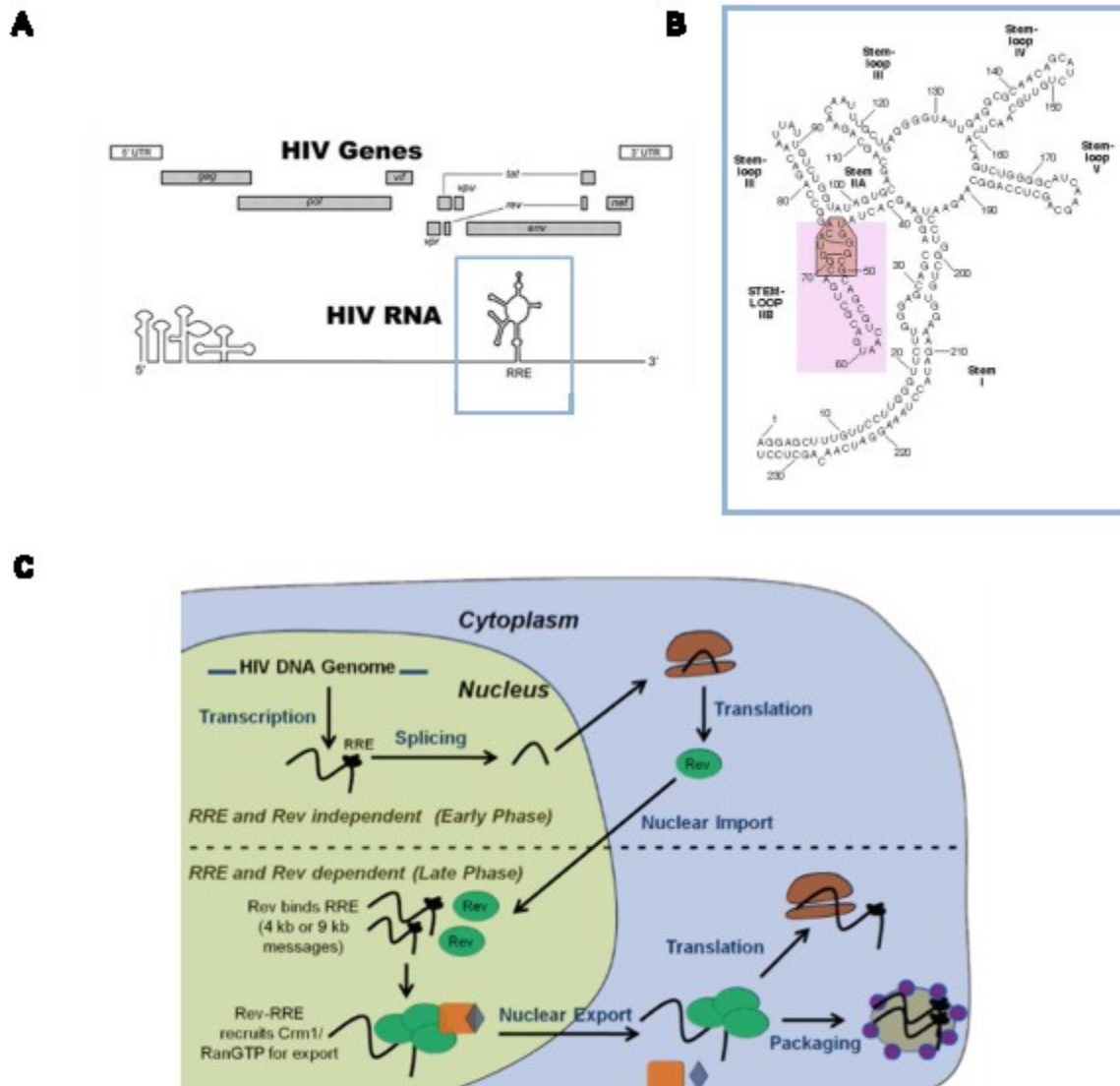


Figure 8 Structure and function of the HIV RRE RNA. (A) Schematic of the HIV-1 genome, showing open reading frames as shaded rectangles and the LTRs as open rectangles. Schematic of the full-length genomic RNA with the position of the Rev-binding site RRE (blue box) (Groom et al. 2009). **(B)** Structure of the HIV RRE element with the Rev binding IIB stem loop (pink square) (homepage, Adriana Heguy) **(C)** HIV RNA export early and late phases. Spliced HIV RNA encoding Rev is exported and translated in the early phase. In the late phase, Rev is imported into the nucleus, where RNA binding and oligomerization occur, accompanied by the formation of an RNP that is a substrate for nuclear export via the Crm1 dependent pathway. Rev and the RRE dissociate in the cytoplasm, Rev shuttles back to the nucleus, and the viral mRNA is targeted for translation or packaging (en.wikipedia.org/wiki/HIV_Rev_response_element).

1.3.3 Rsg1.2 –RRE interaction

Using a bacterial antitermination assay, Harada et al. screened for novel Arginine-rich binding peptides for RRE with non-helical conformation (K Harada, S S Martin, et al. 1996f). The selected Rsg-1 peptide was further mutagenized at 3 positions to yield Rsg 1.2 that binds RRE with 7-fold higher affinity and 15-fold higher specificity than Rev does (Kazuo Harada, Shelley S. Martin, et al. 1997g). Free Rsg 1.2 shows unstructured conformation that becomes partially α -helical upon binding to RRE.

NMR studies reveal two bulged bases (A68, U72) that have different positions when RRE is bound to Rev or RSG-1.2 (Gosser, Hermann, Majumdar, W Hu, Frederick, Jiang, Xu, and Patel 2001a). The widened major groove of RRE is wrapped tighter around Rsg 1.2 than it is around Rev, which may correlate with the higher binding affinity and specificity. A particularly unique feature of the RSG-1.2-RRE interaction is the existence of an amino acid bridge linking the phosphates on one side of the major groove to the other.

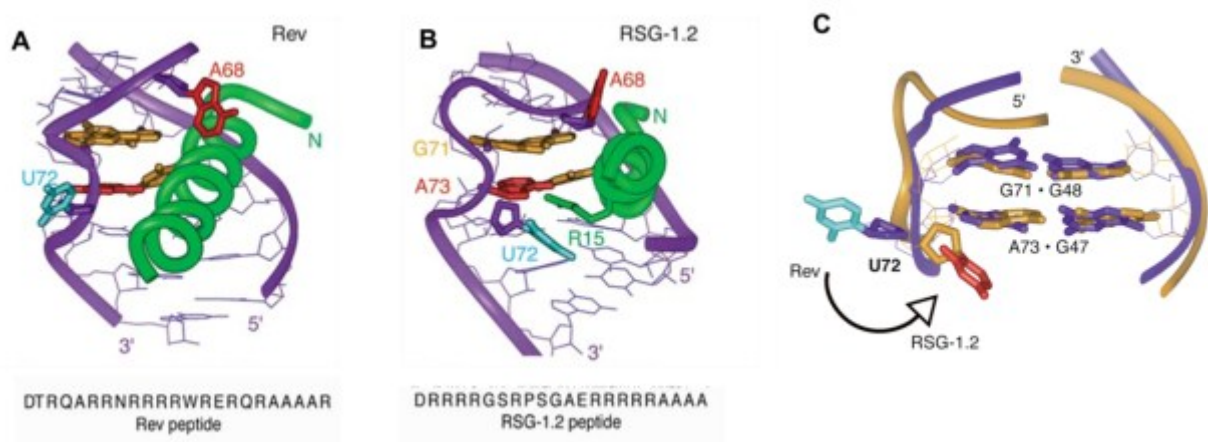


Figure 9 Comparison of the RRE RNA interaction with Rev and Rsg 1.2. (A)(B) The RRE RNA complexed with the Rsg 1.2 peptide (A) or the Rev peptide (B) Sequences (bottom) and crystal structures aligned on the noncanonical G47-A73 and G48-G71 base pairs and in similar orientations. In the Rsg-1.2–RRE-IIB complex, the unpaired U72 is stabilized in the RNA deep groove by stacking with the peptide Arg 15 side chain. U72 is flipped-out into the solvent in the Rev–RRE-IIB complex (C) Conformational transitions of U72 are accommodated by localized changes in the RNA backbone without major disturbances in the flanking noncanonical base pairs. (Gosser, Hermann, Majumdar, W Hu, Frederick, Jiang, Xu, and Patel 2001a)

1.4. Fluorescence imaging

Fluorescence imaging benefits from non-invasiveness and favourable signal-to-noise ratio. This technique has proven suitable for detecting various biological and biochemical processes and has become one of the most powerful tools in biology during the last few decades.

1.4.1 Fluorescent proteins

The bioluminescent Aequorin of the jellyfish *Aequorea victoria* transfers blue light via Resonance Energy Transfer (RET) to green fluorescent protein (GFP) which is expressed in small granules around the rim of the jellyfish belt. Osamu Shimomura was the first to realize that the fluorescent component in the bioluminescent organs of was actually a protein. 20 years later, Prasher cloned the cDNA encoding the 238 amino acids of GFP (Douglas C. Prasher et al. 1992). The unique property of fluorescent proteins to form a visible wavelength chromophore without the need of cofactors was initially shown by the functional recombinant expression of GFP in *E. coli* and sensory neurons of *C. elegans* (Inouye et al. 1985) (Chalfie et al. 1994). Marking a clearly discernible turning point, the biological research community recognized the unique utility of a genetically encoded fluorophore as a marker of gene expression and protein localization. Despite its enormous impact as a tool, the natural purpose of both bioluminescence and GFP fluorescence in jellyfish remains unknown.

X-ray crystal structures revealed that the protein is comprised of an 11-stranded β -sheet wrapped into a cylindrical β -barrel protein, called a β -can (F Yang et al. 1996). The 4-(*p*-hydroxybenzylidene)-5-imidazolidinone moiety that constitutes the actual chromophore (Shimomura 1979) is covalently linked to the polypeptide chain and located near the center of the β -barrel. Chromophore formation by 3 subsequent amino acids Ser 65, Tyr 66, Gly 67 includes cyclization of the main chain, dehydration and oxidation. This spontaneous reaction is facilitated by steric constraints within the β -can and highly conserved residues (Glu 222 Arg 96) (Branchini et al. 1997). In wild type GFP the chromophore exists as an equilibrating mixture of the neutral phenol and the deprotonated, anionic phenolate yielding different absorbance characteristics. The two different protonation states give rise to two absorbance

(at 395 nm and 475 nm) and emission (at 508 nm and 503 nm respectively) maxima (Morise et al. 1974; Heim et al. 1994; Patterson et al. 1997). Excitation of the neutral phenol species results in fast (tens of picoseconds) excited state proton transfer (ESPT) (Chattoraj et al. 1996) of the phenol proton to an internal hydrogen bond network (Brejc et al. 1997). Therefore, regardless of which protonation state is excited, the fluorescence emission spectrum is highly similar.

Structural information constitutes the basis for targeted mutagenesis to generate variants with altered biophysical characteristics. Mutagenesis of the GFP wt includes increased folding efficiency at 37 °C (Cormack et al. 1996) (Cramer et al. 1996) superfolder GFP 2006) as well as reduced dimerization for GFP A206K (David A. Zacharias et al. 2002). Engineering of the wt GFP chromophore resulted in two variants, eGFP (S65T) and Sapphire (T203I) that stabilize the anionic or the neutral state, respectively (Roger Y. Tsien 1998) (Zapata-Hommer and Oliver Griesbeck 2003). Replacing the Y66 by histidine or tryptophan resulted in an imidazole or indole chromophore that emits blue (BFP = blue fluorescent protein) or cyan light (CFP = cyan fluorescent protein) (R Heim et al. 1994) (R Heim and R Y Tsien 1996) (R Heim et al. 1995). A red shift can be achieved by introduction of an aromatic tryptophan at position 203 (T203Y) that creates a stacking interaction with the chromophore (YFP = yellow fluorescent protein) (Ormö et al. 1996) (R M Wachter et al. 1998). As YFP suffers from pH and halide sensitivity, engineering was necessary to yield the more stable variants Citrine (V68L, Q69M, S72A) and Venus (F64L, M153T, V163A, S175G) (Oliver Griesbeck et al. 2001) (Takeharu Nagai et al. 2002).

With the discovery and cloning of fluorescent proteins from reef Anthozoan species (Matz et al. 1999) the FP spectrum could be further broadened. In one of the first examples, a protein named Kusabira Orange (KO) from the mushroom coral *Fungia concinna*. The sequence encoding KO was engineered to add ten amino acids to the N-terminus and mutagenized, resulting in a monomeric version of Kusabira Orange (mKO, $\lambda_{\text{max}}=548$ nm, $\lambda_{\text{em}}=561$ nm) (Karasawa et al. 2004). Recently, the fast-folding variant mKO2 containing 8 additional mutations, was developed for better performance in live cell imaging (Sakaue-Sawano et al. 2008).

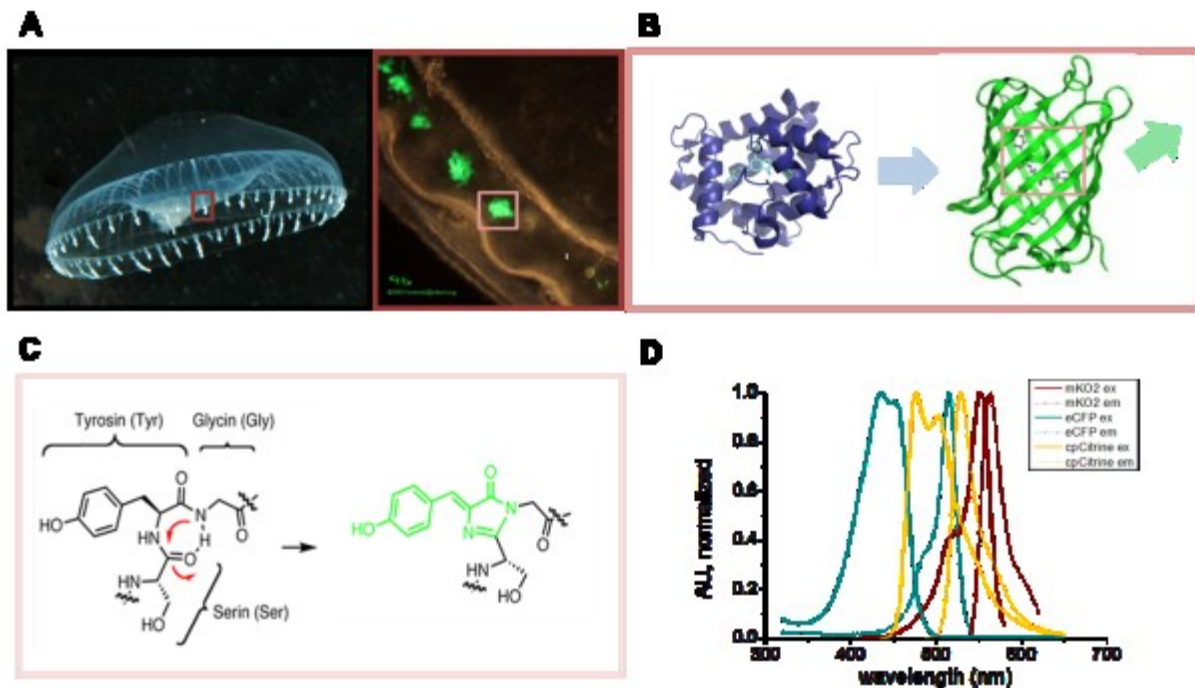


Figure 10 Fluorescent proteins. (A) *Aequoria victoria* and its photoorgans. (Steve Haddock, Monterey Bay Aquarium Research Institute) (B) Structures of Aequorin (1EJ3) that emits blue light to GFP (1EMA) which in turn emits green light. (C) Chromophore formation by GFP amino acid residues. (D) Spectra of FPs used in this study. Excitation (straight) and emission (dotted) spectra.

1.4.2 Genetically encoded fluorescent biosensors

The aim of fluorescent biosensors for live-cell imaging is to convert a molecular event into an optical signal that can be detected microscopically. Fluorescent proteins have been used to generate a variety of biosensors to optically monitor biological phenomena in living cells. Biosensors based on fluorescent proteins have many advantages over synthetic dyes including construction by genetic manipulation, spontaneously acquired fluorescence and simple delivery and intracellular targeting. A potential drawback of FP-based biosensors are their bulkiness, rate-limiting chromophore formation and photobleaching. The strategy is premised on the idea that a cellular signal can induce a change in the FP thus altering fluorescence.

1.4.2.1 Single FP biosensors

The design of single fluorophore biosensors aims at reversibly destabilizing a bright chromophore state. Single FPs exhibit natural pH sensitivity as the deprotonation of the chromophore correlates with high fluorescence quantum yield and an absorption shift from 405 to 488 nm.

This direct correlation was exploited for the design of pH-sensors called pHluorins. The engineering of the redox-sensor roGFP required mutagenesis that renders chromophore protonation dependent on the redox status of the FP was used (Dooley et al. 2004). roGFP contains two surface-exposed cysteines that form disulfide bonds which promote chromophore protonation. Ratios from excitation at 405 and 488 nm indicate the extent of roGFP protonation and oxidation.

In order to render biophysical properties dependent on an analyte molecule, e.g. H_2O_2 or Calcium, a detecting protein is fused to an FP endowing the resulting biosensor with a specific functionality. Detector proteins can be inserted into specific sites of the FP barrel while preserving its fluorescent properties (G S Baird et al. 2000). Circularly permuted FPs (cpFPs) have been opened at these positions and rejoined at the original N- and C-termini thereby destabilizing the deprotonated state of the fluorophore (Nakai et al., 2001). Chimeric proteins GCaMP and pericam contain a cpGFP fused to calmodulin (CaM) and its target peptide, M13. Their spectral properties change reversibly with Ca^{2+} concentration probably due to the interaction between CaM and M13, leading to an alteration of the environment surrounding the chromophore.

1.4.2.2 FRET biosensors

A donor chromophore in its excited state can transfer energy to an acceptor chromophore in a mechanism called Förster (or Fluorescence) Resonance Energy Transfer (FRET). This non-radiative transfer can be described by a dipole-dipole coupling of the chromophores. Effective energy transfer depends on the distance of the two chromophores (usually less than 10 nm) and on the Förster Radius R_0 . R_0 describes the distance between the donor and acceptor at which 50% of the excited state energy is transferred from the donor to the

acceptor. It is dependent on the quantum yield of the donor in the absence of the acceptor (Q_D), the refractive index (n) of the medium, the relative orientation of the transition dipoles (κ^2), and the spectral overlap integral (J). The most sensitive range of the distance between the fluorophores R is $0.7\text{--}1.4 R_0$, corresponding to $90\text{--}10\%$ FRET efficiency. R_0 is usually between 40 \AA to 70 \AA , hence, protein conformational change in this range is ideal for the largest dynamic range in FRET biosensors. The FRET signal of a given FRET pair is also modulated by the orientation of the chromophores. For a FRET pair that is not restricted in its movement, the orientation factor is defined by an averaged value of $2/3$.

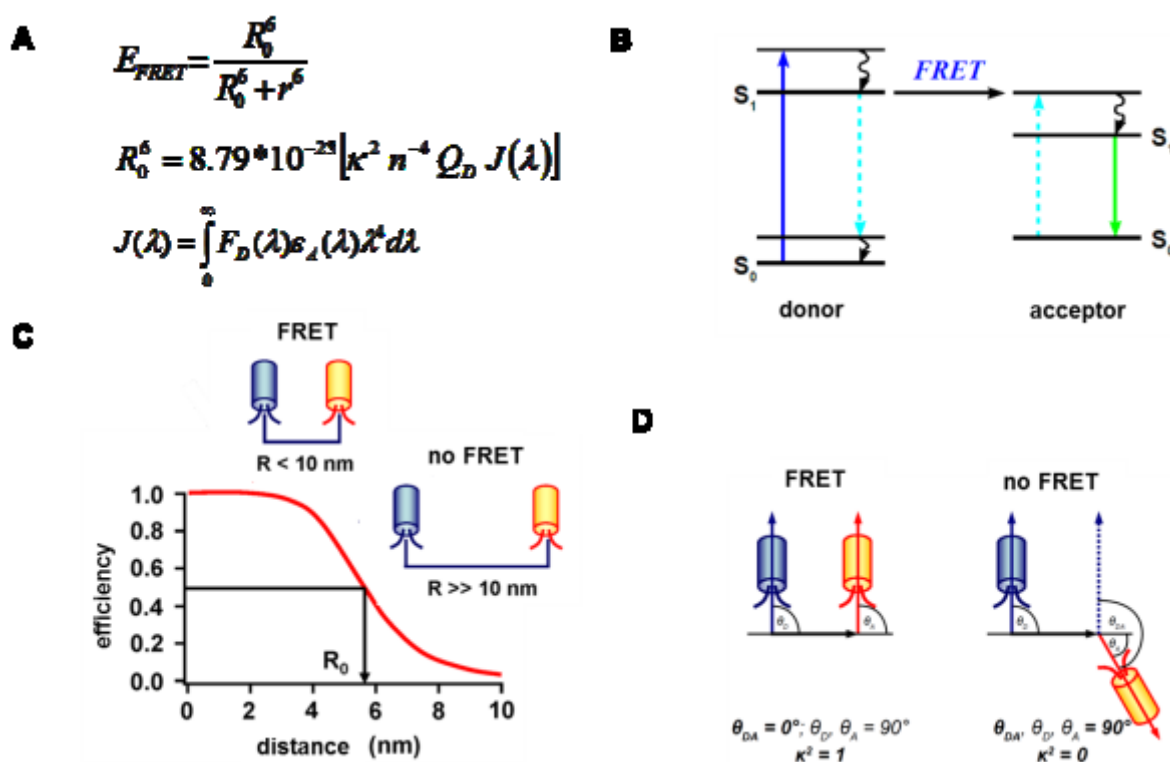


Figure 11 FRET principle. (A) FRET equations E_{FRET} =FRET-efficiency, R_0 =Förster radius [nm], r =distance [nm], R_0^6 =Förster distance [cm^6], n =refractive index of the medium, Q_D =quantum yield of donor in the absence of acceptor, $J(\lambda)$ =overlap integral [$\text{M}^{-1} \text{cm}^3$], $F_D(\lambda)$ =normalized fluorescence intensity of the donor, $\varepsilon_A(\lambda)$ =extinction coefficient of the acceptor at λ [$\text{M}^{-1} \text{cm}^{-1}$], λ =wavelength [cm]. (B) Simplified Jablonski energy diagram for FRET. Donor excitation (blue) acceptor emission (green). (C) FRET efficiency decreases with the distance of the fluorophores and depends on the Förster radius R_0 of the respective FRET pair. (D) FRET rate depends on the orientation of the transition dipole moments of donor and acceptor relative to the vector joining their centers. (Maurel Damien, S. Jähnichen)

Dependency of FRET efficiency on orientation and distance of the donor/acceptor couple can be exploited for the design of biosensors if a detector protein is incorporated. FRET biosensors have been engineered to detect a broad range of molecular events such as protein-binding interactions, conformational changes, catalytic functions and concentration of biomolecules including signaling molecules, cellular metabolites and nucleic acids.

Different FRET biosensor strategies can be distinguished (Figure 12). Bipartite FRET biosensors detect intermolecular interactions and comprise split detector domains that are separately fused to donor or acceptor FP. Intramolecular FRET sensors undergo structural changes in response to the analyte as the FRET pair is covalently linked via a detector domain. FRET protease biosensors consist of a protease cleavage site separating the donor from the acceptor.

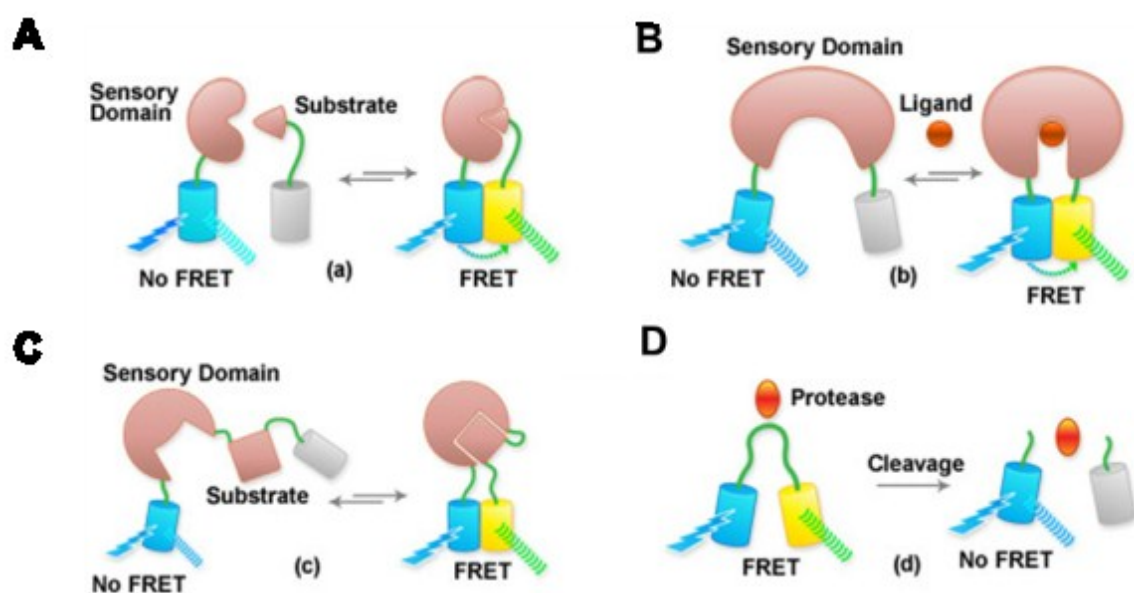


Figure 12 FRET biosensor strategies. (A) FRET between a separate sensory domain and substrate fused to CFP and YFP is induced upon binding. (B) FRET biosensor featuring a single sensory domain and effector ligand that induces a conformational change. (C) Proximity-based FRET sensor based on intramolecular substrate-sensory domain interaction. (D) The FRET pair is separated by a protease cleavage site. CFPs (cyan), YFPs (yellow), sensory domains (flesh-colored), effector ligand (spheres or ellipses) (T.B. Gines, M. W. Davidson, Zeiss tutorial)

Spectral microscopy and confocal microscopy are applied to detect FRET efficiency. Energy transfer results in decreased quantum yield and lifetime of donor fluorescence, the increase

of acceptor fluorescence brightness, and a loss of emission light polarization. These parameters can be measured by stimulated emission (SE) and fluorescence lifetime imaging (FLIM), respectively.

Desirable spectroscopic properties of the FRET pair include sufficient separation in excitation spectra for selective stimulation of the donor GFP, an overlap between the emission spectrum of the donor and the excitation spectrum of the acceptor to obtain efficient energy transfer and reasonable separation in emission spectra between donor and acceptor FPs. Regarding cellular sensor performance, parameters such as bleaching, tissue autofluorescence and pH sensitivity have to be taken into account. Currently, CFP donor and YFP acceptor are the most commonly used FPs to form a FRET pair.

1.5. RNA imaging

Much of the knowledge about intracellular RNA localization has come from RNA visualization in fixed tissues by *in situ* hybridization methods. However, real time *in vivo* imaging techniques are required in order to get insight into dynamics of specific RNAs. In contrast to the protein world, there is no intrinsically fluorescent RNA or aptamer that could be used as a tag for the RNA of interest. In order to render RNAs accessible to fluorescence imaging techniques, several “adaptor technologies” linking both molecule species have been developed. RNA tracking methods comprise labeled oligonucleotide probes, aptamer-binding organic dyes and RNAs targeted by fluorescent proteins.

1.5.1 Chemical RNA dyes

Chemical on-off dyes bind their corresponding RNA aptamer, resulting in an increase in fluorescence emission. RNAs of interest are fused to the aptamer on the DNA level and are transfected and transcribed in cells where the tagged RNA can be visualized after exposure to the dye.

On the molecular level, dye quenching relies on the process of intramolecular photoinduced electron transfer (PET) in which part of a molecule is photoexcited and its fluorescence is quenched by an electron donor species also present in the molecule (Figure 13). The free

dye dissipates stored energy as heat due to rotation and vibration. If a specific aptamer binds to the “surplus” electrons of the donor, then the quenching mechanism is limited, motions are restricted and energy will be released as fluorescence.

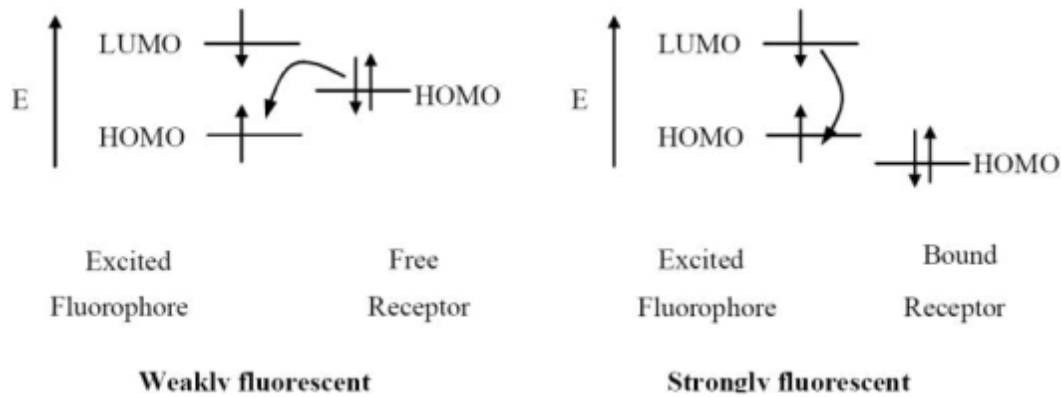


Figure 13 Orbital energy diagram for fluorescent PET sensors before and after RNA binding. HOMO = highest occupied orbital, LUMO = lowest unoccupied orbital. (Fan and WE Jones 2006)

Many short RNA sequences (30-100 nt) that can bind dyes with submicromolar dissociation constant have been developed by *in vitro* selection (SELEX). Initial strategies were based on Triphenylmethane dyes with promising fluorescence enhancement of 2000 fold *in vitro*. An RNA aptamer was initially evolved to bind malachite green (MG) (Grate and C Wilson 1999) but has proven even more suitable to planar MG analogues such as tetramethylrosamine (TMR) and pyronin Y.

The main obstacle in the development of chemical RNA dyes is the transition from *in vitro* to *in vivo* application. Chemical compounds are usually administered exogenously before imaging. Only some hydrophobic synthetic dyes cross passively through the cell membrane. In case of cell impermeability laborious delivery methods such as microinjection have to be used. Once taken up, dye intracellular processing remains unpredictable. Problems range from endosomal entrapment to cytotoxic effects. It was not until the advent of GFP fluorophore-mimicking dyes that aptamer-tagged RNA could be visualized in mammalian cells using a chemical approach (Paige et al. 2011). The SELEX-derived aptamers form a complex called Spinach with the synthetic compounds possessing variable spectral

characteristics similar to FP variants. The system has high multiplexing potential only limited by the number of dyes that can be spectrally distinguished.

1.5.2 Molecular beacons

In order to ensure high specificity and affinity, various attempts have been made to exploit base-pairing ability of RNA for visualization strategies. Fluorescently labeled nucleotide probes, called molecular beacons (MBs), bind to short stretches within the RNA of interest via Watson-Crick base pairing. A fluorophore on one end of the beacon is separated by a short stem-loop from a quencher on the other end.

MBs circumvent target RNA tagging as the probe can be designed to bind to the endogenous RNA sequence. However, target binding potentially causes double-strand-mediated degradation or translational silencing via the RNAi pathway. Target RNA accessibility and specificity require individual optimization and limit the signal-to-noise ratio that doesn't exceed a value of five within cells. Several variations of the MB strategy aim to overcome these problems. (Santangelo 2010) (W Tan et al. 2004). Multiply labeled tetravalent RNA imaging probe (MTRIP) enables the visualization of endogenous RNA with single-molecule sensitivity (Santangelo, Lifland, Curt, Sasaki, Gary J Bassell, Lindquist, and Crowe 2009a). Combining the on-off approach with base-pair complementarity, the Hayashi lab developed the Thiazole Orange dye D514 fused to a probe sequence of interest that becomes fluorescent upon binding to the target RNA (personal communication). Despite these improvements, MBs and chemical dyes still have to deal with the need of invasive delivery methods

1.5.3 Genetically encoded FP-based RNA labels

1.5.3.1 Principle of FP-based RNA labeling

FP-mediated RNA labeling is based on a high-affinity protein-RNA interface. The FP is fused to an RNA binding peptide (RBP) that interacts with an RNA aptamer sequence. This short and specific RNA sequence can be attached to any RNA of interest. Both the FP-fusion

protein and the tagged RNA are encoded within plasmids that have to be transfected into the cell using standard transfection methods. High background signal caused by permanent fluorescence of the FP-fusion protein demands for its subcellular entrapment. Thus, the FP is fused to a nuclear localization signal (NLS) that causes its reimport into the nucleus. Nuclear restriction is only suspended if an aptamer-tagged RNA is exported and transported to more distal subcellular sites (Figure 14A). Non-nuclear FP is only observed if it is bound to the aptamer-tagged RNA of interest which is exported from the nucleus. Consequently, fluorescence in the cytoplasm ideally corresponds to FP-bound RNA of interest (Figure 14B). Application of FP-mediated RNA imaging within the nucleoplasm suffers from a lack of subcellular entrapment of the FP fusion protein. Consequently, high background noise has to be reduced by saturating FP fusion proteins with the target RNA and suitable data processing.

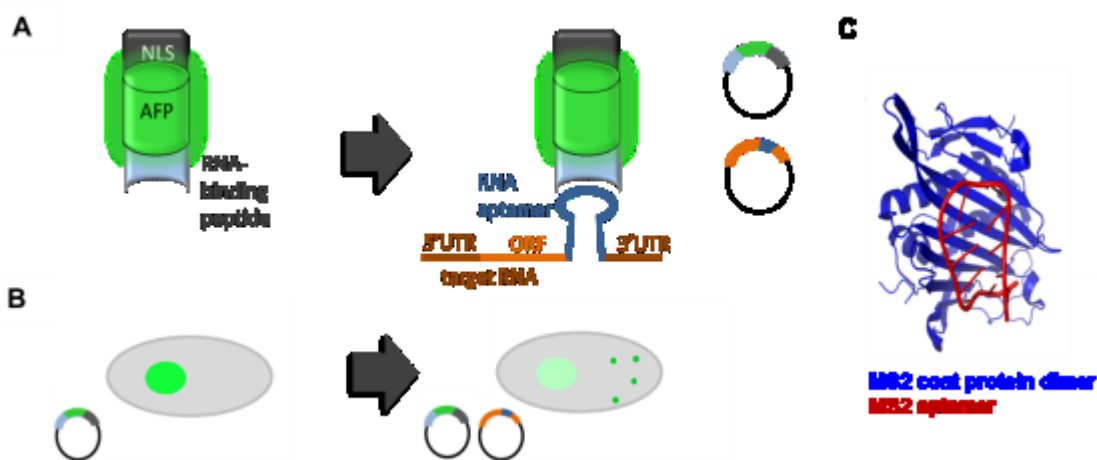


Figure 14 Functional principle of FP-mediated RNA labeling. (A) Schematic of the RNA labeling strategy. An RNA binding peptide is fused to an FP and a nuclear localization signal (NLS). The corresponding RNA aptamer is fused to an RNA of interest. **(B)** Schematic drawing of cells expressing a 3xGFP-4xlambda peptide-NLS fusion protein. In the absence of the aptamer, GFP fluorescence is detected exclusively within the nucleus. Interaction of 4 λ N22 peptides with 4 boxB aptamer repeats indicates localization of boxB-tagged β -actin-zipcode RNA in cells transfected with both constructs (right). **(C)** Crystal structures of the phage MS2 peptide-aptamer complex. The aptamer is forming a hairpin (red) that interacts with a β -sheet structured peptide (PDB 1ZDH).

Current FP-based RNA labeling methods take advantage of naturally evolved high affinity aptamer-peptide pairs. So far, two phage-derived systems have been successfully used for the visualization of RNAs in prokaryotic and eukaryotic cells.

The first genetically encodable RNA sensor for live cell imaging was developed and applied to RNA labeling in *S. cerevisiae* by the lab of Robert Singer (E Bertrand, P Chartrand, et al. 1998a). A dimeric 129 amino acid (aa) MS2 coat protein binds with a K_D of 1 nM to its RNA target (Figure 14B). Affinity has been increased by mutation of both protein and RNA (Peabody and Lim 1996) (Lowary and Uhlenbeck 1987). The MS2 RNA stem-loops are cloned in 6 to 24 repeats in order to enhance signal intensity. Daigle and Ellenberg used a λ N22 derived aptamer-peptide pair for RNA tracking in mammalian cells (Daigle and Ellenberg 2007). The 22 aa α -helix of the phage λ N22 peptide binds to the 15 nt boxB RNA motif with nanomolar affinity ($K_D = 22$ nM) (Figure 7). Again, constructs consisting of 4 copies of the peptide and 4-12 boxB stem-loops have been used. In both MS2 and λ N22 based RNA labeling, no cognate counterpart of the phage RNA aptamer exists in the eukaryotic cell under investigation. Additionally, the two systems are able to discriminately bind in favor of their own RNA by 1000-fold which has been exploited in double RNA labeling (Lange et al. 2008).

An important issue in RNA tagging is the site of aptamer insertion into the RNA of interest. When designing the target RNA-aptamer fusion construct, disruption of important RNA elements has to be avoided. Most established insertion sites are located between the 3'UTR and the poly(A) site (Yamagishi et al. 2009) or between stop codon of the ORF and the 3'UTR (Figure 1A) (E Bertrand, P Chartrand, et al. 1998a). Further undesired impact on RNA function and localization might originate from the secondary structure of the aptamer tag.

1.5.3.2 Application of MS2-based RNA visualization

MS2-based RNA labeling has proven suitable for monitoring different stages of RNA biosynthesis and function in various cell types.

In the first study using MS2, ASH1 mRNA was tagged to 12 MS2 repeats in order to detect single RNA-containing particles transported to the bud tip of *S. cerevisiae* (E Bertrand, P Chartrand, et al. 1998a). Single molecule detection in mammalian cells was not possible

until the attachment of 24 MS2 repeats to β -actin zipcode RNA (Fusco, Accornero, et al. 2003c). This study constitutes a milestone in the analysis of mammalian RNA movement that was detected as static, corralled, diffuse or directed (Figure 15). Most recently, Yamagishi et al. succeeded in defining diffusion coefficients of single β -actin mRNA molecules at the leading edge and the perinuclear region of chicken fibroblasts (Yamagishi et al. 2009). The MS2 system has been proven a versatile tool for RNA tracking in various eukaryotic cell types (Schifferer and Oliver Griesbeck 2009). Particularly, mRNA transport in neuronal axons and dendrites became a field of intense investigation in the last years. MS2-mediated labeling enabled first live images of CaMKII α mRNA moving in anterograde and retrograde directions in dendrites and shed light on its activity-dependent localization (Rook et al. 2000).

Aptamer-tagged RNAs need to be expressed within cells by transfection of plasmid DNA, possibly resulting in overexpression of the aptamer-RNA construct compared to endogenous RNA levels. Overcoming this problem, Haim et al. established a technique called m-TAG for tagging of genomic loci with MS2 repeats in *S. cerevisiae* (Haim-Vilmovsky and Gerst 2011). MS2-based labeling of endogenous mRNA has proven suitable to reveal transcription kinetics in a mammalian cell line (Darzacq, Shav-Tal, et al. 2007b). The generation of a knock-in mouse line with a MS2 binding cassette targeted to the β -actin gene rendered live-cell imaging of single endogenous labeled β -actin mRNA molecules possible (Lionnet, Czaplinski, et al. 2011).

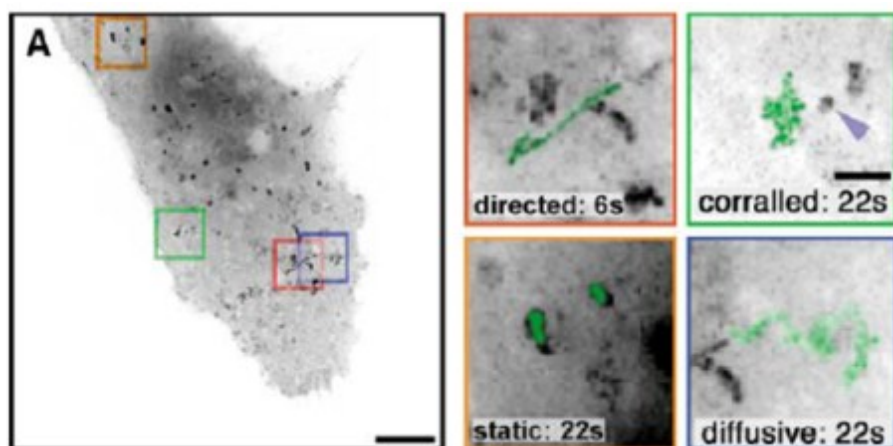


Figure 15 Dynamics of mRNA molecules in the cytoplasm of mammalian cells. Movements of LacZ-14-hGH mRNAs. Cos cells transiently expressing LacZ-24-hGH mRNAs and the MS2-GFP protein were

imaged live. A maximum intensity image projection of 200 time frames on 1 image Scale bars 10 μm (left). mRNA track superimposed (green) from each of the indicated boxed regions scale bar 2 μm (right) (Dahlene Fusco, Nathalie Accornero, et al. 2003c).

1.5.3.3 Short-comings of FP-based RNA label design

A major limitation of the FP-based approach is that free FP fusion proteins cannot be distinguished from ones bound to the target RNA. Permanent fluorescence of the FP necessitates its subcellular restriction in order to distinguish background fluorescence from RNA labeling. In turn, nuclear label import could interfere with the intrinsic targeting of the RNA of interest.

Recent attempts to overcome this lack of specificity take advantage of split FPs (Kerppola 2006) (Rackham and CM Brown 2004). Nonfluorescent N- and C-terminal FP fragments refold to form a functional FP only if they are brought into close proximity to each other. This proximity can be achieved by fusing the split FP halves to two distinct RNA binding peptides that in turn bind to two adjacent target sites on an RNA (Figure 16). In this way, subsequent fluorescence of the complemented FP is rendered dependent on the presence of the RNA of interest. However, split-GFP methods suffer from high background originating from unspecific complementation. The currently used split RNA sensor is based on two halves of the eukaryotic initiation factor eIF4A (Valencia-Burton et al. 2007) and can consequently only be applied for RNA visualization in prokaryotic but not in eukaryotic cells.

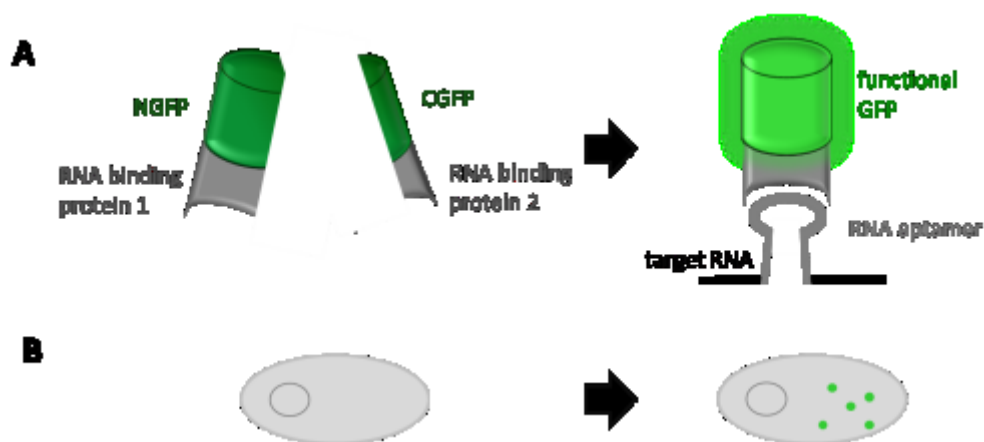


Figure 16 Functional principle of split YFP mediated RNA visualization. (A) The N- and C-terminal fragments of Venus (NYFP and CYFP) are fused to two parts of a split RBP (RBP1, RBP2). Upon coexpression of the corresponding RNA aptamer, peptide complementation promotes reconstitution of Venus. **(B)** Schematic

drawing of a cell expressing the split-YFP label described in (A). In the absence of the aptamer, split YFP fragments are spatially separated and no YFP fluorescence is present (left). Coexpressing plasmids coding for split-YFP and the aptamer-tagged target RNA results in reconstituted YFP emission exclusively at sites where the aptamer-tagged RNA of interest is present (right).

The design of a FRET-based RNA sensor is a strategy to render the fluorescence signal dependent on the presence of the aptamer. The HIV Rev peptide separates the FRET pair only until binding to the target RRE aptamer that results in a conformational change within Rev (Endoh et al. 2005). The induced proximity of donor and acceptor results in a FRET ratio increase that is indicative for RRE-tagged RNAs. However, the first attempt to visualize cellular RNAs failed to show significant signals (Endoh et al. 2008).

Recently, Ozawa et al designed an RNA label that circumvents aptamer attachment to the RNA of interest and allows visualization of native RNA (Ozawa, Natori, et al. 2007d). This approach takes advantage of unique characteristics of the RNA binding domain of human Pumilio1 (PUMHD) (Spassov and Jurecic 2002). PUMHD consists of eight nucleotide contact sites comprised of three crucial amino acids that each mediate high affinity binding to its cognate target RNA. Due to its modular structure, PUMHD can potentially be engineered to bind to any RNA sequence of choice (Cheong and Hall 2006). The main drawback is the reduced affinity to new target RNA sequences even if they are highly similar to the cognate RNA. Another problem of PUMHD-mediated RNA labeling originates from fluorescence generation upon PUMHD fusion to FP fragments in the absence of target RNA resulting in high background noise (Tilsner et al. 2009).

1.5.4 Recent advances in imaging technology

Suitable RNA live cell imaging approaches have to meet several requirements regarding resolution, sensitivity and cytotoxic effects. Depending on the experimental approach, RNA tracking involves long-term imaging of single transcripts of RNPs that move at a speed of up to 3 $\mu\text{m/s}$.

If high sensitivity is required, wide-field microscopy with deconvolution using charge-coupled device (CCD) detectors has proven suitable (Swedlow and Platani 2002). In order to visualize several RNAs or RNA-binding proteins at once, multi-channel imaging with appropriate filters is required (Weil, Parton, et al. 2010). Spearheading techniques including

stimulated emission (STED) (Hell 2003) or photoactivated localization microscopy (PALM) (Betzig et al. 2006)(Bates et al. 2007) allow for nanoscale fluorescence microscopy down to 20 nm lateral resolution that, in turn, shows that the diffraction limit of 200 nm as described by E. Abbé in 1873 is no longer valid. High sensitivity is especially important for the precise localization of low abundant RNAs, e.g. in dendritic spines.

Laser scanning confocal microscopy removes out-of focus light is used in thick tissue in order to increase contrast. For highly dynamic processes, spinning disc confocal imaging is the method of choice. Multiphoton microscopy like 2-photon-microscopy exploits longer wavelength excitation light and therefore achieves larger penetration depths into biological tissue by using a pulsed laser to excite a given chromophore in two steps (Denk et al. 1990). Data analysis involves pre-processing including deconvolution, denoising and contrasting as well as segmentation for object identification.

1.6 Project goal

As RNAs play important roles in neuronal function, it is critical to follow RNA trafficking and processing in real time in live cells and to assess their time-dependent and activity-dependent localization and transport. Therefore, the major objective of this work was to establish an RNA sensor suitable for live imaging of RNAs in neurons.

Even though FP-based RNA imaging methods have been used for RNA labeling in different cell types, methodical obstacles obviate its routine application for dynamic RNA imaging. An optimal protein-to-RNA ratio is essential and needs to be tested empirically. Further background reduction requires nuclear entrapment of the FP reporter. In this configuration the method is not suitable to study RNA trafficking within the nucleus. It is also unclear to what extent the opposing forces of the nuclear localization signal within the FP label and the RNA export mechanisms influence proper RNA sorting. Incomplete nuclear label entrapment in the absence of tagged RNA constitutes a further source of background noise. As FP label signals are not dependent on the presence of the RNA aptamer, it is not clear how aptamer-bound labels respond after degradation of the aptamer-tagged target RNA.

Consequently, dynamic imaging requires an RNA-dependent reporter signal instead of an inflexible labeling technique. In contrast to current split FP methods that stay in the complemented or “on” state after the first aptamer contact, reversible RNA indicators report both aptamer binding and dissociation. Practical insights into problems of static FP-based RNA labels was the trigger to design several dynamic, aptamer-dependent RNA reporters including a synthetic on-off dye a genetically encoded single fluorophore aptamer sensor and FRET-based biosensors.

The synthetic RNA reporter system we aimed to develop consists of a cell-permeable small molecule probe and a short RNA aptamer that can specifically bind the probe (Figure 17B). The probe is not fluorescent but will become fluorescent upon the binding of the aptamer (see 3.2).

As the need of microinjection and non-specific binding constitute a major problem of chemical dye approaches, an analogous reversible FP-based approach would be the method of choice (Figure 17C-E). The key challenge was to render the fluorescence signal dependent on the presence of the aptamer-tagged RNA of interest. Starting with the simplest reporter design, we speculated that RNA aptamer binding to a non-fluorescent protein could directly

or indirectly alter its emission characteristics (Figure 17C, see 3.3.1). As an alternative, we came up with two reporter principles that both rely on a conformational change of a peptide with an Arginine-rich motif (ARM) upon RNA aptamer interaction. This flexure subsequently transduces a dim FP that is fused to the ARM peptide into a bright protein with increased fluorescence emission (Figure 17D, see 3.3.2). Alternatively, the ARM peptide serves as a functional linker between a FRET pair rendering transfer efficiency dependent on the interaction with the aptamer (Figure 17E, see 3.4).

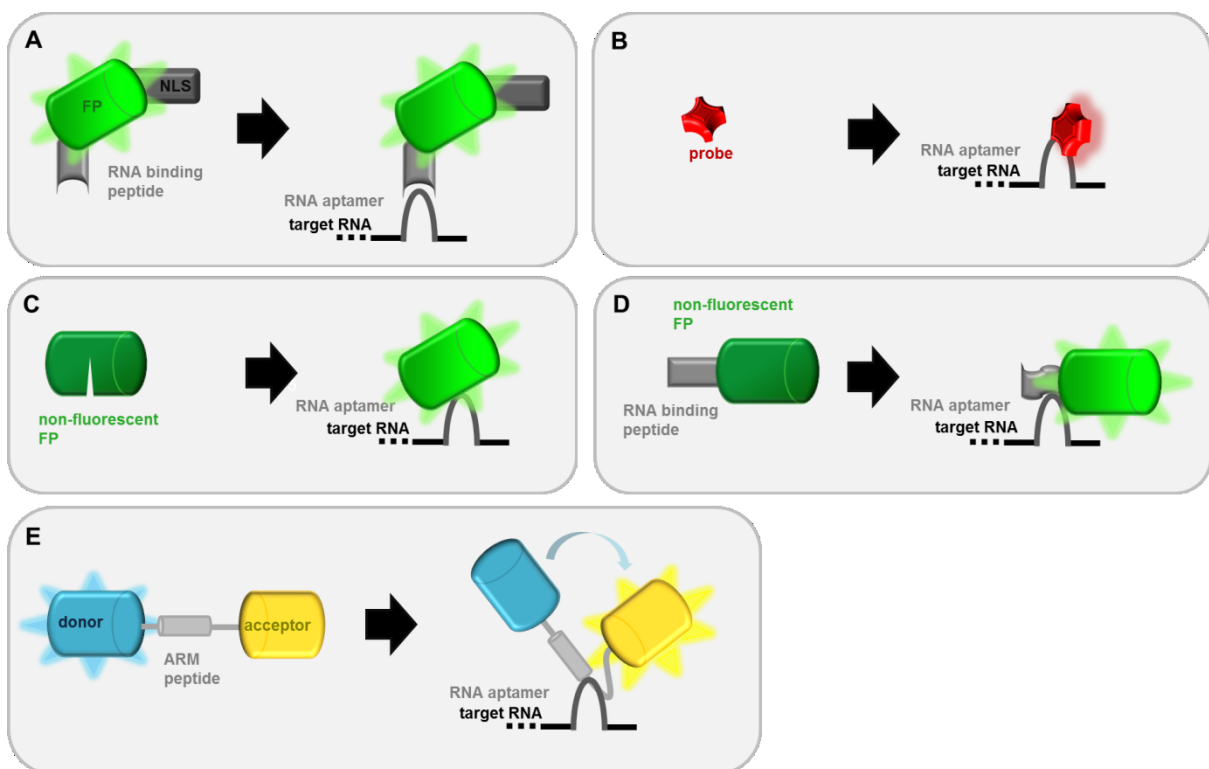


Figure 17 Strategies for RNA labeling and dynamic RNA reporters.

The workflow for sensor development involved initial rational design, recombinant expression and *in vitro* (Figure 18) testing. In order to allow for more powerful molecular evolution, a suitable functional screening method was required (see 3.4.3). The RNA sensor variants with the best *in vitro* characteristics had to be tested in cellular assays probing temporal and spatial dynamics of RNA visualization.

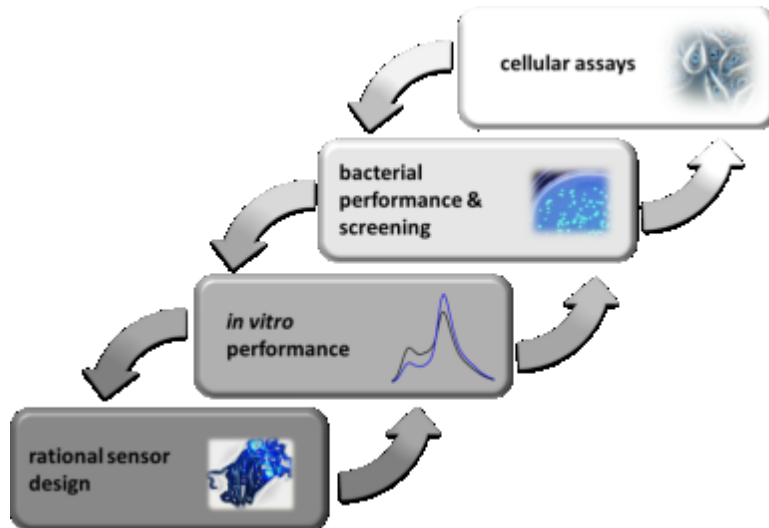


Figure 18 Workflow for biosensor engineering.

Complementing insights obtained from direct RNA tracking, there is a need for fluorescent reporters of RNA binding proteins (RBPs) that control important steps in RNA metabolism. As the EJC is a key player in RNA processing and decay we aimed at the design of a FRET-based fluorescent biosensor that reports different states of the EJC core component eIF4AIII (see 3.5). A FRET eIF4AIII reporter is supposed to allow *in vitro* analysis of EJC formation and disassembly on mRNAs. As eIF4AIII contributes to dendritic mRNA fate, functional imaging would be crucial to investigate its role in neuronal function.

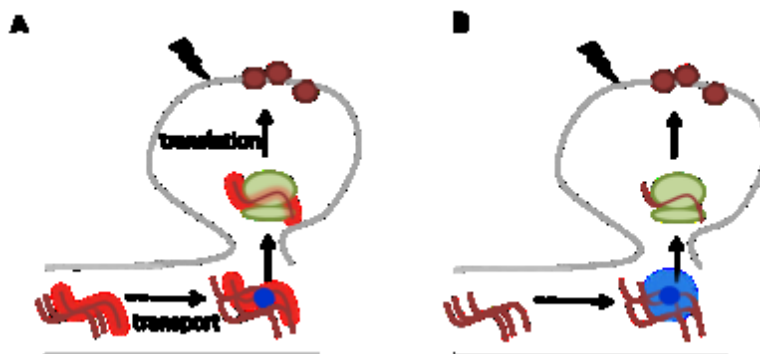


Figure 19 Concepts of visualizing RNA-mediated processes. (A) Tracking of specifically labeled RNAs (red). (B) Functional imaging of RNA-binding proteins (blue)

2. Materials and Methods

2.1. DNA molecular biology

2.1.1 Polymerase Chain Reaction (PCR)

Amplification of DNA by PCR that has initially been developed by Mullis takes advantage of thermally stable DNA polymerases. Bacterial or archeal enzymes that can be used for PCR include Taq, Vent and Pfu DNA polymerases.

Taq polymerase was used for DNA amplification that tolerates or requires mutations resulting from the absence of any proofreading activity.

Fusion of Pfu-based DNA polymerase with high affinity double-stranded DNA binding domain results in Herculase II Fusion enzyme yielding favourable characteristics. Herculase II was used for reactions demanding high yield, excellent reliability due to high proof-reading capacity and shorter cycling times.

PCR-reaction mix		
< 1kb product	>1 kb product	
1.2 µL	1.2 µL	DNA template (~200 ng/ µL)
0.25 µL	0.25 µL	forward primer (100 µM)
0.25 µL	0.25 µL	reverse primer (100 µM)
10 µL	10 µL	5x Herculase II reaction buffer
2 µL	2 µL	DMSO
0.5 µL	0.5 µL	dNTP solution (12.5 mM)
0.5 µL	1 µL	Herculase II fusion DNA polymerase
34.3 µL	34.8 µL	H ₂ O
50 µL	50 µL	total reaction volume

All components were added on ice and the reaction was started by an incubation step at 95 °C. Hot start increases specificity and obviates primer dimer formation.

PCR reaction				
		< 1kb product	>1 kb product	
	95°C	5 min		
29 x	95°C	30 s		denaturation
	52°C	2 min		annealing
	68°C	30 s	1 min	elongation
	68°C	5 min		
	15°C	forever		

2.1.2 Error-prone PCR

For the generation of random mutations during PCR, error prone DNA polymerases and reaction conditions were applied that favor mistakes in the reading of the template strand. The Gene Morph mutagenesis kit (Agilent) used combines Mutazyme II DNA polymerase and a novel *Taq* polymerase mutant without proofreading activity in order to achieve minimal bias for mutation rates at the different nucleotides. The mutation frequency ranging from 1-10 mutations per kb was controlled by the amount of template DNA. In order to increase the rate of single mutations, two sequential PCRs were performed using the purified product of the first one for the second reaction.

PCR-reaction mix	
100 nt product	
1 µL	DNA template (~10 ng/µL)
0.25 µL	forward primer (100 µM)
0.25 µL	reverse primer (100 µM)
5 µL	10x Mutazyme II reaction buffer
1 µL	40 nM dNTP mix (200 µM each final)
1 µL	Mutazyme II DNA polymerase (2.5 U/ µL)
41.5 µL	H ₂ O
50 µL	total reaction volume

PCR reaction			
	95°C	2 min	
15 x	95°C	1 min	denaturation
	55°C	1 min	annealing
	68°C	30 s	elongation
	68°C	10 min	
	15°C	forever	

2.1.3 Site-directed mutagenesis via PCR

In order to introduce a point mutation into a DNA template, mutagenesis method based on Fisher and Pei (1997) was executed.[4]

For PCR amplification, primers containing the desired mutation are used that anneal with roughly 21 nt at both the 5' and 3' positions flanking the mutagenesis site. The oligonucleotide primers, each complementary to opposite strands of the vector, are extended during temperature cycling. Incorporation of the oligonucleotide primers generates a mutated plasmid containing staggered nicks. The *Dpn* I endonuclease (target sequence: 5'-Gm6ATC-3') is specific for methylated and hemimethylated DNA. Template DNA isolated from almost all *E. coli* strains is dam methylated and therefore susceptible to *Dpn* I digestion.[5] *Dpn*I specifically degrades the template plasmid and selects for the vector product yielding the desired mutation.

mutageesis reaction mix		
mutageesis	control	
1 μL	1 μL	DNA template ($\sim 200 \text{ ng}/\mu\text{L}$)
2.5 μL	2.5 μL	forward primer ($50 \text{ ng}/\mu\text{L}$)
2.5 μL	25 μL	reverse primer ($50 \text{ ng}/\mu\text{L}$)
10 μL	10 μL	5x Herculase II reaction buffer
0.8 μL	0.8 μL	dNTP solution (12.5 mM)
0.5 μL	-	Herculase II fusion DNA polymerase
32.7 μL	33.2 μL	H_2O
50 μL	50 μL	total reaction volume

mutagenesis reaction				
		< 1kb product	>1 kb product	
	95°C	30 s		
16 x	95°C	30 s		denaturation
	52°C	1 min		annealing
	68°C	30 s	1 min	elongation
	68°C	5 min		
	15°C	forever		

template digest			
mutagenesis	positive control	negative control	
20 μL	20 μL	20 μL	mutagenesis product
1 μL	-	1 μL	forward primer ($50 \text{ ng}/\mu\text{L}$)
21 μL	21 μL	20 μL	total reaction volume
incubate for 4 h at 37°C			

1 μL of the nicked vector DNA containing the desired mutations (and the control reactions) is then transformed into XL1-Blue competent cells.

2.1.4 DNA purification

For standard purification of DNA > 100 nt, the QIAquick PCR Purification Kit (Qiagen) was used according to the manufacturer's protocol. The Wizard Plasmid DNA Purification System (Promega) provides higher purity and concentration of the DNA needed for special applications. In order to separate DNA of different sizes (> 70 nt) on an agarose gel, the QIAquick Gel Extraction Kit from Qiagen was applied.

2.1.5 Restriction digest of DNA

Naturally, restriction enzymes protect bacteria from infections by viruses. These endonucleases recognize a specific sequence of nucleotides and produce a single- or double-stranded cut in the DNA. While recognition sequences vary between 4 and 8 nucleotides, many of them are palindromic, which correspond to nitrogenous base sequences that read the same backwards and forwards. For molecular cloning, isolated restriction endonucleases and their target sequence provide a tool for specific DNA recombination. Both the vector backbone and the insert are digested preparatively with two different restriction enzymes. This provides substrates for the subsequent ligation reaction producing a directionally cloned product.

In order to test for successful incorporation after cloning, the plasmid preparation is digested analytically using the restriction enzymes used for the ligation reaction.

restriction digest		
analytical digest	preparative digest	
2 μL	10 μL	DNA (100-200 ng)
3 μL	5 μL	10x restriction buffer for restriction enzyme (NEB)
0.3 μL	0.5 μL	100x BSA (bovine serum albumine, NEB)
0.75 μL	1 μL	restriction enzyme 1 (2 U)
0.75 μL	1 μL	restriction enzyme 2 (2 U)
23.2 μL	32.5 μL	H ₂ O
30 μL	50 μL	total reaction volume
3 h	ON	incubation at 37°C

2.1.6 Dephosphorylation of vector DNA

Phosphatases catalyze the removal of 5' phosphate groups from DNA that are required for the ligase reaction. Dephosphorylation of a digested vector can consequently be used to obviate self-ligation. The Antarctic Phosphatase is the enzyme of choice because it can be heat-inactivated and the vector can be used for ligation without any further purification step.

dephosphorylation reaction	
44 μL	DNA (100-200 ng)
5 μL	10x Antarctic Phosphatase buffer (NEB)
1 μL	Antarctic Phosphatase (1U, NEB)
50 μL	total reaction volume
2 h	incubation at 37°C
10 min	Incubation at 70°C

2.1.7 Ligation of DNA fragments

DNA ligases can join two DNA strands that have double-strand break (“blunt ends”) and single-strand break (“sticky ends”). DNA ligases catalyzes the formation of a phosphodiester bond between juxtaposed 5' phosphate and 3' hydroxyl termini in duplex DNA. The commonly used T4 DNA Ligase isolated from bacteriophage T4 is most active at 25°C and requires ATP as a cofactor. T4 ligase was used to directionally join an insert with a vector, both digested by 2 different restriction enzymes. The optimal molar ratio of vector to insert (1:3 to 1:5) was estimated by agarose gel electrophoresis.

ligation reaction			
ligation	vector control	insert control	
1 µL	1 µL	-	vector DNA (~50 ng)
3 µL	-	3 uL	insert DNA
1.5 µL	1.5 µL	1.5 µL	10x T4 ligase buffer
0.75 µL	0.75 µL	0.75 µL	T4 DNA ligase (300 U)
8.8 µL	10.8 µL	10.8 µL	H ₂ O
15 µL	15 µL	15 µL	total reaction volume
4 h incubation at RT			

2.1.8 Preparation of chemically-competent *E. coli*

For rendering bacteria chemically competent, *E. coli* were processed by a modified preparation according to Inoue. For an overnight culture of the *E. coli* strain of choice (XL1 blue, BL21 gold, XL10 gold, Stbl2), 4 ml LB medium were inoculated and grown at 37°C. The following day, the culture was transferred into 300 ml LB medium and grown to a OD₆₀₀ of 0.5-0.6. After 20 min incubation on ice, the cells were harvested by centrifugation (2500 g, 4°C, 20 min). The supernatant was discarded and the cell pellet was resuspended in 60-80 mL ice-cold Inoue transformation buffer. After another centrifugation step (2500 g, 4°C, 15 min) the medium was poured off in order to resuspend the cell pellet in 20 mL Inoue

transformation buffer supplemented with 1.5 mL DMSO. Competent *E. coli* were incubated for 10 min on ice and 50 μ L aliquots were stored at -80°C .

2.1.9 Transformation of chemically-competent *E. coli*

An aliquot of chemically competent cells (see 2.1.7) was thawed for 5 min on ice. Plasmid DNA (5 μ L of a ligation reaction, 100 ng purified vector) was added and incubated for 20-30 min. After a 60 s heat-shock at 42°C , cells were again placed on ice for 2 min. For ampicillin resistant bacteria, cells were directly plated on an agar plate supplemented with ampicillin. All other antibiotic resistance genes overcome inhibition of protein synthesis. Therefore, a further incubation step with 150 μ L LB medium for 1 h at 37°C is required before plating on the agar plate with the corresponding antibiotic.

2.1.10 Bacterial DNA purification

For purification of plasmids expressed by bacteria, mini or midi preparations were used for the DNA yield and concentration required. For up to 10 μ g DNA, 2 mL bacteria cultures were processed by the QIAprep Miniprep Kit protocol (Qiagen). From 200 mL *E. coli* culture, higher amounts of plasmid DNA were isolated using Promega's Plasmid Purification Kit (Midi). DNA was stored at -20°C .

2.2. RNA molecular biology

For all experiments dealing with RNA, RNase-free water was used. Buffers were supplied with DEPC. Absorption at 230, 260 and 280 nm were measured by a NanoDrop 2000 Spectrophotometer (PepLab) and RNA purity and concentration were calculated according to the formulas below.

$$\frac{A_{260}}{A_{280}} \geq 1.8 \qquad \frac{A_{260}}{A_{230}} \geq 1.8 \qquad \text{RNA purity criteria}$$

$$c_{RNA} = 40 \cdot A_{260} \qquad n_{RNA} = \frac{1000 \cdot c_{RNA}}{MW}$$

c_{RNA} = RNA concentration [ng/ μ L]

MW = molecular weight [g/mol]

n_{RNA} = RNA molarity [μ M]

2.2.1 *In vitro* transcription

For *in vitro* experiments, DNA coding for the RNA of interest was cloned into the MCS of pcDNA3. After PCR amplification using primers T7 and sp6 a 60-500 nt PCR product was yielded. After an initial Gel-purification (Qiagen kit) step and subsequent purification using Wizard SV Gel and PCR clean-Up System (Promega) DNA was eluted using 30 μ L RNase-free water. This serves as a template for the *in vitro* transcription reaction by T7 RiboMAX Express Large Scale RNA Production System (Promega). The protocol combines and modifies the standard procedures using HEPES buffer and yeast inorganic pyrophosphatase. The template is mixed with transcription reaction components according to the following protocol

<i>in vitro</i> transcription reaction	
12 μ L	template DNA (~2 μ g)
15 μ L	RiboMAX Express T7 2x Buffer
3 μ L	T7 Express Enzyme Mix
incubate at 37°C for 30 min	

Downstream purification of RNA was optimized testing different protocols. Best result were obtains using the DNA-free RNA kit from Zymo Research with a Fast-Spin column

technology. The template DNA was digested by addition of 1 μ L DNase I (1U, Zymo Research) in the corresponding DNase I buffer and incubation for 15 min. The transcription product was subsequently purified according to the manufacturer's protocol. Elution in 30 μ L RNase-free water yielded up to 5 μ g RNA.

2.2.2 Reverse transcription (RT)

Moloney Murine Leukemia Virus Reverse Transcriptase (M-MLV RT) is an RNA-dependent DNA polymerase. The RNase H activity of M-MLV RT is weaker than other commonly used reverse transcriptases. M-MLV Reverse Transcriptase (Invitrogen) was used for synthesis of first-strand DNA from an RNA template. If the template mRNA was obtained from cellular extraction, an oligo(dT) primer is used to synthesize cDNA. For noncoding RNAs, other specific 3' primers produce first-strand DNA from cellular or *in vitro* transcribed RNA.

reverse transcription reaction	
4 μ L	template RNA
1 μ L	dNTPs
1 μ L	3' primer (2 pmol/ μ L)
6 μ L	H ₂ O
incubate for 5 min at 65°C, then add	
2 μ L	DTT
1 μ L	RNase OUT
4 μ L	5x RT buffer
incubate for 3 min at 37°C, then add	
0.5 μ L	M-MLV RT
incubate for 50 min at 37°C	

reverse transcription PCR program			
	94°C	2 min	
34x	95°C	30 s	denaturation
	55°C	45 s	annealing
	72°C	2 min	elongation
	72°C	5 min	
	15°C	forever	

2.2.3 Systematic Evolution of Ligands by Exponential Enrichment (SELEX)

The "Systematic Evolution of Ligands by Exponential Enrichment" (SELEX) is a combinatorial technique for producing oligonucleotides, in this case RNA, that specifically bind to a target ligand. The sequences selected *in vitro* from a library of oligonucleotides are referred to as aptamers. The process is based on a method by Gold and Tuerk (Tuerk and Gold 1990).

The first step was the generation of a large library consisting of randomly generated sequences of fixed length. A template was synthesized (MWG) bearing a 40 nt random sequence flanked by constant 5' and 3' sites that serve as priming regions for the PCR reaction. The forward primer anneals to the 5' constant region and introduces a T7 promoter sequence and the reverse primer is reverse complementary to the 3' constant region. The number of possible sequences in this library is 4^{40} .

PCR library generation	
1 µL	template DNA (N_{40} , 20 pmol/µL)
4 µL	dNTPs (10 mM)
2 µL	forward primer (100 pmol/µL)
2 µL	reverse primer (100 pmol/µL)
1 µL	taq DNA polymerase
82 µL	H ₂ O
incubate for 50 min at 37°C	

PCR program library generation			
	95°C	2 min	
19 x	92°C	30 s	denaturation
	54°C	20 s	annealing
	72°C	1 min	elongation
	72°C	10 min	
	15°C	forever	

The PCR-product was processed in two steps using gel- and PCR- purification (see 3.1.3). Subsequently, DNA was *in vitro* transcribed (see 3.2.2) into an RNA library.

In the following affinity-selection, the aim was to find RNAs from the library that bind the protein of interest. This recombinantly expressed protein is tagged by a His-rich sequence that was immobilized on a Ni-NTA resin.

In a preincubation step, 10 μ L Ni-NTA beads were supplied with 50 μ L RNA-binding buffer for 30 min at RT. 2 μ L protein (5 μ M) were added for 30 min on ice. The excess off unbound proteins were removed by washing twice (100 μ L RNA-binding buffer, 1000 g, 2 min). Subsequently, 20 μ L of the RNA pool and 1 μ L RNase inhibitor were incubated for 30 min. Unbound RNA was removed by 3 washing steps (100 μ L RNA-binding buffer, 1000 g, 2 min). Protein-bound RNA was eluted by addition of 1 μ L trypsin (1mg/mL) and incubation for 5 min at 50°C.

The concentration of the selected RNA pool was increased by precipitation.

RNA precipitation	
200 μ L	eluted RNA
1 μ L	RNase inhibitor
30 μ L	3M NaAc pH 5.2
700 μ L	95 % ethanol
incubation at -20°C for 1h	

The precipitated RNA was pelleted by centrifugation (12000 rpm, 10 min) and washed twice with 70% ethanol. The pellet was air-dried and dissolved in 4 μ L RNase-free water. The selected RNA was reverse transcribed (see 3.2.2) and amplified by PCR resulting in cDNA coding for the selected RNA aptamers. This cDNA was used for ligation into pLysMOD, sequencing and subsequent rounds of selection in which the stringency of the elution conditions is increased to identify the tightest-binding sequences.

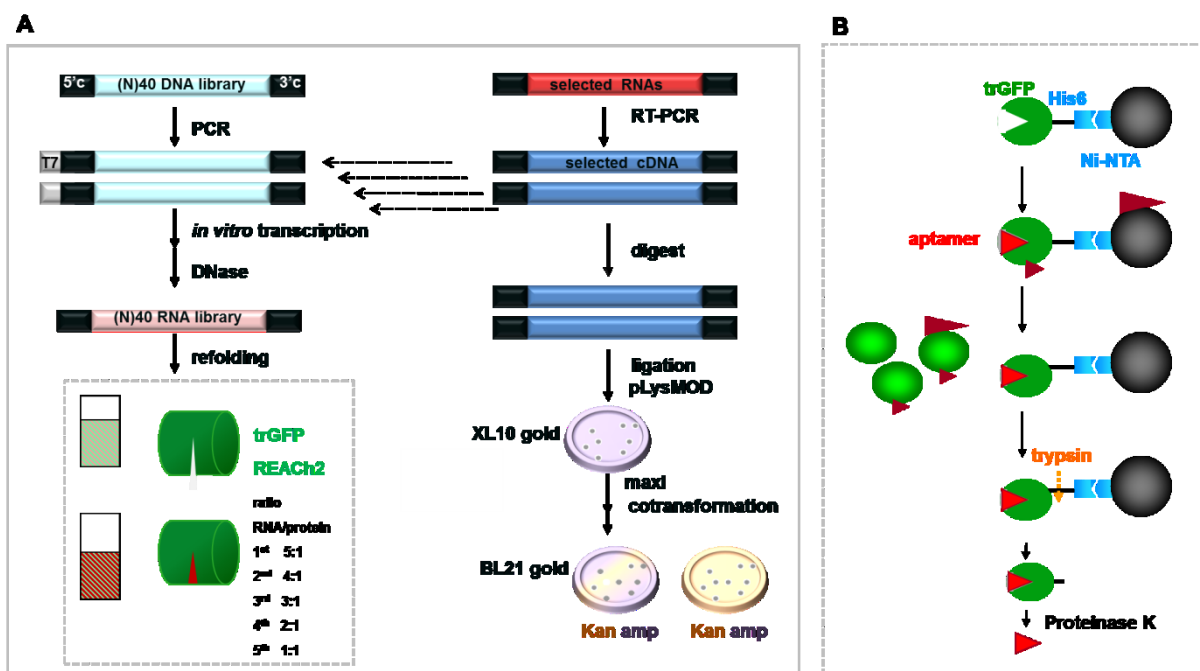


Figure 20 SELEX procedure for the selection of a trGFP binding RNA aptamer. **(A)** SELEX protocol covering the generation of a random library, *in vitro* selection and bacterial testing for fluorescence enhancement. **(B)** *In vitro* selection strategy.

2.3 Protein Biochemistry

2.3.1 Protein expression using the *E. coli* BL21 strain

For recombinant expression of proteins in bacteria, the desired cDNA was cloned into the MCSs of the bacterial expression plasmids pRSETB or pRSFDuet. The cDNA of interest is driven by a T7 promoter and the 6 Histidines at the N-terminus of the recombinant protein allow for affinity purification. The *E. coli* strain BL21 gold used for transformation (see 3.1.8)

takes advantage of the lack of endogenous expression of some proteases and the T7 RNA polymerase promoter to direct high-level expression. After ON inoculation of a 5 mL culture containing the antibiotic (50 mg/ml, 1:1000), cells were grown in 200 mL medium with antibiotics (1:1000) at 37°C to an OD₆₀₀ of 0.8. In order to induce protein expression, 0.5 mM IPTG (Isopropyl-β-D-thiogalactosid) was added and the culture was grown ON at RT with additional antibiotics (1:1000). The next day, bacterial cells were harvested by centrifugation (6000 g, 10 min, 4°C).

2.3.2 Affinity purification of recombinantly expressed proteins

The cell pellet obtained from the 200 mL culture (see 3.3.1) was resuspended in 10 mL protein resuspension buffer. In order to inhibit proteolytic degradation of the recombinant protein, 1 mM PMSF, 5 µg/ml Pepstatin and 1 µg/µL Leupeptin were added. Initiation of bacterial cell lysis is facilitated by freezing the cell suspension at least 1 h at -80°C. After thawing on, 30 min on-ice incubation with lysozyme (1mg) causes the digest of the polysaccharide component of the bacterial cell wall. Cell membranes were solubilized by addition of the detergent Triton-X-100 (0.1%) and DNaseI (5 µg/mL, 50 µL). In a final lysis step, shear forces were introduced by ultrasonification for 20 min. Centrifugation (13000 rpm, 30 min, 4°C) separated the cell debris from the protein extract. His-tag containing recombinant proteins within this supernatant were allowed to bind to Ni-NTA agarose beads (300 µL) for 2 h at 4°C. For separation of Ni-chelated recombinant proteins from endogenous bacterial proteins, the suspension was put into a polypropylene column with a filter withholding the Ni-NTA beads. After 2 washing steps with a resuspension buffer containing 10 mM imidazole that competitively binds to Ni-NTA, recombinant proteins are eluted by the elution buffer bearing an imidazole concentration of 150 mM. The protein was stored at 4°C, for long-term storage -20°C the elution buffer was supplemented with glycerol.

2.3.3 Size exclusion chromatography of recombinantly expressed proteins

For high yield protein expression and purification, a 600 mL E. coli culture was inoculated as described. For affinity chromatographic purification, a 5 mL HisTrap affinity column (GE) was used. Gel filtration was performed using a Superdex 200 (GE) coupled to an ÄKTA-FPLC device (GE Healthcare). The column was equilibrated with SEC buffer (40 mM Tris pH 7.5,

200 mM NaCl, 2 mM β -ME). For each run, 2 mL of sample was loaded and protein separation was performed at 0.3 ml/min.

2.3.4 ATPase assay

ATPase activities of purified eIF4AIII and REFlex were quantified using an ATPase assay according to the manufacturer's protocol (Innova Biosciences).

2.4 Spectroscopy

Fluorescent spectra were taken using a fluorescent spectrophotometer (Varian). cpCitrine/eCFP FRET constructs were diluted in a 100 μ L volume and excited at 432 nm (bandwidth 5 nm) and the emission was recorded from 450 nm to 600 nm (bandwidth 5 nm). To calculate the $\Delta R/R$ value elicited by a given ion the following formula was used:

$$\Delta R/R [\%] = \frac{\text{Ratio}_{\text{RNA bound}} - \text{Ratio}_{\text{no RNA}}}{\text{Ratio}_{\text{no RNA}}} * 100$$

with Ratio R = Peak_{YFP}/Peak_{CFP} (527nm/432nm).

2.4.1 Testing for *in vitro* ratio change of FRET RNA sensors

Purified proteins were diluted in 100 μ L RNA binding buffer (20 mM HEPES (pH 7.25), 125 mM NaCl, 1 mM magnesium diacetate, 1 mM imidazole, 2 mM CaCl₂, 1 mM DTT, 2.5% (v/v) glycerol and 0.1% (w/v) Triton-X-100) and a spectrum was taken from the unbound protein. Another spectrum was recorded after the addition of a molar excess of the corresponding RNA to the RNA indicator.

2.4.2 Spectroscopic determination of K_D -value

The experimental settings were as described in 2.4.1. Small aliquots of RNA were added to the cuvette and a full fluorescence emission spectrum was taken after each addition. $\Delta R/R$ at distinct calcium concentrations was calculated. Extraction of the K_D -value was achieved by fitting a sigmoidal curve to the plotted \log_{10} values of the RNA-free points (in M) versus the normalized signal.

2.4.3 pH titration

For pH titration, we used buffers containing 125 mM NaCl, 1 mM magnesium diacetate, and TRIS (pH 7.5, 7.75, 8.0, 8.25), MOPS (pH 6.5, 6.75, 7.0, 7.25, 7.5, 8.0), MES (5.5, 6.9, 6.5) or citrate (4.5, 5.0, 5.5).

2.4.4 *In vitro* transcription assay

DNA encoding 10 repeats of the RRE aptamer were amplified by PCR using primers that introduce a T7 promoter variant at the 5' end (T7wt_10RRE_f 5'-TAATACGACTCACTATAGGATCCTGTACACGGCCGGGTCTG-3', T7_A8C_10RRE_f 5'-TAATACGCCTCACTATAGGATCCTGTACACGGCCGGGTCTG-3', T7_A8G_10RRE_f 5' TAATACGGCTCACTATAGGATCCTGTACACGGCCGGGTCTG-3'). 1 μ g of purified PCR product was used as a template for the *in vitro* transcription reaction using the RiboMAX T7 Large Scale RNA Production System (promega). RNA generation was monitored by spectroscopy. After 60 min 1U RNaseI was added in order to digest the synthesized RNA.

2.4.5 Spectroscopic REFLEX FRET assay

All purified EJC components as well as the *in vitro* transcribed RNA were mixed on ice in equimolar amounts in RNA interaction buffer. Spectroscopy was performed at 30°C. The reactions were supplied with 2 mM ATP when indicated. Emission spectra were recorded before and after exposure of REFLEX to different EJC components and RNAs as described in 2.4.

2.5 Bacterial screening

2.5.1 Sensor library generation

Different strategies for random mutagenesis were applied in order to create libraries with RNA peptides bearing amino acid substitutions, deletions and insertions. The DNA encoding the FRET sensor variant was subjected to an error-prone PCR (Gene Morph mutagenesis kit, Agilent) using CFP Chr for (5'- CTGACCTGGGGCGTGCAAGTGCTCC-3') and cpCit Chr rev (5'- CGAAGCACCATCAGGCCGTAGCCG-3') primers. The mutation frequency ranging from 1-10 mutations per kb was controlled by the amount of template DNA. In order to increase the rate of single mutations, two sequential PCRs were performed using the purified product of the first one for the second reaction. The PCR product of the second reaction was digested *SphI/SacI* and ligated into a pRSFDuet-1-VAmPIRe vector (modified from Novagen). In another approach, degenerated primers (Eurofins) allowed the introduction of randomized amino acids at defined positions either within the Rsg peptide or at the N- and C-termini during normal PCR reaction.

The pRSFDuet sensor library was transformed into *E. coli* XI1 blue and plated on agar plates with kanamycin. The colonies were pooled and the sensor library DNA was retransformed into *E. coli* XI1 blue with 10 aptamer repeats (10xRRE) that are cloned into pMB133 (kind gift of Natalie Broude) using *HindIII/NotI*. Each colony expresses one FRET sensor variant and the pMB133-10xRRE vector yielding tetracycline-inducible aptamers. The transformations were plated on a double (amp/kana) resistance agar plate, incubated over night at 37 °C and for 24 h at 4°C in order to get full repression of aptamer transcription.

2.5.2 Bacterial colony selection

Plates were imaged at room temperature every 5 min and RNA aptamer transcription was induced by addition of 20 ng/μL anhydrotetracycline (Sigma). A Lambda LS light source (Sutter) was connected to a lambda 10-2 hardware (Sutter) by fiber optic light guides. The excitation filter was D436/40x and the emission filter for CFP was D480/40m and for cpCitrine HQ535/30m (all from Chroma). Images were detected by a CCD camera Coolsnap ES2 (Sutter) and processing was done in MetaFluor software (Meta Imaging series version 7.7). For automated colony ROI selection we used Cell profiler version 10415. Data were

analyzed by Origin 8.1 by plotting the ratio change 200 min after anhydrotetracycline addition over the starting FRET ratio. The selected colonies correspond to the ROIs with a ratio change higher and a starting ratio lower than the average of 6 control colonies with the wt sensor.

On average, 800 colonies were analyzed per plate and 5-20 colonies (1500 in total) selected for minipreparation and subsequent *in vitro* validation. The pRSFDuet-1 vectors bearing the selected VAmPIRe variants were transformed into BL21 and grown in 5 mL LB medium overnight. The preculture was diluted in 12 mL LB medium supplemented with kanamycin and 0.1 mM IPTG for small-scale protein expression. After 4 h, cells were harvested and processed as described above but in a 1 mL volume format. For affinity purification, the lysates were incubated with 25 μ L His Mag Sepharose Ni magnetic beads (GE), processed according to the manufacturer's protocol and protein was eluted in 25 μ L elution buffer. 1-5 μ L of the 25 μ L protein eluate were mixed with the RNA aptamer in 100 μ L RNA binding buffer and FRET ratio change was detected in a fluorescence spectrophotometer as described. The variants with the highest ratio change upon RNA aptamer addition were selected for sequencing and spectral analysis from larger culture volumes as described above.

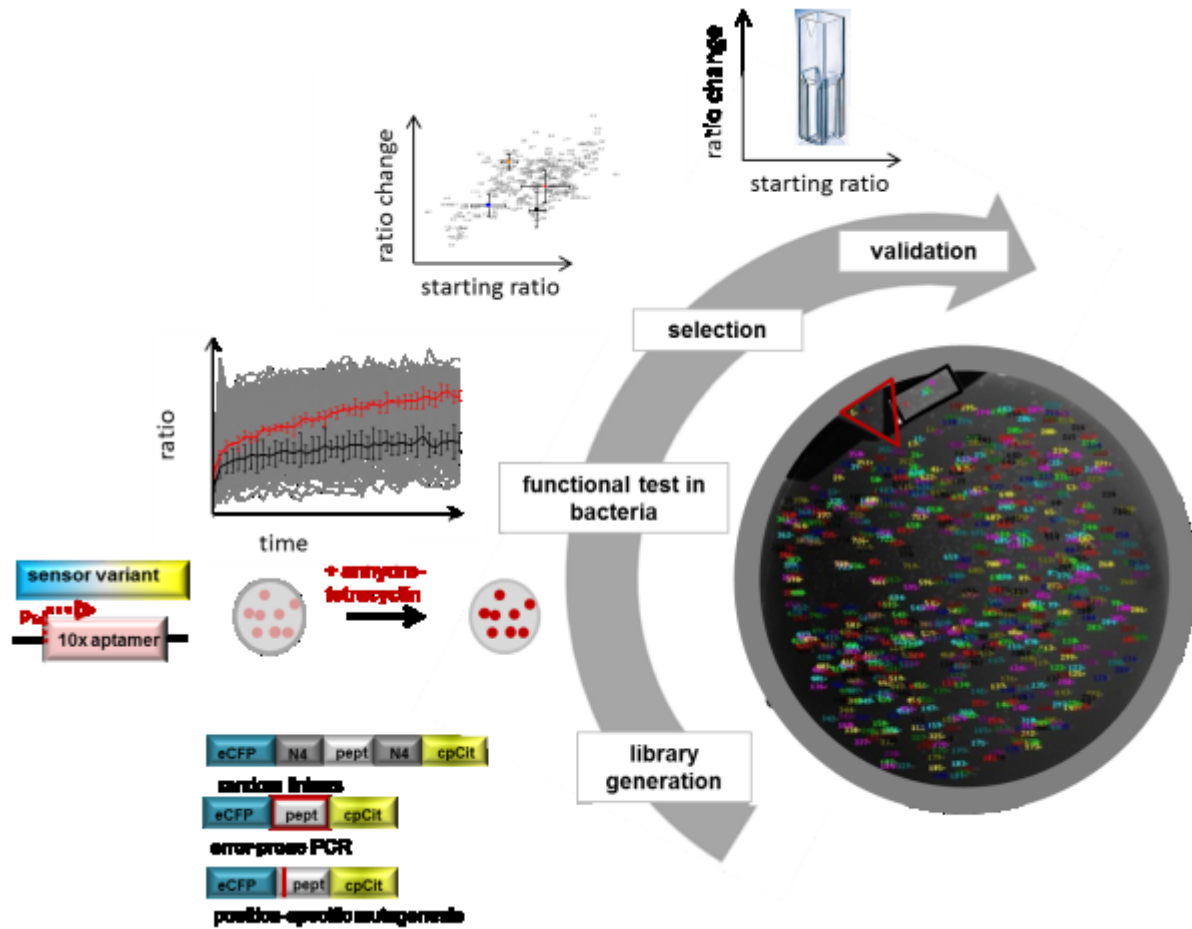


Figure 21 Bacterial colony screening procedure. Library generation by error prone PCR, mutagenesis at selected positions and aa composition. The sensor library is cotransformed with an aTC-inducible target RNA controlled by a tet promoter (red colonies). FRET ratio is recorded before and after addition of aTC for several hours for all colonies from the library (grey) and the control colonies expressing a control sensor with (red) and without the inducible aptamer (black). A number is assigned to each colony (grey) and starting ratio is plotted against the relative temporal ratio change. Variants with high ratio change and low starting ratios are picked and tested in the cuvette.

2.6 Cellular biology

2.6.1 Preparation of dissociated hippocampal neuronal culture

All phases of the dissection were conducted in a laminar flow hood, using sterilized instruments and surgical gloves. Uninterrupted processing was required in order to avoid neuronal apoptosis during resulting in low yield of hippocampal neurons in culture.

Wistar rats were mated and pregnant females (E18) were killed using CO₂. The dam abdomen was sprayed with 95% ethanol and cut from near the vagina to the thoracic cavity.

The uterine horns were identified by their dark red color with the 2 cm-long fetuses separated by constrictions. The horns were removed by cutting their attachments to the abdominal cavity and placed in a sterile petri dish containing PBS. The fetuses were dissected from the uterine horns and placed in sterile HBSS. Using microdissecting forceps and small dissecting scissors, the fetuses are decapitated. The heads was anchored with a forceps pointing into the eyes and subsequently a scissor is oriented along the longitudinal fissure separating the hemispheres. The skin and the skull were sliced forward almost to the pin anchoring the snout avoiding slicing the underlying cerebral cortex. The brain was lifted upward out of the skull and oriented dorsal side up. The hemispheres were separated, oriented with the medial surface upwards and the meninges were removed. A single cut was made from the dorsal-most part of the cerebral hemisphere down through the fimbria in order to define the anterior boundary of the hippocampus. In order to release the hippocampus, a curving incision just dorsal to the hippocampal fissure parallel to the ventral free border of the hippocampus was made. A final snip at the end of the curve incision released the hippocampus. Hippocampi were combined in a 15 mL tube containing 2 mL dispase solution (1mg/mL in HBSS) pre-warmed to 37°C. After sedimentation for 15 min at 37°C, the dispase solution was removed with a sterile pipet. Hippocampi were dissociated by triturating in 2 mL pre-warmed DMEM (10% FCS, 1% Pen/Strep) in order to obtain a single-cell suspension. The neurons were counted using a hemacytometer and plated in a density of 200000 cells per dish. Each E18 hippocampus typically provides ~0.5 to 1 million cells, almost all of which are neurons. Therefore, depending on the size of the litter, a single litter will provide ~6 to 30 million neurons. For cultivating the cells, glass-bottom dishes (35 mm diameter, MatTek) were incubated with poly-L-lysine in borate buffer ON. The dishes were washed with PBS, supplied with 2 ml DMEM (10 % FCS, 1% Pen/Strep) and prewarmed. Freshly triturated cells were seeded into the culture dishes. After 12 hours, the medium was replaced by Neurobasal supplemented with B27. The neuronal culture was kept for up to 3 weeks at 37°C and 5 % CO₂ with a weekly medium change.

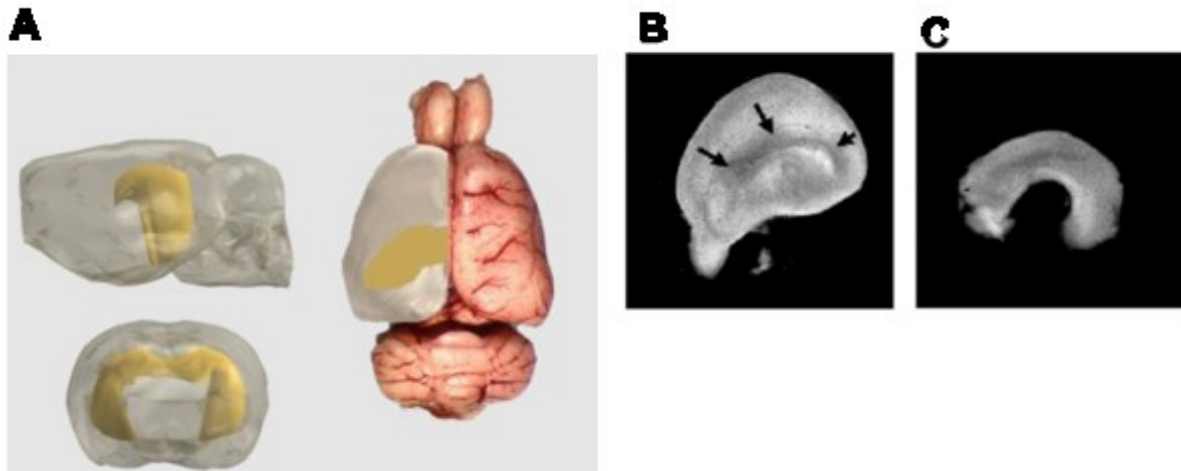


Figure 22 Hippocampal dissection. (A) Reconstruction of the hippocampus (yellow) in its 3D position within the rat's brain. (John C. Fiala and Josef Spacek, LONI's Rat Brain Atlas). **(B)** A view of the medial surface of the left cerebral hemisphere. The arrows indicate the boundaries of the hippocampus. **(C)** The hippocampus after removal from the cerebral hemisphere. (G Audesirk et al. 2001)

2.6.2 Immuncytochemistry

In order to fix the cells, medium was aspirated and 4% PFA/4% sucrose was added. After incubation for 15 min at RT cells were rinsed 3 times with PBS. Quenching with 50 mM Ammonium Chloride for 10 min at RT was followed by 3 washing steps using PBS. 0.25 % Triton/PBS was incubated for 10 min in order to permeabilize the cells. After another 3 washing steps, blocking solution (5 % goat serum in PBS) was added for 1 h at RT (or ON at 4°C) in order to avoid background staining. Subsequently the recommended concentration of the primary antibody was added in 2 % goat serum in PBS ON at 4°C (or for 1h at RT). Cells were rinsed with PBS 4 times and incubated with the secondary antibody diluted in 10 % blocking/PBS solution for 50 min. The washing procedure was repeated and the cell layer covered with Moviol mounting medium immediately after removal of the last PBS residues. Dishes covered in mounting medium were kept refrigerated until imaging analysis.

2.6.3 Fluorescence in situ hybridization (FISH)

In order to fix the cells, medium was aspirated and fixation solution added for 20 min at RT. After 2 washes in PBS, cells are permeabilized and dehydrated by treatment with 70 % ethanol (→ 90 %, 100 %, 2 min each) for at least overnight at 4°C. Cells were rehydrated for 5 min in prehybridization buffer at RT. For probe annealing, hybridization buffer was added and incubated at 37°C ON. After two consecutive 30 min washing steps with washing solution I and II at 50°C DIG-labeled probes were detected by anti-digoxigenin-rhodamine (1:200). Slides were incubated for 1 h at 37°C in antibody solution II and washed twice for 15 min in antibody solution I at RT.

Fixation solution	
1x	PBS
4 %	formaldehyde
10 %	acetic acid

20xSSC	
3.0 M	NaCl
0.3 M	Sodium citrate
pH 7.0	

Prehybridization solution = washing solution I	
2x	SSC
50%	formamide

hybridization solution (40 uL)	
2x	SSC
50%	formamide
0.02%	BSA
2 mM	vanadyl-ribonucleosid complex
10 %	dextrane sulfate
40 µg	tRNA

washing solution II	
0.1 x	SSC
50%	formamide

antibody solution I	
2 x	SSC
8 %	formamide

antibody solution II	
2 x	SSC
8 %	formamide
2 mM	vanadyl-ribonucleosid complex
0.2 %	BSA

2.6.4 Isolation of DNA and RNA from cell lysates

RNA isolation using Trizol (Invitrogen) is based on the single-step method of Chomczynski and Sacchi. Trizol, a monophasic solution of phenol and guanidine isothiocyanate, maintains the integrity of the RNA while disrupting cells and dissolving cell components.

Medium was removed from a 3.5 cm diameter cell culture dish. Cells were resuspended in 1 mL Trizol and homogenized by pipetting. After incubation for 5 min at RT, 0.2 mL chloroform was mixed with the homogenate by vigorous shaking. Centrifugation (12000 g, 15 min, 4°C) caused the separation of an organic phase yielding DNA and protein and an upper aqueous phase that was picked up for further isolation of cellular RNA. The RNA was precipitated by addition of 0.5 mL isopropanol and incubation for 10 min at RT. The RNA precipitate was pelleted by centrifugation (12000 g, 15 min, 4°C). After removal of the supernatant, the pellet was washed with 1 mL 75% ethanol and centrifuged once more (7500 g, 5 min, 4°C). The RNA pellet was air-dried for 10 min and dissolved in 50 µL RNase-free water by incubating for 10 min at 60°C. The RNA was stored at -80°C until further usage.

2.6.5 Transfection methods

2.6.5.1 Lipofectamine transfection

Lipofection is a technique used to transfer genetic material into a cell by means of liposomes, which are vesicles that can easily merge with the cell membrane since they are both made of a phospholipid bilayer. The advantages of this lipid-based transfection technology are its high efficiency, its ability to transfect all types of nucleic acids in a wide range of cell types, its reproducibility and low toxicity. The reagent Lipofectamine 2000 (Invitrogen) was used for transfecting both neurons and mammalian cell lines with DNA. For a cell culture dish of 35 mm diameter 10 µL of Lipofectamine were mixed with 250 µL of Opti-MEM I in order to allow preformation of lipid vesicles. After 5 min, 1-2 µg of plasmid DNA in 250 µL of Opti-MEM I was added. Within 20 min incubation, DNA was allowed to incorporate into the lipid vesicles. For the transfection of mammalian cells, medium containing antibiotics was exchanged by Opti-MEM. For neuronal cultures, 500 µL medium was retained before addition of 500 µL of the transfection mix. After incubation for 2-3 h (37°C, 5% CO₂) cells were washed twice with PBS. DMEM (10% FCS, 1% Pen/Strep) was added to mammalian cell lines and neuronal cells were supplied with a mixture of fresh Neurobasal (+B27, 1.5 mL) and the retained medium (500 µL).

2.6.5.2 Electroporation of hippocampal neurons

The Amaxa Nucleofector system is designed for electroporation of specific types. DNA is directly introduced into the nucleus where it is incorporated into the cell independent of cell division. After preparation of rat hippocampal neurons, 5×10^5 dissociated cells were immediately spun down (5 min, 630 rpm). After removal of the supernatant, neurons were resuspended in 100 μ L Amaxa Rat Neuron Nucleofector Solution and 1-3 μ g DNA (1-3 μ g each plasmid for cotransfections) by careful repeated pipetting. Neurons were transferred into a cuvette and put into the Nucleofector device. The program yielding electrical parameters specifically designed for hippocampal neurons (program O-003) was started. Directly after electroporation, 500 μ L warm MEM-HS was added and cells were resuspended using a small plastic Pasteur pipette. The transfected cell suspension was distributed to 2 poly-Lysine coated culture dishes (cell density of 2.5×10^5) with 2 mL conditioned N2 medium from astrocytes. Neurons were cultured for 1-4 days until image analysis.

2.6.5.3 Semliki Forest Virus infection

Alphaviruses including the Semliki Forest Virus (SFV) only require the host translational machinery for replication. Engineered variants are used for the transduction of a target gene into mammalian cells that results in an expression at a level of up to 25 % of the host's total cellular proteins. One component of a dual plasmid infection system is the helper plasmid pSCAHelper that encodes SFV structural proteins. Virus production is dependent on the presence of a second pSCA β plasmid yielding the packaging signal as well as coding sequences for the target protein and non-structural proteins driven by the CMV promoter. HEK 293 T cells (60-70 % confluency) were transfected by the dual infection system according to a varied lipofection protocol (see 3.5.2). Infectious virus can be obtained by co-transfecting 6-8 μ g of DNA pSCA β with pSCAHelper (molar ratio of 1, 2:3 in μ g) in culture medium (DMEM + 10 X FCS + 1 % Pen/Strep) ON. The next morning, expression of the transfected construct was checked by fluorescence microscopy and the medium was changed. After 2 days, the supernatant was removed and cellular debris separated by centrifugation (10 min, 2500 g, 4°C). The supernatant was filtered using a 0.45 μ m or 0.22 μ m syringe filter with low protein binding characteristics. For concentration and purification,

the virus suspension was ultracentrifuged (20000 rpm, 90 min, 4°C). The supernatant was discarded and completely removed by putting the tube upside-down for 10 min. The remaining virus pellet was resolved in 250 µL TBS (for slices or neurons) or medium (for cell lines) ON at 4°C. Virus aliquots were stored at -80°C.

Mutations within the glycoprotein gene p62 prevent infection unless the virus is proteolytically treated. In order to activate the SFV, an aliquot was defrozen and incubated with 0.5 mg/mL α-chymotrypsin (1:20). After 45 min at RT, protease activity was stopped by addition of 0.4 mg/mL aprotinin (1:15) for 10 min. The activated virus was stored at 4°C for maximal 1 week before infection. The virus titer was determined by infection of HEK 293T cells in wells of a 96 well plate using different dilutions.

2.6.6 Cellular assays and imaging

2.6.6.1 Fibroblast migration assay

The cDNAs encoding VAmPIRe or mKO2-20xRRE were cloned *BamHI/EcoRI* into pcDNA3. For imaging experiments, cells were plated on a 35-mm glassbottom dish (MatTek) in culture medium (Dulbecco's modified Eagle's medium containing 10% Fetal calf serum, 100 U/mL penicillin and 100 µg/mL streptomycin). Confluent NIH 3T3 fibroblasts cells were transfected with pcDNA3-VAmPIRe (0.5 µg) and pcDNA3-mKO2-20xRRE (2 µg) using Lipofectamine 2000 (Invitrogen). The fibroblast monolayer was scraped in a straight line using a scalpel to create a scratch and migrating cells were imaged 2 h afterwards. The VAmPIRe (0.25 µg) and pcDNA3-mKO2-20xRRE (1 µg) were transfected separately into HEK 293T cells. After 24 h, images were taken using the Zeiss VisiScope Cell Explorer System as described.

2.6.6.2 TetOn assay

The T-REx HeLa cell line (Invitrogen) used for the TetOn experiments was expanded in culture medium supplemented with 5 µg/mL blasticidin (Invitrogen). For tetracycline-inducible expression of the aptamer fused to mKO2, mKO2-30xRRE was cloned *HindIII/XbaI* into pcDNA4/TO (Invitrogen). T-Rex HeLa cells were transfected with pcDNA3-VAmPIRe (0.25 µg) and pcDNA4/TO-mKO2-30xRRE (1 µg) using Lipofectamine and cultured for further 24 h. Before imaging, 0.1 µg/mL aTC was added to the medium to induce transcription from

pcDNA4/TO. Images were taken every 10 min at the Zeiss VisiScope Cell Explorer System as described.

2.6.6.3 Stress assay

NIH 3T3 fibroblasts were plated on 35 mm imaging dishes (MatTek). Cells were cotransfected with pcDNA3 plasmids yielding VAmPIRe and mKO2-10xRRE-zip or VAmPIRe, 10xRRE-zip and ZBP1-mRFP and incubated ON. DMEM was replaced by HBSS containing 2.5 mM arsenate. Stress granule formation was imaged every 5 min after 30-60 min.

2.6.6.4 Imaging Setup and image analysis

Confocal images were acquired at a Leica TCS SP2 confocal laser scanning microscope. We used a 63X oil immersion objective and 488 nm excitation laser for EGFP as well as the 543 nm laser for RFPs.

For live cell imaging we used a Zeiss VisiScope Cell Explorer System with a plan-apochromat 63x/1.4 oil objective (Zeiss) and FRET (436/20x, 535/30M), CFP (436/20x, 480/40M) and RFP (560/40x, 630/75M) filters (all from Chroma). Emitted light was detected by a Cool Snap HQ² CCD camera (Visitron). Cells were maintained at 37°C (Tempcontrol 37-2 digital, heating unit, Pecon) and the system was controlled and processed by MetaMorph software (Meta Imaging Series 7.7). Fluorescence of the individual channels was collected subsequently through two emission filters placed in a filterwheel. Acquisition time and frequency were adjusted to the FPs.

Image J software was used for image analysis. Background was corrected by subtracting the intensity of a region close to the cell of interest. FRET ratio was calculated by division of the YFP by the CFP channel. Fluorescence intensity and FRET of a region of interest were plotted.

2.7 Materials

2.7.1 Instruments

Name	Supplier
Autoflow CO ₂ Water-Jacketed Incubator	NuAire (USA)
Cary 100 Scan UV-Visible Spectrophotometer	Varian (Australia)
Cary Eclipse fluorescence spectrophotometer	Varian (Australia)
CCD-Camera Cool Snap HQ	Roper Scientific (USA)
CCD-Camera Cool Snap ES2	Roper Scientific (USA)
Confocal microscope TCS Sp2	Leica Mikrosysteme GmbH (Germany)
Dissecting Microscope	Leitz (Germany)
Dyad DNA Engine Peltier Thermal Cycler	MJ Research Inc. (USA)
Lambda LS Light Source	Sutter Instruments (USA)
Magna Rack 12	Invitrogen (Germany)
Metafluor 7.7 imaging software	Universal Imaging (USA)
Microscope Axiovert 35M	Zeiss (Germany)
Nanodrop spectrophotometer	Nanodrop Technologies (USA)
Origin 8.1 software	OriginLab Corporation (USA)
Shutter Lambda 10-2	Sutter Instruments (USA)

2.7.2 Consumables

Name	Supplier
BCA Protein Assay kit	Pierce (Germany)
Domed Cap Strips for 48 Well Plates	AB-Gene (UK)
Elutip-D Minicolumns	Schleicher & Schüll (USA)
Error-prone Kit	Jena Biosciences (Germany)

Falcon Tissue Culture Plate, 12 Well	Becton Dickinson (USA)
Gene Morph mutagenesis kit	Agilent (USA)
Glass Bottom Culture Dishes 35mm, Nr. P35G-0-14-C	MatTek Corp. (USA)
Herculase II Fusion DNA Polymerase	Agilent (USA)
High Capacity cDNA Reverse Transcription Kit	Applied Biosystems (Germany)
His Mag Sepharose Ni	GE Healthcare (UK)
Polypropylene Columns	Qiagen (Germany)
QIAquick Gel Extraction Kit	Qiagen (Germany)
QIAquick PCR Purification Kit	Qiagen (Germany)
T7 RIBOMAX™ Express Large Scale RNA Production System Kit	Promega (Germany)

2.7.3 Buffers, solutions and media

Name	Recipe
DMEM/10 % FCS	500 ml DMEM 50 ml FCS, heat-inactivated
DNA Gel Loading Buffer (10 x)	100 mM Tris/HCl, pH 7.5 10 mM EDTA 50 % Glycerol 1 % Orange G
DNA Purification Buffer: High Salt	20 mM Tris/HCl, pH 7.4 1 M NaCl 1 mM EDTA
DNA Purification Buffer: Low Salt	20 mM Tris/HCl, pH 7.4 200 mM NaCl 1 mM EDTA

Name	Recipe
HBSS	25 mM HEPES pH 7.4 140 mM NaCl 5 mM KCl 1 mM CaCl ₂ 1 mM MgCl ₂ 1 mM Glucose 0.25% BSA
Inoue Transformation Buffer for competent cells	10 mM PIPES, pH 6.7 250 mM KCl 15 mM CaCl ₂ 55 mM MnCl ₂
LB (Luria-Bertani) medium	20 g/l LB broth base pH 7,0 in ddH ₂ O
LB Agar	LB Medium 15 g Agar in 1 l ddH ₂ O
MOPS Buffer for fluorescence spectroscopy	10 mM MOPS, pH 7.5 100 mM KCl
Neurobasal/B27	500 ml Neurobasal medium 10 ml B27 supplement
PBS (10 x)	100 mM Na ₂ HPO ₄ , pH 7.4 20 mM KH ₂ PO ₄ 1.37 M NaCl 27 mM KCl
Poly-L-Lysine	0.01 % (w/v) Poly-L-Lysine Hydrobromide in H ₂ O
Protein Resuspension Buffer	20 mM NaPO ₄ , pH 7.8 300 mM NaCl
RNA binding buffer	20 mM HEPES pH 7.25 125 mM NaCl

Name	Recipe
	1 mM magnesium diacetate 1 mM midazole 2 mM CaCl ₂ 1 mM DTT 2.5% (v/v) glycerol 0.1% (w/v) Triton-X-100
SEC buffer	40 mM Tris pH 7.5 200 mM NaCl 2 mM β-ME
TAE (10 x)	8.4 g Tris base 11.4 ml glacial acetic acid 20 ml of 0.5 M EDTA, pH 8.0 add H ₂ O to 1 liter
TAE (1 x)	40 mM Tris-acetate 1 mM EDTA
TE (1 x)	10 mM Tris/HCl, pH 8.4; 1 mM EDTA

2.7.4 Chemicals

Name	Supplier
Agar	Sigma (USA)
Ampicillin, sodium salt	Roth (Germany)
Anhydrotetracycline hydrochloride	Sigma (USA)
BES	Roth (Germany)
Bovine Serum Albumin (BSA)	Sigma (USA)
Calcium Chloride, dihydrate	Sigma (USA)
Deoxyribouclease	Sigma (USA)

Name	Supplier
Dispase	Gibco (USA)
Dithiothreitol	Sigma (USA)
DMSO (Dimethylsulfoxide)	Sigma (USA)
Doxycycline	Clontech (USA)
Dulbecco's modified Eagle's medium (DMEM) w/o Sodium Pyruvate; w/ 4500 mg/ml Glucose; w/ Pyridoxine-HCl	Invitrogen (USA)
Dulbecco's modified Eagle's medium /F12	Invitrogen (USA)
Fetal Bovine Serum	Gibco (USA)
Glucose (D-(+)-Glucose anhydrous, min 99%)	Sigma (USA)
Glycine	Merck (Germany)
HEPES free acid	Sigma (USA)
Imidazole	Merck (Germany)
Leupeptin hydrochloride	Sigma (USA)
L-Glutamic acid	Roth (Germany)
Lipofectamine 2000	Invitrogen (USA)
Lysozyme	Sigma (USA)
Magnesium chloride hexahydrate	Merck (Germany)
MES monohydrate	Sigma (USA)
MOPS	Merck (Germany)
NeuroBasal medium	Gibco (USA)
Ni-NTA Agarose	Qiagen (Germany)
Opti-MEM I	Invitrogen (USA)
Penicillin-Streptomycin	Gibco (USA)
Pepstatin A	Sigma (USA)
Phenylmethylsulfonylfluoride (PMSF)	Sigma (USA)
Poly-L-lysine hydrobromide	Sigma (USA)

Name	Supplier
Potassium chloride	Merck (Germany)
Ribonuclease A	Sigma (USA)
Ribonucleic acid, transfer from baker`s yeast	Sigma (USA)
Saccharose	Merck (Germany)
Sepharose CL6B	Sigma (USA)
Sodium arsenate	Sigma (USA)
Sodium bicarbonate	Sigma (USA)
Sodium chloride	Sigma (USA)
Sodium phosphate monobasic, anhydrous	Sigma (USA)
T4-Ligase	New England Biolabs (USA)
Triton-X-100	Sigma (USA)
Trizma Base	Sigma (USA)
Trypsin	Sigma (USA)
Trypsin-EDTA	Gibco (USA)
Yeast extract	Sigma (USA)
Zeocin	Invitrogen (USA)

2.7.5. Plasmids, bacterial strains, cell-lines and flies

Plasmid name	Supplier
pcDNA3	Invitrogen (USA)
pcDNA4/TO	Invitrogen (USA)
pRSETB	Invitrogen (USA)
pRSFDuet-1	Novagen (Germany)
pEGFP-N2	Clontech (USA)

Strain name	Supplier
BL21(DE3)	Invitrogen (USA)
Stbl-2	Invitrogen (USA)
T-REx-HeLa cell line	Invitrogen (USA)
XL-1 Blue	Invitrogen (USA)
XL-10 gold	Invitrogen (USA)

Cell line	Supplier
HEK 293T	Invitrogen (USA)
HeLa	Invitrogen (USA)
NIH 3T3	Invitrogen (USA)
T-REx-HeLa cell line	Invitrogen (USA)

3. Results

3.1 Application of genetically encodable RNA labels for imaging of neuronal RNAs

3.1.1. Dual RNA imaging in neurons

Fusion of fluorescent proteins (FPs) to the MS2 or the λ N22 peptide, enables the visualization of single RNAs in neurons. The modular character of AFP-based labeling provides all prerequisites to track several specific RNAs at the same time. This has proven possible for the first time by tagging two distinct mRNA in yeast in real time (Lange et al. 2008).

In order to get insight into distribution and transport kinetics of several specific RNAs in one cell we are taking advantage of these viral RNA reporters for the tagging of neuronal RNAs of interest. We constructed a fusion protein yielding either the λ N22 peptide or the MS2 peptide, 3 copies of EGFP or mKO2, respectively, and the SV40 nuclear localization signal (NLS) driven by the CMV promoter. Rat hippocampal neurons DIV10 transiently transfected with both RNA labels were stimulated using 40 mM KCl for 2 h (Figure 23). We tagged several mRNAs including CaMKII α with the corresponding aptamers boxB or MS2. Nuclear export efficiency for the single labeling systems were determined by counting cells with exclusive nuclear versus nuclear and dendritic fluorescence signal (Figure 23B). In the presence of MS2-tagged CaMKII α the MS2-3xmKO2-NLS reporter was exported from the nucleus in 43% of the neurons compared to 34% in the absence of any tagged RNA. For the λ N22-3xEGFP-NLS construct the difference was 38% with CaMKII α -boxB cotransfection compared to 35% with the reporter construct only. Double labeling using the MS2- and the λ N22-systems showed mainly nuclear localized fluorescence of both reporter without any transiently expressed mRNA (Figure 23C). Serving as a direct comparison of the two labeling systems, 5 copies of the boxb and 24 copies of MS2 aptamers were cloned between the CaMKII α ORF and the 5'UTR or 3'UTR. mKO2 and EGFP signals were detected at the dendrite with EGFP showing a rather proximal and granular pattern compared to the mKO2-tagged MS2 peptide (Figure 23D). Expression of CaMKII α tagged with boxB only resulted in dendritic localization of λ N22-3xEGFP-NLS but nuclear red fluorescence (Figure 23E). This indicates the lack of interference of both labeling systems.

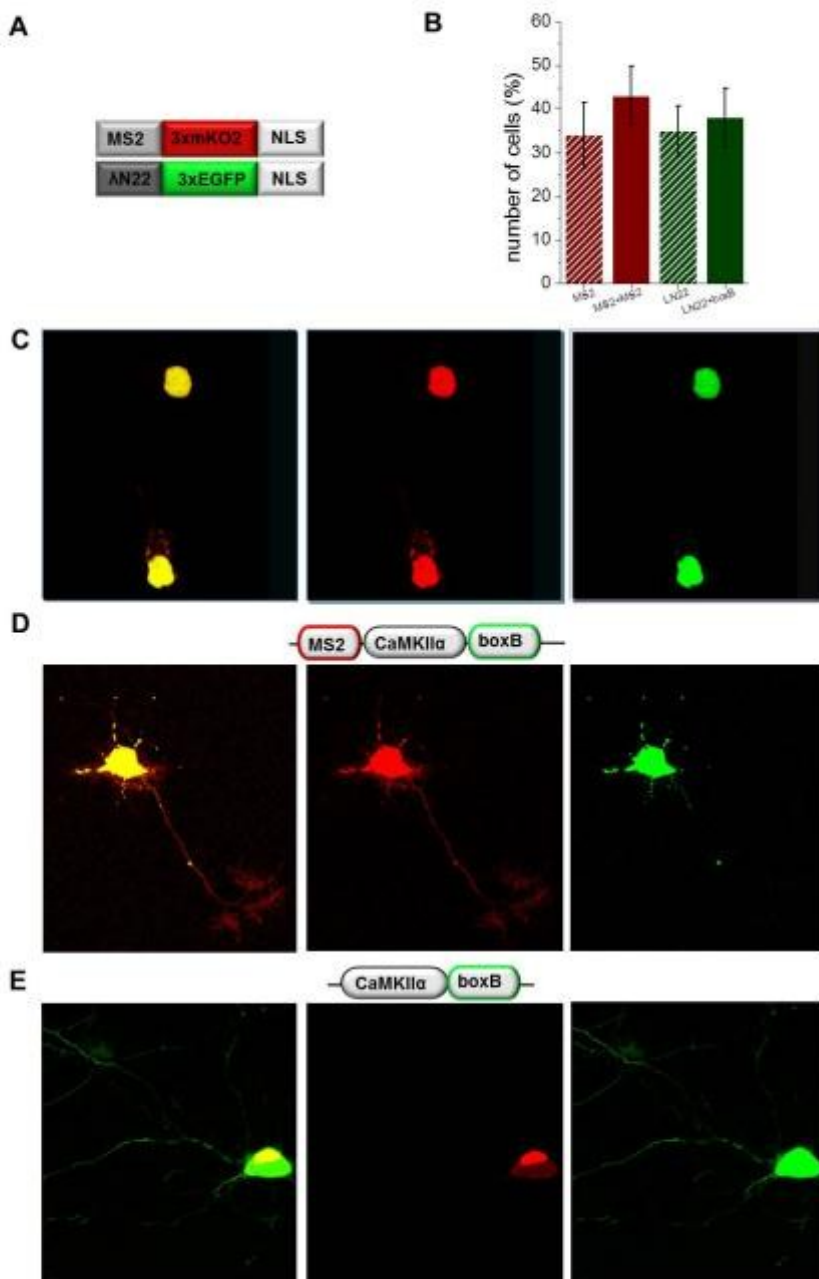


Figure 23 MS2 and AN22 labeling in rat hippocampal neurons. (A) RNA label constructs used for transfection. (B) Quantification of RNA label nuclear export in rat hippocampal neurons, DIV10. Percentage of cells with somatic signal of the fluorescent labels. Hatched bars indicate cells transfected with the reporter only, filled bars represent neurons expressing both label and tagged RNA. MS system (red), AN22 system (green). (C-E) Confocal images of rat hippocampal neurons, DIV10, transiently transfected using lipofectamine. Neurons expressing MS2-3xmKO2-NLS and AN22-3xEGFP-NLS only (C), with boxB- and MS2-tagged CaMKII α (D) or CaMKII α -boxB (E).

3.1.2. NMDAR1 splicing reporter

The MS2- and λ N22-RNA labeling systems were used to establish a reporter for NMDAR1 alternative splicing of exon 21. We constructed a splice reporter based on the established exon 21 minigene (Wenqing Zhang et al. 2002) (J Han 2005). The MS2 tag was inserted between the 5'UTR and exon20 followed by an intron and a boxB-tagged exon 21, another intron, exon 22 and the 3'UTR (Figure 24). Both alternative splice variants are tagged by MS2 but only the variant bearing exon 21 keeps the boxB aptamer after intron removal.

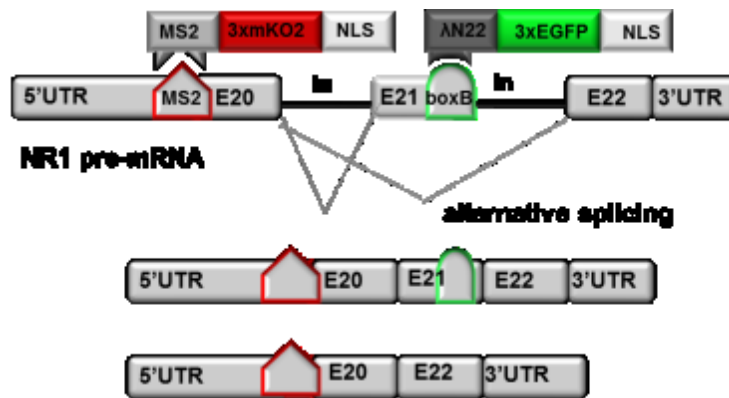


Figure 24 NMDAR1 splicing reporter strategy. The artificial NMDAR1 pre-mRNA reporter construct contains both RNA tags that can be bound by MS2-3xmKO2-NLS and λ N22-3xEGFP-NLS. After splicing, exon 21 bearing the boxB tag at the 3'end is retained or spliced depending on splice site selection.

The NMDAR1 splicing reporter RNA and λ N22-3xEGFP-NLS were transiently expressed in hippocampal neurons, DIV10. We observed dendritic granular labeling that was further characterized by costaining with different markers. The λ N22 label did not colocalize with lysotracker, the ER or P-body marker DCP1. NMDAR1 signal partially overlapped with S6 ribosomal protein and with FMRP in stress granules (Figure 25).

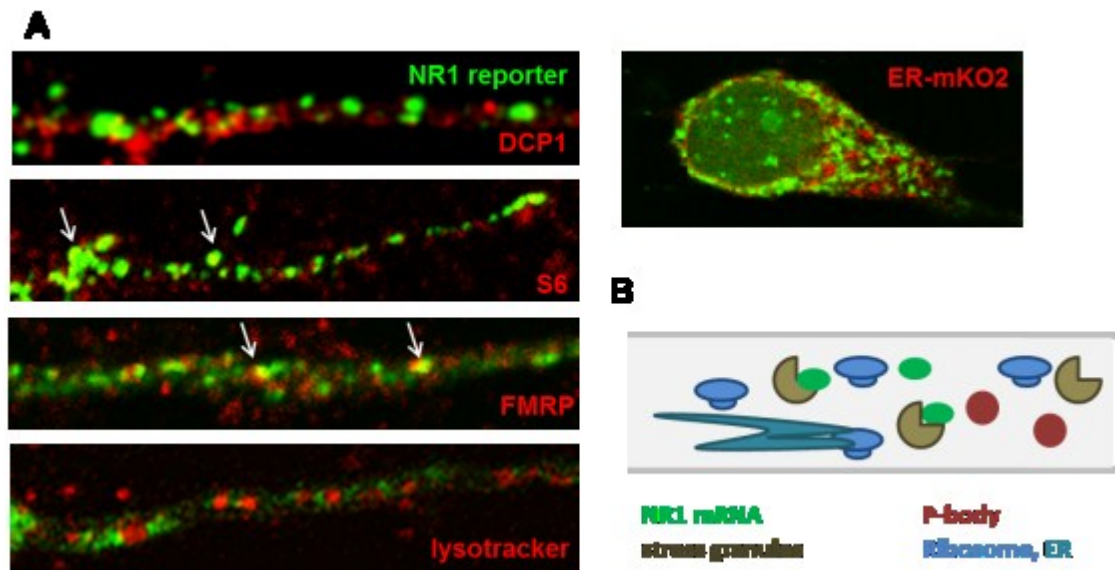


Figure 25 NMDAR1 splice reporter granule characterization. (A) Confocal images of rat hippocampal neuron dendritic branches expressing NMDAR1 RNA reporter and λ N22-3xEGFP-NLS. Neurons were either fixed and costained with antibodies for DCP1, S6 ribosomal protein and FMRP using a Cy3 secondary or antibody. Alternatively, cells were supplied with lysotracker or the ER-targeted mKO2 was coexpressed. **(B)** Schematic of NMDAR1 reporter association with dendritic structures.

The NMDAR1 splicing RNA construct and both, the MS2 and the λ N22 labels were transfected into hippocampal neurons. Confocal imaging revealed different distribution of fluorescence emission of the two fluorescent proteins (Figure 26A). Double-labeled granules correspond to locations of NMDAR1 reporter pre-mRNA or exon 21-retained splice variant. Regions with EGFP but no mKO2 emission indicated the presence of exon 21-spliced NMDAR1 reporter RNA. A program was written by Friedrich Förstner that measures emission intensity ratio IR/G of mKO2 and EGFP and reassigns red colour for IR/G>1 and green colour for IR/G<1 (Figure 26B). mKO2 and EGFP emission intensities were plotted as a function of distance from the nucleus by defining a region within the nucleus as the r=0 (Figure 26C). Different neurons and dendrites show varying distribution of the two reporter signals.

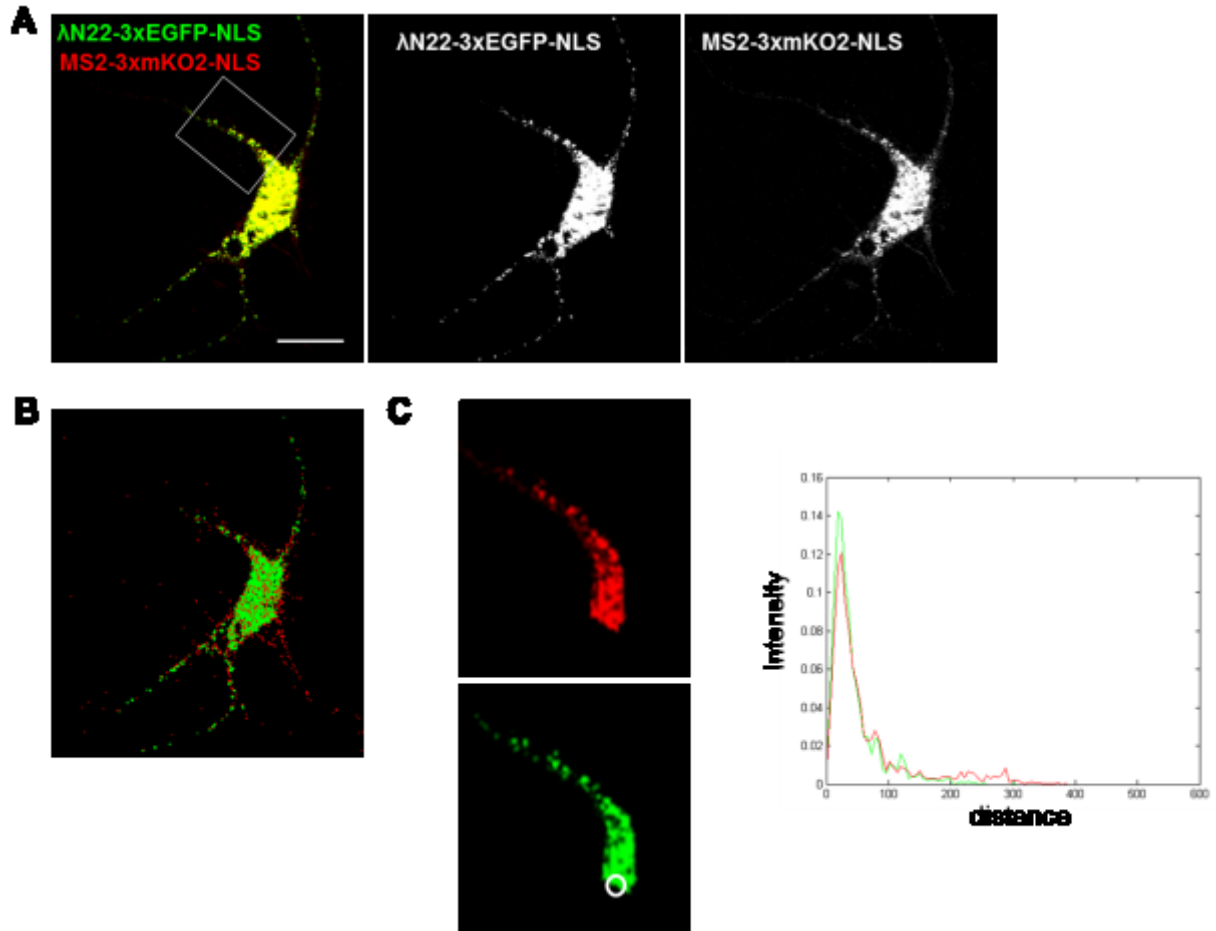


Figure 26 NMDAR1 exon21 alternative splice variant imaging in hippocampal neurons. **(A)** NMDAR (NR1) splicing RNA reporter construct and the MS2-3xmKO2-NLS (red) and λ N22-3xEGFP-NLS (green) were transiently expressed in hippocampal neurons, DIV10 and cells were stimulated by 40 mM KCl for 2 h. **(B)** Red and green colors were assigned to regions of $I_{R/G} > 1$ and $I_{R/G} < 1$, respectively. **(C)** Magnifications from the fluorescence image (A, white box) of both channels with a white circle labeling the region at the proximal dendrite defined as $r=0$. EGFP or mKO2 emission intensity are dependent on the distance to the predefined region.

3.2. RNA imaging using an on-off chemical dye

In collaboration with J. Rao's lab we designed an RNA visualization strategy based on an on-off chemical compound. The RNA of interest is tagged with a short, unique RNA aptamer sequence that exhibits high affinity to a specific membrane permeable dye and enhances its fluorescence (Figure 27A). Once expressed, this RNA tag binds to its exogenously administered probe that emits fluorescent light thereby indicating the subcellular localization of the tagged RNA of interest.

3.2.1 *In vitro* development of the on-off dye – aptamer pair

The Rao lab has designed a small molecule fluorogenic probe based on fluorescently quenched sulforhodamine (ASR). Quenching originates from an aniline substitution on one of the amine groups via a photoinduced electron transfer mechanism (Figure 27B). The second amino group was alkylated for better water solubility and to introduce a carboxylate group for enabling further biotinylation for immobilization on the beads for *in vitro* SELEX selection.

The SELEX procedure and fluorescence screening in *E. coli* have been applied by the Rao lab to screen for a 60 nt random RNA sequence (10^{13} variants) that specifically binds and activates the fluorogen. ASR was immobilized on beads and 8 rounds of affinity selection yielded several of high-affinity aptamers. The selected pool of RNA aptamers was further screened for their light-up property in *E. coli* by fluorescence imaging. One of the aptamers, Apt10, binds ASR with an affinity of $39.1 \pm 7.6 \mu\text{M}$ and F_{max} (expected fluorescence fold enhancement at saturation) of 135 ± 15 (Figure 27C, D).

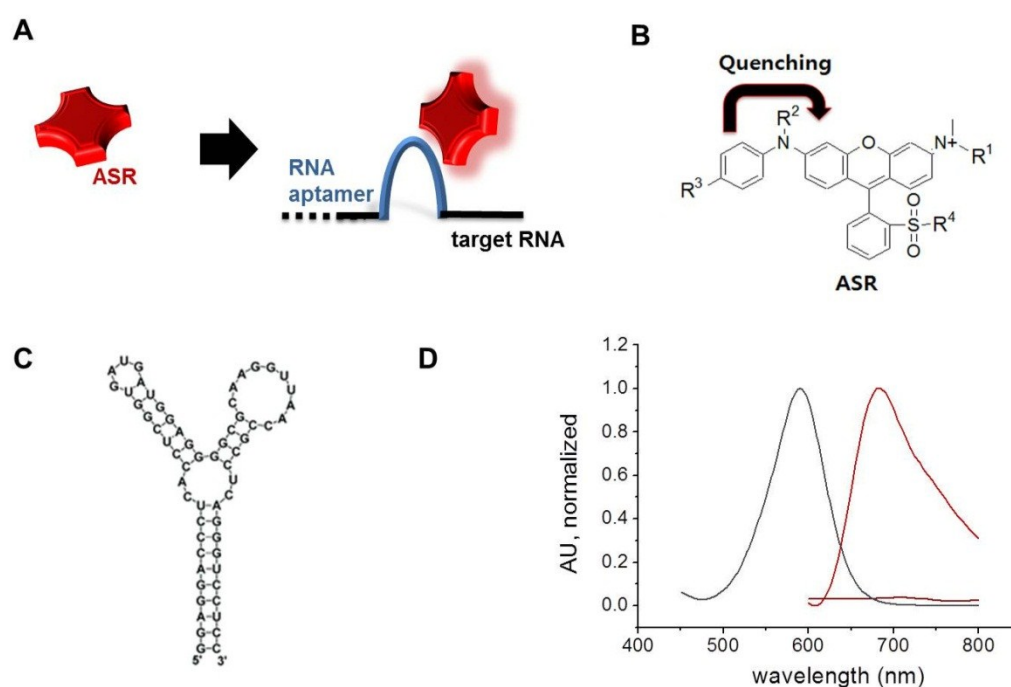


Figure 27 Principle of aptamer-induced fluorescence of a chemical compound. (A) Sulforhodamine-based compound derivatised by an aromatic moiety for internal quenching. Compound becomes fluorescent upon binding to an RNA aptamer. Attachment of aptamer to target RNA enables imaging and tracking of any RNA of interest. **(B)** The general structure of ASR ($R_1 = \text{CH}_2\text{CO}_2^-$, $R_2 = \text{Me}$, $R_3 = \text{H}$, $R_4 = \text{O}^-$ for ASR 1 as the SELEX target) (J Lee et al. 2010). **(C)** ASR *in vitro* measurements. Excitation

spectrum (emission =700 nm) (grey), emission spectrum (excitation=590 nm) in the presence (light red) or absence (dark red) of APT10. (APT10: GCAGGACCCTCACCTCGGTGATGATGGAGG GCGCAAGGTTAACCGCCTCAGGGTCCTCG)

3.2.2 On-off dye performance in mammalian cell lines

In order to test *in vivo* performance of the system, seven repeats of the selected aptamer were cloned downstream the CMV promoter in pEGFP. Primary hippocampal neurons were transfected with the pEGFP vector with or without (control) the aptamer repeats. The initial ASR dye with an indoline based quenching group was applied for 5 min to 24 h in concentrations ranging from 0.2 to 10 μ M. In any circumstance, the dye precipitated before entering the cells and was only stable for several days in DMSO (Figure 28). Poor solubility and stability were presumably due to the indoline residue based quenching group. Improving performance of the probe, an aniline-based dye (with a guanidine group for better stability) was tested as mentioned above. Even though the modified ASR dye did not precipitate, staining was not observed inside the cell but exclusively in proximity to cell membranes.

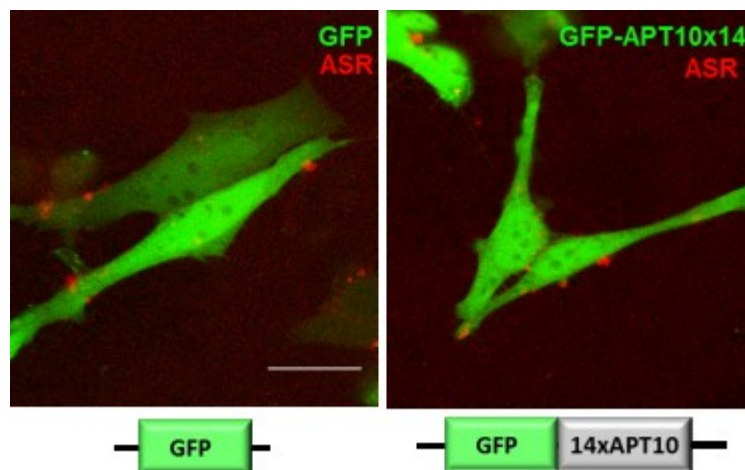


Figure 28 Chemical compound approach performance in HeLa cells. Seven aptamers were cloned into a pEGFP vector yielding a CMV promoter. HeLa cells transfected with the pEGFP vector with (right) or without (left) APT10 repeats. 1 μ M ASR was applied for 15 min precipitated before entering the cells and was unstable.

As applicability of the first-generation RNA dye in cells was limited by cell-impermeability, the Rao lab has modified the dye by conjugation with a tat peptide derived from the HIV-1

tat peptide (=RKKRRQRRR) (Schwarze et al. 1999). Attachment of the tat peptide has improved the cellular delivery of various biologically active molecules in different cell types including hippocampal neurons (Vives 2005). Similarly, ASR-tat was detected inside HeLa cells but granular staining was observed most probably originating from dye entrapment in endosomes (Figure 29B). As compound emission could be detected in cells expressing APT10 as well as in control cells that lack the specific aptamer, cellular environment possibly leads to fluorescence emission increase of the dye. This could be due to a pH-sensitivity of the dye resulting in fluorescence increase within the acidic endosomal lumen. Supporting this hypothesis, attempts to disrupt endosomes by sucrose incubation totally abolished compound emission (Figure 29C). Polynucleus formation additionally points towards a cytotoxic effect of dye application.

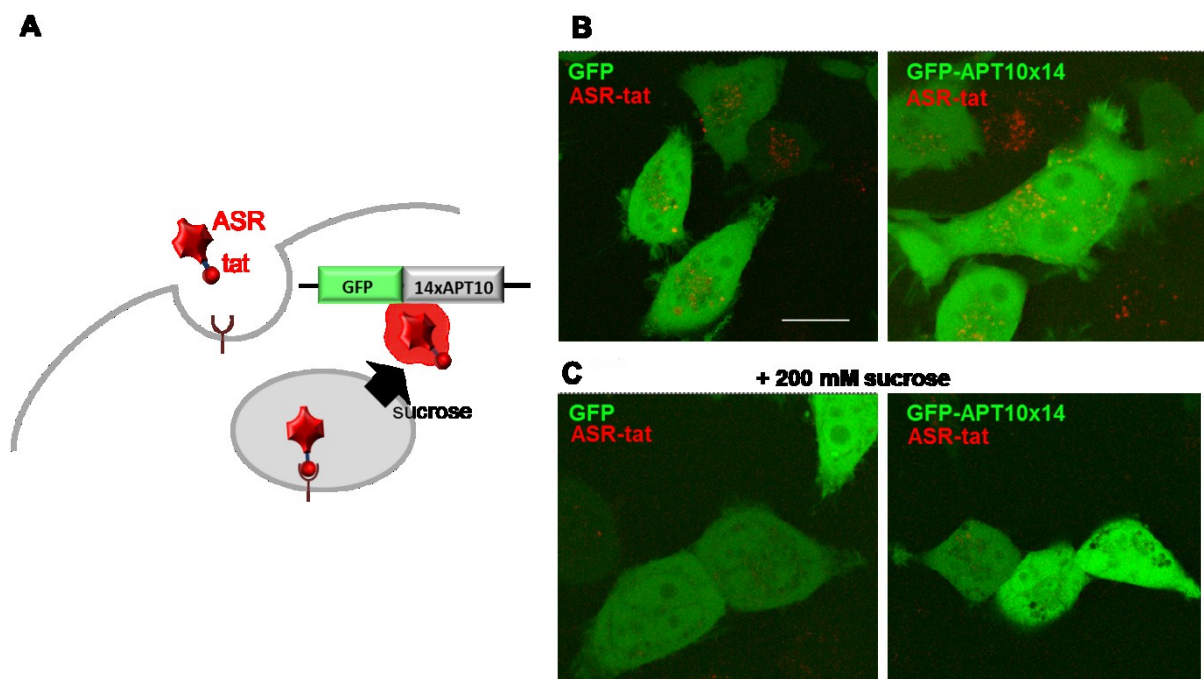


Figure 29 Staining of HeLa cells with a tat-conjugated on-off RNA dye. (A) Scheme of ASR-tat receptor-mediated endocytosis. **(B)** Excitation of the dye at 532 nm and detection window using confocal microscopy. **(B) (C)** 5 μ M ASR-tat was applied for 30 min to HeLa cells transfected with GFP or with GFP and APT10 respectively (left, right). **(C)** Coincubation of the tat dye with 200 mM sucrose for 2 h reduced dye emission (right).

3.3. Development of a genetically encodable dynamic single fluorophore RNA sensor

In order to render fluorescence emission of a single FP dependent on the presence of an aptamer-tagged target RNA we pursued two different strategies. Both are based on an RNA aptamer that is fused to the RNA of interest and functions like a tag. One reporter principle includes direct binding of the aptamer to a nonfluorescent FP thereby enhancing its fluorescence emission (Figure 30A). In another approach, an RNA binding peptide known to bind a specific RNA aptamer was incorporated into the FP (Figure 30B). In both cases, interaction of the engineered FP with the aptamer induces a conformational change that enhances fluorescence emission.

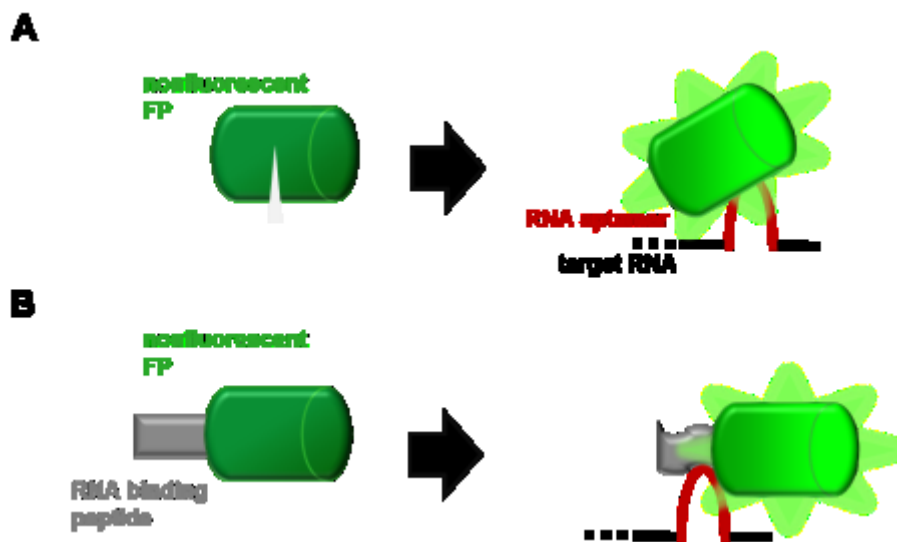


Figure 30 Design principles of dynamic single-FP RNA sensors. (A) Direct binding of an RNA aptamer to a nonfluorescent protein increases its fluorescence emission. **(B)** The RNA aptamer binds to a peptide that is fused to a nonfluorescent protein and induces an increase in emission. The RNA aptamer is fused to a target RNA of interest.

3.3.1 FP emission change upon direct aptamer interaction

We constructed two different proteins that were still able to absorb light at a certain wavelength but poorly emit. In this state the protein was on the verge of being fluorescent which should facilitate the RNA-mediated switch to high fluorescence emission. We chose the nonfluorescent YFP variant REACh2 (= Resonance Energy-Accepting Chromoprotein,

Y145W, H248V) (Ganesan et al. 2006) and an EGFP truncated 13 amino acids from the C-terminal end that poorly emits at 514 nm (Figure 31B).

For the SELEX procedure, a random RNA library comprising 40 nt was created by degenerated primers (Figure 31A). The aptamer library was incubated *in vitro* with His-tagged nonfluorescent proteins, immobilized on Ni-NTA agarose beads. After several rounds of washing, RNA aptamers bound to the protein of interest were eluted with a high-imidazole buffer. Preselected aptamers were coexpressed with the corresponding nonfluorescent protein in *E. coli* XL1 blue. Bright colonies were picked and plasmid DNA encoding the selected RNA aptamer was sequenced. HeLa cells expressing the nonfluorescent protein were compared to cells coexpressing the RNA aptamer under the control of a CMV promoter.

We did 8 rounds of *in vitro* selection and selected 4 bright bacterial colonies. Two of the bright colonies expressed EGFP leaving two candidates, one per target protein for cellular testing. Coexpression of the positively selected aptamers with their target constructs did not increase fluorescence emission compared to cells only expressing REACh2 or trGFP.

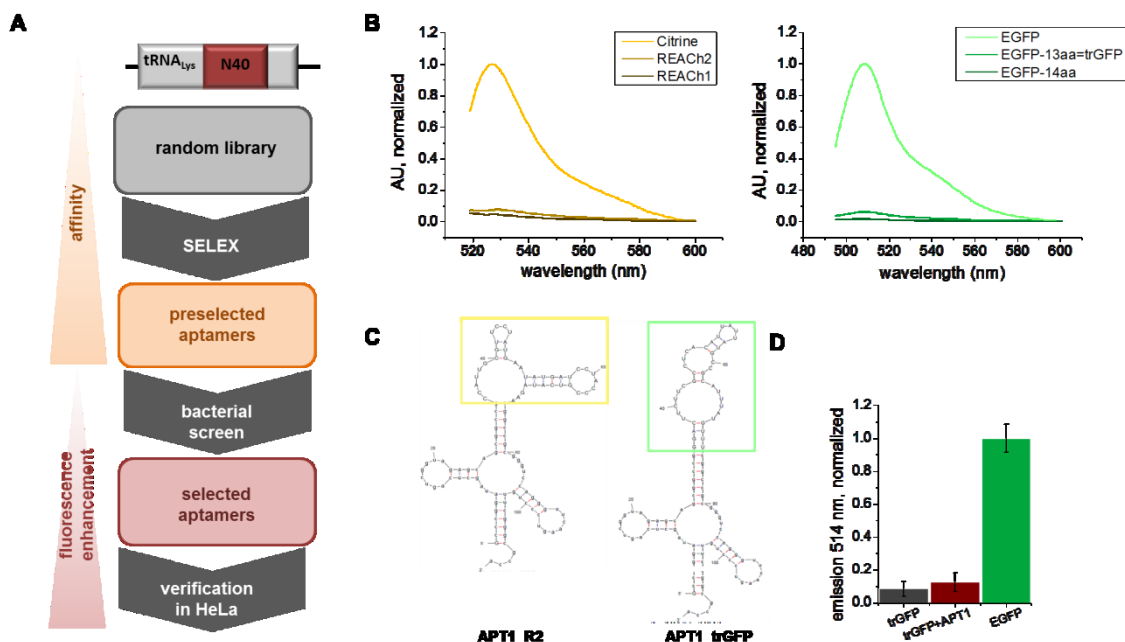


Figure 31 Strategy for engineering aptamer-induced protein fluorescence. (A) Work flow for the selection of an RNA aptamer that is binding and enhancing emission of a nonfluorescent protein. An RNA library of 40 random nucleotides was inserted into a tRNA_{Lys} scaffold for proper folding in bacteria (top) (Ponchon et al. 2009). The library was first screened *in vitro* (SELEX) for affinity to trGFP or REACh2. Prescreened aptamers were subjected to bacterial selection for fluorescence

enhancement, sequenced and transfected into HeLa cells. **(B)** Fluorescence emission spectra of FPs and mutated nonfluorescent proteins that constitute targets for aptamer-induced fluorescence tuning. Citrine (yellow) variants REACh1 (ocher) and REACh2 (orange) exhibit reduced emission at 534 nm. C-terminal shortening of EGFP (light green) by 13aa (= trGFP, grass-green) or 14aa (dark green) decreased fluorescence emission at 514 nm. **(C)** Structures of the selected aptamers from the bacterial screen as predicted by mfold. Shown are the tRNA_{Lys} scaffolds and the selected 40 nt sequences APT1_R2 (yellow box), selected for the REACh2 and APT_trGFP (green box) for trGFP. **(D)** trGFP fluorescence emission intensity at 514 nm with and without coexpressed APT1_trGFP in HeLa cells compared to EGFP.

3.3.2 Aptamer-dependent emission change in a FP-peptide hybrid

Building on known viral peptide-aptamer interactions we inserted peptides into FP in order to render spectral properties dependent on the RNA aptamer binding.

We replaced different regions within EGFP with the 18 aa α -helical peptide λ N22 that binds to boxB RNA (13 nt) with a $K_D=20$ nM (Figure 32B). Regions within EGFP were chosen at the C-terminal end (deleting 8 or 10 amino acids; Cter8, Cter10), within a short and a long loop (sloop, lloop) and an α -helical domain (helix) (Figure 32A) and the corresponding hybrid proteins were called lamGFP. Only lamGFP_sloop and lamGFP_Cter10 were able to absorb light at 488 nm. Upon boxB aptamer addition, hybrid EGFP fluorescence emission could not be increased for any variant (Figure 32D). lamGFP_Cter10 emission decreased 12% upon boxB RNA supplementation.

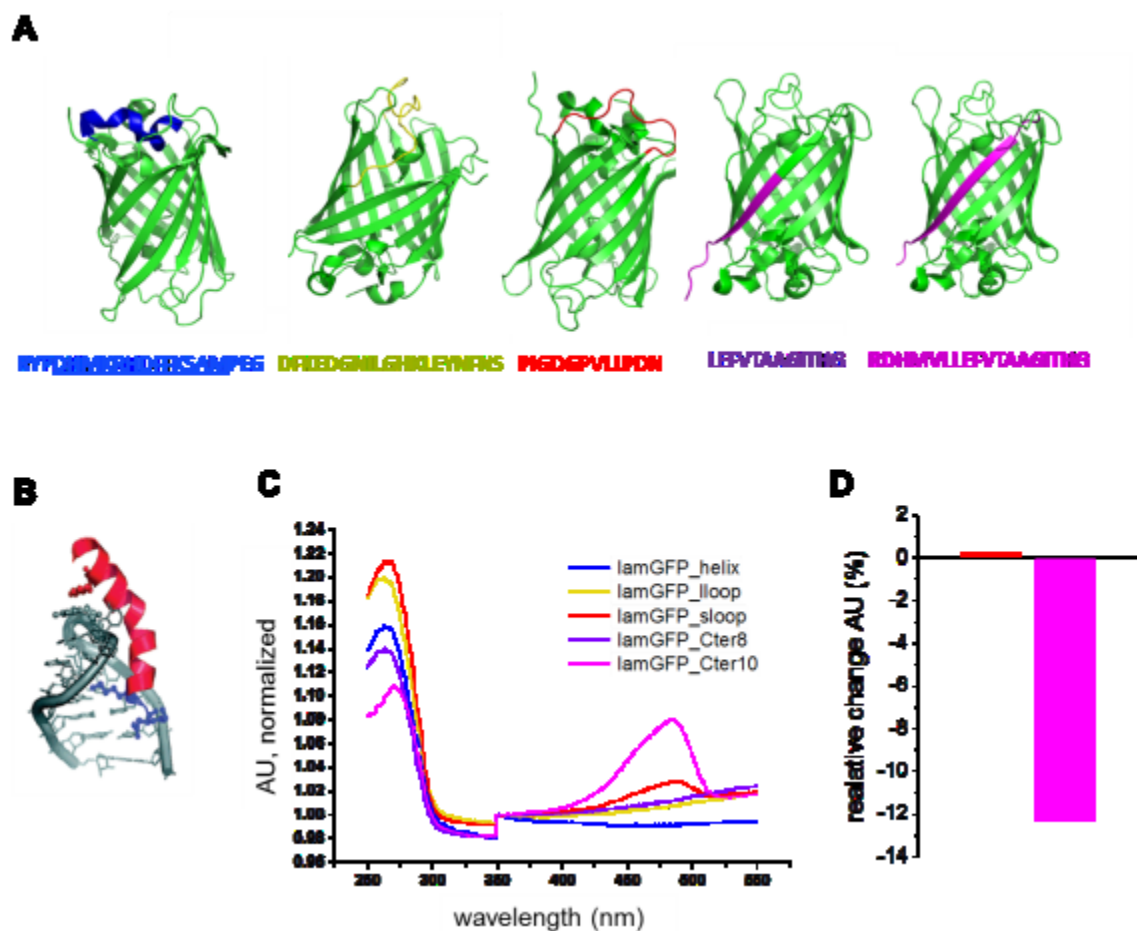


Figure 32 λ N22 peptide insertion into EGFP. **(A)** EGFP crystal structures with target regions for replacement with the λ N22 peptide labeled in different colors. Deleted EGFP sequences are indicated below. **(B)** Structure of the λ N22 peptide-boxB complex (PDB 1QFQ). **(C)** Absorption spectra of different recombinantly expressed lamGFP hybrid constructs. **(D)** Relative intensity change (514 nm) after 488 nm excitation of lamGFP proteins upon addition of *in vitro* transcribed boxB RNA. lamGFP_sloop shows negligible emission intensity change and lamGFP_Cter10 fluorescence decreases 12 %.

In another approach, we tested different peptide-aptamer pairs in a circularly permuted EGFP (cpEGFP) scaffold. This resembles the design of the Calcium sensor GCamP which is composed of a cpEGFP with a M13 peptide at the N-terminus and the Calcium binding moiety, so-called EF hands, at the C-terminus. We inserted the viral RNA binding peptides BIV tat, Rsg1.2, Phi21 N or P22 N into 3 different sites of GCamP2 (Figure 33). The highest change in EGFP emission upon 488 nm excitation of -46% was observed for the cpEGFP-BIV tat peptide construct after addition of the corresponding BIV tar aptamer (Figure 33A).

Excitation of cpEGFP-BIV at 405 nm resulted in an emission increase at 514 nm after BIV tar supplementation.

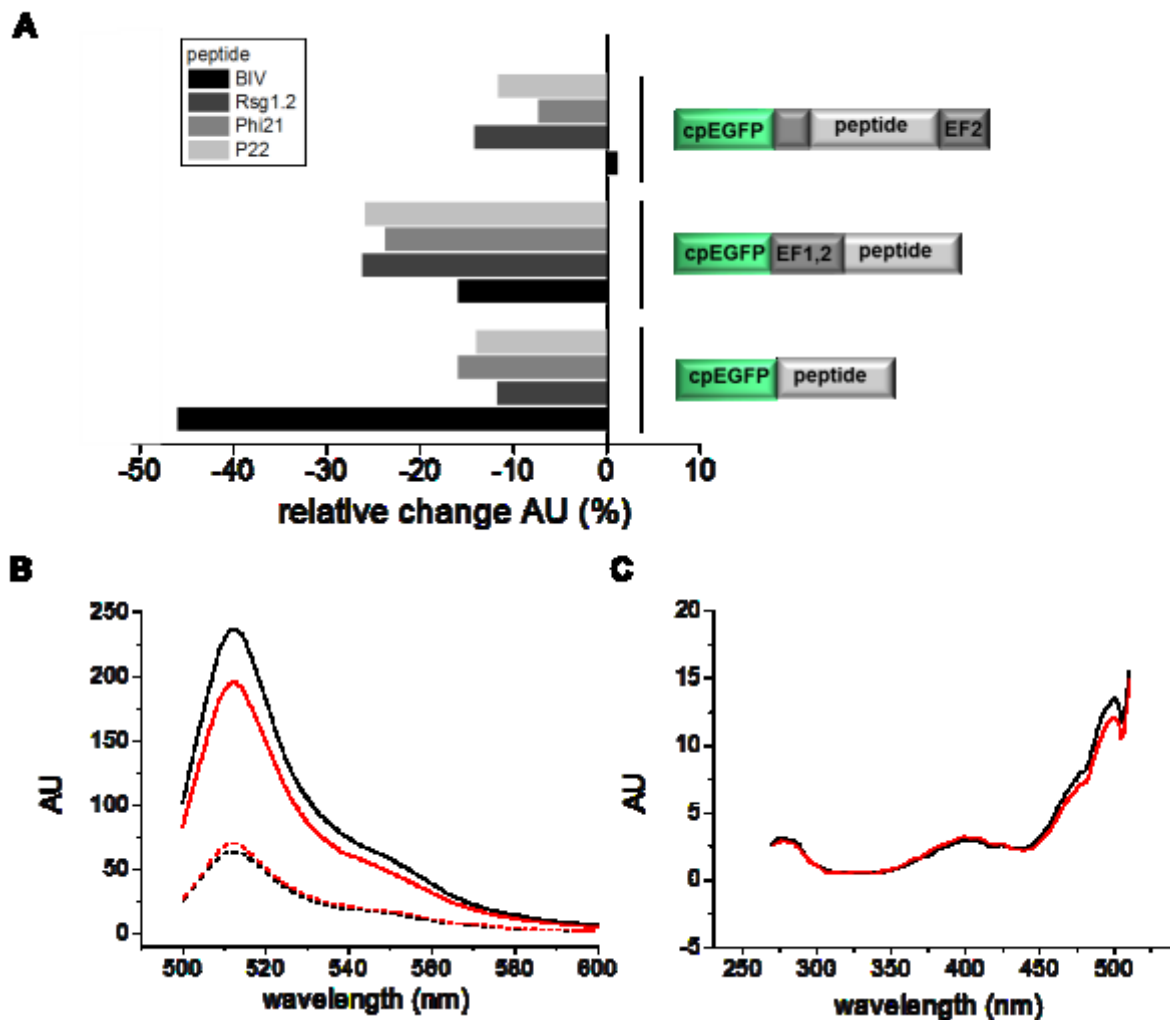


Figure 33 Aptamer-dependent fluorescence of a cpEGFP-viral peptide hybrid. **(A)** BIV tar, Rsg1.2, Phi21 N or P22 N peptides were inserted into the GCaMP 2 scaffold at the positions indicated. (EF = EF hand). Single fluorophore recombinant proteins were excited at 488 nm and the emission intensity at 514 nm was measured before and after addition of in vitro transcribed BIV tar, RRE, Phi 21 boxB or P22 boxB respectively. **(B)** cpEGFP-BIV emission spectrum at 488 nm (solid line) and 405 nm (dashed line) excitation before (black) and after (red) addition of BIV tar RNA. **(C)** cpEGFP-BIV excitation spectrum for emission at 514 nm before (black) and after (red) addition of BIV tar RNA.

3.4 Engineering of the FRET-based RNA biosensor VAmPIRe

3.4.1 Aptamer-peptide pair selection for the FRET biosensor

The FRET RNA sensor design is based on the FRET pair linked by a peptide that is supposed to undergo a conformational change upon interaction with a specific aptamer. This renders FRET efficiency, determined by distance and orientation of the FRET donor and acceptor, dependent on the peptide-aptamer interaction (Figure 34). An RNA of interest can be tagged by the aptamer on the DNA level which results in a fusion RNA construct after transcription in cells.

We used enhanced CFP (eCFP) and a circularly permuted YFP variant cpCitrine (Mank et al. 2006) as FRET donor and acceptor, respectively. Suitable peptide-aptamer pairs were tested for their ability to alter FRET efficiency in dependence of the presence of the specific aptamer. Crucial for biosensor function is the conformational change of the peptide upon binding to its RNA aptamer. Viral ARM peptide-aptamer pairs not only fulfill this criterion but meet the demands of high affinity binding as well as the applicability in prokaryotic and eukaryotic cells by avoidance of sensor interaction with endogenous transcripts.

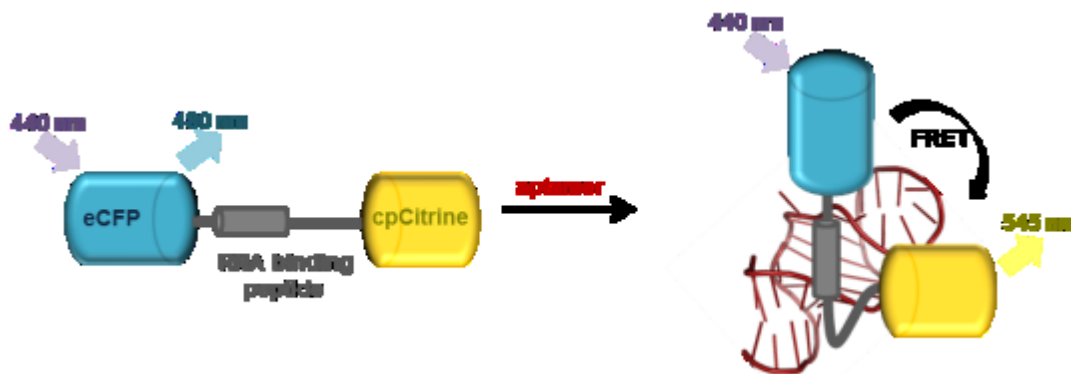


Figure 34 FRET RNA biosensor principle. A viral peptide separates the enhanced cyan donor FP (eCFP) from the yellow FP cpCitrine. Upon binding of a specific RNA aptamer the peptide undergoes a conformational change that results in an alteration of distance and/or orientation of the FPs. Increased emission of the YFP acceptor indicates the presence of the aptamer. Molecular model of the peptide-aptamer complex (right).

For biosensor design, we needed to find a peptide-aptamer pair with a conformational change upon interaction that allows FRET change to occur. Therefore, we inserted 7 different ARM peptides into the eCFP-cpCitrine FRET pair backbone by using *SphI* and *SacI* restriction sites. A biosensor library was constructed by recombinant expression of the FRET

fusion constructs. The corresponding RNA aptamer-coding DNA was synthesized and subsequently transcribed *in vitro* into RNA, purified and refolded. The fluorescence intensity ratio of eCFP and cpCitrine emission of the FRET sensor was compared before and after addition of the corresponding aptamer. As a control, unspecific RNA aptamers were added. Largest emission ratio change upon specific aptamer addition was found for the bovine immunodeficiency virus BIV tat-BIV tar peptide/aptamer pair (30 % ratio change) and the synthetic peptide Rsg 1.2 binding to the HIV RRE RNA stem loop IIB34 (Malim et al. 1990) (MD Daugherty et al. 2010) (FR-Rsg1.2, 40 % ratio change, Table 1). The BIV tat peptide based sensor showed 31 % ratio change upon addition of the BIV tar aptamer. The ratio changes are reversible, demonstrated by addition of RNase. We chose the sensor FR-Rsg1.2 for preliminary characterization and further engineering.

peptide	aptamer	K_D (nM)	FRET ratio change (%)
BIV tat	BIV tar	0.5	30
HIV-1 Rev	RRE	40	-
Rsg 1.2	RRE	6	40
HTLV Rex	HTLV apt	6	-
P22	boxB	100	-23
Φ 21	boxB	80	-23
λ N21	boxB	20	-

Table 1: Ratio change in FRET biosensor constructs using selected ARM peptides as sensing moiety. Peptides were sandwiched between the fluorescent proteins CFP and cpCitrine. The maximal ratio change after binding to the corresponding aptamer is shown. Positive values indicate increased energy transfer, a negative value decreased energy transfer from donor to acceptor. K_D refer to the interaction of free peptide with its specific aptamer.

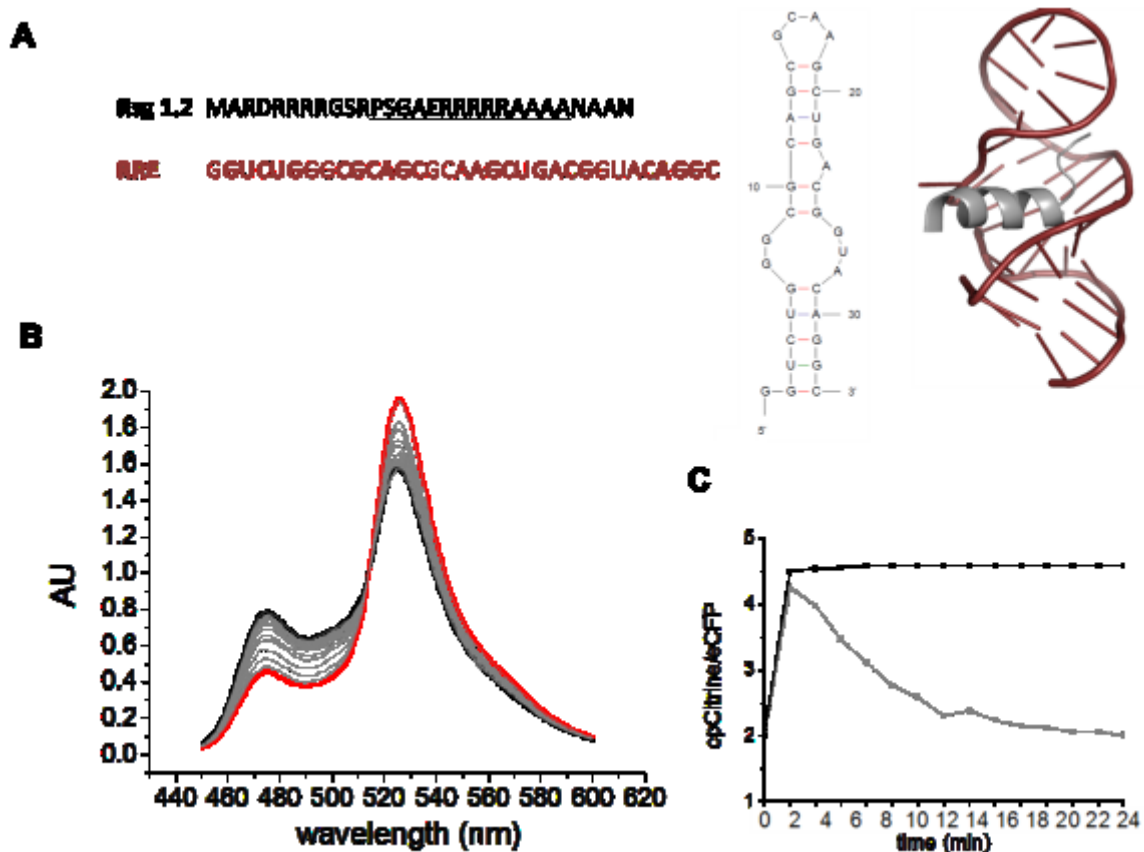


Figure 35 FRET YFP/CFP measurements in the cuvette. (A) Sequences of the Rsg 1.2 peptide with the RNA-binding site underlined and the RRE aptamer with pairing bases marked bold. The RRE secondary structure (middle) was created by mfold and the model of the complex NMR structure (right, PDB 1G70) by Pymol. **(B)** Emission spectrum of the recombinantly expressed FRET RNA sensor excited at 434 nm. Addition of the *in vitro* transcribed specific aptamer in a 1:1 molar ratio results in 100% cpCitrine/eCFP emission ratio change. **(B) (C)** Aptamer-induced FRET ratio change is fully reversible by addition of RNase after 2 min (grey lines, $\Delta t = 2\text{min}$). **(C)** FRET ratio could not be reversed by addition of DNase after 2 min (black line).

FR-Rsg1.2 ratio change upon RRE RNA supplementation was high compared to the reverse RRE sequence (Figure 36). For some RRE single nucleotide mutants with identical secondary structure that have been reported to bind to Rev (Kazuo Harada et al. 2008), a FRET change was observed (Figure 36B).

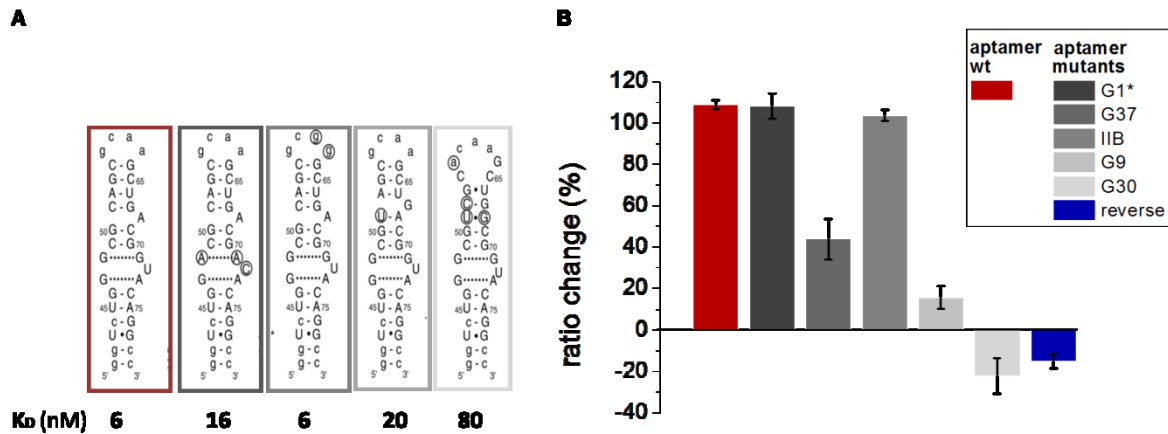


Figure 36 FR-Rsg1.2 RNA aptamer specificity. Recombinant FR-Rsg1.2 was supplied with different *in vitro* transcribed RNA aptamer variants. **(A)** Secondary structures and affinity of the corresponding aptamer (wt RRE, red; mutant aptamers grey, reverse wt RRE sequence blue) to the Rev peptide are shown (right) (Kazuo Harada et al. 2008). **(B)** Normalized cpCitricine/eCFP ratio change upon addition of the corresponding aptamer.

3.4.2 Rational engineering of FR-Rsg1.2

3.4.2.1 Linker design

A well-described method to boost sensor performance is to reduce the FRET ratio in the resting state while conserving the high FRET aptamer-bound state. A common target is to increase FRET pair distance by the introduction of additional amino acids at the regions flanking the RNA binding peptide. This strategy aims at rendering the two different states maximally dependent on FRET efficiency on FP distance (Figure 11). Insertion of flexible and helical linkers or Rsg 1.2 peptide multiplication resulted in decreased starting ratio depending on the number of amino acids. However, the ratio change was dramatically reduced for all linkers tested.

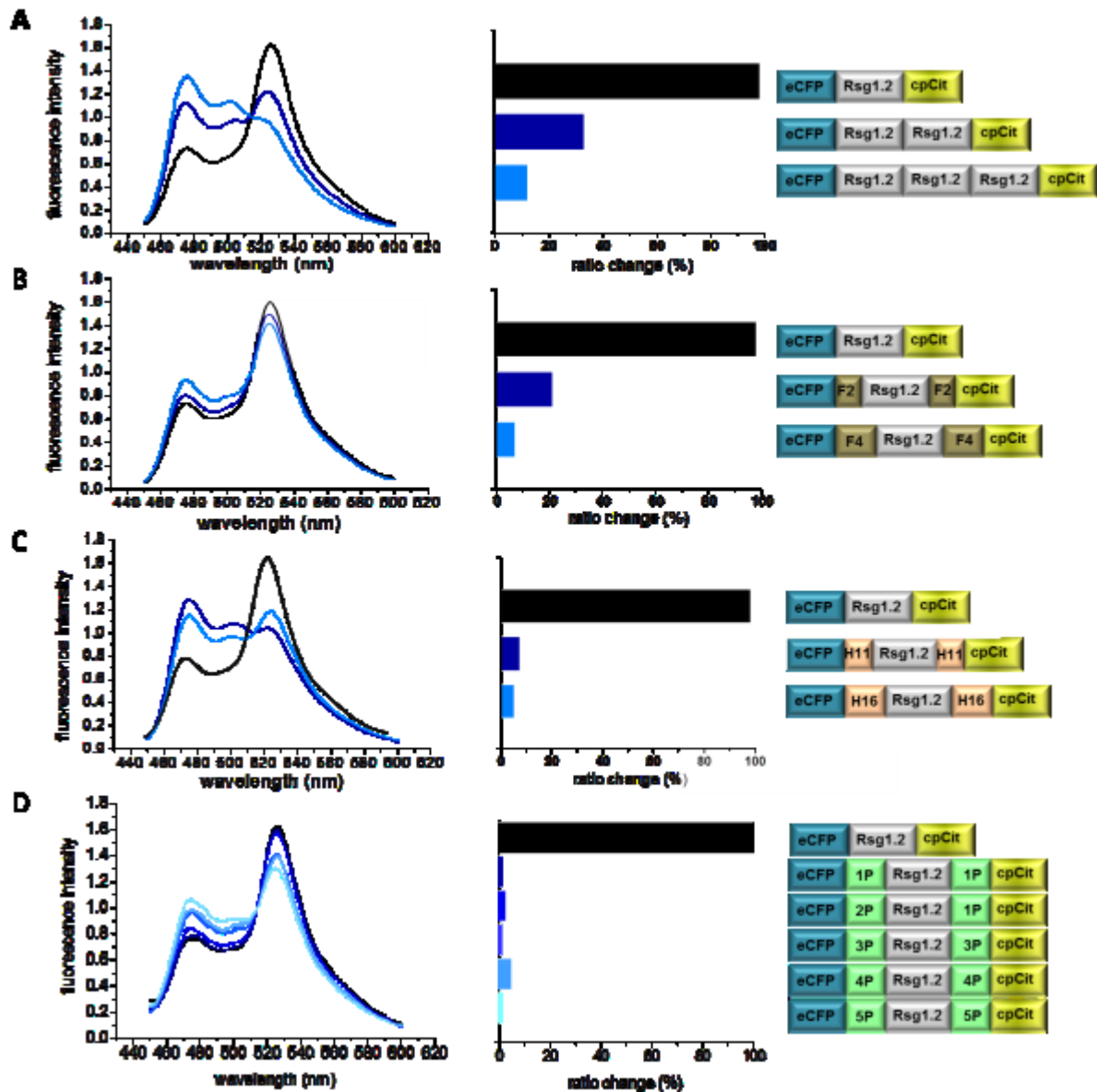
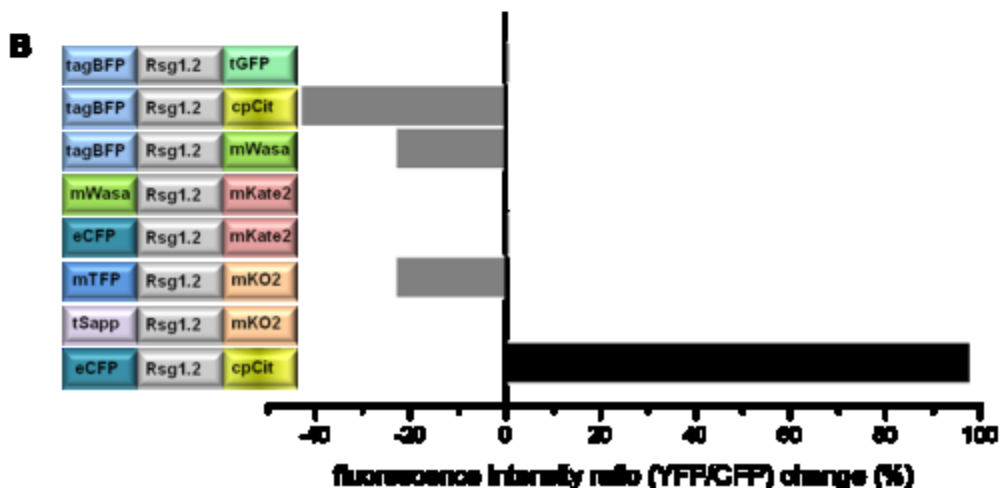
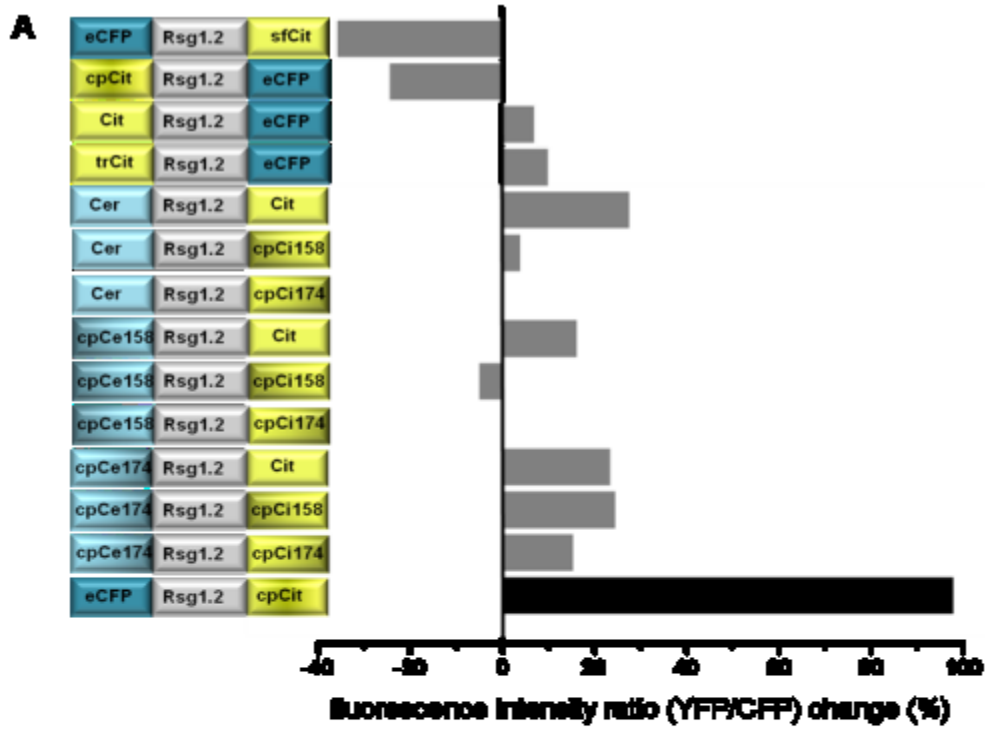


Figure 37 Peptide multiplication and rational linker design. Emission spectra ($\lambda_{ex}=432\text{nm}$) (left), normalized FRET ratio change (middle) and construct schematics (right) of FR-Rsg1.2 variants (blue) compared to the wt FR-Rsg1.2 sensor (black). Rational design strategies include Rsg1.2 multiplication (top) and linker extension using flexible (F, middle) or helical (H, bottom) linkers of different length (number of amino acids is indicated). F4=GGGS, F8=GGSGGGS, H11=KLYPYDVPDYA, H16=KLYPYDVPDYALEYDV. All spectra were measured at pH=8.

3.4.2.2 FRET pair engineering

Another rational FRET sensor design strategy involves testing of different FRET pairs bearing various Förster distances and biophysical characteristics. We expressed several FR-Rsg1.2 variants using various cyan donors and yellow acceptor FPs. The initial eCFP-cpCitrine FPs

showed highest ratio change. Spectrally shifted FP pairs possess different Förster radii (YFP/CFP $R_0=4.9$ nm) and especially red-shifted variants have advantages for in vivo application. The Rsg-RRE interaction induced a mTFP1-mKO2 ratio change of -22% with a Förster distance $R_0=5.3$ nm.



C

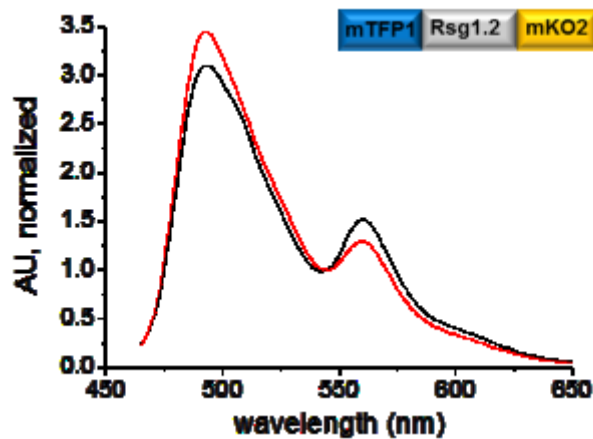


Figure 38 Ratio change of a spectrally shifted RNA FRET sensor. (A) FRET sensors based on Rsg1.2 fused to different CFP-YFP variants **(B)** or spectrally shifted FRET pairs. Construct schematics (left) and the corresponding ratio changes upon RRE aptamer addition (right) are shown. **(C)** Emission spectrum ($\lambda_{\text{ex}} = 458\text{nm}$) of the recombinantly expressed mTFP1-Rsg1.2-mKO2 construct before (black) and after (red) addition of *in vitro* transcribed RRE RNA. (Cer = Cerulean, sfCit = superfolder Citrine, trCitrine = Citrine-11aa, cpCitrine 158/174 = Citrine with circular permutation at positions 158 or 174, mWas = mWasabi, tSapp = tSapphire)

3.4.2.3 Rsg1.2 peptide engineering

Another target for FRET performance engineering is the Rsg 1.2 peptide itself outside the actual aptamer binding region. Rsg 1.2 incorporates three mutations compared to the initially selected Rsg 1 (D4R P12R E16S) and one compared to Rsg 1.1 (D4R) but all peptides exhibit affinity to the RRE aptamer. However, only FRET sensors using Rsg 1.2 show a ratio change upon aptamer addition. Particularly interesting is the Proline that seems to be not crucial for binding but introduces a kink in the peptide backbone. Mutagenesis at this position 12 resulted in mutant sensors with markedly increased starting ratio and negative or zero FRET ratio change (Figure 39).

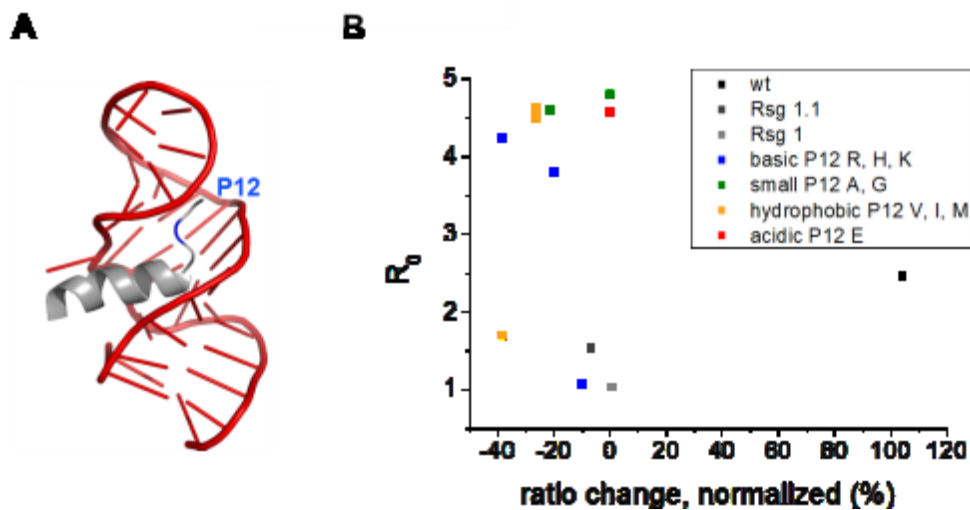


Figure 39 Rsg1.2 peptide Proline 12 mutagenesis. (A) Rsg1.2-RRE aptamer complex crystal structure with position P12 in Rsg1.2 highlighted (blue) (PDB ID 1G70) **(B)** Performance of FRET sensors with replacements at position 12. Rsg 1 (=Rsg1.2 D4R P12R E16S), Rsg 1.1 (D4R) (Kazuo Harada, Shelley S. Martin, et al. 1997h)

FR-Rsg1.2 FRET ratio change was strongly dependent on the pH showing increasing signal output at higher pH values (Figure 40A). As worse sensor performance in an acidic environment probably results from charge effects, pH sensitivity was decreased by engineering of positively-charged residues in order to shift the performance optimum to a physiological pH. N-terminal Arginine residues R3, R5, R6, R7, R8 and R11 that are not situated within the aptamer binding pocket were selected for mutagenesis. We replaced Arginine with amino acids yielding lower pK_a values and a positively charged (Lysine, K), short hydrophobic (Alanine, A) or polar and uncharged (Glutamine, Q) side chain (Figure 40B). With site-specific mutagenesis of FR-Rsg1.2 we created two variants FR-Rsg 7A and FR-Rsg 8Q with improved performance at pH 7.25 and decreased pH-dependency. The combination of these mutations in the double mutant FR-Rsg 7A8Q resulted in 100 % increase of sensor performance at physiological pH compared to FR-Rsg1.2. Both starting ratio is decreased and aptamer-bound FRET ratio is increased in FR-Rsg R7A R8Q (Figure 40C).

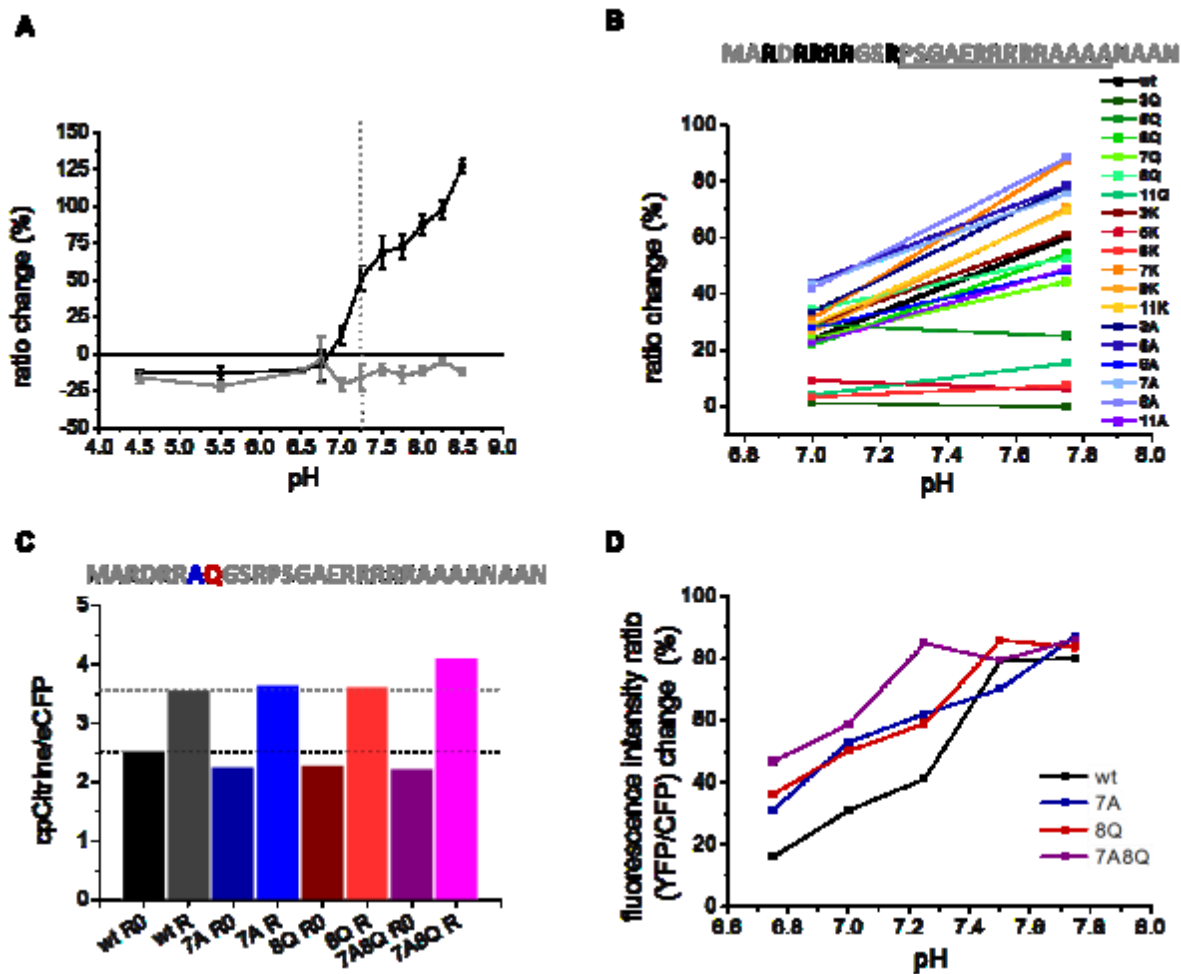


Figure 40 FR-Rsg1.2 pH-sensitivity engineering by Arginine substitution. (A) FR-Rsg1.2 ratio change upon RRE aptamer (black) or unspecific RNA (grey) addition at different pH values. (B) Arginine substitutions at different positions within Rsg1.2 (bold; RNA-binding region underlined) to Glutamine (greens), Lysine (reds) or Alanine (blues). Ratio change at pH 7.0 and 7.75 were measured for all variants. (C) Starting ratio (R_0) and ratio after RRE aptamer addition (R) of FR-Rsg1.2 wt (black, grey), FR-Rsg 7A (blues), FR-Rsg 8Q (reds) and FR-Rsg 7A8Q (purples). (D) pH Dependency of different FR-Rsg1.2 variant ratio changes.

3.4.3 Development of a functional screen for FRET sensor performance in bacteria

With targeted mutagenesis of specific amino acids within Rsg-1.2 we were able to manipulate pH-dependency. With the introduction of linker sequences between the peptide and the FPs we aimed at decreasing the initial ratio and thereby increasing the dynamic range. However, one by one testing of several linkers showed unpredictable characteristics regarding initial ratio and ratio change. Consequently, a large number of random variants had to be created and tested following the model of molecular evolution. The generation of

a huge number of candidate sensors necessitates the establishment of a suitable testing system for high-throughput screening. Bacteria colonies allow both testing in a biological context and easy handling of a large number of library members.

In order to develop a functional screen for improved sensor characteristics we tested FRET sensor performance in bacterial colonies. FRET ratios of bacterial colonies expressing FR-Rsg 7A8Q were significantly lower compared to colonies expressing both the sensor and 10 repeats of an aptamer at different time points after transformation (Figure 41A). In an inverse approach, we used a membrane to blot colonies expressing FR-Rsg1.2 and the aptamer repeats fused to mKO2 on a plate lacking one antibiotic necessary to select for the aptamer repeats. Lacking selection pressure, bacteria lose the mKO2-10xaptamer plasmid visualized by decreased mKO2 emission (Figure 41B). The decrease in FRET ratio after blotting was not significant. Nonetheless, both experiments show that the bacterial system is suitable for screening of FR-Rsg1.2 variants.

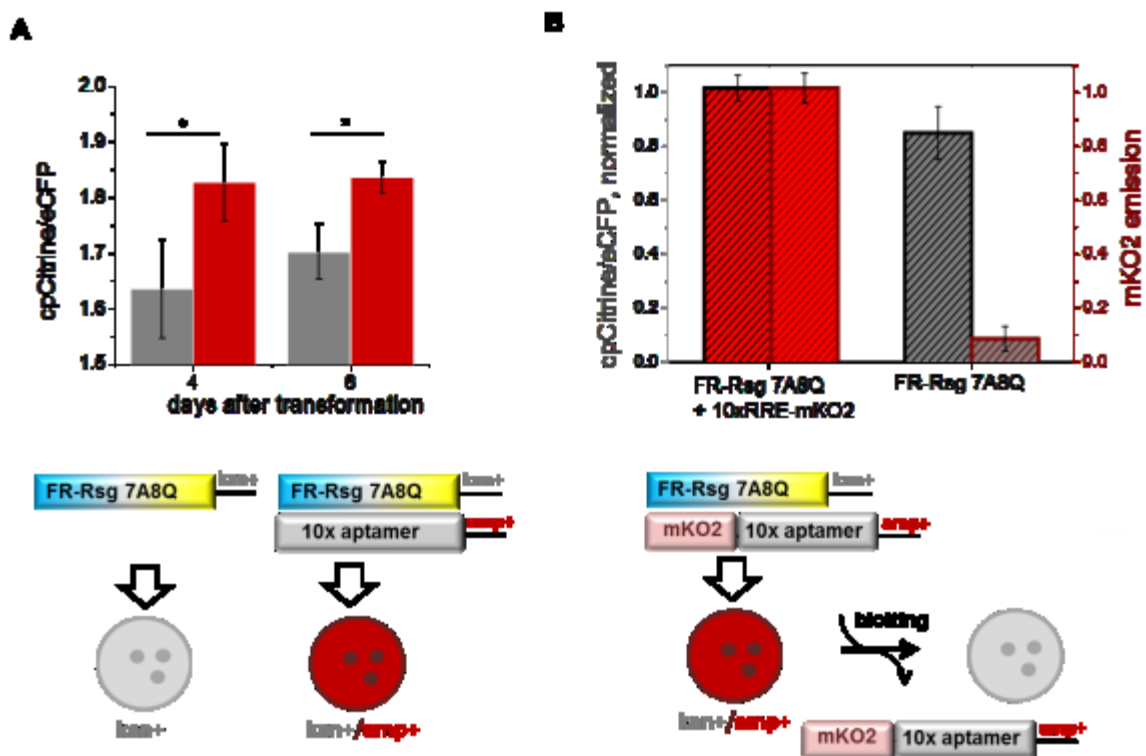


Figure 41 FR-Rsg1.2 7A8Q performance in bacteria. (A) Cotransformation of *E. coli* XL1 blue with FR-Rsg 7A8Q and 10xaptamer (red) compared to transformation with FR-Rsg 7A8Q only (grey). FRET ratio was recorded at different days after transformation. (B) Colonies from a bacterial plate transformed with FR-Rsg 7A8Q and an mKO2-10xaptamer construct (red filling) were subsequently transferred to a plate with no ampicillin using a Nitrocellulose membrane. Loss of selection pressure for ampicillin resistency conferred by mKO2-10xaptamer leads to removal of this plasmid after 2

blotting steps (grey filling). Average colony mKO2 emission (dark red stripes) and cpCitrine/eCFP ratio (black stripes) are plotted.

For the generation of a mutagenized sensor library we followed 3 different strategies (Figure 42A). In a random approach we performed error-prone PCR on the Rsg 7A8Q peptide using CFP Chr for and cpCit Chr rev primers thereby introducing mutations at undefined sites. Using another strategy, degenerated primers (Eurofins) allowed the introduction of randomized amino acids at defined positions during normal PCR reaction (see 3.2.1). The last library comprises linker constructs with random amino acids at both Rsg 7A8Q peptide-FP junctions. The peptide was amplified using degenerated primers that introduce triplets coding for 1, 2, 3, 4 or 8 amino acids. Resulting peptide elongation was supposed to conserve peptide dynamics while increasing the distance between the FRET pair.

The mutagenized peptide libraries were digested cloned into *SphI/SacI* and ligated into a pRSFDuet-eCFP-cpCit vector (Kana⁺) for weak protein expression. 10 aptamer repeats were cloned using *HindIII/NotI* into pMB133 which is designed to turn off the expression of the aptamer-containing RNA via TetR-*tetO* interactions in the promoter region (Valencia-Burton et al. 2009). This inhibition is released in the presence of anhydrotetracycline (aTC) which results in RNA aptamer expression. The sensor library was co-transformed into XL1 blue together with the pMB α 3-10xRRE plasmid (Amp⁺).

On every bacterial plate, we placed two control patches with colonies expressing FR-Rsg 7A8Q only or FR-Rsg 7A8Q and pMB133-10xRRE. Using wide field CCD camera imaging of bacterial agar plates we were able to image simultaneously up to 1000 bacterial colonies each harboring a diversified sensor and to follow FRET changes upon induction of aptamer transcription (Figure 21) using 20 ng/ μ L aTC. For data analysis, one ROI per colony was automatically selected by a program written by David Ng using Cell Profiler. Data were analyzed by Origin 8.1 by plotting the ratio change 200 min after aTC induction over the starting FRET ratio. The selected colonies correspond to the ROIs with a ratio change higher and a starting ratio lower than the average of 6 control colonies.

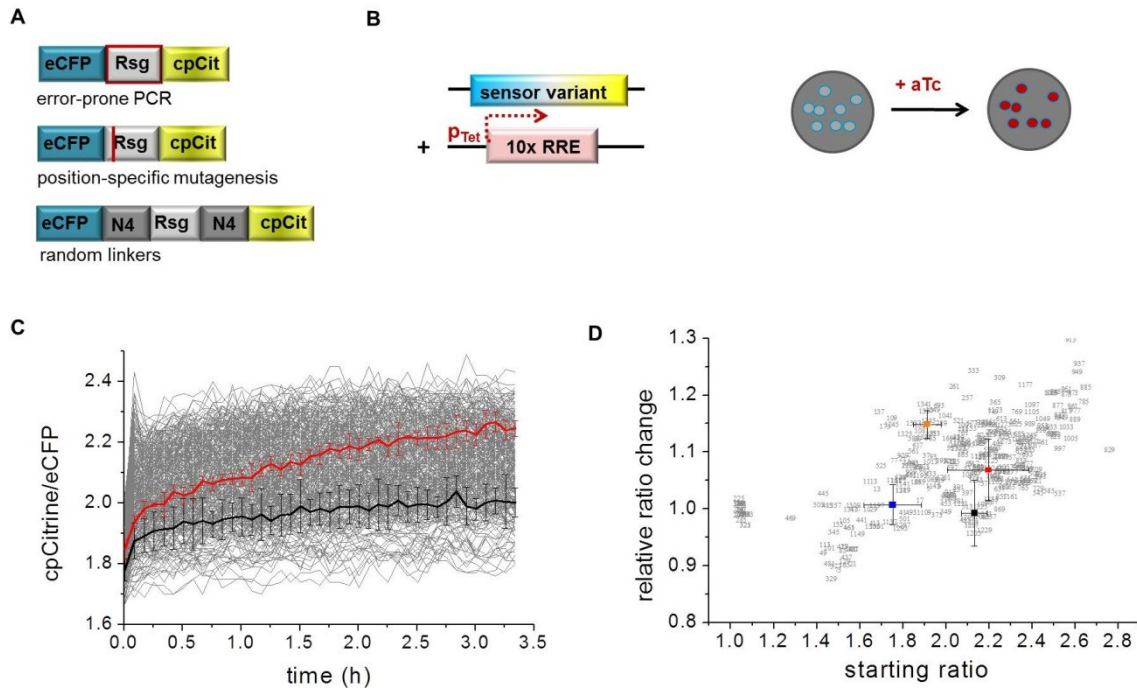


Figure 42 Screening for aptamer-induced FRET ratio change in bacteria. (A) Library generation by error prone PCR of Rsg1.2, mutagenesis at selected positions within the peptide or FP-peptide linkers of variable length and aa composition. **(B)** The sensor library is cotransformed with a 10xRRE construct controlled by a tet promoter. Addition of aTc to the bacterial colonies on the plate induces 10xRRE transcription (red colonies). **(C)** FRET ratio is recorded before and after addition of aTC for 2-4 h for all colonies from the library (grey) and the control colonies expressing FR-Rsg1.2 7A8Q with (red) and without the inducible aptamer (black). n=4 **(D)** A number is assigned to each colony (grey) and starting ratio is plotted against the relative temporal ratio change. 4 control colonies expression FR-Rsg1.2 7A8Q with (red; VAmPIRe, orange) and without the inducible aptamer (black; VAmPIRe, blue). Variants with high ratio change and low starting ratios are picked and *in vitro* tested. n=4

Overall about 60000 indicator variants with diversified linkers were pre-screened by imaging and 1500 indicators selected and subsequently purified for further spectroscopic analysis *in vitro*. Some variants with a starting ratio close to 1 showed lower ratio change after aptamer addition compared to FR-Rsg7A8Q (#47) (Figure 43). Evolutionary linker extension yielded variants with significantly enhanced FRET change, with the best variants (#678, # 95) now showing up to 160 % maximal change in emission ratio after aptamer binding (Figure 43). The best evolved sensor was called VAmPIRe (Viral Aptamer binding Peptide based Indicator for RNA detection).

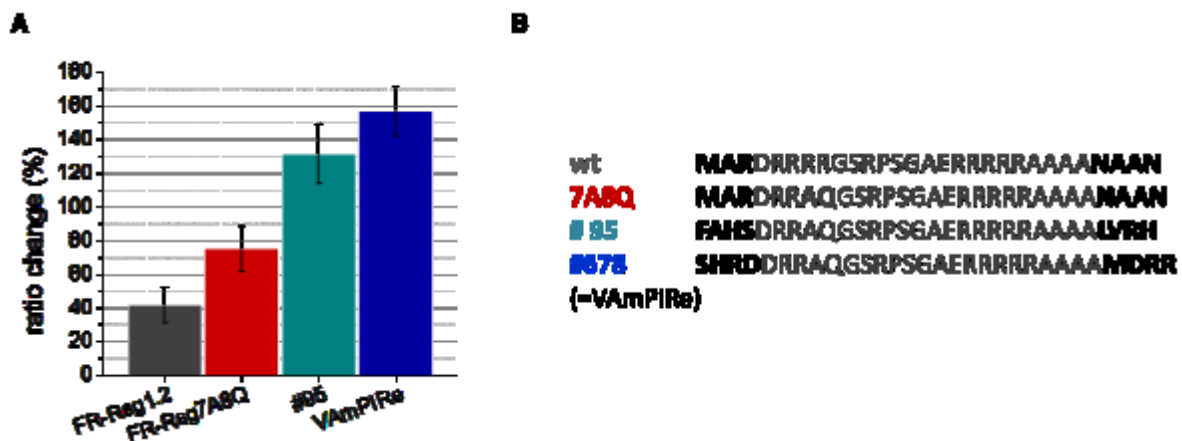


Figure 43 Performance of selected sensor variants. (A) Ratio change is plotted for FR-Rsg1.2 (wt, grey), FR-Rsg1.2 7A8Q (red) and sensor variants selected by bacterial screening (blue, green). **(B)** Peptide sequences of the variants in (A).

3.4.4 VAmPIRe *in vitro* characterization

As ARM peptides tend to aggregate we investigated the oligomerization behaviour of VAmPIRe in solution. Analytical size exclusion chromatography of recombinant purified VAmPIRe protein showed a single peak monomeric elution profile (Figure 44A), confirmed by dynamic light scattering.

The majority of the VAmPIRe's ratio change originates from an increase in cpCitrine emission, less decrease is observed for eCFP (Figure 44B). For another FRET pair, mTurquoise-cpVenus this effect is reversed (Figure 44C). In order to characterize VAmPIRe's FRET characteristics, we replaced one of the FPs with a nonfluorescent but folding Y67C mutant of eCFP (Blamber) or cpCitrine (cpAmber) (Koushik et al. 2006). Upon addition of the RNA aptamer and excitation at 433 nm, Blamber-Rsg-cpCitrine shows a slight increase in cpCitrine emission whereas eCFP emission decreases for the eCFP-Rsg-cpAmber construct. This indicates an effect of the aptamer on the FPs that reinforces VAmPIRe's FRET effect synergistically. FRET ratio change upon aptamer addition was observed when mixing both (Bl)Amber constructs in an equimolar ratio (Figure 44D). This indicates that the dynamic range of VAmPIRe is not only based on the change of intramolecular FRET but instead involves an intermolecular interaction between neighboring (aggregated) sensors.

Additionally or alternatively, aptamer binding could also have direct effects on eCFP and/or cpCitrine brightness.

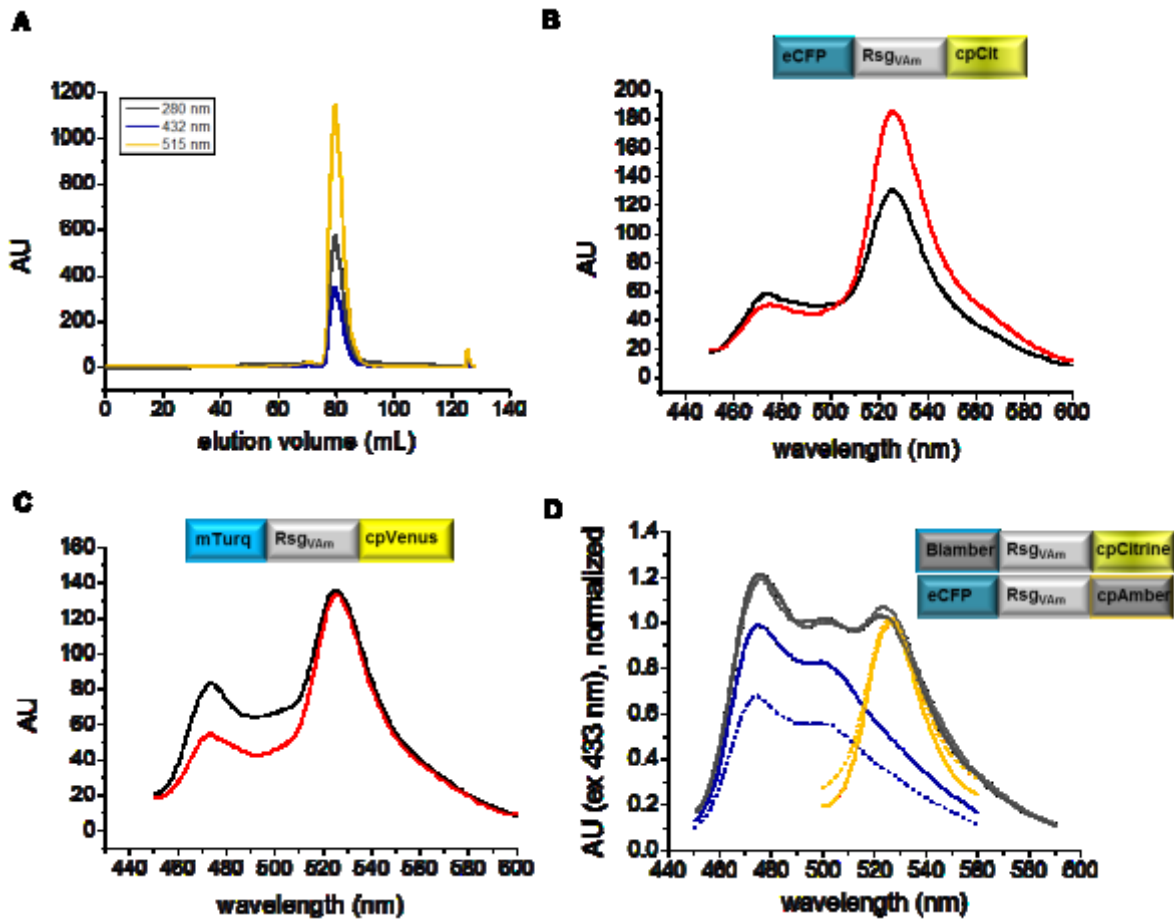


Figure 44 VAmPIRE FRET characteristics. (A) VAmPIRE SEC (ÄKTA) elution profile with excitation at the indicated wavelength for detection of proteins (black, 280 nm), eCFP emission (432 nm), cpCitrine emission (515 nm) (B) Emission spectra ($\lambda_{\text{ex}}=432$ nm) of VAmPIRE and (C) VAmPIRE variant bearing a mTurquoise and cpVenus FRET pair before (black) and after RRE aptamer addition (red). (D) Emission spectra ($\lambda_{\text{ex}}=432$ nm) of Blamber- (“blue Amber”, yellow), cpAmber (blue) VAmPIRE variants or both in an equimolar ratio (grey) before (solid line) and after (dashed line) RRE aptamer addition.

VAmPIRE dynamics were tested by titrating recombinant sensor with *in vitro* transcribed RNA. As increasing aptamer concentrations resulted in higher sensor output (Figure 45A). VAmPIRE quantitatively reported aptamer levels and had an apparent K_D of 100 nM (Figure 45). Variant #95 had an even higher affinity but showed increased pH-dependency compared to VAmPIRE (Figure 45B).

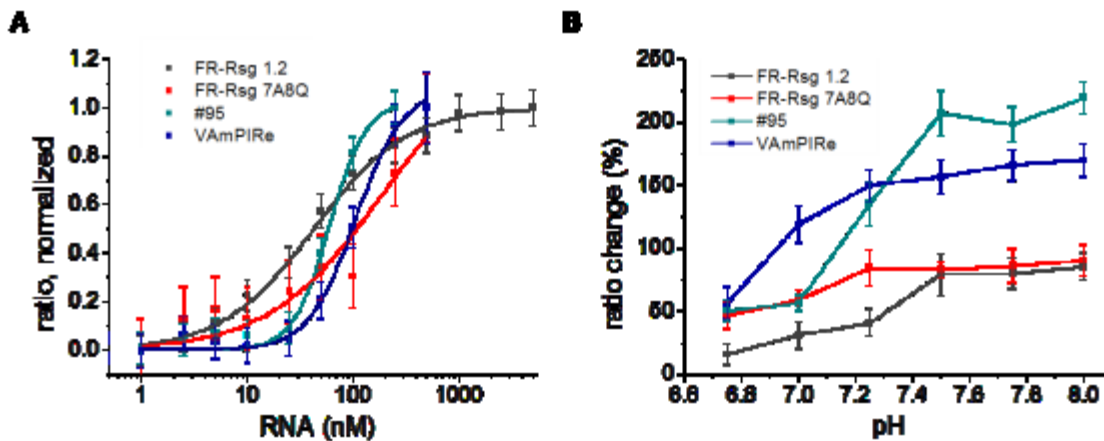


Figure 45 VAmPIRe *in vitro* properties. (A) Affinity titration of VAmPIRe (blue), mutant #95 (cyan), FR-Rsg 7A8Q (red) and the parental FR-Rsg 1.2 (grey). (Dose Response Fit) **(B)** pH-dependence of maximal FRET ratio change in VAmPIRe, #95, FR-Rsg 7A8Q and FR-Rsg 1.2 .

Building on the ability to quantitatively detect different aptamer concentrations, we tested VAmPIRe's ability to monitor dynamic aptamer levels. We set up an *in vitro* transcription reaction including recombinant VAmPIRe. T7 RNA polymerase was applied to transcribe the DNA templates coding for the RRE aptamer driven by a T7 promoter. 2 min upon polymerase addition, RNA transcription product can be detected and after 20 min the reaction is completed as has been shown by other quantification methods. Next, 3 promoter variants yielding a single nucleotide mutation at position 10 were tested for transcription kinetics and RNA product yield. Promoters mutated at position A10 to A10C and A10G have been reported to exhibit lower binding affinities for T7 polymerase (Raskin et al. 1993). Transcription product monitoring by FRET measurements shows slower kinetics and similar RNA product for the A10C and very slow kinetics and lower transcript levels for the A10G mutants compared to the A10 wt. FRET monitoring of *in vitro* transcription reveals the potential of VAmPIRe to quantitatively detect RNA aptamer levels in real time. Moreover, subsequent addition of RNase completely abolished FRET changes rapidly (Figure 46), demonstrating the ability of the sensor to dynamically and reversibly report RRE aptamer levels in real time *in vitro*.

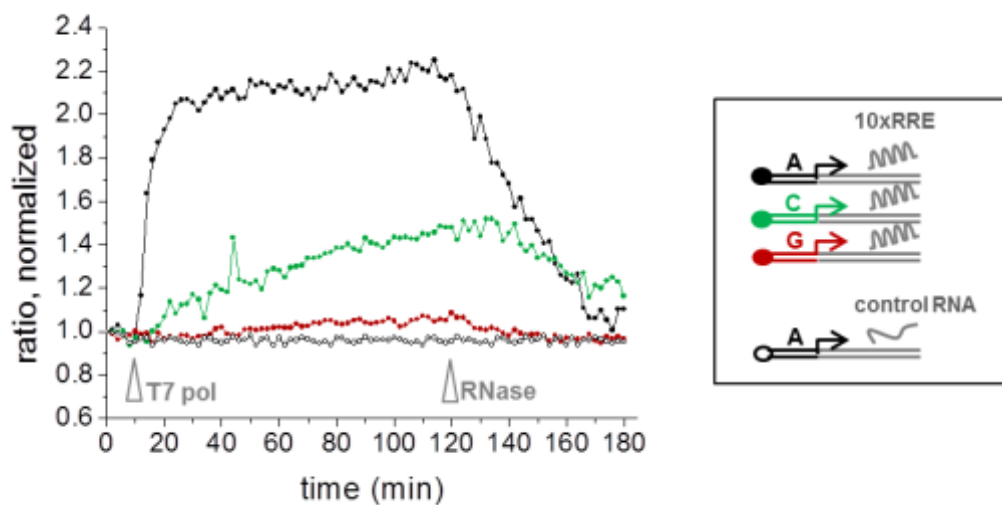


Figure 46 Dynamic and reversible imaging of RNA transcription and decay *in vitro*. The T7 promoter (black line and circles) and two less efficient mutant promoters harboring single nucleotide exchanges (blue and red lines and circles) were used for *in vitro* transcription of 10x RRE. Addition of T7 polymerase to start transcription is indicated (T7 pol, arrowhead), as is addition of RNase A (RNase, arrowhead). Note complete reversion of ratio change after degradation of 10x RRE RNA. Transcription of a control RNA not fused to 10xRRE did not elicit any VAmPIRe ratio change (open circles).

3.4.5 Aptamer engineering

As signal amplification is crucial for successful *in vivo* performance we tested whether multiple copies of the RRE aptamer could be fused in tandems. We constructed variants with 10-30 copies of the RRE aptamer in tandem with varying numbers of linking nucleotides in between. As simple multiplication of the RRE aptamer did not lead to satisfying results, multimers were initially optimized *in silico* for predicting correct folding of the RRE secondary structure within the multimer repeats using the program mfold (Zuker 2003) (Figure 47A). For a 10 nucleotide linker sequence mfold predicted proper folding of 4 RRE stem loops whereas 10 Rsg binding loops were formed with 10 nucleotides in-between the repetitive motif. We then tested these constructs *in vitro* using defined stoichiometric molar ratios of sensor and the corresponding RRE constructs (Figure 47B). These results demonstrated that multimerization resulted in functional concatenated aptamers. Better performance of the 10xRRE_L10 aptamer compared to 10xRRE_L6 confirmed the *in silico*

prediction. Constituting an important prerequisite for target RNA tagging, the attachment of the mKO2 ORF to the 10 aptamer repeats did not seriously alter VAmPIRe performance.

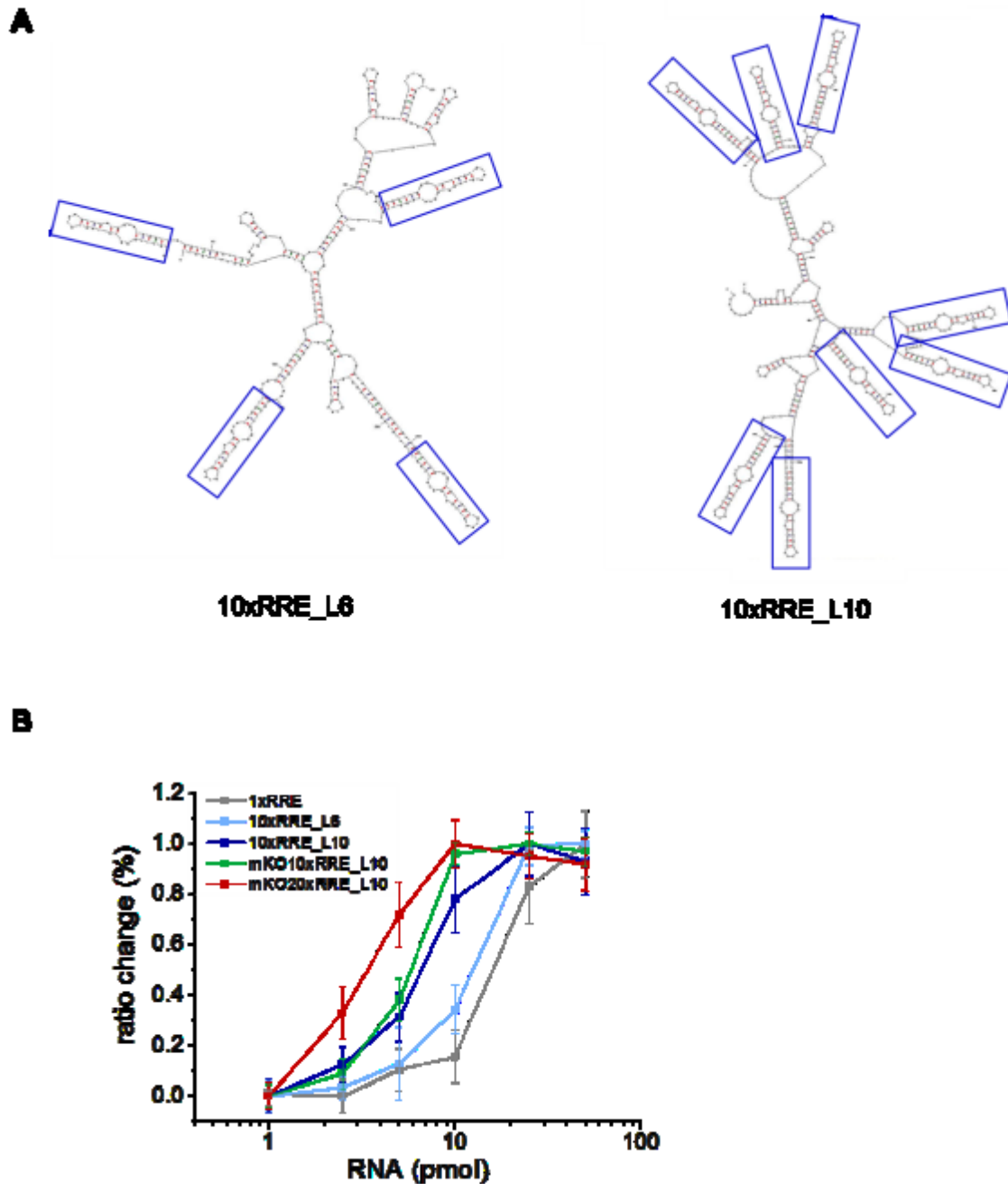


Figure 47 RRE aptamer multimerization. (A) mfold secondary structure prediction of RRE repeats. 10 aptamer repeats are separated by 6 (left) or 10 nucleotides (right), respectively. The energetically most favorable structures are shown. Correctly folded RRE stem loops are highlighted (blue box). (B) VAmPIRe ratio change at given quantity of RRE aptamer tagged RNA is plotted for an RNA with 1 x RRE (grey line), 10 x RRE with 6 nucleotide or optimized 10 nucleotide linkers (light blue and dark blue lines), mKO2 ORF tagged 10xRRE and 20 x RRE with optimized 10 nucleotide linkers (green and red lines, respectively).

3.4.6 Cellular RNA imaging using VAmPIRe

In order to test the ability of VAmPIRe to report expression of RNA in living cells we constructed a reporter RNA consisting of the open reading frame (ORF) of the orange fluorescent protein Kusabira Orange 2 (mKO2) (Sakaue-Sawano et al. 2008) fused to 20 RRE aptamer repeats.

In steady state experiments HEK 293T cells transfected over-night to express only VAmPIRe or VAmPIRe and the reporter mKO2 with RRE tag could be easily distinguished by ratiometric imaging from non-transfected cells or cells transfected with mKO2 mRNA not fused to RRE (Figure 48).

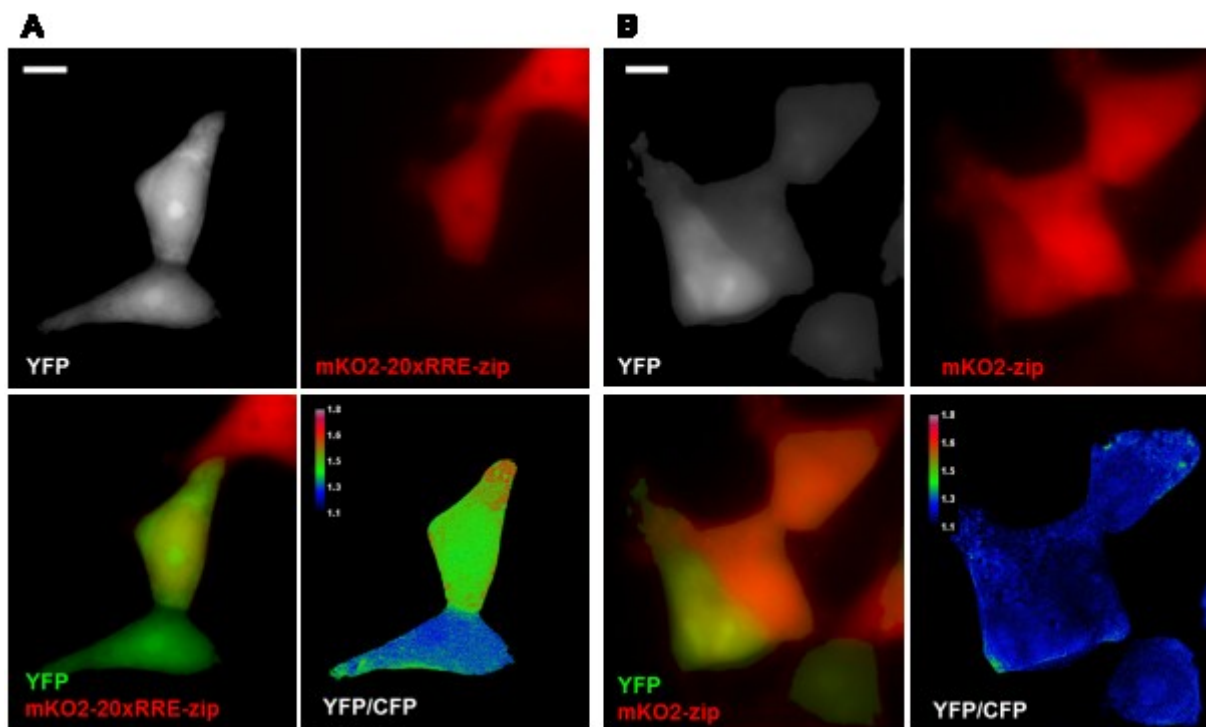


Figure 48 VAmPIRe performance in living mammalian cells. (A) VAmPIRe cpCitrine/CFP ratio (right lower image) reports expression of mKO2-20xRRE-zip. A cell that does not express mKO2-20xRRE-zip is distinguished by ratiometric imaging. Left upper image, cpCitrine FRET channel; upper right image, mKO2 intensity channel. Scale bar, 20 μ m **(B)** Control HeLa cells expressing VAmPIRe and mKO2-zip mRNA without the RRE tag. Left image merge of cpCitrine FRET and mKO2 intensity channels, left image, VAmPIRe cpCitrine/CFP emission ratio. Scale bar, 20 μ m.

We used ratiometric live cell imaging to follow transcription of mKO2-20xRRE under control of an inducible promoter in HeLa cells. Leakiness of the promoter resulted in minimal mKO2 fluorescence and slightly elevated nuclear VAmPIRe ratios under resting conditions (Figure

49). Upon induction with tetracycline RNA levels increased initially within the nucleus. We could then follow mRNA translocation and signal spread from nucleus to the cytosol in real time (Figure 49). Subsequently the translation product mKO2 appeared, leading to bright orange fluorescence within cells 6-8h after induction of expression. Interestingly, RNA levels remained consistently higher in the nucleus than in the cytosol, probably because of incomplete nuclear export. VAmPIRe was an efficient reporter of RNA expression.

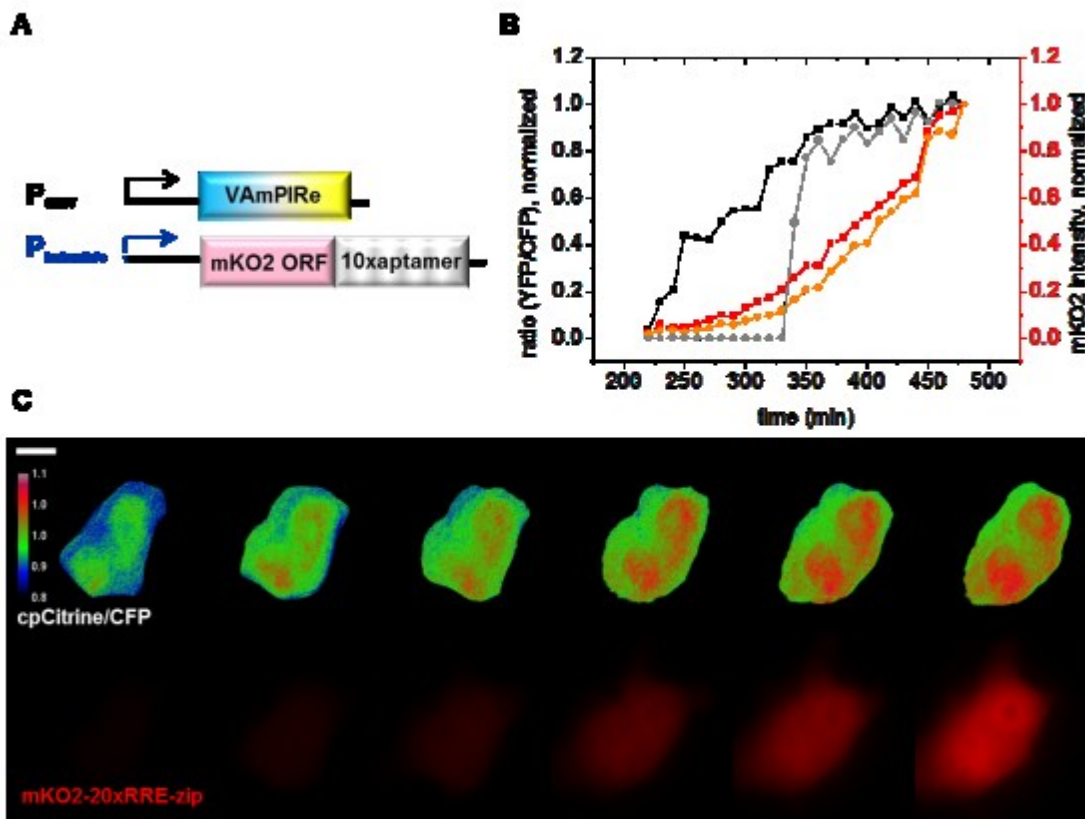


Figure 49 Imaging temporal RNA dynamics. (A) VAmPIRe and inducible aptamer constructs for transfection. (B-C) Time course of expression of 20xRRE tagged mRNA coding for mKO2 in a living HeLa cell. cpCitricine/CFP nuclear (black) and cytosolic (grey) ratio and corresponding nuclear (orange) and cytosolic (red) mKO2 intensity plots of the cell depicted in (C). (C) Upper lane, VAmPIRe ratio cpCitricine/CFP, lower lane, mKO2 intensity. Scale bar, 20 μ m

The zipcode sequence derived from β -actin mRNA serves as a localization tag that targets the reporter RNA to sites of β -actin mRNA presence (Kislauskis, Zhu, and R H Singer 1994b). Addition of the β -actin zip code sequence to mKO2-20xRRE lead to significant ratio increases at the leading edges of moving filopodia in migrating NIH mouse fibroblasts (Figure 50), showing the potential of VAmPIRe to be used for RNA localization studies within living cells.

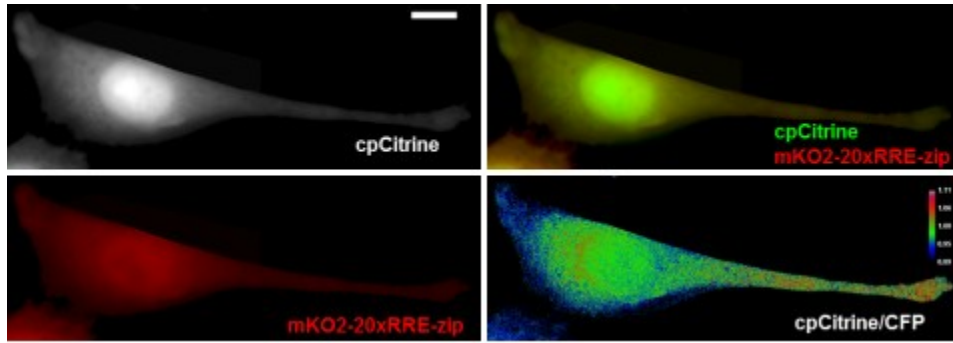


Figure 50 Intracellular RNA localization in fibroblasts. NIH3T3 transiently expressing VAmPIRe and mKO2 ORF fused to 20 aptamer repeats and a β -actin zipcode sequence. High FRET ratio was observed at perinuclear regions and at the leading edge of migrating cells. Scale bar, 20 μ m

ZBP1 fused to a red FP (mRFP) interacts with the zipcode RNA and indicates endogenous β -actin mRNA as well as reporter RNA localization. During stress response, RNAs are transiently stored within RNPs called stress granules. We induced stress in NIH 3T3 fibroblasts transiently expressing VAmPIRe, the RNA reporter construct and ZBP1-mRFP1 by addition of arsenate. 30 min after induction, ZBP1-mRFP was incorporated into cytosolic granules (Figure 51B). Many of these particles showed sensor accumulation independent of red FP localization (Figure 51A) probably due to aptamer binding with a subset of those granules exhibiting higher ratio compared to the cytosolic surrounding.

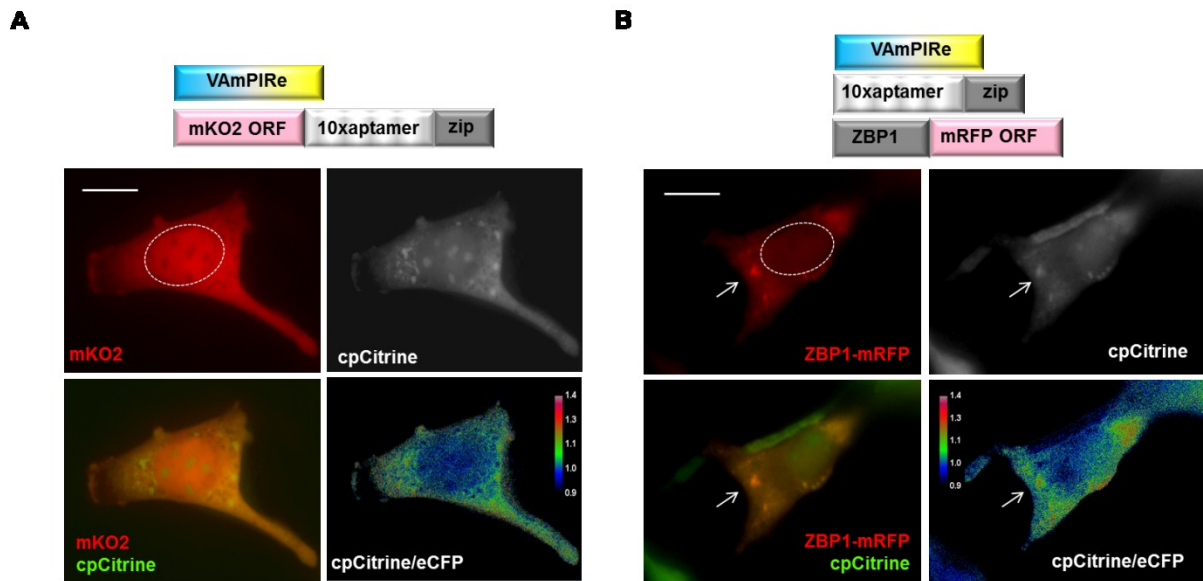


Figure 51 Stress granule formation in fibroblasts. NIH 3T3 transiently expressing VAmPIRe and a zipcode-tagged 10xaptamer construct. Stress was induced by supplementation 2.5 mM arsenate to the medium for 30 min. **(A)** The localization of the aptamer construct fused to mKO2 ORF was determined by high FRET ratio values in granular cytoplasmic structures. Scale bar, 20 μm **(B)** The stress granule marker ZBP1-mRFP was coexpressed and colocalized with regions of high FRET. Scale bar, 20 μm

3.5. Development of the EJC FRET sensor REFlex

3.5.1 eIF4AIII FRET biosensor design and incorporation into the EJC

The sensor named REFlex (**re**porter of **eIF4AIII flexure**) indicates the present conformational status of eIF4AIII via fluorescence resonance energy transfer (FRET) change. The FRET donor, an 11 amino-acid truncated enhanced Cyan Fluorescent Protein (eCFP) was fused to the human eIF4AIII N-terminus. A circularly permuted variant of the yellow FP Citrine (cpCitrine) (O Griesbeck et al. 2001) was attached to the C-terminus, downstream of the second RecA domain (Figure 52A, B). REFlex shows slightly decreased ATPase activity compared to native eIF4AIII (Figure 52C). In order to explore the FRET characteristics of this biosensor in the open and closed state we set up an *in vitro* assembly of the EJC. It has been shown before that EJC formation can be recapitulated *in vitro* in the presence of all constituent components of the complex (TØ Tange, A Nott, et al. 2004j). In addition to the protein components Barentsz and Mago-Y14, ATP and single stranded RNA without complicated secondary structure were combined in a suitable buffer. cpCitrine emission decreased and eCFP emission increased upon addition of all EJC core components to REFlex, reporting the switch from open to closed conformation in eIF4AIII. We calculated a ~25% decrease in cpCitrine/eCFP emission ratio change upon conversion to the ATP-bound closed state that could be further enhanced by introducing 2 mutations at the surface of each of the FPs. We substituted Serine 208 and Valine 224 with hydrophobic Phenylalanine and Leucine, respectively (Vinkenburg et al. 2007). These mutations enhanced the change in cpCitrine/eCFP emission ratio change to ~38% (Figure 52).

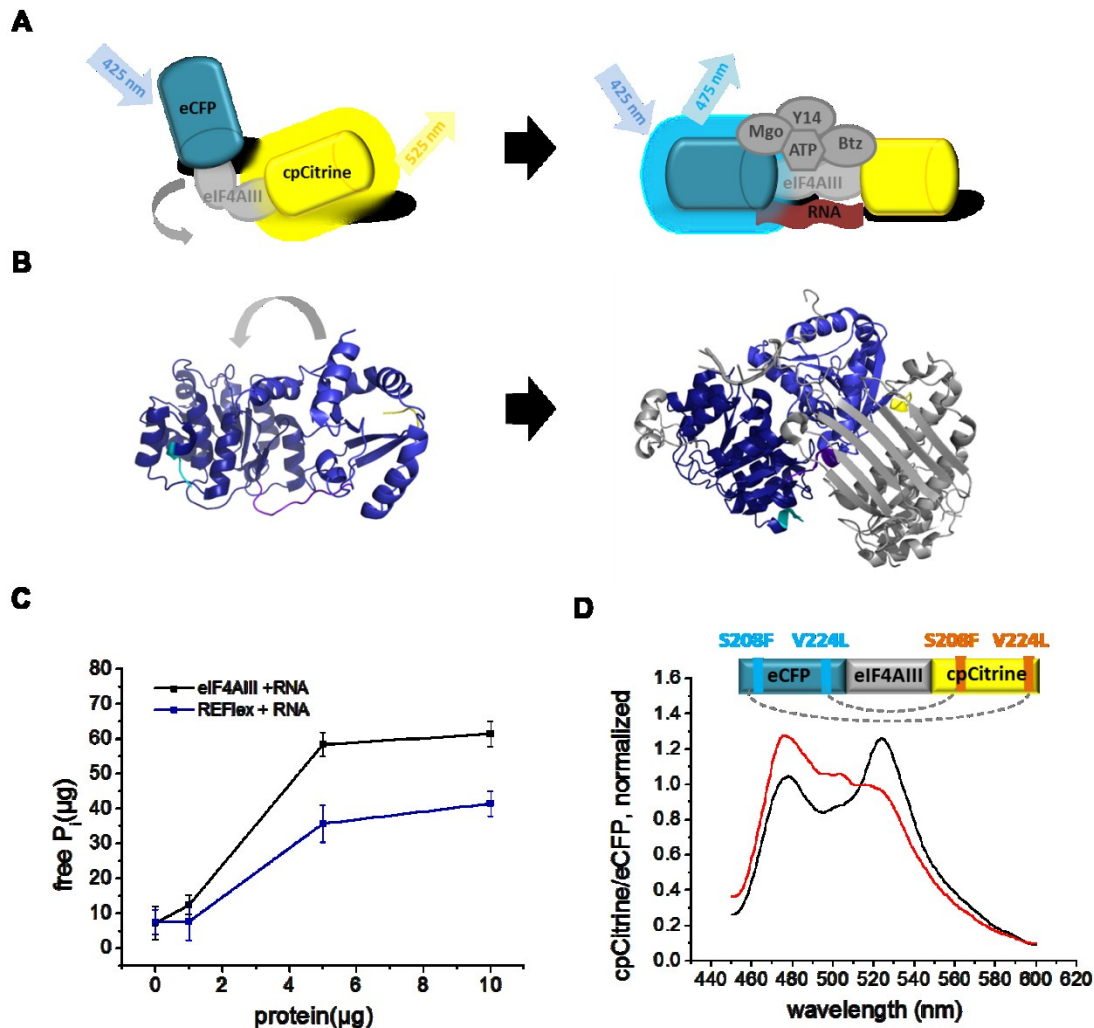


Figure 52 REFlex engineering and performance. (A) Schematic of REFlex design. The two eIF4AIII RecA domains are represented as grey circles. eCFP and cpCitrine are the donor and acceptor fluorescent proteins. Upon binding RNA and ATP REFlex switches from open to closed conformation, reported by altered FRET. Mgo = MAGO, Btz = Barentsz (B) Structure of eIF4AIII with Barentsz (left) and the EJC core components (right) modified from the PDB ID 2J0U and 2HYI (Bono et al., 2006), respectively, by PyMOL (DeLano, 2002). The RecA domains are highlighted in navy and dark blue with a purple linker. The N- and C-termini fused to the fluorescent proteins in REFlex are shown in cyan and yellow, respectively. (C, D) *In vitro* FRET measurements showing enhancement of FRET change by introduction of mutations L208FV224L into the fluorescent proteins. The graphs depict REFLEX spectra of the open (black lines) and closed state (red lines) after addition of MAGO-Y14, Barentsz, ATP and RNA in an equimolar ratio.

3.5.2 ATP and RNA are necessary for REFlex FRET change.

Next we investigated the necessity of those components for FRET change to occur. Addition of all EJC components except ATP does not lead to any FRET change within 30 min,

demonstrating the absolute requirement for ATP for the FRET change to occur (Figure 53A). Similar results were obtained when all components apart from RNA were added (Figure 53B). In the presence of ATP and mRNA coding for the fluorescent protein mKO2, Barentsz or Mago-Y14 were also required for FRET change to occur (Figure 53A). In order to prove that the observed FRET change does not result from charge effects, we added DNA or NTPs instead of RNA to REFlex and the EJC components (Figure 53B). Consistent with the exclusive deposition of eIF4AIII on RNAs within a cellular environment, no REFlex FRET change was detected with DNA or NTPs.

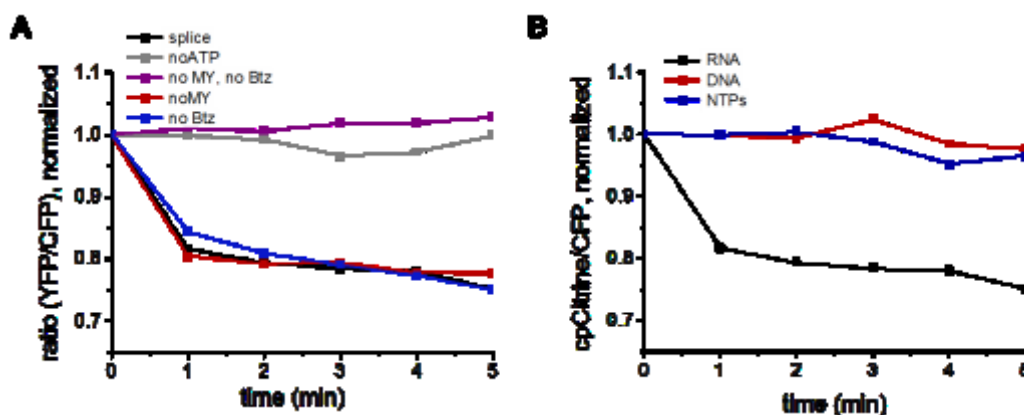


Figure 53 REFlex FRET change reports assembly of the EJC and requires ATP and RNA. RNA and all protein components were supplied in a 2:1 molar ratio to REFlex. cpCitrine/CFP FRET change was monitored over time. **(A)** REFlex FRET change after addition of 100 nM mKO2 mRNA at time = 0 min to assemble the core EJC with all components (ATP, mKO2 mRNA, Mago-Y14 (MY), Barentsz (Btz), black line) or when omitting the indicated component. Omitting ATP (grey line) abolishes any FRET change. **(B)** Core EJC assembly reported by REFlex depends on addition of RNA (black line) but not DNA (red line) or NTPs (blue line)

3.5.3 PYM or Imp13 binding to MAGO-Y14 results in EJC disassembly.

The combination of all EJC core components including RNA and ATP shifted the sensor to the closed state indicating the assembly of the EJC. We performed the *in vitro* FRET assay in order to investigate if the PYM-mediated EJC disassembly can be detected by REFlex. The addition of PYM in a 1:1 molar ratio to MAGO-Y14 completely reversed the FRET ratio induced by the EJC core components including RNA back to the open state (Figure 54A). In contrast, PYM had no effect in presence of the MAGO mutant E73R that is known to lack

PYM binding ability (Gehring, Lamprinaki, Kulozik, and Hentze 2009b) (Figure 54C). This suggests that PYM binding to MAGO-Y14 is able to disassemble the EJC indicated by eIF4AIII conformational change. We thus confirm the ability of PYM to contact MAGO-Y14 within fully assembled EJC. In contrast, immunoprecipitation experiments showed that EJC intermediates are resistant to PYM disassembly (Gehring, Lamprinaki, Kulozik, and Hentze 2009b). It is unclear if this is due to a protective role of spliceosomal components, the subcellular localization of PYM or an altered accessibility of the PYM-binding site of MAGO-Y14 after spliceosome removal. We next pre-incubated all EJC components including ATP and PYM for 30 min on ice. FRET monitoring showed a FRET ratio decrease upon subsequent addition of RNA even in the presence of pre-incubated PYM (Figure 54B). However, the FRET ratio slowly increased within a period of 30 min indicating EJC disassembly. This finding is in line with observations of a PYM-MAGO-Y14 interaction that is dependent on its incorporation into mature EJCs (Bono, AG Cook, Grünwald, Ebert, and Conti 2010a) (Gehring, Lamprinaki, Kulozik, and Hentze 2009b). This specificity can be observed in the absence of the spliceosome or any other cofactors. Our data suggest that the MAGO-Y14 binding site for PYM is directly modified upon its incorporation into the EJC, which enables MAGO-Y14 uncoupling by PYM.

Nuclear import factors like Imp13 that binds MAGO-Y14 ensure EJC protein reimport into the nucleus where they are reloaded onto mRNAs. We investigated if Imp13 is able to bind to MAGO-Y14 and thereby disassemble the EJC. After complex formation monitored by FRET we added Imp13 in equimolar ratio to MAGO-Y14. The subsequent FRET ratio increase indicated that Imp13 is able to convert REFlex to the “off” state independent of PYM (Figure 54B). EJCs bearing a mutated Imp13-binding site of MAGO-Y14 (E73R) could not be disassembled by the nuclear import factor (Figure 54B). This finding is in contrast to the hypothesis stating that MAGO-Y14 incorporated in EJCs is sterically inaccessible to Imp13 (Bono, AG Cook, Grünwald, Ebert, and Conti 2010b).

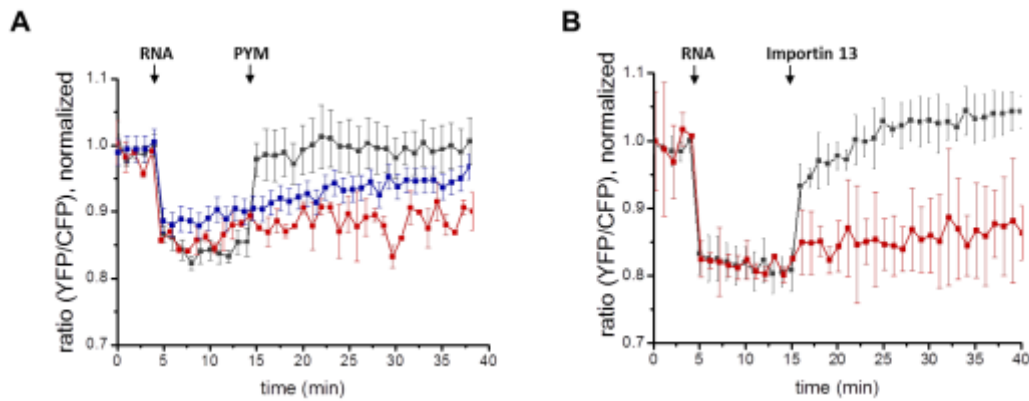


Figure 54 REFLEX reports EJC disassembly by PYM and Imp13. (A) REFLEX switches from open to closed conformation after addition of mKO2 mRNA (+RNA, 100 nM) to all core components of the EJC and reverts after addition of PYM (+PYM) (grey line). If MAGO E73R replaces MAGO addition of PYM has no effect (red line). Preincubation of PYM allows initial formation of the core EJC that is subsequently slowly disassembled (blue line) ($n = 3 \pm \text{s.e.m.}$). **(B)** Assembly of the core EJC after RNA addition (+RNA) and disassembly by Importin 13 (+Importin13) (grey line). Importin13 had no effect if Mago was replaced by its mutant E73R (redline). ($n = 3 \pm \text{s.e.m.}$)

3.5.4 Monitoring RNA binding to eIF4AIII by FRET

There is evidence of exclusive deposition of the EJC on certain RNAs (Sauliere et al. 2010). eIF4AIII could be a candidate for conferring target specificity as it directly contacts the RNA, but its binding of RNA has been considered indiscriminate. In line with this, our experiments on EJC formation suggested no preferences in RNA binding in the presence of Barentsz or Mago-Y14. The EJC may however not in all cases be preassembled before binding to an RNA target. We therefore also analyzed binding of certain RNAs to REFLEX in the absence of all other core protein components of the EJC. The exon-intron-exon constructs CG7956 (*Drosophila* homologue of phosphatidylinositide phosphatase SAC2) and CG3686 (tyrosine decarboxylase 1, *Drosophila*) are 3' untranslated regions of mRNAs that have been shown to be subjected to nonsense-mediated decay (NMD) in an eIF4AIII dependent manner (Sauliere et al. 2010). While CG7956 RNA is immunoprecipitated with all tested EJC components, CG3686 was only detected with MAGO-Y14 and Barentsz but not with eIF4AIII. We attempted to monitor REFLEX binding of these different RNA constructs. We combined REFLEX with ATP in a protein-RNA interaction buffer and added different concentrations of RNA to the reaction. We observed a concentration dependent ratio change when adding CG7956 or CG3686, respectively. We also tested CG7956 binding without its short intronic

sequence. REFLEX had apparent K_D s for these RNAs of 6 nM (CG7956), 4 nM (intronless CG7956), 16 nM (CG3686). We also added a non-related intron-less RNA construct coding for the red FP mKO2. Interestingly, mKO2 had hardly any effect on REFLEX conformational change under these conditions (Figure 55), in contrast to results obtained with the same mRNA when used for EJC (Figure 53). Thus, REFLEX is able to distinguish between different RNA targets in the absence of further accessory components apart from ATP.

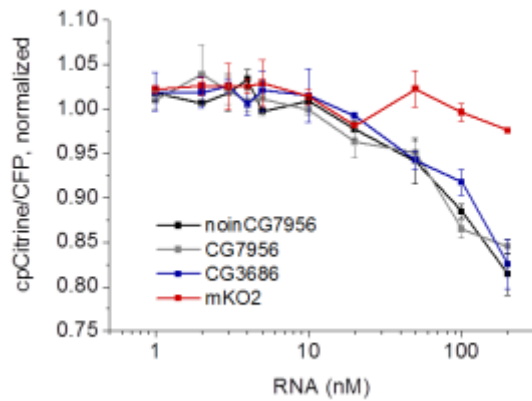


Figure 55 REFLEX sensitivity for different RNA targets. In the absence of core EJC components the titration assay including REFLEX and ATP was performed with different *in vitro* transcribed RNAs: CG7956 with (grey line) and without the 66 nucleotide long intron (noinCG7956, black line), CG3686 (blue) and mKO2 (red). Note the lack of FRET change with mKO2 mRNA. ($n = 3 \pm \text{s.e.m.}$)

4.1 Evaluation of dual FP-based RNA labeling using MS2 and λ N22

Application of MS2 and λ N22 systems revealed independent action enabling simultaneous imaging of two different RNAs. Specificity of the respective aptamer-peptide interaction seems high enough to allow exclusive labeling. Similar results have been obtained in an attempt to label ASH1 and IST2 mRNAs in *S. cerevisiae* (Lange et al. 2008) and in a recent study that investigates PSD95 and CaMKII α mRNA localization in neurons (Subramanian et al. 2011).

Both studies mention problems arising from the application of two different labeling systems. Due to differences in affinity, specificity, number of aptamers and resulting mobility of the labeled complex, the two reporters cannot be directly compared in a quantitative manner. Another important point to consider is the expression levels of tagged aptamer and FP construct. Due to natural but unpredictable amplification of fluorescent fusion protein upon translation compared to the aptamer-tagged RNA, FP expression has to be tightly restricted to reduce background signal. Even higher overexpression of the fluorescent reporter can cause artifacts including aggregation and accumulation in granules. Further concerns about the significance of the fluorescent signal include the reporter fate after target mRNA degradation. The stem-loop structure of the aptamer could confer higher stability compared to the RNA of interest. Even though the entire RNA construct is degraded, the fate of the fluorescent label remains unclear. Turnover could be slower compared to the lifetime of the RNA and the protein could be entrapped at the site of the degraded RNA even though already degraded. This was the reason for the development of dynamic RNA reporters with a fluorescent readout that depends on the presence of the aptamer.

In this perspective, NMDAR1 splice reporter results have to be interpreted with caution. At least, partial colocalization with FMRP indicates the labeling of real RNA transport granules (Figure 25). Especially, many labs have tried the λ N22 approach for localization experiments in different cell types without success (EMBO referee report (Subramanian et al. 2011), Edouard Bertrand, personal communications). In our hands, the MS2 system proved better than the λ N22 labeling but the difference was not significant (Figure 23B). The NMDAR1 reporter construct would have to be optimized for different cellular systems considering that there are inter-lab differences for single labeling using the MS2 system. The RNA

labeling seems to be especially sensitive in the neuronal context (Kevin Czaplinski, personal communications). For example, attempts are made to improve the stringency of the NLS for hippocampal neurons. On the other hand, a strong NLS could interfere with the targeting signals of the aptamer-tagged RNA of interest. In our CaMKII α experiments we observed inefficient export of 40% for both systems (Figure 23B).

4.2 Imaging cellular RNAs by synthetic on-off ASR dyes

Chemical on-off RNA dyes aim at overcoming both bulkiness and the requirement of subcellular FP label restriction. With our synthetic ASR dye approach we envisaged high signal-to-noise while preserving the biological properties of the tagged RNA.

The SELEX strategy applied by Jianghong Rao's lab was efficient for the selection of affine ($K_D \sim 40 \mu\text{M}$) RNA aptamers. There is room for improvement by further competitive rounds and optimized strategies of *in vitro* selection. For example, the recently published Spinach approach that is based on a GFP-mimicking dye binds its aptamer with 500 nM affinity (Paige et al. 2011).

In bacteria, ASR fluorescence emission was increased 135 fold upon binding of the specific aptamer, Apt10. Even though *in vitro* and bacterial performance showed promising results, application in mammalian cells was hindered by several problems including unspecific fluorescence emission and delivery.

In cells, we observed ASR fluorescence even in the absence of any aptamer (Figure 28, Figure 29). Similar to other triphenylmethane dyes, ASR is nonfluorescent in water but can be activated in a nonspecific manner within the cellular environment (Meech 2009). Fluorescence increase originates from a transition from nonradiative decay pathways (e.g. *cis-trans* isomerization) to radiative decay (Dugave and Demange 2003). This conversion can be triggered by the specific RNA but also by macromolecule binding or increased solvent viscosity (Ippen et al. 1976) (Sundstroem and Gillbro 1982). Another styryl dye, FM1-43 becomes fluorescent upon incorporation into membranes and is therefore used to monitor endocytosis, exocytosis and vesicle trafficking in neurons (Cochilla et al. 1999). It has to be investigated if the on-off mechanism underlying the fluorescence enhancement of ASR is able to allow specific RNA detection in a cellular context. In contrast to ASR, the above-

mentioned GFP-mimicking RNA fluorophore takes advantage of a dye that for the first time overcomes this nonspecificity (Paige et al. 2011). Fluorescence emission is induced by releasing restriction of intramolecular movements that are thought to be independent of cellular constituents. Cellular RNA imaging by Spinach also benefits from low dye cytotoxicity and resistance to photobleaching (Paige et al. 2011).

Cellular delivery is another major problem inherent to chemical approaches including the ASR strategy. ASR permeability for HeLa cells was achieved by conjugation to the positively charged tat peptide. Charge neutralization of anionic membranes with cationic peptides has been shown to induce a lamellar to inverted hexagonal phase transition, resulting in membrane translocation through inverted micelle formation (Ragin et al. 2002). Endocytotic processing resulted in ASR dye entrapment within endosomes (Figure 29). Similar failure of cytoplasmic or nuclear delivery by tat peptide-dependent endosomal entrapment has been reported for tat-conjugated peptides and quantum dots (Tkachenko et al. 2004) (Ruan et al. 2007). We tried to release ASR from endosomes by sucrose which resulted in disappearance of fluorescence emission (Figure 29). Similarly, chloroquine could be applied for destabilization and swelling of endosomes (Turner et al. 2005). Dye lipofection provides another possibility to circumvent the cellular endocytotic pathway. However, the design of an RNA labeling method should be both as simple and as generalizable as possible. For every cell type, different delivery protocols have to be elaborated due to differences in membrane composition and small molecule uptake mechanisms.

For improved ASR dyes, we are aiming at the optimization of cellular testing. Repeats of the Apt10 will be attached to subcellular targeting sequence (e.g. β -actin zipcode) to concentrate the dye subcellularly which should increase signal-to-noise. Further characteristics including pH-sensitivity and cytotoxic effects have to be considered (Liao et al. 1994).

Only if these challenges are overcome, on-off chemical RNA dyes will allow dynamic RNA imaging and profit by the inherent multiplexing potential. Especially imaging of short RNA, including the neuronal activity-dependent noncoding BC1 RNA, could be facilitated by a small-molecule approach (Schratt et al. 2006).

4.3 Performance and potential of single fluorophore RNA sensors

Overcoming these problems of synthetic dyes we aimed at the design of genetically encodable on-off RNA sensors based on FPs. Different strategies for reversible FP destabilization were explored. We showed that it is possible to design single fluorophore sensors but further engineering is needed for RNA imaging in cells.

4.3.1 Aptamer-induced FP emission

For the first single-FP approach we were aiming to find an RNA that would directly bind to and induce fluorescence of a non-fluorescent FP. We constructed a non-fluorescent trGFP and selected one affine RNA aptamer, APT1_trGFP that enhances trGFP fluorescence in bacteria but not in mammalian cells (Figure 31).

The first step was to find a suitable FP that allows aptamer-dependent switching between a dim and a bright state of the FP. Mechanistically, the engineered FP still absorbs light and is on the edge of being fluorescent. We designed trGFP, a truncated FP that is non-fluorescent *in vitro*, in prokaryotic and eukaryotic cells (Figure 31). TrGFP itself revealed interesting features as repositioning of the His-tag from the N- to the C-terminus resulted in fluorescence emission restoration of trGFP. This indicates that the GFP C-terminus is susceptible for replacement with other amino acids sequences. Insertion of a protease cleavage site at the C-terminus could be used for the design of biosensors that become dim upon protease cleavage.

The second challenge for this RNA imaging approach was to find a suitable RNA aptamer. The aptamer is supposed to either assist folding or to electrostatically or sterically change the environment of the fluorophore and thereby increase the quantum yield. A well-studied example includes the solvent channel to the GFP chromophore that can be exposed or “sealed” (Tansila et al.). With the SELEX procedure we only selected for affinity of the aptamer to the dim FP. The selected aptamer pool was subsequently tested in bacteria and mammalian cells for fluorescence enhancement. However the aptamer selected in the prokaryotic system was not able to enhance fluorescence in a cellular context. The cellular testing can be improved by aptamer multimerization and subcellular RNA targeting, e.g. using the β -actin zipcode sequence.

In order to find a suitable aptamer, further rounds of competitive SELEX with the preselected library have to be carried out. Random aptamer length could be varied in order to create RNA structures with different secondary and tertiary structures. In order to verify binding ability of selected aptamers we already started to establish a gel-shift assay which could additionally help to optimize screening conditions. For further rounds of selection, stringency could be gradually increased by using suitable buffers with varying imidazole concentrations. Repositioning of the His-tag on trGFP could also help to increase the pool of modes of interaction between aptamers and their target protein.

Instead of or supplementary to *in vitro* SELEX, a bacterial selection system like the kanamycin antitermination assay (KAN) could be introduced (PELED-ZEHA VI et al. 2003) (K Harada, S S Martin, et al. 1996f). In this two-plasmid assay, one plasmid encodes an RNA binding peptide - N protein fusion, a second reporter plasmid engineered such that without binding of the peptide to a member of an RNA random library, N causes transcription antitermination of the neomycin phosphotransferase gene (NPT II) (Figure 56). As NPT II confers kanamycin resistance this renders bacterial survival dependent on the interaction of the aptamer with the target protein.

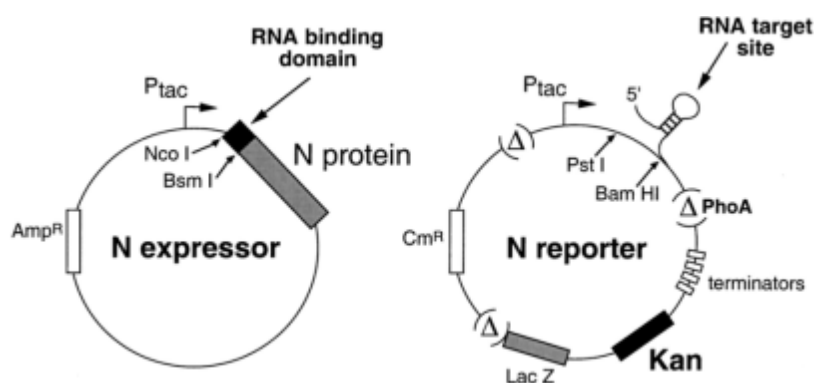


Figure 56 Two-plasmid KAN antitermination assay. Cells only survive on kanamycin if the RNA binding domain binds to the RNA target site thereby preventing N protein from binding to one of the terminators. (PELED-ZEHA VI et al. 2003)

Other groups independently also followed the approach of aptamer selection for GFP fluorescence increase. The lab of Jianghong Rao selected aptamers that can bind nonfluorescent GFP variants and turn on its fluorescence emission in *E. coli*. The GFP variants were truncated by 11 amino acids and mutated at position A226 to Q or R,

respectively. We tested these constructs in mammalian cells but could not see any difference in fluorescence emission of the GFP variants between HEK 293T cells expressing the corresponding aptamer (Apt1 for the A226Q and Apt7 for the A226R mutant) and single-transfected cells (data not shown).

The Kotlikoff lab has identified different RNA aptamers that specifically bind to spectral variants of wild type GFP including YFP and CFP with high affinity ($K_D = 14$ nM) (US 2009/0197271 A1). Upon this interaction, fluorescence emission was markedly reduced presumably through a decreased molar extinction coefficient.

GFP-binding aptamers can be used as molecular adaptors for the generation of multifunctional RNAs. Fusion of the GFP-binding aptamer from the Kotlikoff lab to an aptamer that binds to opsonins, could promote GFP clearance by opsonization (Mallik et al. 2010). Modularity of this strategy will allow furnishing of RNA parts with both GFP-binding ability and a multitude of functionalities. Target systems include all cell types and transgenic animals expressing GFP fusion proteins.

4.3.2 RNA binding peptide-EGFP hybrid

We created two single fluorophore sensors, lamGFP_Cterm10 (Figure 32) and cpEGFP-BIV (Figure 33) that exhibit aptamer-dependent fluorescence emission decrease *in vitro*. Both reporters are based on an instable FP fused at the C-terminus to a viral RNA binding peptide that exhibits high affinity to a specific RNA aptamer. The decrease in fluorescence emission of Cterm10 further demonstrates that this region is highly sensitive to environmental changes (Figure 32) (see 4.3.1).

Fusion of the BIV peptide to cpEGFP yielded the ratiometric sensor cpEGFP-BIV with a shift in absorption from 475 nm to 395 nm. Direct fusion of the peptide rendered the cpEGFP more sensitive to aptamer binding compared to the insertion in the GCaMP scaffold. For events that require quantification, ratiometric- or FRET-based probes are generally preferred over intensity based probes.

The dynamic range of both RNA reporters has to be improved to render them suitable for cellular application. The introduction of a linker between the FP and the viral peptide in combination with a variation of the exact insertion site could constitute promising means.

Randomized linkers could be screened using the established bacterial RNA induction assay. In contrast to FRET sensors, another (red) FP has to be coexpressed with the single fluorophore sensor as a standard.

It remains unclear if interaction of aptamer-binding domains at both ends of cpEGFP like in GCaMP would increase the intensity change. Possible sensor design strategies include the fusion of two different peptides to the N- and the C-terminus (Figure 57). Binding of the fusion protein to an RNA construct containing the two corresponding aptamers would possibly induce changes in the environment of the chromophore. Further strategies include the reconstitution of an RNA binding peptide by binding of split peptide parts to the aptamer.

Fluorescence decrease is not directly suitable as readout for RNA tracking but could be exploited to build a quencher construct (see 4.3.3).

Generally, this RNA reporter design benefits from the use of peptides that are known to bind to a certain aptamer with high affinity. Due to the modular strategy, multiplexing would be possible using different peptide-aptamer pairs and spectral variants of GFP.

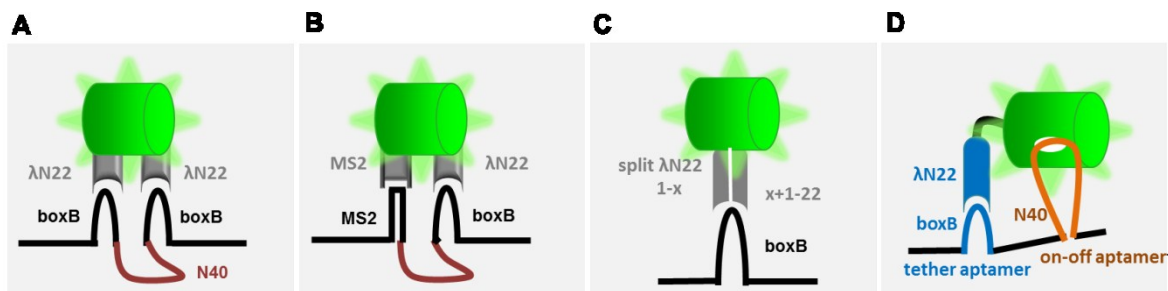


Figure 57 Single fluorophore RNA sensor strategies. All strategies are based on fluorescence enhancement upon aptamer binding. **(A)(B)** Binding of two peptides that are fused to the dim FP termini to two adjacent aptamers. The aptamers are separated by a linker (N40) that can be selected from a random library. **(A)** Two identical peptides and aptamers. **(B)** Different peptides binding to their aptamers. **(C)** An RNA binding peptide is split and each part is fused to the two termini of the dim FP. Peptide restoration upon aptamer binding leads to fluorescence enhancement. **(D)** Affinity of the RNA construct to the dim FP is ensured by λ N22 interaction with boxB (tether aptamer, blue). A random RNA library is selected for fluorescence enhancement (on-off aptamer, orange).

4.3.3 Design of novel single fluorophore sensor

VAmPIRe has proven suitable for RNA imaging in living cells. For single transcript imaging even higher signal-to-noise ratios are required. Beyond the improvement of VAmPIRe itself, we could exploit the observed conformational changes within the ARM peptides for the design of a single fluorophore sensor, potentially with higher dynamic ranges (Table 1). Especially, the FRET ratio decrease of BIV tat upon binding to BIV tar can be used to engineer aptamer-induced dequenching (Figure 66A). Replacement of the FRET acceptor with a quencher would result in low donor emission that becomes dequenched upon BIV tar aptamer interaction. Optimization of this sensor construct can be achieved using our established bacterial screening assay.



Figure 58 Design of novel RNA biosensors. Single fluorophore sensor with a donor-BIV tat-quencher reporter exploiting the BIV tat-tar interaction.

4.4 VAmPIRe sensor performance

4.4.1 VAmPIRe *in vitro* performance

4.4.1.1 Selection of the Rsg1.2-RRE complex and multiplexing

We created a dynamic genetically encoded RNA reporter based on intramolecular FRET. In this work, we executed the first systematic testing of potentially suitable peptide-aptamer pairs for their ability to induce FRET change upon aptamer addition. The criteria included viral or synthetic origin, high affinity and conformational change upon binding. The Rsg1.2-HIV RRE pair was selected for further engineering, while P22-boxb, ϕ 21-boxB and BIV tat-tar also showed decent ratio change. Interestingly, both the P22 and ϕ 21 pairs showed negative FRET change indicating a similar binding mode that differs from the BIV and HIV ones.

As the sensor modular design supports the selection of different peptide-aptamer pairs as well as FRET pairs, this provides a basis for the development of a family of FRET sensors with orthogonal spectral properties. Multiplexing presupposes detailed testing of cross specificity of the different ARM peptides for their aptamers in the context of the FRET pair construct. Many ARM peptides bind their target RNA with high specificity. For example, during antitermination the ARM peptide from phage λ N22 binds its own boxB RNA 16-fold better than the related phage P22 boxB RNA (R Tan and A D Frankel 1995). However, structural characterization of ARMs has revealed the flexibility of some ARM structures allowing the recognition of a few different RNAs. Indeed, the JDV tat ARM was shown to bind its own tar and BIV tar via a β -hairpin structure, while it bound HIV tar in an extended conformation (Colin A. Smith et al. 2000). It remains unclear to which extent Arginine-RNA contacts intrinsically allow flexibility for cross-recognition.

The intention of creating red-shifted FRET pair variants of VAmPIRe was to provide powerful sensors for tissue imaging (Figure 38). Both the lower influence of cellular autofluorescence leading to increased contrast and less scattering are desirable features. The higher Förster distance of green/cyan-red FRET pairs compared to cyan-yellow ones adds further possibilities to explore optimal FRET efficiency for a given conformational change. However, red FPs are more prone to aggregation, incomplete chromophore formation and often perform poorly in fusions (MW Davidson and Robert E Campbell 2009). Although an alternative to the CFP YFP FRET pairs would be desirable also for multiplexing, there is no consensus on the best green/cyan-red combination (Ai et al. 2008) (Niino et al. 2009) (Grant et al. 2008) pointing to the need for further engineering. The mTFP1 has been considered a suitable donor for Citrine variants (Day et al. 2008) and mKO2 (Y Sun et al. 2009) in sensitized emission and FLIM experiments (Kumagai et al. 2011). However, this would not allow multiplexing with CFP/YFP.

4.4.1.2 *In vitro* performance and application

In vitro RNase digestion of FR-Rsg1.2 revealed the reversibility of the FRET ratio required for the investigation of RNA dynamics. FRET ratio decrease despite the presence of nucleotides

after cleavage reveals that the initial ratio increase was not triggered by unspecific charge effects. *In vitro* RNA titration and monitoring of transcription demonstrates the applicability of VAmPIRe for RNA quantification. After calibration, synthesis and degradation of a particular aptamer-tagged RNA can be measured online. In contrast to synthetic intercalating RNA dyes like SYBR Green (Promega), VAmPIRe is able to indicate the levels of a specific RNA within a mixture. Possible applications include on-line quantification of RNA transcripts during quantitative RT-PCR or RNA degradation assays. The engineering of spectral variants would allow online monitoring of differentially tagged RNAs at the same time. VAmPIRe monitoring provides a tool for promoter testing which is especially interesting for epigenetically altered promoters (Murgatroyd et al. 2009). Furthermore *cis*-acting enhancer or repressor elements as well as uncharacterized potential trans-acting factors can be tested *in vitro*.

4.4.2 FRET RNA sensor engineering

4.4.2.1 Aptamer optimization

Aptamer multimerization requires linkers that allow both folding of a maximum of RRE stem loops and accessibility of the Rsg peptide. The energetically preferred conformation of a repetitive RNA stretch often involves intramolecular base pairing of aptamer nucleotides with other aptamers or linkers. This decreases the available number of aptamer stem loops for sensor binding (Figure 47). Aptamer multimers have been synthetically created using 5-20 nucleotide linker segments that support proper folding (F Nishikawa et al. 2003) (Furukawa et al. 2008). Spacers between the RRE aptamer have to fulfill an additional requirement in allowing an adaptive conformational change to occur upon binding to the Rsg peptide (Gosser, Hermann, Majumdar, W Hu, Frederick, Jiang, Xu, and Patel 2001a).

Educated guess-driven *in silico* testing using mfold yielded different linker stretches with as many as 10 nucleotides each. Potentially suitable linkers include polynucleotide stretches like polyuridines of varying length used by other groups (Yiu et al. 2011). However, it has to be considered that RNA-Polymerase III which transcribes DNA coding for small RNAs would stop at polyuridine sequences. We tested 5 guanine or 5 uridine nucleotide linkers for 10 RRE copies by mfold (Figure 59). While two stem loops were correctly folded for polyuridine

linkers, guanine stretches allowed folding of all 10 aptamer structures. Potential suitable or randomized linkers between the RRE aptamers could be tested with the established bacterial screen.

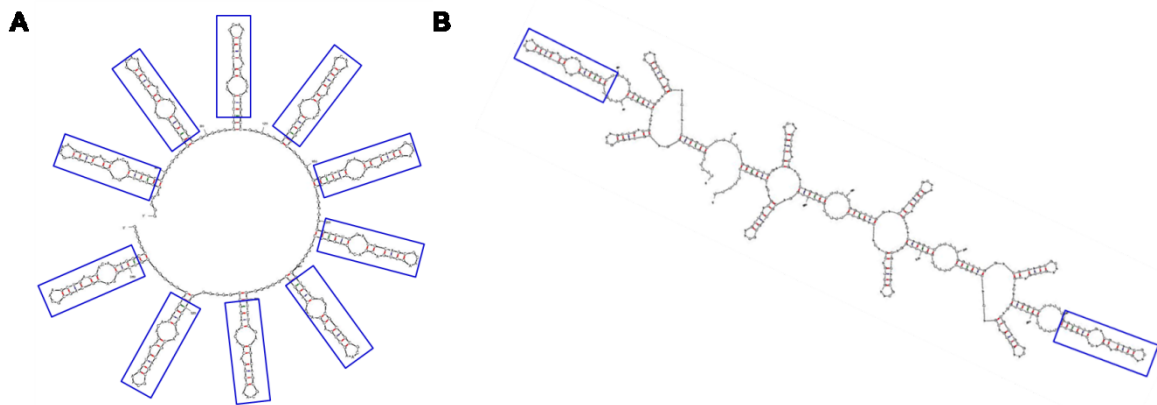


Figure 59 Aptamer linker design. Mfold structure prediction of 10 copies of the RRE aptamer separated by 5 (A) guanines ($\Delta G = -212$ kcal/mol) or (B) uridines ($\Delta G = -193$ kcal/mol). Correctly folded RRE stem loops are highlighted (blue box).

As RNA architectures can dictate the folds of ARM peptides (BAYER et al. 2005) it is worth testing RRE aptamer variants as RNA tags. VAmPIRe may exhibit a similar “chameleon-like behavior” regarding the binding of similar aptamers. The challenge will be to find RNA sequences that bind to the Rsg peptide with high affinity. One could revert to isostructural RRE mutants RRE_{AA} (G8A G25A) (Aoyama et al. 2009) and RRE_{AAC} (G8A G25A U26C) (Tae Maeda, personal communications) that have been described to bind at least the Rev and Rev-similar peptides with higher affinity ($K_D(\text{RRE}) = 40$ nM, $K_D(\text{RRE}_{\text{AAC}}) = 6$ nM). In a more unbiased approach, a bacterial screen for RRE positional mutants could help to identify new RNA variants that bind to the peptide and thereby increase VAmPIRe FRET ratio.

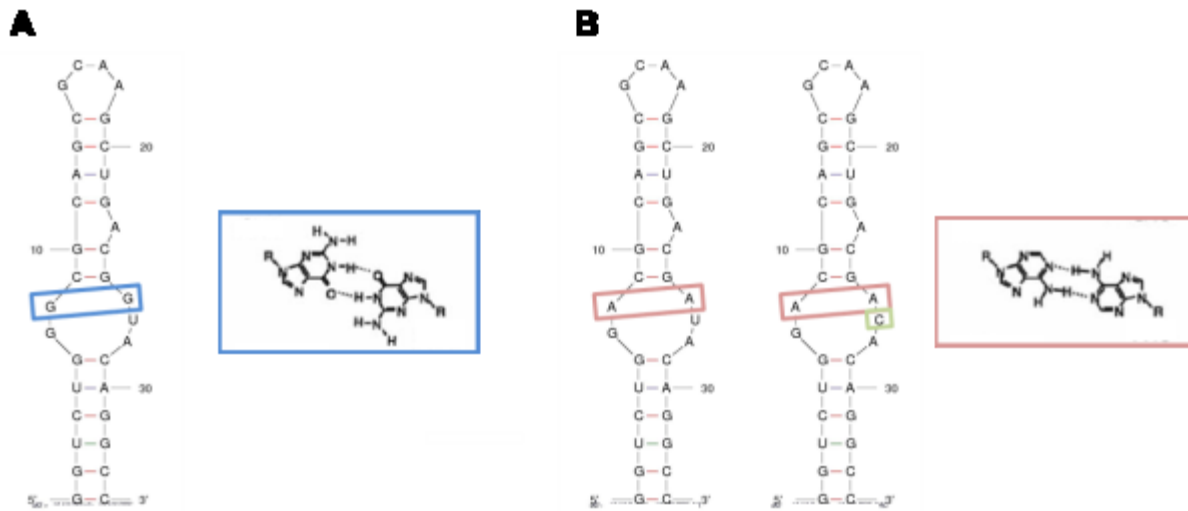


Figure 60 RRE aptamer mutants. Mfold structures of wild type RRE (A) yielding the GG base pair (blue box) and the mutant aptamers RRE_{AA} (left) and RRE_{AAC} (right) with the AA pairing (red box) with an additional Cytosine mutation (green box) in RRE_{AAC} (B) (Aoyama et al. 2009)

4.4.2.2 Rsg peptide engineering

The Rsg1.2 peptide itself was only mutated at regions outside the actual aptamer binding site. This is in accord with the finding that up to seven N-terminal residues could be removed without decreasing the RNA binding affinity (Kazuo Harada, Shelley S. Martin, et al. 1997h). The observation of a disordered N-terminus in the NMR structure corroborates the tolerance of mutations within that site (Gosser, Hermann, Majumdar, W Hu, Frederick, Jiang, Xu, and Patel 2001a). Additional target amino acids for mutagenesis involve positions that have been modified in peptide variants that are known to bind to RRE.

In spite of a careful choice of sites for randomization molecular evolution resulted in many nonfunctional FRET sensor variants. The lack of FRET change can be explained by one of two scenarios: either there is no binding affinity or there is binding but no FRET change. The general view of ARM peptides is that poly-Arginines act as platforms for Arginine recognition where all other residues play a lesser if not potentially negative role (BAYER et al. 2005). The internal Proline P12 was targeted by exhaustive mutagenesis (data not shown). Interestingly, many P12N mutants showed highly increased initial FRET ratio. This indicates that the kink in the peptide backbone introduced by the wild type Proline

decreases distance and/or orientation of the fluorophores. Surprisingly, a further reorientation expected from Proline linkers did not result in any increase in FRET change. The lack of FRET change in P12N mutants could indirectly result from the loss of nonpolar interactions with hydrophobic patches of the RNA (Gosser, Hermann, Majumdar, W Hu, Frederick, Jiang, Xu, and Patel 2001a).

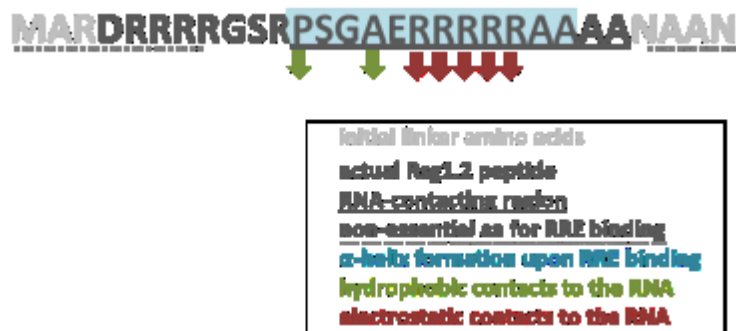


Figure 61 Rsg1.2 peptide functional assignment of amino acids. The actual Rsg1.2 peptide is shown (grey) with initial linker amino acids (light grey) and the α -helical part shaded (blue). RNA contacting regions (solid line) and non-essential amino acids for RRE binding (dotted line) are underlined. Arrows indicate amino acids that undergo hydrophobic (green arrow) and electrostatic (red arrow) interactions.

Sensor aggregation caused by electrostatic interaction as well as sensor accumulation on neighboring aptamer repeats can increase intermolecular FRET. It has been shown that high FP concentrations increase the FRET efficiency especially if the intermolecular donor-acceptor separation is higher than the intermolecular distance (Corry et al. 2005). The *in vitro* measurements of the VAmPIRe cpAmber and Blamber constructs also show FRET that has emerged from intermolecular interactions. It has to be tested if this is also concentration-dependent. For the RNA quantification using VAmPIRe one has to be aware that intermolecular FRET could contribute to the observed FRET change, especially for multimeric aptamers with short distances.

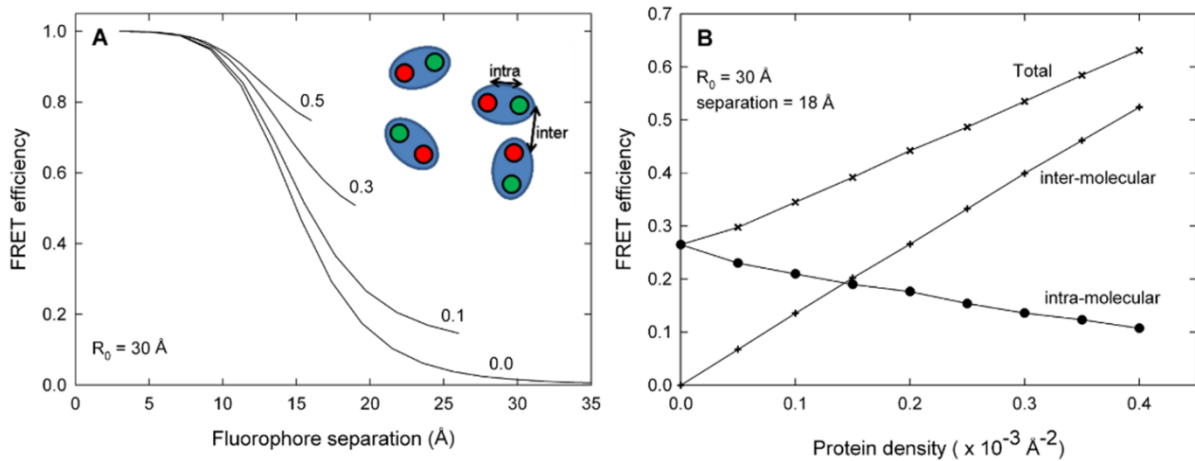


Figure 62 FRET efficiency for linked donor-acceptor pairs distributed in three dimensions. (A) FRET efficiency is plotted against the donor-acceptor distance with a given $R_0 = 30 \text{ \AA}$. The different lines represent different concentrations. **(B)** Effect of pair concentration on transfer efficiency, plotted at two R_0 and two R values (Corry et al. 2005).

Restrictions to intramolecular movements upon aptamer interaction potentially decrease the actual conformational change resulting in a poor dynamic range. Therefore, sensor aggregation that typically results from relatively weak noncovalent protein interactions has to be prevented. Aggregation may be caused by 'sticky' hydrophobic patches on the molecular surface (Eaton and Hofrichter 1990) or electrostatic interactions between positively and negatively charged surfaces (Serina et al. 1996). In general, proteins are least soluble at their isoelectric point where they bear a net charge of zero (Loeb 1921). For VAmPIRe, the FP negative net charge of -14 may compensate the positively charge of the Arginine-rich Rsg peptide (MS Lawrence et al. 2007).

In this study, we employed site-directed mutagenesis of basic residues located near the N-termini of FPs to resolve the problems of aggregation and pH-sensitivity. Arginines excluded from mutagenesis include Arg 17 and 18 that interact via hydrogen bonding and stacking as well as Arg 19-21 side chains contacting the RNA phosphate backbone (Gosser, Hermann, Majumdar, W Hu, Frederick, Jiang, Xu, and Patel 2001a). Arginines 3, 5, 6, 7 and 8 were subjected to mutagenesis in order to reduce both pH-dependency and aggregation. However it remains unclear if RNA affinity is also dependent on the total number of Arginines determining the net charge of the peptide. According to the model of Bayer et al., individual Arg residues govern binding to an RNA ligand and the inherent flexibility of the

peptide backbone may make it possible for semi-specific recognition of a discrete set of RNAs by a discrete set of ARM peptides and protein (BAYER et al. 2005).

As the effects of directed manipulation of peptide or FP (MS Lawrence et al. 2007) charges are rather unpredictable, improvements rely on a solubility screen.

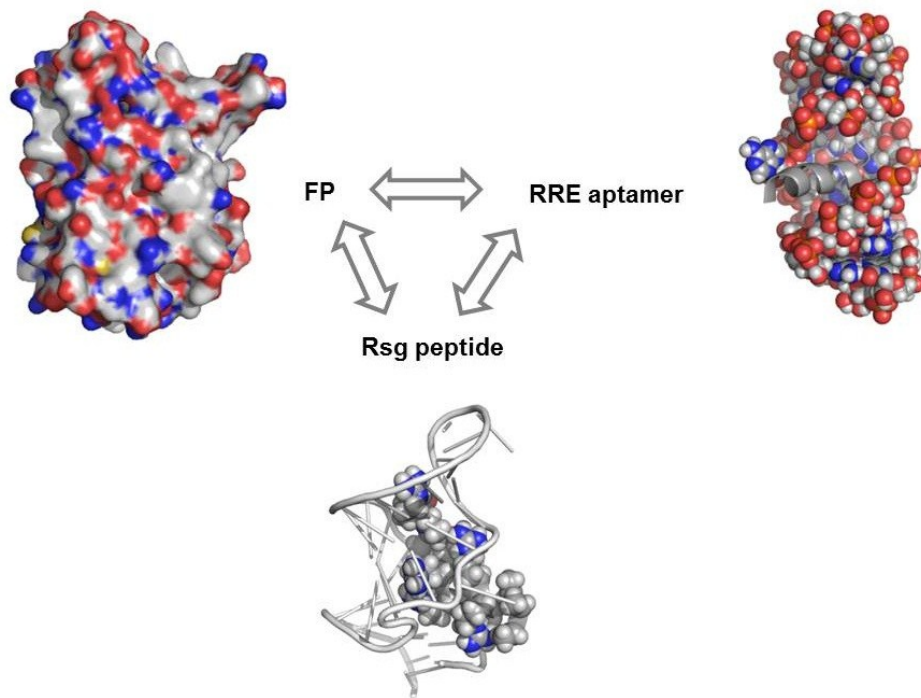


Figure 63 Charge effect on the interaction of VAmPIRe components. Pymol structures: GFP model surface, nucleotide spheres and peptide cartoon (right), RNA cartoon and peptide side chain spheres (bottom). Negative (red) and positive (blue) charges are colour-coded.

4.4.2.3 Linker engineering

We aimed at the rational improvement of FR-Rsg1.2 by insertion of linker amino acids between Rsg1.2 and the FPs. Peptide extension by linkers was supposed to decrease the initial FRET ratio while conserving the aptamer-bound FRET state. Insertion of various defined linkers resulted in decreased initial FRET ratios but the dynamic ranges were lower than for the initial FR-Rsg1.2 sensor. High-throughput screening was required to find a linker that improves FRET sensor performance.

It has been postulated that FP orientation rather than distance might have the greatest impact on the overall dynamic range. This is in line with the great increase in FRET change

upon exchange of the acceptor FP by the corresponding cp variant (T. Nagai 2004) (Palmer et al. 2006) (Mank et al. 2006). Other studies show that number and identity of amino acids between the FPs have profound impact on the FRET change (Miyawaki and Roger Y. Tsien 2000). Optimal linkers potentially increase distance, alter orientation and reduce interference of the fluorophores.

Peptide linkers consisting of glycine and serine amino acids are considered as flexible due to their small side chain. We tested flexible linkers like the commonly used GGGs motif of different length which dramatically reduced the FRET ratio change (Figure 37B). Flexible linkers may allow two FPs to interact with each other. This property of glycine-rich regions is evident in many natural systems, e.g. the NF κ B glycine-rich hinge allows one terminus to fold back on to the other (Henkel et al. 1992). The fold-back property of polyglycine has been shown empirically in pulse-radiolysis experiments (Bobrowski et al. 1990). This possibly indicates that flexible linkers did not rigidly fix distance and orientation of FRET RNA sensor FPs. Instead, the on- and off-states were defined by multiple conformations resulting in an average FRET ratio value.

In contrast to glycine homopolymers, Prolines maintain a predictable end-to-end distance over a length of more than 100 residues (Schimmel and Flory 1967). High steric restriction about the peptide ϕ and ψ and bonds and the almost exclusive *trans* conformation reduce the rotational freedom in Proline polymers. Consequently, poly-L-Proline spectroscopic has been used a ruler to measure distances of energy transfer between attached moieties ranging from 12 to 46 Å (Stryer and Haugland 1967) (Isied et al. 1992). We observed predictable separation distances between the FPs based on the number of Proline residues inserted (Figure 37D). This contradicts the ability of Proline to introduce kinks in the peptide backbone and thereby alter not only distance but also orientation of the FRET pair. Prolines are also favoured because of their inability to donate hydrogen bonds or participate comfortably in any regular secondary structure conformation (George and Heringa 2002). In spite of this predicted rigid separation, the introduction of Proline linkers dramatically reduced the dynamic range of the sensor (Figure 37D).

So-called molecular rulers have proven suitable to render linkers more rigid without changing FP orientation. Most commonly, stable helices have been used to measure the effect of different depths of binding pockets on various properties of proteins of interest

(Johnson et al. 2003). The biggest effect on the starting ratio of our FRET RNA sensor was observed for helical linkers that were able to control the distance between two FPs (Arai et al. 2001) (Figure 37C).

As the ratio change was dramatically reduced in all rationally designed linker variants this suggests that intramolecular interactions with the linker interfere with peptide-aptamer binding or fluorophore movement.

Using our bacterial screen we selected two linkers from a randomized library that increased the dynamic range of the FRET RNA sensor. Both linkers contain several Arginines and Histidines with positively charged, bulky side chains (Figure 43) and no Proline.

4.4.2.4 FRET pair engineering

FRET pair engineering showed that the initial VAmPIRe with the eCFP-cpCitrine FRET pair possesses the highest dynamic range. Replacement of cpCitrine with Citrine resulted in a reversed ratio change which could possibly be due to a reorientation of the dipole. Cerulean exhibits a higher quantum yield than eCFP but performs worse as a FRET donor similar to other studies (Rizzo et al. 2004). Novel cyan FRET donors Cerulean 3 (Markwardt et al. 2011) and mTurquoise 2 (Klarenbeek et al. 2011) exhibit enhanced brightness, have shown a higher dynamic range and their fluorescent lifetime fits to a single exponential time constant suitable for FLIM experiments. Cerulean 3 possesses a quantum yield of 0.87 and greatly reduced fluorescence photoswitching behaviour compared to mTurquoise. A fusion protein with mCerulean 3 and mVenus showed FRET ratios with higher signal-to-noise and less variance in living cells than mTurquoise-mVenus constructs.

As mTFP1 has proven a suitable FRET donor for YFPs and RFPs it would be interesting to test it also for VAmPIRe (Day et al. 2008) (Y Sun et al. 2009) (Ai et al. 2008) (Padilla-Parra et al. 2009).

Fluorophore dimerization in Aequoria FPs has been found to influence the dynamic range of a FRET biosensor (Vinkenborg et al. 2007). Kotera et al. observed higher FRET ratio change for donor and acceptor pairs with the native dimer-interface in different biosensors including TN-XL (Kotera et al. 2010). Further dimer-enhancing replacements at positions S208F and V224L however, reduced sensor performance.

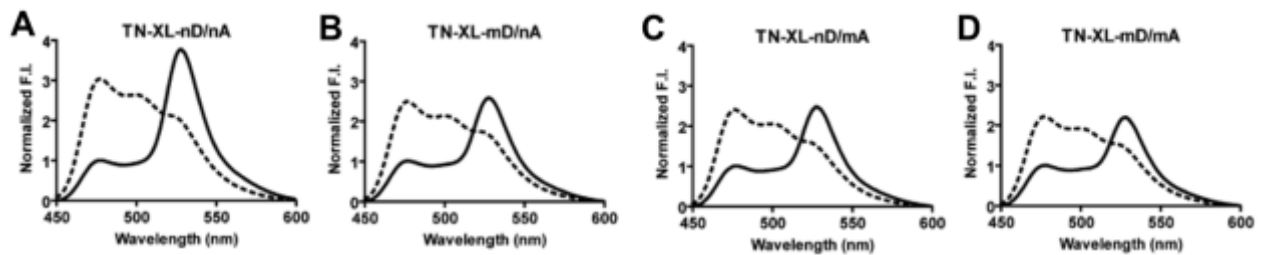


Figure 64 FRET pair dimer interface engineering. Fluorescence spectra of TN-XL variants. **(A)** Original TN-XL eCFP A206K cpCitrine A206K, **(B)** TN-XL eCFP A206 cpCitrine A206K, **(C)** TN-XL eCFP A206 cpCitrine A206, **(D)** TN-XL eCFP A206 cpCitrine A206. (Kotera et al. 2010)

We observed poor ratio changes when we integrated a red FP variant into VAmPIRe. As one of the reasons, red FPs (e.g. mKate, data not shown) fused to other proteins are very dim, probably due to poor folding. Optimized RFP variants could be tested in the future.

4.4.2.5 FRET RNA sensor engineering – conclusion and outlook

Here we show that all components, the RNA binding peptide, the aptamer, linkers and the FRET pair have to be optimized in the context of the FRET RNA sensor. Screening of random linker libraries has proven more powerful than rational engineering. For retrospective analysis, we are creating SAXS structures of the FR-Rsg1.2, FR-Rsg1.2 7A8Q, variant #95 and VAmPIRe sensor variants in the bound and unbound states (in collaboration with Gregor Witte and Anselm Geiger).

With all engineering we tried to maximize the FRET readout with a given conformational change (Figure 65). It remains unclear if the actual conformational change of the peptide allows further improvement of VAmPIRe's dynamic range. NMR studies (Gosser, Hermann, Majumdar, W Hu, Frederick, Jiang, Xu, and Patel 2001b) and circular dichroism (CD) data (Kazuo Harada, Shelley S. Martin, et al. 1997g) revealed a transition from the predominantly disordered free peptide conformation to extensive secondary structure formation upon RRE binding. This allocation only affects amino acids ranging from Serin 13 till Alanine 23. It remains unclear how the transition from unstructured to an ordered secondary structure

changes distance and orientation of the fluorophore. Additionally, the unbound state may adapt different conformations resulting in a diffuse average positioning of the FRET pair.

The theoretical limit of the peptide flexure itself could be overcome by peptide multiplication (Figure 37A). However, linkerless multiplication resulted in poor negative FRET change. A randomized linker sequence between the two peptides could be introduced to optimize the independent action of both peptides. In parallel, distance of the two adjacent target aptamers has to be optimized in order to allow the sensor to bind them at once. However, multi-peptide sensors are prone to crosslinking by aptamer repeats.

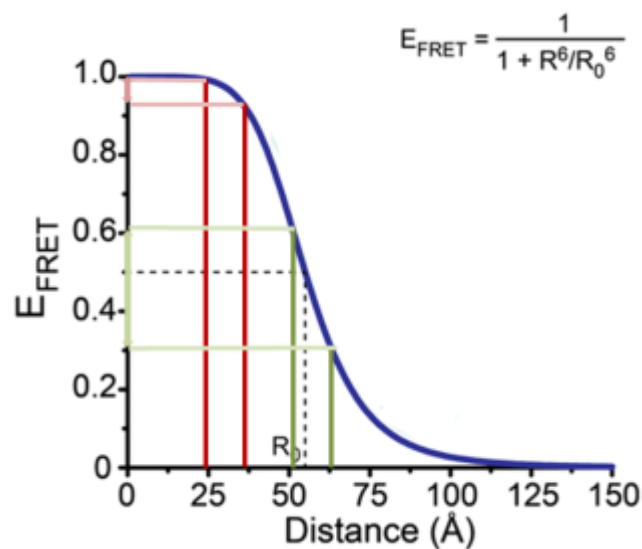


Figure 65 FRET efficiency in dependence of distance. With a given conformational change, the change in distance is constant (vertical dark coloured boxes.) but can have different effects on the FRET efficiency depending on the initial fluorophore distance. Initial sensor (red), optimal sensor with a distance close to R_0 (green).

4.4.3 Cellular performance

VAmPIRe performance in cells has been tested in several assays. We have designed an RNA reporter with mKO2 ORF fused to the RRE aptamer repeats allowing synchronous protein and mRNA monitoring.

We were able to distinguish HeLa cells overexpressing the RNA reporter from other cells by comparison of their FRET ratio (Figure 48).

For the TetON experiment (Figure 49), the RNA reporter was controlled by an inducible promoter. Increasing RNA and protein levels upon induction could be monitored by FRET change and mKO2 emission, respectively. Time-delayed increase of mKO2 emission is due to time needed for translation, folding and oxidation of mKO2. FRET ratio increases first in the nucleus and subsequently spreads to the cytoplasm (Figure 49B) which probably reflects nuclear transcription and subsequent export to the cytoplasm.

VAmPIRe is also suitable to monitor the subcellular distribution of overexpressed β -actin mRNA in fibroblasts (Figure 50). High FRET ratio in perinuclear regions and the leading edge nicely corresponds to RNA localization detected by other approaches (Figure 2G). Subcellular RNA dynamics can be tested in a migration assay.

Upon induction of stress, high FRET ratios compared to the surroundings were observed in cytoplasmic particles (Figure 51). Particles with increased FRET ratio likely originate from cytosolic VAmPIRe bound by the aptamer repeats and incorporated into stress granules via the zipcode. These particles were characterized as stress granules due to their colocalization with ZBP1. Timelapse imaging will provide an insight into spatial dynamics of stress granule formation.

This reveals the potential of VAmPIRe to resolve spatial and temporal dynamics of aptamer-tagged RNAs.

4.4.3.1 Aptamer-tagging of the RNA of interest

For our FRET reporter approach aptamer attachment to the RNA of interest is essential. However, this harbors the danger of disturbance of the RNA of interest regarding folding, transport, translation and stability. FR-Rsg1.2 *in vitro* measurements show that attachment of 10 RRE repeats to the mKO2 ORF did not significantly alter the FRET signal. Target RNA functionality after aptamer fusion has to be considered for each RNA of interest. The site of aptamer insertion has to be chosen with the aim to minimally interfere with coding, stability or localization elements. For other aptamer tagging strategies, the site between ORF and 3'UTR has proven most suitable (Rook et al. 2000).

4.4.3.2 VAmPIRe RNA specificity

Coexpression experiments with aptamer-tagged and unlabeled mKO2 RNA clearly showed the specificity of VAmPIRe for the RRE aptamer in cells.

Investigation of *in vitro* specificity showed that some RRE aptamer mutants that are known to bind Rev still induce a FRET ratio change. A reverse complementary RNA that is similar in nucleotide composition and length slightly decreased the FRET ratio. However, the absence of endogenous RNA stretches similar to RRE has to be assured. Considering the functionality of HIV assembly in eukaryotic cells that relies on the RRE recognition by Rev, any crossreactivity seems unlikely.

4.4.3.3 VAmPIRe pH sensitivity

Beyond the known pH sensitivity of FPs, VAmPIRe starting ratio and dynamic range are pH-dependent. This probably originates from the Arginine-rich Rsg peptide. Better performance at basic pH values renders the sensor suitable for applications in mitochondria. Mitochondrial targeting of a FRET RNA sensor has been tested in cell culture (data not shown). The higher pH within bacterial cells contributes to the differences in sensor performance in prokaryotic and eukaryotic systems. For cell experiments unspecific signal caused by pH changes have to be taken into account.

4.4.3.4 Comparison of VAmPIRe to the MS2/ λ N22 system

The aim of this study was to create a novel, aptamer-dependent RNA reporter that is genetically encoded. Currently, the MS2 and the λ N22 systems are the methods of choice for live cell RNA imaging. Mainly MS2 but also λ N22 tagging has proven valuable for different mRNAs in various cell types (Schifferer and Oliver Griesbeck 2009) including the use of endogenous promoters. Therefore, VAmPIRe's performance can be best evaluated by a comparison to these state-of-the-art techniques.

An important criterion for a reporter is a high affinity to the specifically tagged RNA of interest. Optimally, the apparent dissociation constant is at or near the expected concentration. As changes in concentration are most efficiently detected within $\pm 5 \times K_D$ a

high reporter sensitivity also assures a favourable dynamic range. The MS2 peptide binds to the MS2 RNA motif with a dissociation constant of 39 nM (Lago et al. 1998). The Rsg1.2-RRE interaction possesses similar affinity ($K_D = 6$ nM) but the K_D for the isolated mutated VAmPIRe peptide has not been determined. A direct comparison of the affinities of the actual fusion proteins ($K_D(\text{VAmPIRe}) = 100$ nM) is not possible as the value for the MS2 label is missing. The FRET sensor variant #95 performed better than VAmPIRe regarding affinity and therefore will also be tested in cells.

The MS2/ λ N22 systems rely on accumulation of the MS2-labelled GFP on the aptamer repeats. Signal-to-noise ratio is increased by subcellular restriction which has been shown by us and others to be inefficient in certain cell types and might interfere with the targeting of the RNA of interest. VAmPIRe circumvents the need of subcellular restriction although a NLS could be beneficially introduced for background reduction in some contexts. In contrast to a simple GFP label this dynamic visualization strategy allows imaging in the nucleus. Instability of implementation of the MS2 system forcedly includes a tight control regarding leakiness of the subcellular restriction and RNP-like aggregate formation (see 3.4.1, Figure 23).

Every MS2 aptamer can be contacted by two MS2-GFP labels. Up to 30 MS2 reporter molecules bind to 24 MS2 aptamer repeats (S. Hüttelmaier, personal communication). For the detection of mRNAs that are less abundant than β -actin, 3 copies of GFP have to be fused to the MS2 peptide to assure proper fluorescence emission. The number of aptamer repeats can also be adapted to the desired sensitivity depending on the prevalence of the RNA of interest. For most MS2 experiments 24 repeats similar to the 20 RRE multimer were applied, however as few as 6 MS2 repeats were sufficient for imaging of ASH1 RNPs in *S. cerevisiae* (E Bertrand, P Chartrand, et al. 1998a). There is also a limit on the number of loops that can be introduced into the endogenous mRNA because of the difficulty in cloning repeats and the effect of increasing the size of the RNA considerably. For some applications long aptamer stretches bear a high potential of interference with the tagged RNA of interest. This was the reason for insertion of as few as 4 MS2 aptamers into the intron of an RNA construct that was used to report splicing by the absence of the MS2 tag (E. Bertrand, personal communication).

Generally, the VAmPIRe approach can be applied to all cellular systems similarly to MS2/N22 without the usage of a NLS and higher reliability of the signal. Quantitative evaluation of the methods is only possible if VAmPIRe is directly compared to MS2/ λ N22 in one experiment, e.g. for oskar mRNA tracking in *Drosophila* oocytes.

Table 2 Comparison of VAmPIRe with the MS2/ λ N22 systems.

	VAmPIRe	MS2	λ N22
affinity peptide-aptamer	6 nM (wt Rsg 1.2)	39 nM	22 nM
affinity GFP label-aptamer-tagged RNA	100 nM	n.d.	n.d.
NLS restriction	not necessary but possible	required	required
read-out error		33 %	36 %

VAmPIRe and the MS2 system have proven suitable for RNA imaging in living cells. The introduction of an additional aptamer-dependent switch would improve signal-to-noise ratios and reliability of the MS2 approach. Therefore, we propose the design of a FRET RNA sensor that benefits from the widespread applicability of the MS2 aptamer system. Dimeric binding of MS2 peptides to the MS2 aptamer can be exploited to create a FRET RNA indicator. A FRET pair separated by two MS2 peptides is linked by a long linker assuring low starting FRET ratio (Figure 66B). FRET is induced only upon dimeric binding of the two peptides of the same sensor molecule to the MS2 aptamer. The possibility of two sensors binding to one MS2 aptamer has to be considered. This FRET sensor could potentially be applied in all the different cell lines or transgenic animals stably expressing target RNAs tagged with MS2 RNA repeats.

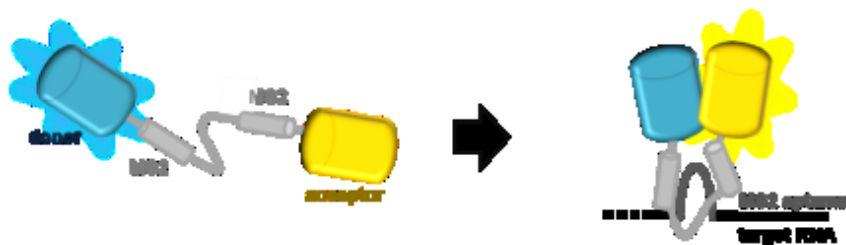


Figure 66 Design of novel RNA biosensors. FRET sensor with two MS2 peptides that assemble on one MS2 aptamer.

4.4.3.5 Comparison of VAmPIRe to existing RNA FRET sensors

Independently, the lab of E. Kobatake has established a similar RNA reporter called Rev sensor. Without any documented screening for a suitable peptide aptamer-pair the Rev-RRE complex was chosen. The Rev peptide was cloned without any linkers into an eYFP(Δ 11aa)-eCFP FRET pair in contrast to VAmPIRe's eCFP(Δ 11aa)-cpCit. For the Rev sensor, the introduction of flexible linkers was not beneficial but instead reduced the FRET ratio change upon RRE addition. The dynamic range of approximately 30 % was determined in a HeLa cell lysate and is much lower than VAmPIRe's 160 % ratio change measured in a buffer with well-defined composition. The wt Rsg1.2-RRE interaction is 7 times more affine and 15 fold more specific than the Rev-RRE one. As the affinity for Rev sensor-RRE ($K_D = 2.5$ nM) and VAmPIRe-RRE ($K_D = 100$ nM) were determined under different experimental conditions they are not directly comparable.

On the aptamer side we optimized the multimerization of 10, 20 and 30 RRE stem loops whereas the Kobatake lab published a maximum of 16 aptamers without any control of efficient folding. Rev sensor strategy includes a split RRE aptamer fused to a sequence that is reverse complementary to a target RNA sequence. Upon binding of the two RNA segments to the template the RRE aptamer is reconstituted and the FRET fusion protein can bind. This requires individual optimization of the split RNA construct for all RNAs of interest. In contrast, the VAmPIRe strategy involves the attachment of RRE repeats to the target RNAs. Cellular application comprises a comparison of HeLa cells transfected with the Rev sensor only or cotransfection of 4 to 16 RRE repeats. There was a difference between the FRET intensity of both groups that was not significant. Consequently, the authors could not convincingly demonstrate the functionality of the Rev sensor in mammalian cells. Contrarily, VAmPIRe performance was tested in different systems including coexpression experiments within one dish and inducible aptamer expression that monitors dynamic RNA levels within the same cell.

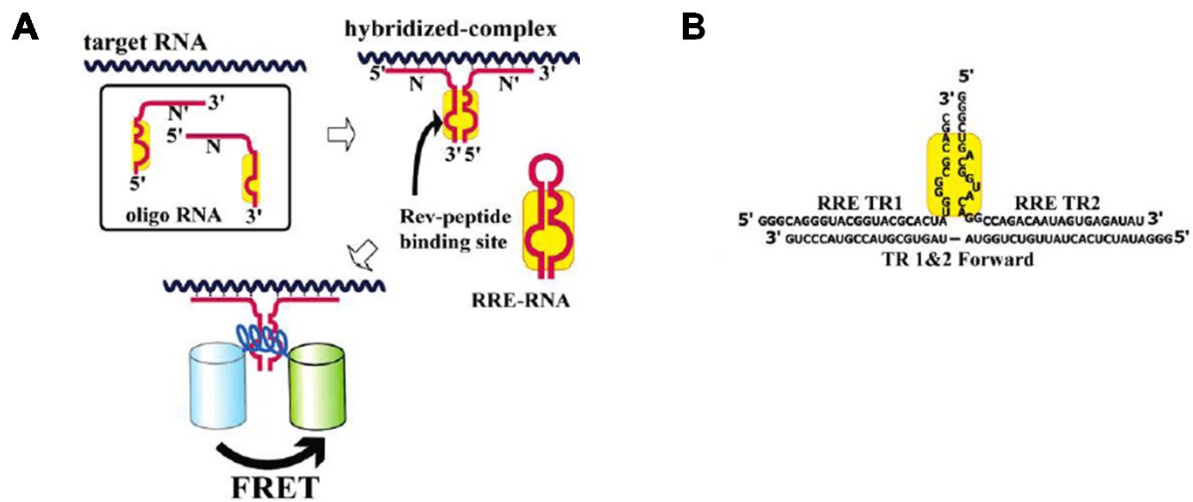


Figure 67 Rev sensor strategy. (A) Principle of target nucleic acid detection by FRET signal change. In the presence of target nucleic acids, two synthetic oligonucleotides hybridize to the adjacent region of the target nucleic acids and reform a Rev-peptide binding site on the hybridized complex. Then the YRGOC-11ad binds to the hybridized complex with a FRET increase mediated by Rev-peptide conformational change. (B) Secondary structure and sequence of the hybridized complex. Minimal RRE-RNA element necessary for Rev-peptide binding was surrounded. (Endoh et al. 2005)

Table 3 Comparison of VAmPIRe to the Rev sensor.

	Rev sensor	VAmPIRe
FRET pair	eYFP(Δ 11aa)-eCFP	eCFP(Δ 11aa)-cpCit
peptide	Rev	Rsg 1.2 7A8Q, linkers
aptamer	split RRE 1x, 4x, 16x RRE	RRE 1x, 5x, 10x, 20x, (30x) RRE
mechanism	split aptamer complementary binding to target RNA	aptamer fusion to target RNA
ratio change	~ 30% (HeLa cell lysate)	160 % (recombinantly expressed, purified pH 7.25)
affinity sensor	2.5 nM	100 nM
affinity peptide	40 nM	6 nM (Rsg1.2)
specificity	negative ratio change for one unspecific RNA	negative ratio change for unspecific RNAs Rsg 1.2 (wt) 15 fold higher specificity than Rev

4.4.3.6 Imaging of dendritic mRNAs

Imaging of single transcripts in neuronal dendrites requires high sensitivity. On the sensor part, improvements include the increase of the dynamic range and the addition of more and optimized aptamer repeats.

A further requirement for RNA imaging involves a microscopy technique that is able to detect single labeled RNA molecules in light-scattering brain slices. Spine size varies from 0.2 to 2 μm in length which can be resolved by confocal or two-photon microscopy with a lateral resolution of 200 nm. However, imaging of submicron RNA particles will be restricted by diffraction-limited resolution. Recently, STED (stimulated emission depletion) microscopy, a far-field optical technique with subdiffraction resolution was used to monitor morphological plasticity of dendritic spines (Nägerl et al. 2008). In this study, Lifeact-YFP was used to image actin structures inside dendritic spines of hippocampal neurons in organotypic slices (Figure 68).

FLIM is an imaging technique for producing an image based on the differences in the exponential decay rate of the fluorescence from a fluorescent sample. It can be used as an imaging technique in confocal microscopy and Two-photon excitation microscopy. The lifetime of the fluorophore signal is used to create the image in FLIM. Energy transfer from the donor molecule to the acceptor molecule will decrease the lifetime of the donor. Thus, FRET measurements using FLIM can provide a method to discriminate between the states of the fluorophore. In contrast to intensity-based FRET measurements, the FLIM-based FRET measurements are insensitive to the concentration of fluorophores and can thus filter out artifacts introduced by variations in the concentration and emission intensity across the sample. Furthermore, FLIM minimizes the effect of photon scattering in thick layers of sample. We are planning to apply VAmPIRe in FLIM imaging. Therefore, the eCFP is replaced by a donor with single exponential decay including Cerulean 3 and Turquoise 2.

As bleaching will be limiting for following the fate of single localizing transcripts from transcription to degradation the FRET pair has to be optimized regarding photostability. The availability of backup-biosensor for bleached areas will have to be balanced with high signal-to-noise ratio that requires low reporter expression. Generally, this could be an advantage of VAmPIRe compared to the MS2 system as the dynamic FRET signal allows for high background expression in the surrounding of the aptamer-tagged RNA of interest.

Novel imaging tools have to be combined with automated particle tracking algorithms will make an invaluable contribution to post-acquisition image processing (Jaqaman et al. 2008). Overcoming these technical obstacles, functional FRET RNA imaging could contribute to get more insight into activity-dependent RNA transport, translation and turnover.

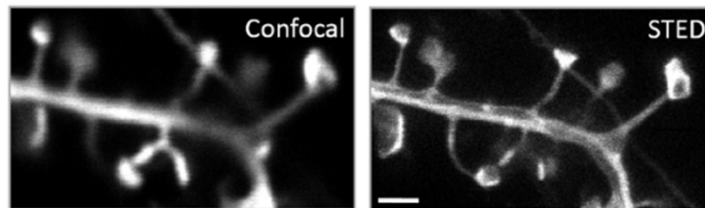


Figure 68 Comparison of confocal and STED microscopy in spines. Lifeact-EYFP in organotypic hippocampal brain slices. Confocal (left) and STED microscopy (right) (Nägerl and Bonhoeffer 2010)

4.4.3.7 Ectopic localization of RNAs in spines

Beyond simple tracking functions, VAmPIRe might be useful to ectopically localize RNAs to study their local function. A subcellular targeting signal is fused to VAmPIRe that binds the tagged RNA and carries it to the site of interest, e.g. dendritic spines.

We created a vector with the neuronal Thy1 promoter and Lifeact, a targeting sequence for neuronal spines derived from actin (Riedl et al. 2008). In a control experiment GFP nicely localized to neuronal spines in rat hippocampal neurons suggesting that VAmPIRe might be targeted similarly using Lifeact (Figure 69A). This would allow the visualization and ectopic localization of mRNAs or small RNAs to spines and to study the impact on neuronal functioning.

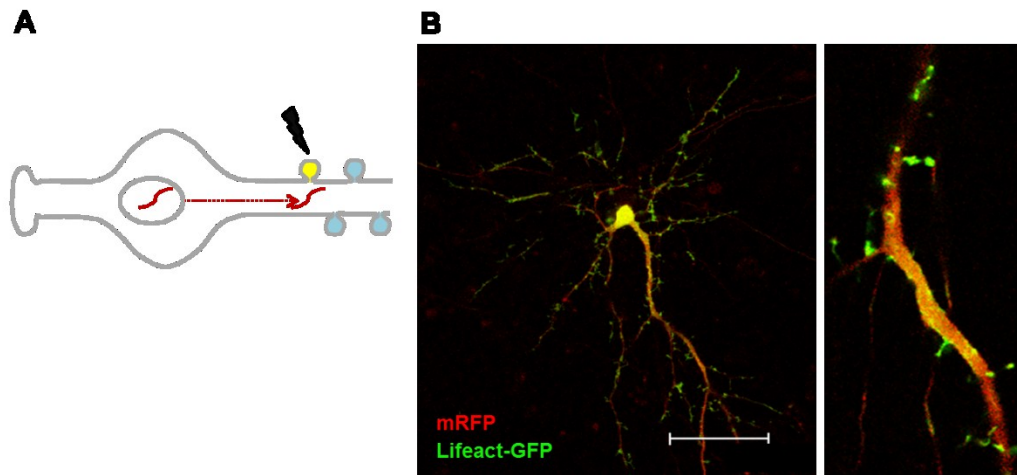


Figure 69 Ectopic spine targeting by Lifeact. (A) Scheme of dendritic RNA imaging by spine-localized Lifeact-VAmPIRe. RRE-tagged RNA of interest (red) is transported to neuronal spines upon activation (black bolt) and induces a VAmPIRe FRET change (yellow). **(B)** Confocal imaging of rat hippocampal neurons DIV 14 lipofected with mRFP and Lifeact-GFP. Magnification (right). Scale bar 50 μm .

4.4.3.8 Imaging of HIV particle assembly

VAmPIRe was designed to image specific RNAs of interest by RRE aptamer tagging. The RRE itself is an integral part of the HIV genome and can potentially also be imaged using the VAmPIRe. Current methods for HIV imaging include HIV Gag protein fusion to FPs or the introduction of a SNAP tagged Gag. (Ivanchenko et al. 2009) (Eckhardt et al. 2011). These reporters have been successfully used for live-cell imaging analyses of HIV-cell interactions and allow direct visualization of dynamic events and individual steps in the viral life cycle. For viral RNA imaging the accessibility of sensor to the RRE aptamer challenged by particle assembly has to be considered. Furthermore, VAmPIRe functionality within virus particles has to be investigated as entry and budding of enveloped viruses like HIV depends on pH-changes within different cellular compartments (Chazal and Gerlier 2003). Overcoming these hurdles, MS2 repeats have been introduced into the HIV genome (Jouvenet et al. 2009). Simultaneous tracking of Gag-mCherry and the GFP-labeled MS2-HIV genome allowed analysis of Gag-genome interaction during several stages of virus assembly. Endogenous HIV genome imaging by VAmPIRe would circumvent the insertion of additional RNA sequences but suffer from the availability of only one RRE binding site which could cause sensitivity problems.

4.4.3.9 Visualization of endogenous RNA

Aptamer-tagged RNAs need to be expressed within cells by transfection of plasmid DNA, possibly resulting in overexpression of the aptamer-RNA construct compared to endogenous RNA levels.

Overcoming this problem, cell lines that stably express an aptamer-tagged RNA of interest have to be established. Single human osteosarcoma cells (U2OS) have proven suitable to tolerate the stable integration of DNA and RNA repeats into a single locus (Xavier Darzacq, Yaron Shav-Tal, et al. 2007b). The technique called m-TAG was established for tagging of genomic loci with MS2 repeats in *S. cerevisiae* by homologous recombination (Haim-Vilmovsky and Gerst 2011). Recently, a knock-in mouse expressing 24 MS2 repeats attached to the actin mRNA has been generated (Timothée Lionnet, Kevin Czaplinski, et al. 2011). Cell isolation and transient transfection with the MS2-GFP-NLS label allows the visualization of endogenous actin transcripts in primary cells.

4.4.4 Screening for FRET sensor performance

Improvement of VAmPIRe's dynamic range by rational engineering is limited by the lack of structural information. Molecular evolution by random mutagenesis has proven powerful for engineering of enzymes and fluorescent proteins (Goedhart et al. 2010) (Shaner et al. 2008) (Ai et al. 2006) (Bevis and Glick 2002). With the initial aim to increase VAmPIRe's dynamic range, we established the first functional screen that allows high-throughput testing of fluorescent sensor variant libraries in bacterial colonies.

4.4.4.1 Bacterial FRET screen

With a major contribution of Julia Litzlbauer, we designed the first functional bacterial colony assay for the directed evolution of FRET sensors. Colony imaging during induction of aptamer transcription allows to detect the off and the on state of the biosensor. Selection criteria included both the initial FRET ratio and the dynamic range.

We tested different induction reagents including tetracycline (TC), doxycycline and anhydrotetracycline (aTC) in various concentrations and observed the best induction with aTC. aTC is known to be more stable and bind the Tet repressor more efficiently than TC

(Gossen and Bujard 1993) (Oliva et al. 1992). In contrast to TC, aTC does not interfere with the bacterial translation apparatus. This would be advantageous for the screening of sensors detecting proteins.

As the FRET signal depends on many different aspects, the absolute FRET ratio is not comparable between different experiments. This variability was balanced by integration of a standard FRET sensor of known performance. Given a standardized experimental procedure including time point of imaging after transformation and plate medium thickness still colony size and starting ratios of control sensors showed fairly high variation. Technical improvements include uniform plate illumination and standardized medium composition (Julia Litzlbauer).

Although using the same promoter and bacterial strain, sensor and aptamer expression levels were not reliable. Similar differences in RNA expression in different bacteria upon aTC induction has been observed in other studies (Valencia-Burton et al. 2009) (Yiu et al. 2011). Possible reasons include leakiness of the TetOn system, pH changes, bacterial growth and metabolism as well as subcellular RNA distribution. Previous studies show that RNA levels after induction can vary significantly between individual bacteria within the same population (Figure 70). Inter-experimental differences are even more pronounced (Figure 70B).

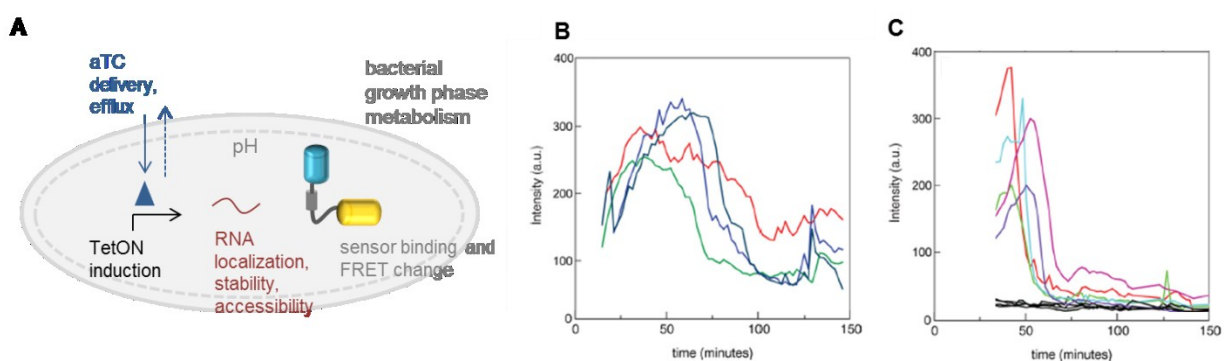


Figure 70 RNA induction in bacteria using the TetON system. (A) Schematic of a bacterium showing parameters that influence FRET readout in an RNA induction experiment. **(B, C)** RNA kinetics in single *E. coli* cells upon induction with aTC. Time course of total fluorescence in individual *E. coli* cells in two representative experiments. RNA levels were recorded using the split-GFP reporter (see 1.5.3.3). The $t=0$ time is defined as the moment of aTC addition to cells. Measurements are taken at 2-min intervals. (Valencia-Burton et al. 2009)

One way to stabilize RNA induction is to assure stable aTC levels within the bacteria. The standard assumption emerging from population measurements has been that cells exposed to steady levels of inducer would produce a steady transcription activity. Conversely, real-time RNA profiling within single cells reveals that drug-inducible transcription leads to the pulsating, cell-cycle dependent generation of mRNAs (Le et al. 2005). We observed FRET fluctuations 1-3 h after aTC addition that are probably due to active, unspecific efflux pumping mechanisms (Nikaido 1996). Bacterial xenobiotic metabolism of aTC can be bypassed by host bacterial cells that lack efflux pumps (Δ acrAB) and presumably tolerate more aTC (Okusu et al. 1996) (Figure 71A). We already tested different efflux pump inhibitors (EPIs) including chlorpromazine and cyanide *m*-chlorophenylhydrazone (Stavri et al. 2007) (Pagès and Amaral 2009). Combined EPI and aTC application didn't have any effect on the induction experiment (data not shown).

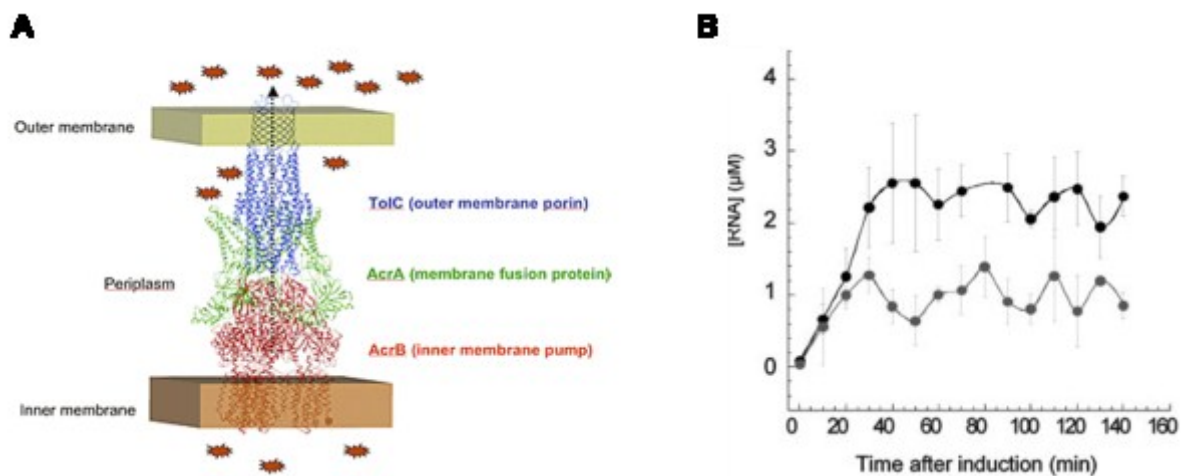


Figure 71 Effect of *acrAB* efflux pumps on RNA induction by TC. (A) Structural organization of the tripartite efflux system, *acrAB*-TolC from *E. coli*. (www.mpexpharma.com/efflux.html) **(B)** Induced RNA expression in wild type *E. coli* with (dark grey) and without (light grey) 400 ng/mL TC and *E. coli* Δ *acrAB* (black) with TC. MS2-RNA concentration was determined in a cell population by fluorescence correlation spectroscopy (FCS). Cells were grown at constant density in M9 medium at 30°C. (Le et al. 2005)

The bacterial screen has proven suitable to increase the dynamic range of the RNA FRET sensor from 80 % to 160 % (Figure 43). Insertion of randomized linkers was more successful than random mutagenesis of the Rsg peptide itself. As nature and number of variants with

better characteristics remains unpredictable, further rounds of screening have to follow. High throughput screening requires automated colony analysis. Elisabeth Hopp (Department Borst) developed a program (Matlab) that selects colonies according to fixed criteria. This program is also applied for the screening of Calcium sensors. Further optimization includes the format of high-throughput protein expression and *in vitro* test measurements which could be performed in 96-well plates.

It remains unclear if most of the variants bind without changing their FRET signal or if linker insertion also modulates peptide-aptamer affinity. In the latter case, an additional bacterial antitermination assay (see 4.3.1) could preselect for sensors that still interact with the RRE aptamer.

Evolutionary methods such as the one introduced and used here, although not exhaustively, may become increasingly important in optimizing performance of many biosensors relying on FRET between fluorescent proteins.

4.4.4.2 Cellular screening

Bacterial screening profits from ease of manipulation resulting in a big library size that can be screened. So far, we validated sensors from the bacterial screen first *in vitro* and afterwards in a cellular assay. Screening in mammalian cells is more expensive and allows a lower number of variants to be screened but would meet the demands of functionality for live cell imaging. Especially aptamer folding and affinity of reporter and RNA construct can vary in different systems. A recently introduced method combines generation and cellular analysis (Piljić et al. 2011) of a set of 36 different FRET reporters. The cloned variants were spotted on DNA arrays serving as a platform for reverse transfection of and subsequent semiautomated microscopy of HEK-293 cells.

There are several ways of testing cellular sensor performance. The first possibility requires a sensor library that is expressed transiently in a mammalian cell line expressing the aptamer under the control of an inducible promoter, similar to the bacterial screen. In another approach, a stable cell line permanently expressing the aptamer could be transiently transfected with the sensor library and stressed resulting in stress granule formation. A third way of testing library reporters consists of infection by viruses with an aptamer-tagged RNA

genome. In each case FRET ratio changes are recorded and cellular DNA is isolated and sequenced. Viral infection was already tested using the Semliki Forest Virus (SFV) with the RRE aptamer repeats incorporated (data not shown). On one hand the virus titer was low probably due to the repetitive sequences that were introduced, on the other hand infection of HEK 293 T cells resulted in low cell survival.

Another possible selection procedure includes cell FACSing (fluorescence activated cell sorting) according to the FRET ratio (AW Nguyen and PS Daugherty 2005). Beyond the technical challenge this method would include selection and pooling of similar low FRET ratios before RRE expression and a second FACS step after coexpression of the aptamer thereby selecting for high FRET ratio.

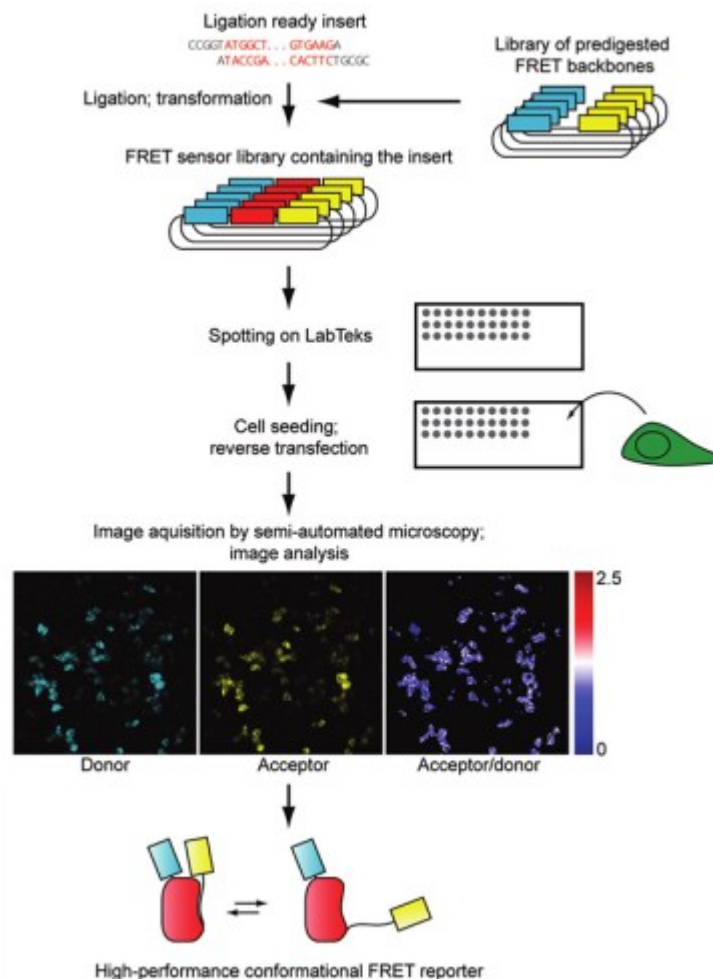


Figure 72 Workflow for the cellular screening of FRET sensors. A library was constructed by cloning a specific protein domain into different FRET scaffolds with variable linkers. For reverse transfection, library plasmid DNA was spotted on LabTek coverglass. Images were acquired by semiautomated microscopy and analyzed for high performance (Piljić et al. 2011).

4.5 REFlex sensor performance

4.5.1 REFlex assay *in vitro* application

Using REFlex we were able to monitor assembly and disassembly of the EJC in solution. *In vitro* REFlex assay provides a fast and convenient tool to test candidates or screen for factors stabilizing or destabilizing the EJC. Single molecule FRET studies on RNA helicase conformational change as performed on the helicase YxiN are shedding light on the switching behaviour and function of these proteins (Theissen et al. 2008). Our FRET sensor REFlex might be a useful complementation to biochemical and structural studies in gaining more insight into the eIF4AIII interactome and elucidating its function in RNA regulation. The design principle can be applied to other members of the RNA helicase family.

In particular, we verified that PYM is only able to bind MAGO-Y14 if it is incorporated in the EJC. Our data support the hypothesis that this is due to conformational changes of MAGO-Y14 and does not depend on the subcellular separation of free cytosolic PYM and nuclear MAGO-Y14 (Gehring, Lamprinaki, Kulozik, and Hentze 2009c). FRET monitoring by REFlex demonstrates that Imp13 is sufficient to induce the transition of eIF4AIII to the open state in the absence of PYM. It will be interesting to study the relevance of this finding in the cellular context, in particular if one considers that Imp13 has a higher affinity for MAGO compared to PYM (Budiman et al. 2009).

RNA binding of REFLEX in the presence of EJC core components was found to be unspecific. In the absence of these EJC components, however, in minimal assays employing only REFLEX and ATP, a higher selectivity for a given RNA target was found. While RNAs representing the 3' UTRs of two mRNAs subject to EJC related NMD (Sauliere et al. 2010) proved efficient targets for REFLEX, no FRET change could be seen when an unrelated intronless mRNA coding for the fluorescent protein mKO2 was used in concentrations that were efficient in promoting EJC assembly in the presence of MAGO-Y14 and Barentsz. This suggests a reduced RNA selectivity of eIF4AIII when situated within the EJC core, while free eIF4AIII apparently retains preference for some RNA motifs over others. Along these lines, free eIF4AIII was reported to preferentially bind certain RNA loop structures within mRNAs coding for selenoproteins (Budiman et al. 2009). However, there is also recent evidence for RNA sequence-specific deposition of the EJC (Sauliere et al. 2010). In view of our data this

could be explained by an initial binding of preferred sites by free eIF4AIII, which is subsequently stabilized and complemented by the other components of the EJC. It will be interesting to repeat the REFlex specificity test with a nuclear extract supplement including splice factors.

4.5.2 REFlex application for cellular imaging

4.5.2.1 REFlex function in cells

REFlex is a genetically encoded FRET sensor that is potentially suitable to study eIF4AIII in its two different states in living cells. Assigning the subcellular FRET signals to either the eIF4AIII bound or unbound form would provide a powerful tool to get functional insights.

REFlex was transiently expressed under the control of a CMV promoter in HEK 293T cells as well as neurons. Within the endogenous cellular context, EJC components are expressed at a specific ratio (Gehring, Lamprinaki, Kulozik, and Hentze 2009b). Consequently, cellular REFlex as well as endogenous EJC component expression levels will be crucial for the study of eIF4AIII function. Particularly, endogenous eIF4AIII replacement by REFlex using a knock-in strategy would ensure usual cellular protein levels.

As live cell application requires high reporter sensitivity, sensor engineering is required. REFlex performance has been improved by insertion of mutations that favor FP dimerization. Targeted mutagenesis of amino acids at the dimer interface (Kotera et al. 2010), random linker insertion or random mutagenesis provide further means to improve the dynamic range even further.

4.5.2.2 Future application of REFlex for cellular imaging

In *Drosophila* oocytes, localization of oskar mRNA to the posterior pole is dependent on the nuclear formation of an RNP including the EJC. Another prerequisite for proper oskar mRNA targeting is splicing of the first intron. In the absence of eIF4AIII, oskar mRNA is evenly distributed in the oocyte. Labeling of oskar mRNA and REFlex coexpression would allow to subcellularly determine the pool of eIF4AIII-bound oskar mRNA compared to the dissociated

situation. In this way, REFlex serves as a tool to study the requirement of EJC binding for proper cellular targeting.

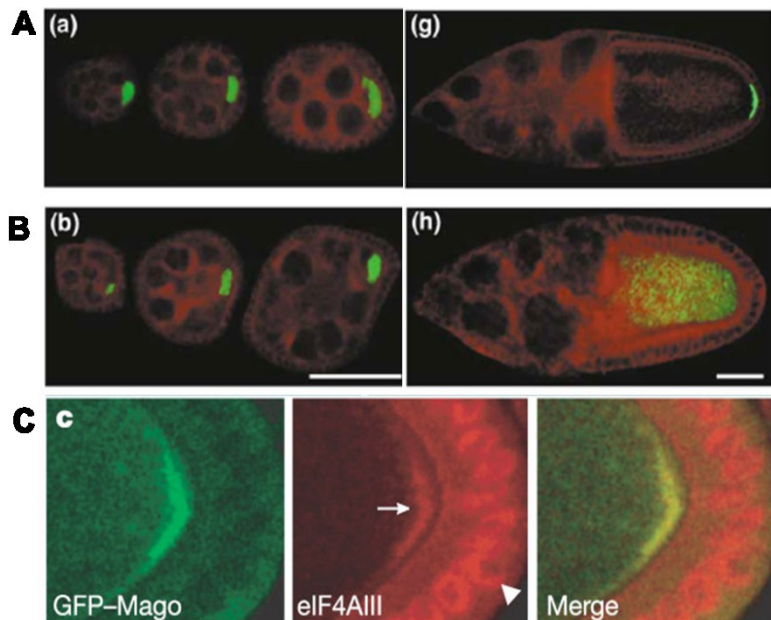


Figure 73 Oskar mRNA and the EJC in *Drosophila* oogenesis. (A)(B) Stages 3-5 and 10b of oogenesis. Oskar mRNA (green) oocyte autofluorescence (red) (A) wt oocytes with oskar mRNA posterior localization (B) Y14 oocytes with oskar mRNA random distribution (Hachet and Ephrussi 2001e) (C) Antibody staining for eIF4AIII during oogenesis. Posterior region of a stage 9 egg chamber expressing GFP-Mago (Isabel M. Palacios, Gatfield, Daniel St Johnston, and Izaurralde 2004b).

REFlex expression in neurons shows a somatodendritic distribution with granular localization in dendrites (Figure 74). Giorgi et al. found that eIF4AIII is associated with neuronal mRNA granules and dendritic mRNAs (Giorgi, Yeo, et al. 2007c). eIF4AIII knockdown increases both synaptic strength and GLUR1 AMPA receptor abundance at synapses. The expression of some proteins including Arc, which is required for maintenance of LTP, is increased by eIF4AIII depletion. The EJC is supposed to mediate translation-dependent mRNA decay that might advantageously function as critical brakes for protein synthesis in neurons that are highly dependent on spatially and temporally restricted protein expression. The association of eIF4AIII with dendritic mRNAs suggests that they have

not yet undergone translation (Maquat 2004). REFlex provides a tool to get further insight into the role of eIF4AIII and its target mRNAs in maintaining synaptic strength.

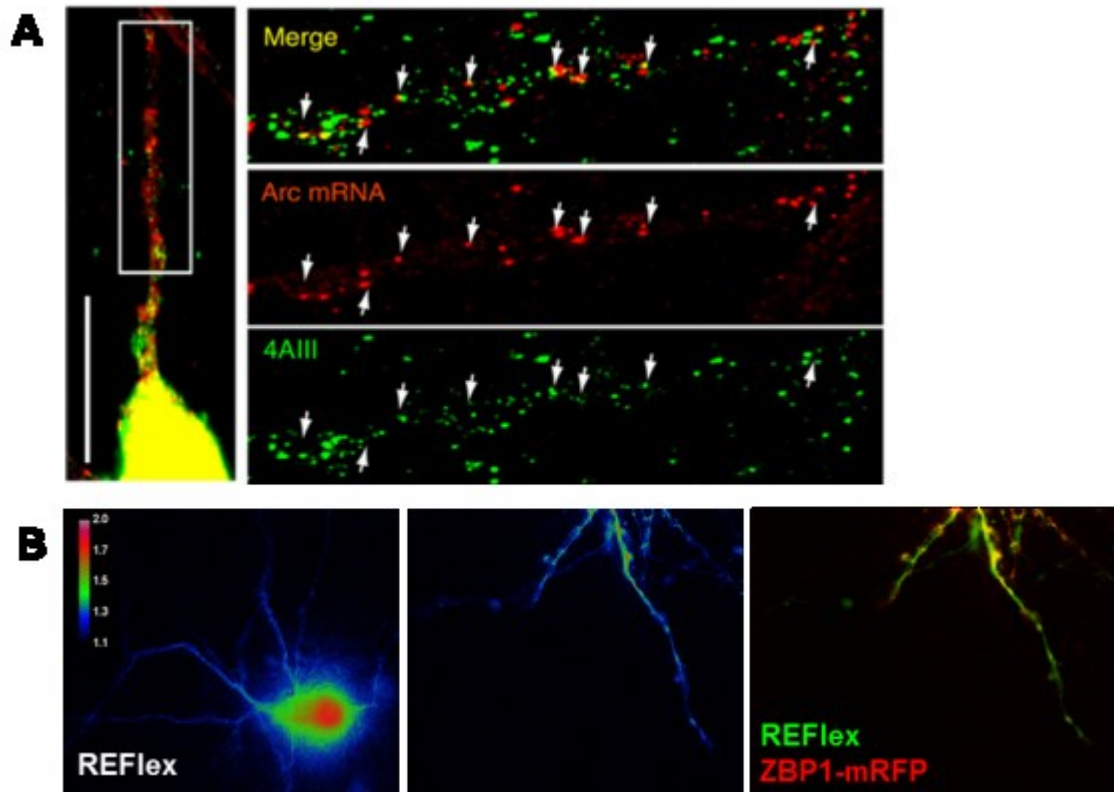


Figure 74 eIF4AIII in neurons. (A) FISH of Arc mRNA (red) and immunofluorescence of 4AIII (green) after BDNF treatment. Right panels: enlargement of indicated dendritic region. Arrows indicate examples of colocalization. scale bar 10 μ m. (C Giorgi, GW Yeo, et al. 2007c). **(B)** Hippocampal neurons transiently expressing REFlex (left, middle, right: green) and dendritic RNP marker ZBP1-mRFP (red, right).

4.6 Conclusion

The studies presented here reveal the necessity of a sensitive and dynamic RNA imaging approach. For live cell imaging, genetically encodable FP-based RNA reporters are preferred over chemical on-off compounds that hamper cellular application because of ineffective dye delivery and insufficient specificity.

Our FRET RNA sensor VAmPIRe provides a tool for the dynamic detection of RNAs *in vitro* and in living cells.

Circumventing the need of an NLS, VAmPIRe will be especially useful for the visualization of nuclear processes including transcription and splicing. Exceeding the claims for ion or small molecule sensors, long-term RNA visualization of specific single transcripts within the cellular transcriptome requires high sensitivity and specificity of the RNA indicator. Proper aptamer repeat folding and accessibility within the context of a RNP are prerequisites to high intracellular affinity and sensitivity. Further improvement of VAmPIRe's dynamic range is desirable for advanced applications like the long-term visualization of single transcripts in primary neurons. Biosensor design and novel imaging and data processing techniques have to converge to render RNA tracking possible.

Regarding sensor design we revealed benefits and problems of using ARM peptides. On the one hand affinity, small sizing and non-eukaryotic origin is desirable on the other hand, inherent cross-specificity and charge effects complicate FRET sensor design. It remains unclear if the small conformational change upon RNA binding constitutes a limiting factor for further sensor improvement.

We showed that random approaches are more powerful than rational engineering as long as detailed structural information is missing. Combining the established high-throughput bacterial screen with large-scale cellular testing will technically allow further sensor improvement. With further automation this method will be powerful for high-throughput testing of novel fluorescent biosensors in a biological context.

We identified further suitable peptides for the FRET approach as well as single-fluorophore RNA sensors with lower dynamic range. This may allow the development of a range of conditional aptamer reporters with orthogonal spectral properties. We are also planning to design single fluorophore sensors based on a donor-quencher principle that holds the promise of a high dynamic range.

With REFlex we established a new sensor design principle that can potentially be applied to many other RNA helicases. Suitability for *in vitro* studies has been shown but has to compete with existing single molecule techniques. As soon as sensitivity is improved, genetic encodability of REFlex can be exploited for functional imaging of eIF4AIII in living cells.

References

- Ai, H.-wang, Hazelwood, K.L., Davidson, M.W., and Campbell, Robert E. 2008. Fluorescent protein FRET pairs for ratiometric imaging of dual biosensors. *Nat Meth* **5**: 401-403.
- Ai, H.-wang, Henderson, J.N., Remington, S James, and Campbell, Robert E. 2006. Directed evolution of a monomeric, bright and photostable version of *Clavularia* cyan fluorescent protein: structural characterization and applications in fluorescence imaging. *The Biochemical Journal* **400**: 531-540.
- An, P., and Grabowski, P.J. 2007. Exon Silencing by UAGG Motifs in Response to Neuronal Excitation. *PLoS Biol* **5**: e36.
- Andersen, C.B.F. et al. 2006. Structure of the Exon Junction Core Complex with a Trapped DEAD-Box ATPase Bound to RNA. *Science* **313**: 1968 -1972.
- Aoyama, S., Sugaya, M., Kobayashi, C., Masuda, K., Maeda, T., Sakamoto, T., Kawai, G., Katoh, A., and Harada, Kazuo. 2009. An isostructural G-G to A-A substitution within the HIV RRE RNA switches the specificity towards arginine-rich peptides. *Nucleic Acids Symposium Series (2004)* 271-272.
- Arai, R., Ueda, H., Kitayama, A., Kamiya, N., and Nagamune, T. 2001. Design of the linkers which effectively separate domains of a bifunctional fusion protein. *Protein Engineering* **14**: 529 -532.
- Audesirk, G., Audesirk, T., and Ferguson, C. 2001. Culturing Rat Hippocampal Neurons. In *Current Protocols in Toxicology* (eds. L.G. Costa, E. Hodgson, D.A. Lawrence, and D.J. Reed), John Wiley & Sons, Inc., Hoboken, NJ, USA <http://www.currentprotocols.com/protocol/tx1203> (Accessed August 17, 2011).
- BASSELL, G.J., OLEJNIKOV, Y., and SINGER, R.H. 1999. The travels of mRNAs through all cells large and small. *The FASEB Journal* **13**: 447 -454.
- BAYER, T.S., BOOTH, L.N., KNUDSEN, S.M., and ELLINGTON, A.D. 2005. Arginine-rich motifs present multiple interfaces for specific binding by RNA. *RNA* **11**: 1848 -1857.
- Baird, G S, Zacharias, D A, and Tsien, R Y. 2000. Biochemistry, mutagenesis, and oligomerization of DsRed, a red fluorescent protein from coral. *Proceedings of the National Academy of Sciences of the United States of America* **97**: 11984-11989.
- Bartel, D.P., Zapp, M.L., Green, M.R., and Szostak, J.W. 1991. HIV-1 rev regulation involves recognition of non-Watson-Crick base pairs in viral RNA. *Cell* **67**: 529-536.

- Bassell, Gary J, and Kelic, S. 2004. Binding proteins for mRNA localization and local translation, and their dysfunction in genetic neurological disease. *Current Opinion in Neurobiology* **14**: 574-581.
- Bassell, Gary J, and Twiss, J.L. 2006. RNA exodus to Israel: RNA controlling function in the far reaches of the neuron. *EMBO reports* **7**: 31-35.
- Bates, M., Huang, B., Dempsey, G.T., and Zhuang, X. 2007. Multicolor Super-Resolution Imaging with Photo-Switchable Fluorescent Probes. *Science* **317**: 1749 -1753.
- Battiste, J.L., Mao, H., Rao, N.S., Tan, Ruoying, Muhandiram, D.R., Kay, L.E., Frankel, Alan D., and Williamson, J.R. 1996. α Helix-RNA Major Groove Recognition in an HIV-1 Rev Peptide-RRE RNA Complex. *Science* **273**: 1547 -1551.
- Bertrand, E, Chartrand, P., Schaefer, M., Shenoy, S M, Singer, R H, and Long, R.M. 1998. Localization of ASH1 mRNA particles in living yeast. *Molecular Cell* **2**: 437-445.
- Betzig, E., Patterson, G.H., Sougrat, R., Lindwasser, O.W., Olenych, S., Bonifacino, J.S., Davidson, M.W., Lippincott-Schwartz, J., and Hess, H.F. 2006. Imaging Intracellular Fluorescent Proteins at Nanometer Resolution. *Science* **313**: 1642 -1645.
- Bevis, B.J., and Glick, B.S. 2002. Rapidly maturing variants of the Discosoma red fluorescent protein (DsRed). *Nature Biotechnology* **20**: 83-87.
- Bliss, T.V.P., and Collingridge, G.L. 1993. A synaptic model of memory: long-term potentiation in the hippocampus. *Nature* **361**: 31-39.
- Bobrowski, K., Wierzchowski, K.L., Holcman, J., and Ciurak, M. 1990. Intramolecular Electron Transfer in Peptides Containing Methionine, Tryptophan and Tyrosine: A Pulse Radiolysis Study. *International Journal of Radiation Biology* **57**: 919-932.
- Bono, F., Cook, A.G., Grünwald, M., Ebert, J., and Conti, E. 2010a. Nuclear Import Mechanism of the EJC Component Mago-Y14 Revealed by Structural Studies of Importin 13. *Molecular Cell* **37**: 211-222.
- Bono, F., Cook, A.G., Grünwald, M., Ebert, J., and Conti, E. 2010b. Nuclear Import Mechanism of the EJC Component Mago-Y14 Revealed by Structural Studies of Importin 13. *Molecular Cell* **37**: 211-222.
- Bono, F., Ebert, J., Lorentzen, E., and Conti, E. 2006. The Crystal Structure of the Exon Junction Complex Reveals How It Maintains a Stable Grip on mRNA. *Cell* **126**: 713-725.

- Bono, F., Ebert, J., Unterholzner, L., Güttler, T., Izaurralde, E., and Conti, E. 2004. Molecular insights into the interaction of PYM with the Mago-Y14 core of the exon junction complex. *EMBO reports* **5**: 304-310.
- Boswell, R.E., Prout, M.E., and Steichen, J.C. 1991. Mutations in a newly identified *Drosophila melanogaster* gene, mago nashi, disrupt germ cell formation and result in the formation of mirror-image symmetrical double abdomen embryos. *Development* **113**: 373-384.
- Bradley, J., Carter, S.R., Rao, V.R., Wang, J., and Finkbeiner, S. 2006. Splice Variants of the NR1 Subunit Differentially Induce NMDA Receptor-Dependent Gene Expression. *The Journal of Neuroscience* **26**: 1065 -1076.
- Branchini, B.R., Lusins, J.O., and Zimmer, M. 1997. A molecular mechanics and database analysis of the structural preorganization and activation of the chromophore-containing hexapeptide fragment in green fluorescent protein. *Journal of Biomolecular Structure & Dynamics* **14**: 441-448.
- Brejč, K., Sixma, T.K., Kitts, P.A., Kain, S.R., Tsien, R Y, Ormö, M., and Remington, S J. 1997. Structural basis for dual excitation and photoisomerization of the *Aequorea victoria* green fluorescent protein. *Proceedings of the National Academy of Sciences of the United States of America* **94**: 2306-2311.
- Brittis, P.A., Lu, Q., and Flanagan, J.G. 2002. Axonal Protein Synthesis Provides a Mechanism for Localized Regulation at an Intermediate Target. *Cell* **110**: 223-235.
- Budiman, M.E., Bubenik, J.L., Miniard, A.C., Middleton, L.M., Gerber, C.A., Cash, A., and Driscoll, D.M. 2009. Eukaryotic Initiation Factor 4a3 Is a Selenium-Regulated RNA-Binding Protein that Selectively Inhibits Selenocysteine Incorporation. *Molecular Cell* **35**: 479-489.
- Chalfie, M., Tu, Y., Euskirchen, G., Ward, W., and Prasher, D. 1994. Green fluorescent protein as a marker for gene expression. *Science* **263**: 802 -805.
- Chattoraj, M., King, B.A., Bublitz, G.U., and Boxer, S.G. 1996. Ultra-fast excited state dynamics in green fluorescent protein: multiple states and proton transfer. *Proceedings of the National Academy of Sciences of the United States of America* **93**: 8362-8367.

- Chazal, N., and Gerlier, D. 2003. Virus Entry, Assembly, Budding, and Membrane Rafts. *Microbiol. Mol. Biol. Rev.* **67**: 226-237.
- Cheong, C.-G., and Hall, T.M.T. 2006. Engineering RNA sequence specificity of Pumilio repeats. *Proceedings of the National Academy of Sciences* **103**: 13635 -13639.
- Chicurel, M.E., Singer, Robert H., Meyer, C.J., and Ingber, D.E. 1998. Integrin binding and mechanical tension induce movement of mRNA and ribosomes to focal adhesions. *Nature* **392**: 730-733.
- Cochilla, A.J., Angleson, J.K., and Betz, W.J. 1999. MONITORING SECRETORY MEMBRANE WITH FM1-43 FLUORESCENCE. *Annual Review of Neuroscience* **22**: 1-10.
- Cordin, O., Banroques, J., Tanner, N.K., and Linder, P. 2006. The DEAD-box protein family of RNA helicases. *Gene* **367**: 17-37.
- Cormack, B.P., Valdivia, R.H., and Falkow, S. 1996. FACS-optimized mutants of the green fluorescent protein (GFP). *Gene* **173**: 33-38.
- Corry, B., Jayatilaka, D., and Rigby, P. 2005. A Flexible Approach to the Calculation of Resonance Energy Transfer Efficiency between Multiple Donors and Acceptors in Complex Geometries. *Biophysical Journal* **89**: 3822-3836.
- Crameri, A., Whitehorn, E.A., Tate, E., and Stemmer, W.P. 1996. Improved green fluorescent protein by molecular evolution using DNA shuffling. *Nature Biotechnology* **14**: 315-319.
- Cull-Candy, S., Brickley, S., and Farrant, M. 2001. NMDA receptor subunits: diversity, development and disease. *Current Opinion in Neurobiology* **11**: 327-335.
- Daigle, N., and Ellenberg, J. 2007. LambdaN-GFP: an RNA reporter system for live-cell imaging. *Nature Methods* **4**: 633-636.
- Daly, T.J., Cook, K.S., Gray, G.S., Maione, T.E., and Rusche, J R. 1989. Specific binding of HIV-1 recombinant Rev protein to the Rev-responsive element in vitro. *Nature* **342**: 816-819.
- Darnell, J.C., Jensen, K.B., Jin, P., Brown, V., Warren, S.T., and Darnell, R.B. 2001. Fragile X Mental Retardation Protein Targets G Quartet mRNAs Important for Neuronal Function. *Cell* **107**: 489-499.

- Darzacq, X., Shav-Tal, Y., de Turrís, V., Brody, Y., Shenoy, Shailesh M, Phair, R.D., and Singer, Robert H. 2007. In vivo dynamics of RNA polymerase II transcription. *Nat Struct Mol Biol* **14**: 796-806.
- Daugherty, M.D., Liu, B., and Frankel, Alan D. 2010. Structural basis for cooperative RNA binding and export complex assembly by HIV Rev. *Nat Struct Mol Biol* **17**: 1337-1342.
- Davidson, M.W., and Campbell, Robert E. 2009. Engineered fluorescent proteins: innovations and applications. *Nat Meth* **6**: 713-717.
- Day, R.N., Booker, C.F., and Periasamy, A. 2008. Characterization of an improved donor fluorescent protein for Förster resonance energy transfer microscopy. *Journal of biomedical optics* **13**: 031203-031203.
- Degot, S., Le Hir, Hervé, Alpy, F., Kedinger, V., Stoll, I., Wendling, C., Seraphin, B., Rio, M.-C., and Tomasetto, C. 2004. Association of the Breast Cancer Protein MLN51 with the Exon Junction Complex via Its Speckle Localizer and RNA Binding Module. *Journal of Biological Chemistry* **279**: 33702 -33715.
- Denk, W., Strickler, J., and Webb, W. 1990. Two-photon laser scanning fluorescence microscopy. *Science* **248**: 73 -76.
- Dooley, C.T., Dore, T.M., Hanson, George T., Jackson, W.C., Remington, S. James, and Tsien, Roger Y. 2004. Imaging Dynamic Redox Changes in Mammalian Cells with Green Fluorescent Protein Indicators. *Journal of Biological Chemistry* **279**: 22284 -22293.
- Dostie, J., and Dreyfuss, G. 2002. Translation Is Required to Remove Y14 from mRNAs in the Cytoplasm. *Current Biology* **12**: 1060-1067.
- Dugave, C., and Demange, L. 2003. Cis-Trans Isomerization of Organic Molecules and Biomolecules: Implications and Applications†. *Chemical Reviews* **103**: 2475-2532.
- Eaton, W.A., and Hofrichter, J. 1990. Sick Cell Hemoglobin Polymerization. Vol. Volume 40 of, pp. 63-279, Academic Press <http://www.sciencedirect.com/science/article/pii/S0065323308602879> (Accessed August 8, 2011).
- Eckhardt, M., Anders, M., Muranyi, W., Heilemann, M., Krijnse-Locker, J., and Müller, B. 2011. A SNAP-Tagged Derivative of HIV-1—A Versatile Tool to Study Virus-Cell Interactions. *PLoS ONE* **6**: e22007.

- Ehlers, M.D., Fung, E.T., O'Brien, R.J., and Huganir, R L. 1998. Splice variant-specific interaction of the NMDA receptor subunit NR1 with neuronal intermediate filaments. *The Journal of Neuroscience: The Official Journal of the Society for Neuroscience* **18**: 720-730.
- Ellington, A.D., and Szostak, J.W. 1990. In vitro selection of RNA molecules that bind specific ligands. *Nature* **346**: 818-822.
- Endoh, T., Funabashi, H., Mie, M., and Kobatake, E. 2005. Method for Detection of Specific Nucleic Acids by Recombinant Protein with Fluorescent Resonance Energy Transfer. *Analytical Chemistry* **77**: 4308-4314.
- Endoh, T., Mie, M., and Kobatake, E. 2008. Direct detection of RNA transcription by FRET imaging using fluorescent protein probe. *Journal of Biotechnology* **133**: 413-417.
- Eom, Taesun, Antar, L.N., Singer, Robert H, and Bassell, Gary J. 2003. Localization of a beta-actin messenger ribonucleoprotein complex with zipcode-binding protein modulates the density of dendritic filopodia and filopodial synapses. *The Journal of Neuroscience: The Official Journal of the Society for Neuroscience* **23**: 10433-10444.
- Fan, L.-J., and Jones, W.E. 2006. Studies of Photoinduced Electron Transfer (PET) and Energy Migration in a Conjugated Polymer System for Fluorescence "Turn-on" Chemosensor Applications. *The journal of physical chemistry. B* **110**: 7777-7782.
- Feig, S., and Lipton, P. 1993. Pairing the cholinergic agonist carbachol with patterned Schaffer collateral stimulation initiates protein synthesis in hippocampal CA1 pyramidal cell dendrites via a muscarinic, NMDA-dependent mechanism. *Journal of Neuroscience* **13**: 1010-1021.
- Ferrandon, D., Elphick, L., Nüsslein-Volhard, C., and St Johnston, D. 1994. Stauf protein associates with the 3'UTR of bicoid mRNA to form particles that move in a microtubule-dependent manner. *Cell* **79**: 1221-1232.
- Filonov, G.S., Piatkevich, K.D., Ting, L.-M., Zhang, J., Kim, K., and Verkhusha, V.V. 2011. Bright and stable near-infrared fluorescent protein for in vivo imaging. *Nat Biotech* **29**: 757-761.
- Flexner, J.B., Flexner, L.B., and Stellar, E. 1963. Memory in Mice as Affected by Intracerebral Puromycin. *Science* **141**: 57 -59.

- Frey, Uwe, and Morris, R.G.M. 1997. Synaptic tagging and long-term potentiation. *Nature* **385**: 533-536.
- Furukawa, K., Abe, H., Abe, N., Harada, M., Tsuneda, S., and Ito, Y. 2008. Fluorescence generation from tandem repeats of a malachite green RNA aptamer using rolling circle transcription. *Bioorganic & Medicinal Chemistry Letters* **18**: 4562-4565.
- Fusco, D., Accornero, N., Lavoie, B., Shenoy, Shailesh M., Blanchard, J.-M., Singer, Robert H., and Bertrand, Edouard. 2003. Single mRNA Molecules Demonstrate Probabilistic Movement in Living Mammalian Cells. *Current Biology* **13**: 161-167.
- Ganesan, S., Ameer-beg, S.M., Ng, T.T.C., Vojnovic, B., and Wouters, F.S. 2006. A dark yellow fluorescent protein (YFP)-based Resonance Energy-Accepting Chromoprotein (REACH) for Förster resonance energy transfer with GFP. *Proceedings of the National Academy of Sciences of the United States of America* **103**: 4089 -4094.
- Garber, K., Smith, K.T., Reines, D., and Warren, S.T. 2006. Transcription, translation and fragile X syndrome. *Current Opinion in Genetics & Development* **16**: 270-275.
- Gazzaley, A.H., Benson, D.L., Huntley, G.W., and Morrison, J.H. 1997. Differential Subcellular Regulation of NMDAR1 Protein and mRNA in Dendrites of Dentate Gyrus Granule Cells after Perforant Path Transection. *The Journal of Neuroscience* **17**: 2006 -2017.
- Gehring, N.H., Lamprinaki, S., Hentze, M.W., and Kulozik, A.E. 2009a. The Hierarchy of Exon-Junction Complex Assembly by the Spliceosome Explains Key Features of Mammalian Nonsense-Mediated mRNA Decay. *PLoS Biol* **7**: e1000120.
- Gehring, N.H., Lamprinaki, S., Kulozik, A.E., and Hentze, M.W. 2009b. Disassembly of Exon Junction Complexes by PYM. *Cell* **137**: 536-548.
- Gehring, N.H., Lamprinaki, S., Kulozik, A.E., and Hentze, M.W. 2009c. Disassembly of Exon Junction Complexes by PYM. *Cell* **137**: 536-548.
- George, R.A., and Heringa, J. 2002. An analysis of protein domain linkers: their classification and role in protein folding. *Protein Engineering* **15**: 871 -879.
- Gilbert, W. 1986. Origin of life: The RNA world. *Nature* **319**: 618.
- Giorgi, C., Yeo, G.W., Stone, M.E., Katz, D.B., Burge, C., Turrigiano, G., and Moore, M.J. 2007. The EJC Factor eIF4AIII Modulates Synaptic Strength and Neuronal Protein Expression. *Cell* **130**: 179-191.

- Goedhart, J., van Weeren, L., Hink, M.A., Vischer, N.O.E., Jalink, K., and Gadella, T.W.J. 2010. Bright cyan fluorescent protein variants identified by fluorescence lifetime screening. *Nat Meth* **7**: 137-139.
- Gossen, M., and Bujard, H. 1993. Anhydrotetracycline, a novel effector for tetracycline controlled gene expression systems in eukaryotic cells. *Nucleic Acids Research* **21**: 4411-4412.
- Gosser, Y., Hermann, T., Majumdar, A., Hu, W., Frederick, R., Jiang, F., Xu, W., and Patel, D.J. 2001a. Peptide-triggered conformational switch in HIV-1 RRE RNA complexes. *Nat Struct Mol Biol* **8**: 146-150.
- Gosser, Y., Hermann, T., Majumdar, A., Hu, W., Frederick, R., Jiang, F., Xu, W., and Patel, D.J. 2001b. Peptide-triggered conformational switch in HIV-1 RRE RNA complexes. *Nat Struct Mol Biol* **8**: 146-150.
- Grant, D.M. et al. 2008. Multiplexed FRET to Image Multiple Signaling Events in Live Cells. *Biophysical Journal* **95**: L69-L71.
- Grate, D., and Wilson, C. 1999. Laser-mediated, site-specific inactivation of RNA transcripts. *Proceedings of the National Academy of Sciences* **96**: 6131 -6136.
- Griesbeck, O, Baird, G S, Campbell, R E, Zacharias, D A, and Tsien, R Y. 2001. Reducing the environmental sensitivity of yellow fluorescent protein. Mechanism and applications. *The Journal of Biological Chemistry* **276**: 29188-29194.
- Griesbeck, Oliver, Baird, Geoffrey S., Campbell, Robert E., Zacharias, David A., and Tsien, Roger Y. 2001. Reducing the Environmental Sensitivity of Yellow Fluorescent Protein. *Journal of Biological Chemistry* **276**: 29188 -29194.
- Griffith, L.C., Lu, C.S., and Sun, X.X. 2003. CaMKII, an Enzyme on the Move: Regulation of Temporospacial Localization. *Molecular Interventions* **3**: 386 -403.
- Groom, H.C.T., Anderson, E.C., and Lever, A.M.L. 2009. Rev: beyond nuclear export. *The Journal of General Virology* **90**: 1303-1318.
- Gurskaya, N.G., Fradkov, A F, Tersikh, A., Matz, M.V., Labas, Y.A., Martynov, V.I., Yanushevich, Y.G., Lukyanov, K A, and Lukyanov, S.A. 2001. GFP-like chromoproteins as a source of far-red fluorescent proteins. *FEBS Letters* **507**: 16-20.
- Hachet, O., and Ephrussi, A. 2001a. Drosophila Y14 shuttles to the posterior of the oocyte and is required for oskar mRNA transport. *Current Biology* **11**: 1666-1674.

- Hachet, O., and Ephrussi, A. 2001b. *Drosophila* Y14 shuttles to the posterior of the oocyte and is required for oskar mRNA transport. *Current Biology* **11**: 1666-1674.
- Haim-Vilmovsky, L., and Gerst, J.E. 2011. Visualizing endogenous mRNAs in living yeast using m-TAG, a PCR-based RNA aptamer integration method, and fluorescence microscopy. *Methods in Molecular Biology (Clifton, N.J.)* **714**: 237-247.
- Han, J. 2005. Identification of CELF splicing activation and repression domains in vivo. *Nucleic Acids Research* **33**: 2769-2780.
- Harada, K, Martin, S S, and Frankel, A D. 1996. Selection of RNA-binding peptides in vivo. *Nature* **380**: 175-179.
- Harada, Kazuo, Martin, Shelley S., Tan, Ruoying, and Frankel, Alan D. 1997a. Molding a peptide into an RNA site by in vivo peptide evolution. *Proceedings of the National Academy of Sciences of the United States of America* **94**: 11887-11892.
- Harada, Kazuo, Martin, Shelley S., Tan, Ruoying, and Frankel, Alan D. 1997b. Molding a peptide into an RNA site by in vivo peptide evolution. *Proceedings of the National Academy of Sciences of the United States of America* **94**: 11887-11892.
- Harada, Kazuo, Sugaya, M., Nishimura, F., and Katoh, A. 2008. Manipulation of the peptide-binding specificity of an RNA in a rational manner by combinations of specificity-altering mutations. *Nucleic Acids Symposium Series* **52**: 13 -14.
- Heim, R., Cubitt, A.B., and Tsien, R Y. 1995. Improved green fluorescence. *Nature* **373**: 663-664.
- Heim, R., Prasher, D C, and Tsien, R Y. 1994. Wavelength mutations and posttranslational autoxidation of green fluorescent protein. *Proceedings of the National Academy of Sciences of the United States of America* **91**: 12501-12504.
- Heim, R., and Tsien, R Y. 1996. Engineering green fluorescent protein for improved brightness, longer wavelengths and fluorescence resonance energy transfer. *Current Biology: CB* **6**: 178-182.
- Hell, S.W. 2003. Toward fluorescence nanoscopy. *Nat Biotech* **21**: 1347-1355.
- Henkel, T., Zabel, U., van Zee, K., Müller, J.M., Fanning, E., and Baeuerle, P.A. 1992. Intramolecular masking of the nuclear location signal and dimerization domain in the precursor for the p50 NF-[kappa]B subunit. *Cell* **68**: 1121-1133.

- Hermann, T., and Patel, D.J. 2000. RNA bulges as architectural and recognition motifs. *Structure* **8**: R47-R54.
- Inouye, S., Noguchi, M., Sakaki, Y., Takagi, Y., Miyata, T., Iwanaga, S., Miyata, T., and Tsuji, F.I. 1985. Cloning and sequence analysis of cDNA for the luminescent protein aequorin. *Proceedings of the National Academy of Sciences of the United States of America* **82**: 3154-3158.
- Ippen, E.P., Shank, C.V., and Bergman, A. 1976. Picosecond recovery dynamics of malachite green. *Chemical Physics Letters* **38**: 611-614.
- Isied, S.S., Ogawa, M.Y., and Wishart, J.F. 1992. Peptide-mediated intramolecular electron transfer: long-range distance dependence. *Chemical Reviews* **92**: 381-394.
- Isken, O., and Maquat, L.E. 2007. Quality control of eukaryotic mRNA: safeguarding cells from abnormal mRNA function. *Genes & Development* **21**: 1833 -3856.
- Ivanchenko, S., Godinez, W.J., Lampe, M., Kräusslich, H.-G., Eils, R., Rohr, K., Bräuchle, C., Müller, B., and Lamb, D.C. 2009. Dynamics of HIV-1 Assembly and Release. *PLoS Pathog* **5**: e1000652.
- Jaqaman, K., Loerke, D., Mettlen, M., Kuwata, H., Grinstein, S., Schmid, S.L., and Danuser, G. 2008. Robust single-particle tracking in live-cell time-lapse sequences. *Nat Meth* **5**: 695-702.
- Jazwinska, A., Kirov, N., Wieschaus, E., Roth, S., and Rushlow, C. 1999. The Drosophila Gene brinker Reveals a Novel Mechanism of Dpp Target Gene Regulation. *Cell* **96**: 563-573.
- Johnson, J.L., Cusack, B., Hughes, T.F., McCullough, E.H., Fauq, A., Romanovskis, P., Spatola, A.F., and Rosenberry, T.L. 2003. Inhibitors tethered near the acetylcholinesterase active site serve as molecular rulers of the peripheral and acylation sites. *The Journal of Biological Chemistry* **278**: 38948-38955.
- Jouvenet, N., Simon, S.M., and Bieniasz, P.D. 2009. Imaging the interaction of HIV-1 genomes and Gag during assembly of individual viral particles. *Proceedings of the National Academy of Sciences* **106**: 19114 -19119.
- Köhrmann, M., Luo, M., Kaether, C., DesGroseillers, L., Dotti, C.G., and Kiebler, M.A. 1999. Microtubule-dependent recruitment of Staufen-green fluorescent protein into large RNA-containing granules and subsequent dendritic transport in living hippocampal neurons. *Molecular Biology of the Cell* **10**: 2945-2953.

- Kanai, Y., Dohmae, N., and Hirokawa, N. 2004. Kinesin Transports RNA. *Neuron* **43**: 513-525.
- Kang, H., and Schuman, E.M. 1996. A Requirement for Local Protein Synthesis in Neurotrophin-Induced Hippocampal Synaptic Plasticity. *Science* **273**: 1402 -1406.
- Karasawa, S., Araki, T., Nagai, Takeharu, Mizuno, H., and Miyawaki, A. 2004. Cyan-emitting and orange-emitting fluorescent proteins as a donor/acceptor pair for fluorescence resonance energy transfer. *Biochemical Journal* **381**: 307-312.
- Kerppola, T.K. 2006. Visualization of molecular interactions by fluorescence complementation. *Nat Rev Mol Cell Biol* **7**: 449-456.
- Kim-Ha, J., Smith, J.L., and Macdonald, P.M. 1991. oskar mRNA is localized to the posterior pole of the *Drosophila* oocyte. *Cell* **66**: 23-35.
- Kislauskis, E.H., Zhu, X., and Singer, R H. 1994a. Sequences responsible for intracellular localization of beta-actin messenger RNA also affect cell phenotype. *The Journal of Cell Biology* **127**: 441-451.
- Kislauskis, E.H., Zhu, X., and Singer, R H. 1994b. Sequences responsible for intracellular localization of beta-actin messenger RNA also affect cell phenotype. *The Journal of Cell Biology* **127**: 441 -451.
- Klarenbeek, J.B., Goedhart, J., Hink, M.A., Gadella, T.W.J., and Jalink, K. 2011. A mTurquoise-Based cAMP Sensor for Both FLIM and Ratiometric Read-Out Has Improved Dynamic Range. *PLoS ONE* **6**: e19170.
- Kotera, I., Iwasaki, T., Imamura, H., Noji, H., and Nagai, Takeharu. 2010. Reversible Dimerization of *Aequorea victoria* Fluorescent Proteins Increases the Dynamic Range of FRET-Based Indicators. *ACS Chemical Biology* **5**: 215-222.
- Kruger, K., Grabowski, P.J., Zaug, A.J., Sands, J., Gottschling, D.E., and Cech, T.R. 1982. Self-splicing RNA: Autoexcision and autocyclization of the ribosomal RNA intervening sequence of tetrahymena. *Cell* **31**: 147-157.
- Kumagai, Y., Kamioka, Y., Yagi, S., Matsuda, M., and Kiyokawa, E. 2011. A genetically encoded Förster resonance energy transfer biosensor for two-photon excitation microscopy. *Analytical Biochemistry* **413**: 192-199.
- Lago, H., Fonseca, S.A., Murray, J.B., Stonehouse, N.J., and Stockley, P.G. 1998. Dissecting the key recognition features of the MS2 bacteriophage translational repression complex. *Nucleic Acids Research* **26**: 1337 -1344.

- Lange, S., Katayama, Y., Schmid, M., Burkacky, O., Bruchle, C., Lamb, D.C., and Jansen, R.-P. 2008. Simultaneous Transport of Different Localized mRNA Species Revealed by Live-Cell Imaging. *Traffic* **9**: 1256-1267.
- Lawrence, J.B., and Singer, R. H. 1986. Intracellular localization of messenger RNAs for cytoskeletal proteins. *Cell* **45**: 407-415.
- Lawrence, M.S., Phillips, K.J., and Liu, D.R. 2007. Supercharging Proteins Can Impart Unusual Resilience. *Journal of the American Chemical Society* **129**: 10110.
- Le Hir, Hervé, and Séraphin, B. 2008. EJC's at the Heart of Translational Control. *Cell* **133**: 213-216.
- Le Hir, Herve, Izaurralde, E., Maquat, L.E., and Moore, M.J. 2000. The spliceosome deposits multiple proteins 20-24 nucleotides upstream of mRNA exon-exon junctions. *EMBO J* **19**: 6860-6869.
- Le, T.T., Harlepp, S., Guet, C.C., Dittmar, K., Emonet, T., Pan, T., and Cluzel, P. 2005. Real-time RNA profiling within a single bacterium. *Proceedings of the National Academy of Sciences of the United States of America* **102**: 9160 -9164.
- Lee, J.-A., Xing, Y., Nguyen, D., Xie, J., Lee, C.J., and Black, D.L. 2007. Depolarization and CaM Kinase IV Modulate NMDA Receptor Splicing through Two Essential RNA Elements. *PLoS Biol* **5**: e40.
- Lee, J., Lee, K.H., Jeon, J., Dragulescu-Andrasi, A., Xiao, F., and Rao, J. 2010. Combining SELEX screening and rational design to develop light-up fluorophore-RNA aptamer pairs for RNA tagging. *ACS Chemical Biology* **5**: 1065-1074.
- Liao, J.C., Roider, J., and Jay, D.G. 1994. Chromophore-assisted laser inactivation of proteins is mediated by the photogeneration of free radicals. *Proceedings of the National Academy of Sciences* **91**: 2659 -2663.
- Link, W., Konietzko, U., Kauselmann, G., Krug, M., Schwanke, B., Frey, U, and Kuhl, D. 1995. Somatodendritic expression of an immediate early gene is regulated by synaptic activity. *Proceedings of the National Academy of Sciences of the United States of America* **92**: 5734-5738.
- Lionnet, T. et al. 2011. A transgenic mouse for in vivo detection of endogenous labeled mRNA. *Nat Meth* **8**: 165-170.

- Loeb, J. 1921. CHEMICAL AND PHYSICAL BEHAVIOR OF CASEIN SOLUTIONS. *The Journal of General Physiology* **3**: 547-555.
- Lowary, P.T., and Uhlenbeck, O.C. 1987. An RNA mutation that increases the affinity of an RNA-protein interaction. *Nucleic Acids Research* **15**: 10483-10493.
- Malim, M.H., Tiley, L.S., McCarn, D.F., Rusche, James R., Hauber, J., and Cullen, B.R. 1990. HIV-1 structural gene expression requires binding of the rev trans-activator to its RNA target sequence. *Cell* **60**: 675-683.
- Mallik, P.K., Nishikawa, K., Millis, A.J.T., and Shi, H. 2010. Commandeering a biological pathway using aptamer-derived molecular adaptors. **38**: e93-e93.
- Mank, M., Reiff, D.F., Heim, N., Friedrich, M.W., Borst, A., and Griesbeck, Oliver. 2006. A FRET-Based Calcium Biosensor with Fast Signal Kinetics and High Fluorescence Change. *Biophysical Journal* **90**: 1790-1796.
- Mann, D.A. et al. 1994. A molecular rheostat. Co-operative rev binding to stem I of the rev-response element modulates human immunodeficiency virus type-1 late gene expression. *Journal of Molecular Biology* **241**: 193-207.
- Maquat, L.E. 2004. Nonsense-mediated mRNA decay: splicing, translation and mRNP dynamics. *Nat Rev Mol Cell Biol* **5**: 89-99.
- Markwardt, M.L. et al. 2011. An Improved Cerulean Fluorescent Protein with Enhanced Brightness and Reduced Reversible Photoswitching. *PLoS ONE* **6**: e17896.
- Matz, M.V., Fradkov, A F, Labas, Y.A., Savitsky, A.P., Zaraisky, A G, Markelov, M.L., and Lukyanov, S.A. 1999. Fluorescent proteins from nonbioluminescent Anthozoa species. *Nature Biotechnology* **17**: 969-973.
- Mayford, M., Baranes, D., Podsypanina, K., and Kandel, E.R. 1996. The 3'-untranslated region of CaMKII α is a cis-acting signal for the localization and translation of mRNA in dendrites. *Proceedings of the National Academy of Sciences of the United States of America* **93**: 13250-13255.
- Meech, S.R. 2009. Excited state reactions in fluorescent proteins. *Chemical Society Reviews* **38**: 2922.
- Mendez, R., and Richter, J.D. 2001. Translational control by CPEB: a means to the end. *Nat Rev Mol Cell Biol* **2**: 521-529.

- Miller, S., Yasuda, M., Coats, J.K., Jones, Y., Martone, M.E., and Mayford, M. 2002a. Disruption of Dendritic Translation of CaMKII[alpha] Impairs Stabilization of Synaptic Plasticity and Memory Consolidation. *Neuron* **36**: 507-519.
- Miller, S., Yasuda, M., Coats, J.K., Jones, Y., Martone, M.E., and Mayford, M. 2002b. Disruption of Dendritic Translation of CaMKII α Impairs Stabilization of Synaptic Plasticity and Memory Consolidation. *Neuron* **36**: 507-519.
- Ming, G.-li, Wong, S.T., Henley, J., Yuan, X.-bing, Song, H.-jun, Spitzer, N.C., and Poo, M.-ming. 2002. Adaptation in the chemotactic guidance of nerve growth cones. *Nature* **417**: 411-418.
- Mingot, J.-M., Kostka, S., Kraft, R., Hartmann, E., and Gorlich, D. 2001. Importin 13: a novel mediator of nuclear import and export. *EMBO J* **20**: 3685-3694.
- Miyawaki, A., and Tsien, Roger Y. 2000. Monitoring protein conformations and interactions by fluorescence resonance energy transfer between mutants of green fluorescent protein. In *Applications of Chimeric Genes and Hybrid Proteins - Part B: Cell Biology and Physiology*, Vol. Volume 327 of, pp. 472-500, Academic Press <http://www.sciencedirect.com/science/article/pii/S0076687900272972> (Accessed June 9, 2011).
- Mori, Y., Imaizumi, K., Katayama, T., Yoneda, T., and Tohyama, M. 2000. Two cis-acting elements in the 3' untranslated region of alpha-CaMKII regulate its dendritic targeting. *Nature Neuroscience* **3**: 1079-1084.
- Murgatroyd, C. et al. 2009. Dynamic DNA methylation programs persistent adverse effects of early-life stress. *Nat Neurosci* **12**: 1559-1566.
- Muslimov, I.A., Titmus, M., Koenig, E., and Tiedge, H. 2002. Transport of Neuronal BC1 RNA in Mauthner Axons. *The Journal of neuroscience : the official journal of the Society for Neuroscience* **22**: 4293-4301.
- Nägerl, U.V., and Bonhoeffer, T. 2010. Imaging Living Synapses at the Nanoscale by STED Microscopy. *The Journal of Neuroscience* **30**: 9341 -9346.
- Nägerl, U.V., Willig, K.I., Hein, B., Hell, S.W., and Bonhoeffer, T. 2008. Live-cell imaging of dendritic spines by STED microscopy. *Proceedings of the National Academy of Sciences* **105**: 18982 -18987.

- Nagai, T. 2004. Expanded dynamic range of fluorescent indicators for Ca²⁺ by circularly permuted yellow fluorescent proteins. *Proceedings of the National Academy of Sciences* **101**: 10554-10559.
- Nagai, Takeharu, Ibata, K., Park, E.S., Kubota, M., Mikoshiba, K., and Miyawaki, A. 2002. A variant of yellow fluorescent protein with fast and efficient maturation for cell-biological applications. *Nat Biotech* **20**: 87-90.
- Nasmyth, K., and Jansen, R.P. 1997. The cytoskeleton in mRNA localization and cell differentiation. *Current Opinion in Cell Biology* **9**: 396-400.
- Nguyen, A.W., and Daugherty, P.S. 2005. Evolutionary optimization of fluorescent proteins for intracellular FRET. *Nat Biotech* **23**: 355-360.
- Nielsen, K.H., Chamieh, H., Andersen, C.B.F., Fredslund, F., Hamborg, K., Le Hir, Hervé, and Andersen, Gregers R. 2009. Mechanism of ATP turnover inhibition in the EJC. *RNA* **15**: 67-75.
- Niino, Y., Hotta, K., and Oka, K. 2009. Simultaneous Live Cell Imaging Using Dual FRET Sensors with a Single Excitation Light. *PLoS ONE* **4**: e6036.
- Nikaido, H. 1996. Multidrug efflux pumps of gram-negative bacteria. *Journal of Bacteriology* **178**: 5853-5859.
- Nishikawa, F., Kakiuchi, N., Funaji, K., Fukuda, K., Sekiya, S., and Nishikawa, S. 2003. Inhibition of HCV NS3 protease by RNA aptamers in cells. *Nucleic Acids Research* **31**: 1935-1943.
- Okabe, S, Miwa, A., and Okado, H. 1999. Alternative splicing of the C-terminal domain regulates cell surface expression of the NMDA receptor NR1 subunit. *The Journal of Neuroscience: The Official Journal of the Society for Neuroscience* **19**: 7781-7792.
- Okusu, H., Ma, D., and Nikaido, H. 1996. AcrAB efflux pump plays a major role in the antibiotic resistance phenotype of Escherichia coli multiple-antibiotic-resistance (Mar) mutants. *Journal of Bacteriology* **178**: 306-308.
- Oliva, B., Gordon, G., McNicholas, P., Ellestad, G., and Chopra, I. 1992. Evidence that tetracycline analogs whose primary target is not the bacterial ribosome cause lysis of Escherichia coli. *Antimicrob. Agents Chemother.* **36**: 913-919.

- Ormö, M., Cubitt, A.B., Kallio, K., Gross, L.A., Tsien, R Y, and Remington, S J. 1996. Crystal structure of the *Aequorea victoria* green fluorescent protein. *Science (New York, N.Y.)* **273**: 1392-1395.
- Ouyang, Y., Rosenstein, A., Kreiman, G., Schuman, E.M., and Kennedy, M.B. 1999. Tetanic Stimulation Leads to Increased Accumulation of Ca²⁺/Calmodulin-Dependent Protein Kinase II via Dendritic Protein Synthesis in Hippocampal Neurons. *The Journal of Neuroscience* **19**: 7823 -7833.
- Ozawa, T., Natori, Y., Sato, M., and Umezawa, Y. 2007. Imaging dynamics of endogenous mitochondrial RNA in single living cells. *Nat Meth* **4**: 413-419.
- PELED-ZEHAVID, H., HORIYA, S., DAS, C., HARADA, K., and FRANKEL, A.D. 2003. Selection of RRE RNA binding peptides using a kanamycin antitermination assay. *RNA* **9**: 252 -261.
- Padilla-Parra, S., Audugé, N., Lalucque, H., Mevel, J.-C., Coppey-Moisan, M., and Tramier, M. 2009. Quantitative comparison of different fluorescent protein couples for fast FRET-FLIM acquisition. *Biophysical Journal* **97**: 2368-2376.
- Pagès, J.-M., and Amaral, L. 2009. Mechanisms of drug efflux and strategies to combat them: Challenging the efflux pump of Gram-negative bacteria. *Biochimica et Biophysica Acta (BBA) - Proteins & Proteomics* **1794**: 826-833.
- Paige, J.S., Wu, K.Y., and Jaffrey, S.R. 2011. RNA Mimics of Green Fluorescent Protein. *Science* **333**: 642 -646.
- Palacios, Isabel M., Gatfield, D., St Johnston, Daniel, and Izaurralde, E. 2004. An eIF4AIII-containing complex required for mRNA localization and nonsense-mediated mRNA decay. *Nature* **427**: 753-757.
- Palacios, Isabel M., and Johnston, D.S. 2001. GETTING THE MESSAGE ACROSS : The Intracellular Localization of mRNAs in Higher Eukaryotes. *Annual Review of Cell and Developmental Biology* **17**: 569-614.
- Palmer, A.E., Giacomello, M., Kortemme, T., Hires, S.A., Lev-Ram, V., Baker, D., and Tsien, Roger Y. 2006. Ca²⁺ Indicators Based on Computationally Redesigned Calmodulin-Peptide Pairs. *Chemistry & Biology* **13**: 521-530.
- Parker, R., and Sheth, U. 2007. P Bodies and the Control of mRNA Translation and Degradation. *Molecular Cell* **25**: 635-646.

- Peabody, D.S., and Lim, F. 1996. Complementation of RNA binding site mutations in MS2 coat protein heterodimers. *Nucleic Acids Research* **24**: 2352-2359.
- Piljić, A., de Diego, I., Wilmanns, M., and Schultz, C. 2011. Rapid Development of Genetically Encoded FRET Reporters. *ACS Chemical Biology* **6**: 685-691.
- Ponchon, L., Beauvais, G., Nonin-Lecomte, S., and Dardel, F. 2009. A generic protocol for the expression and purification of recombinant RNA in Escherichia coli using a tRNA scaffold. *Nat. Protocols* **4**: 947-959.
- Prasher, Douglas C., Eckenrode, V.K., Ward, W.W., Prendergast, F.G., and Cormier, M.J. 1992. Primary structure of the Aequorea victoria green-fluorescent protein. *Gene* **111**: 229-233.
- Rackham, O., and Brown, C.M. 2004. Visualization of RNA-protein interactions in living cells: FMRP and IMP1 interact on mRNAs. *EMBO J* **23**: 3346-3355.
- Rafelski, S.M., and Theriot, J.A. 2004. Crawling toward a unified model of cell mobility: spatial and temporal regulation of actin dynamics. *Annual Review of Biochemistry* **73**: 209-239.
- Ragin, A.D., Morgan, R.A., and Chmielewski, J. 2002. Cellular Import Mediated by Nuclear Localization Signal Peptide Sequences. *Chemistry & Biology* **9**: 943-948.
- Raskin, C.A., Diaz, G.A., and McAllister, W.T. 1993. T7 RNA polymerase mutants with altered promoter specificities. *Proceedings of the National Academy of Sciences of the United States of America* **90**: 3147-3151.
- Riedl, J. et al. 2008. Lifeact: a versatile marker to visualize F-actin. *Nat Meth* **5**: 605-607.
- Rizzo, M.A., Springer, G.H., Granada, B., and Piston, D.W. 2004. An improved cyan fluorescent protein variant useful for FRET. *Nat Biotech* **22**: 445-449.
- Rodriguez, A.J., Shenoy, Shailesh M., Singer, Robert H., and Condeelis, J. 2006. Visualization of mRNA translation in living cells. *The Journal of Cell Biology* **175**: 67 -76.
- Rook, M.S., Lu, M., and Kosik, K.S. 2000. CaMKII α 3' Untranslated Region-Directed mRNA Translocation in Living Neurons: Visualization by GFP Linkage. *The Journal of Neuroscience* **20**: 6385 -6393.
- Ruan, G., Agrawal, A., Marcus, A.I., and Nie, S. 2007. Imaging and Tracking of Tat Peptide-Conjugated Quantum Dots in Living Cells: New Insights into Nanoparticle Uptake,

- Intracellular Transport, and Vesicle Shedding. *Journal of the American Chemical Society* **129**: 14759-14766.
- Sakaue-Sawano, A. et al. 2008. Visualizing Spatiotemporal Dynamics of Multicellular Cell-Cycle Progression. *Cell* **132**: 487-498.
- Salazar, M., Fedoroff, O.Y., Miller, J.M., Ribeiro, N.S., and Reid, B.R. 1993. The DNA strand in DNA.cntdot.RNA hybrid duplexes is neither B-form nor A-form in solution. *Biochemistry* **32**: 4207-4215.
- Santangelo, P.J., Lifland, A.W., Curt, P., Sasaki, Y., Bassell, Gary J, Lindquist, M.E., and Crowe, J.E. 2009. Single molecule-sensitive probes for imaging RNA in live cells. *Nat Meth* **6**: 347-349.
- Santangelo, P.J. 2010. Molecular beacons and related probes for intracellular RNA imaging. *Wiley Interdisciplinary Reviews: Nanomedicine and Nanobiotechnology* **2**: 11-19.
- Sasakura, Y., Ogasawara, M., and Makabe, K.W. 2000. Two Pathways of Maternal RNA Localization at the Posterior-Vegetal Cytoplasm in Early Ascidian Embryos. *Developmental Biology* **220**: 365-378.
- Sauliere, J., Haque, N., Harms, S., Barbosa, I., Blanchette, M., and Le Hir, Herve. 2010. The exon junction complex differentially marks spliced junctions. *Nat Struct Mol Biol* **17**: 1269-1271.
- Schifferer, M., and Griesbeck, Oliver. 2009. Application of aptamers and autofluorescent proteins for RNA visualization. *Integrative Biology* **1**: 499.
- Schimmel, P.R., and Flory, P.J. 1967. Conformational energy and configurational statistics of poly-L-proline. *Proceedings of the National Academy of Sciences of the United States of America* **58**: 52-59.
- Schratt, G.M., Tuebing, F., Nigh, E.A., Kane, C.G., Sabatini, M.E., Kiebler, M., and Greenberg, M.E. 2006. A brain-specific microRNA regulates dendritic spine development. *Nature* **439**: 283-289.
- Schwarze, S.R., Ho, A., Vocero-Akbani, A., and Dowdy, S.F. 1999. In Vivo Protein Transduction: Delivery of a Biologically Active Protein into the Mouse. *Science* **285**: 1569 -1572.
- Scott, D.B., Blanpied, T.A., Swanson, G.T., Zhang, C., and Ehlers, M.D. 2001. An NMDA receptor ER retention signal regulated by phosphorylation and alternative splicing.

- The Journal of Neuroscience: The Official Journal of the Society for Neuroscience* **21**: 3063-3072.
- Serina, L. et al. 1996. Structural Properties of UMP-Kinase from *Escherichia coli*: Modulation of Protein Solubility by pH and UTP⁺. *Biochemistry* **35**: 7003-7011.
- Shaner, N.C., Campbell, Robert E, Steinbach, P.A., Giepmans, B.N.G., Palmer, A.E., and Tsien, Roger Y. 2004. Improved monomeric red, orange and yellow fluorescent proteins derived from *Discosoma* sp. red fluorescent protein. *Nature Biotechnology* **22**: 1567-1572.
- Shaner, N.C., Lin, M.Z., McKeown, M.R., Steinbach, P.A., Hazelwood, K.L., Davidson, M.W., and Tsien, Roger Y. 2008. Improving the photostability of bright monomeric orange and red fluorescent proteins. *Nature Methods* **5**: 545-551.
- Shcherbo, D. et al. 2007. Bright far-red fluorescent protein for whole-body imaging. *Nat Meth* **4**: 741-746.
- Shimomura, O. 1979. Structure of the chromophore of *Aequorea* green fluorescent protein. *FEBS Letters* **104**: 220-222.
- Sil, A., and Herskowitz, I. 1996. Identification of asymmetrically localized determinant, Ash1p, required for lineage-specific transcription of the yeast HO gene. *Cell* **84**: 711-722.
- Smith, C A, Chen, L., and Frankel, A D. 2000. Using peptides as models of RNA-protein interactions. *Methods in Enzymology* **318**: 423-438.
- Smith, Colin A., Calabro, V., and Frankel, Alan D. 2000. An RNA-Binding Chameleon. *Molecular Cell* **6**: 1067-1076.
- Soderling, T.R. 2000. CaM-kinases: modulators of synaptic plasticity. *Current Opinion in Neurobiology* **10**: 375-380.
- Spassov, D.S., and Jurecic, R. 2002. Cloning and comparative sequence analysis of PUM1 and PUM2 genes, human members of the Pumilio family of RNA-binding proteins. *Gene* **299**: 195-204.
- Standley, S., Roche, K.W., McCallum, J., Sans, N., and Wenthold, R.J. 2000. PDZ Domain Suppression of an ER Retention Signal in NMDA Receptor NR1 Splice Variants. *Neuron* **28**: 887-898.

- Stavri, M., Piddock, L.J.V., and Gibbons, S. 2007. Bacterial efflux pump inhibitors from natural sources. *Journal of Antimicrobial Chemotherapy* **59**: 1247 -1260.
- Steward, O, and Levy, W. 1982. Preferential localization of polyribosomes under the base of dendritic spines in granule cells of the dentate gyrus. *The Journal of Neuroscience* **2**: 284 -291.
- Steward, Oswald, and Worley, P.F. 2001. Selective Targeting of Newly Synthesized Arc mRNA to Active Synapses Requires NMDA Receptor Activation. *Neuron* **30**: 227-240.
- Stryer, L., and Haugland, R.P. 1967. Energy transfer: a spectroscopic ruler. *Proceedings of the National Academy of Sciences of the United States of America* **58**: 719-726.
- Subramanian, M., Rage, F., Tabet, R., Flatter, E., Mandel, J.-L., and Moine, H. 2011. G-quadruplex RNA structure as a signal for neurite mRNA targeting. *EMBO Rep* **12**: 697-704.
- Sudarsan, N., Lee, E.R., Weinberg, Z., Moy, R.H., Kim, J.N., Link, K.H., and Breaker, R.R. 2008. Riboswitches in Eubacteria Sense the Second Messenger Cyclic Di-GMP. *Science* **321**: 411 -413.
- Sun, Y., Booker, C.F., Kumari, S., Day, R.N., Davidson, M., and Periasamy, A. 2009. Characterization of an orange acceptor fluorescent protein for sensitized spectral fluorescence resonance energy transfer microscopy using a white-light laser. *Journal of Biomedical Optics* **14**: 054009.
- Sundstroem, V., and Gillbro, T. 1982. Viscosity-dependent isomerization yields of some cyanine dyes. A picosecond laser spectroscopy study. *The Journal of Physical Chemistry* **86**: 1788-1794.
- Swedlow, J.R., and Platani, M. 2002. *Cell Structure and Function* **27**: 335-341.
- Tan, R, and Frankel, A D. 1995. Structural variety of arginine-rich RNA-binding peptides. *Proceedings of the National Academy of Sciences* **92**: 5282 -5286.
- Tan, W., Wang, K., and Drake, T.J. 2004. Molecular beacons. *Current Opinion in Chemical Biology* **8**: 547-553.
- Tange, T.Ø., Nott, A., and Moore, M.J. 2004. The ever-increasing complexities of the exon junction complex. *Current Opinion in Cell Biology* **16**: 279-284.
- Tanner, N.K., and Linder, P. 2001. DExD/H Box RNA Helicases From Generic Motors to Specific Dissociation Functions. *Molecular Cell* **8**: 251-262.

- Tansila, N., Tantimongcolwat, T., Isarankura-Na-Ayudhya, C., Nantasenamat, C., and Prachayasittikul, V. Rational Design of Analyte Channels of the Green Fluorescent Protein for Biosensor Applications. *International Journal of Biological Sciences* **3**: 463-470.
- Theissen, B., Karow, A.R., Köhler, J., Gubaev, A., and Klostermeier, D. 2008. Cooperative binding of ATP and RNA induces a closed conformation in a DEAD box RNA helicase. *Proceedings of the National Academy of Sciences of the United States of America* **105**: 548-553.
- Tilsner, J., Linnik, O., Christensen, N.M., Bell, K., Roberts, I.M., Lacomme, C., and Oparka, K.J. 2009. Live-cell imaging of viral RNA genomes using a Pumilio-based reporter. *The Plant Journal* **57**: 758-770.
- Tingley, W.G., Roche, K.W., Thompson, A.K., and Huganir, Richard L. 1993. Regulation of NMDA receptor phosphorylation by alternative splicing of the C-terminal domain. *Nature* **364**: 70-73.
- Tkachenko, A.G., Xie, H., Liu, Y., Coleman, D., Ryan, J., Glomm, W.R., Shipton, M.K., Franzen, S., and Feldheim, D.L. 2004. Cellular Trajectories of Peptide-Modified Gold Particle Complexes: Comparison of Nuclear Localization Signals and Peptide Transduction Domains. *Bioconjugate Chemistry* **15**: 482-490.
- Tsien, Roger Y. 1998. THE GREEN FLUORESCENT PROTEIN. *Annual Review of Biochemistry* **67**: 509-544.
- Tuerk, C., and Gold, L. 1990. Systematic evolution of ligands by exponential enrichment: RNA ligands to bacteriophage T4 DNA polymerase. *Science* **249**: 505 -510.
- Turner, J.J., Ivanova, G.D., Verbeure, B., Williams, D., Arzumanov, A.A., Abes, S., Lebleu, B., and Gait, Michael J. 2005. Cell-penetrating peptide conjugates of peptide nucleic acids (PNA) as inhibitors of HIV-1 Tat-dependent trans-activation in cells. *Nucleic Acids Research* **33**: 6837-6849.
- Ule, J. et al. 2005. Nova regulates brain-specific splicing to shape the synapse. *Nat Genet* **37**: 844-852.
- Valencia-Burton, M., McCullough, R.M., Cantor, C.R., and Broude, N.E. 2007. RNA visualization in live bacterial cells using fluorescent protein complementation. *Nature Methods* **4**: 421-427.

- Valencia-Burton, M., Shah, A., Sutin, J., Borogovac, A., McCullough, R.M., Cantor, C.R., Meller, A., and Broude, N.E. 2009. Spatiotemporal patterns and transcription kinetics of induced RNA in single bacterial cells. **106**: 16399-16404.
- Van Eeden, F.J.M., Palacios, I.M., Petronczki, M., Weston, M.J.D., and St. Johnston, D.S. 2001. Barentsz is essential for the posterior localization of oskar mRNA and colocalizes with it to the posterior pole. *Journal of Cell Biology* **154**: 511-523.
- Vinkenborg, J.L., Evers, T.H., Reulen, S.W.A., Meijer, E.W., and Merkx, M. 2007. Enhanced Sensitivity of FRET-Based Protease Sensors by Redesign of the GFP Dimerization Interface. *ChemBioChem* **8**: 1119-1121.
- Vives, E. 2005. Present and future of cell-penetrating peptide mediated delivery systems: "Is the Trojan horse too wild to go only to Troy?" *Journal of Controlled Release* **109**: 77-85.
- Wachter, R M, Elsliger, M.A., Kallio, K., Hanson, G T, and Remington, S J. 1998. Structural basis of spectral shifts in the yellow-emission variants of green fluorescent protein. *Structure (London, England: 1993)* **6**: 1267-1277.
- Weil, T.T., Parton, R.M., and Davis, I. 2010. Making the message clear: visualizing mRNA localization. *Trends in Cell Biology* **20**: 380-390.
- Weiss, M.A., and Narayana, N. 1998. RNA recognition by arginine-rich peptide motifs. *Biopolymers* **48**: 167-180.
- Wriggers, W., Chakravarty, S., and Jennings, P.A. 2005. Control of protein functional dynamics by peptide linkers. *Biopolymers* **80**: 736-746.
- Wu, L., and Belasco, J.G. 2008. Let Me Count the Ways: Mechanisms of Gene Regulation by miRNAs and siRNAs. *Molecular Cell* **29**: 1-7.
- Yamagishi, M., Ishihama, Y., Shirasaki, Y., Kurama, H., and Funatsu, T. 2009. Single-molecule imaging of beta-actin mRNAs in the cytoplasm of a living cell. *Experimental Cell Research* **315**: 1142-1147.
- Yamauchi, T. 2005. *Biological & Pharmaceutical Bulletin* **28**: 1342-1354.
- Yang, F., Moss, L.G., and Phillips, G.N. 1996. The molecular structure of green fluorescent protein. *Nat Biotech* **14**: 1246-1251.

- Yang, Y.Y.L., Yin, G.L., and Darnell, R.B. 1998. The neuronal RNA-binding protein Nova-2 is implicated as the autoantigen targeted in POMA patients with dementia. *Proceedings of the National Academy of Sciences* **95**: 13254 -13259.
- Yiu, H.-W., Demidov, V.V., Toran, P., Cantor, C.R., and Broude, N.E. 2011. RNA Detection in Live Bacterial Cells Using Fluorescent Protein Complementation Triggered by Interaction of Two RNA Aptamers with Two RNA-Binding Peptides. *Pharmaceuticals* **4**: 494-508.
- Yoshimura, A., Fujii, R., Watanabe, Y., Okabe, Shigeo, Fukui, K., and Takumi, T. 2006. Myosin-Va Facilitates the Accumulation of mRNA/Protein Complex in Dendritic Spines. *Current Biology* **16**: 2345-2351.
- ZHANG, L., LIU, W., and GRABOWSKI, P.J. 1999. Coordinate Repression of a Trio of Neuron-Specific Splicing Events by the Splicing Regulator PTB. *RNA* **5**: 117-130.
- ZHANG, W., LIU, H., HAN, K., and GRABOWSKI, P.J. 2002. Region-Specific Alternative Splicing in the Nervous System: Implications for Regulation by the RNA-Binding Protein NAPOR. *RNA* **8**: 671-685.
- Zacharias, David A., Violin, J.D., Newton, A.C., and Tsien, Roger Y. 2002. Partitioning of Lipid-Modified Monomeric GFPs into Membrane Microdomains of Live Cells. *Science* **296**: 913 -916.
- Zapata-Hommer, O., and Griesbeck, Oliver. 2003. Efficiently folding and circularly permuted variants of the Sapphire mutant of GFP. *BMC Biotechnology* **3**: 5.
- Zhang, H.L., Eom, T., Oleynikov, Y., Shenoy, S.M., Liebelt, D.A., Dichtenberg, J.B., Singer, R.H., and Bassell, G.J. 2001. Neurotrophin-Induced Transport of a [beta]-Actin mRNP Complex Increases [beta]-Actin Levels and Stimulates Growth Cone Motility. *Neuron* **31**: 261-275.
- Zhang, Q., Harada, Kazuo, Cho, H.S., Frankel, Alan D., and Wemmer, D.E. 2001. Structural characterization of the complex of the Rev response element RNA with a selected peptide. *Chemistry & Biology* **8**: 511-520.
- Zhang, Wenqing, Liu, H., Han, K., and Grabowski, P.J. 2002. Region-specific alternative splicing in the nervous system: implications for regulation by the RNA-binding protein NAPOR. *RNA* **8**: 671-685.

- Zhang, X.-hui, and Poo, M.-ming. 2002. Localized Synaptic Potentiation by BDNF Requires Local Protein Synthesis in the Developing Axon. *Neuron* **36**: 675-688.
- Zuker, M. 2003. Mfold web server for nucleic acid folding and hybridization prediction. *Nucleic Acids Research* **31**: 3406 -3415.
- Zukin, R.S., and Bennett, M.V. 1995. Alternatively spliced isoforms of the NMDAR1 receptor subunit. *Trends in Neurosciences* **18**: 306-313.



**„Endless steps“
(Max BILL, 1991)
sculpture illustrating Ernst Bloch's
„principle of hope“**

Acknowledgements

First and foremost I would like to thank my supervisor Oliver Griesbeck for consigning this interesting and challenging topic to me. His faith in the project and in my abilities to overcome all the problems always exceeded mine. Endless creative discussions, an independent working atmosphere and his optimistic, sisyphian attitude towards science left permanent impression. "The struggle itself...is enough to fill a man's heart. One must imagine Sisyphus happy." (Albert Camus)

I'd like to express my gratitude to Axel Borst for his willingness to be the "Doktorvater" of an RNA project and for his valuable outside the box advice during my Thesis Committees.

I would like to thank the whole Griesbeck group for the most free, entertaining and creative working atmosphere I could think of, especially for all the odds and ends of every-day lab life rendered my time here so special. I very much appreciate the 4 years I spent with you. Many thanks to Steph for facilitating my start in the group, for nice neighbourhood in P1 and all his help especially regarding imaging. Many thanks to my bench neighbor and IPP colleague Jonny for mental, practical and very British support. Gayane was always there for girl`s distractions not only in the lab. Working back-to-back with Dane was among the most entertaining lab times. Thanks to Anselm for as controversial as exciting discussions, his chemist`s help and the support with the SAXS experiments. I`m especially grateful for Julia`s enthusiasm to get the screening done and for being a great friend. Recently, David and Michael nicely amended our group.

Anja Moritz and her labbrain facilitated my start in lab work and she was a great help for the screening. Many thanks to our lab mum Birgit Kunkel for fostering cells, mice and PhD students and for doing everything I wouldn`t have dared or forgot to ask for.

Special thanks to Marco for facilitating a smooth start, realistic and elaborated discussions and his continuous support even until now. Thanks also to current and former lab- or P1- members Adrian, Amrita, Chris, Martina, Matthias, Nina and Vroni for a nice atmosphere. The practical students John and Lydia kindly contributed to this work. Mille Grazie to Giovanni for emergency first-aid supplies.

Many thanks to the whole Borst Group for the exceptionally nice atmosphere, especially to Dierck and everybody who had an open ear also in hard times.

Many thanks to my third Thesis committee member Gunter Meister and his students for contributing with his RNA biology knowledge. I would like to thank Jianghong Rao for being an inspiring lab host and Anca for sharing ideas on the ASR approach. Fei not only introduced me into the SELEX technology but, together with his wife, he was also a courteous host in Palo Alto. I'm indebted to Elena Conti and her lab, especially Atlanta, Sutapa and Gretel for helpful comments on and material for the REFlex project. Many thanks to Gregor for starting a collaboration on the SAXS experiments. Last but not least, I am grateful for the cooperative and inspiring atmosphere I enjoyed at the MPI of Neurobiology. Special thanks to Elena, Marsilius, Wolfgang, "Bradkes" and "Kleins" and all the MPI staff.

Finally I have to express my gratitude to my parents, Bernhard and my friends for tolerating long evening lab-sessions and above all for supporting me in whatever I was doing.

Curriculum Vitae

Personal information

Name Martina Schifferer-Waritschlager
Date of birth 16th August 1982
Nationality German

Education

Since 07/2007 **PhD thesis** at the Max-Planck-Institute of Neurobiology, Martinsried, Germany (Dr. O. Griesbeck): *“Development of a dynamic RNA sensor”*

02/2007 - 06/2007 **Graduate studies** at the Max Planck Institute of Psychiatry, Munich (Prof. Dr. R. Landgraf): *“Epigenetics in a mouse model for high and low anxiety”*

09/2006 - 07/2007 **Undergraduate studies** at the Hochschule für Philosophie, Munich

09/2004 - 09/2006 **Master studies** in Molecular Biotechnology at the Technical University Munich, Germany
 Master thesis at the Max Planck Institute of Biochemistry (Prof. Dr. R. Fässler): *“Analysis of Kindlin-2 knock-out mice”*

09/2001 - 07/2004 **Bachelor studies** in Molecular Biotechnology at the Technical University Munich, Germany
 Bachelor thesis at the Technical University Munich (Prof. Dr. A. Skerra): *“Structural and functional analysis of the Skp protein”*

06/2001 Graduation from **High School** (Gymnasium der Maria-Ward Schulstiftung, Altötting, Germany)

Publications

Montanez E, Ussar S, **Schifferer M**, Bösl M, Zent R, Moser M, Fässler R (2008) Kindlin-2 controls bidirectional signaling of integrins. *Genes & Development* 22(10): 1325-1330

Schifferer M, Griesbeck O (2009) Application of aptamers and autofluorescent proteins for RNA visualization. *Integrative Biology* 1(8-9): 499.

Schifferer M, MacKinnon J, Rao J, Griesbeck O. Probing eIF4AIII Function With Fluorescence Resonance Energy Transfer. (submitted)

Schifferer M, Griesbeck O. An Engineered Biosensor-Aptamer Pair to Image RNA Expression in Living Cells. (submitted)

Conferences

Gordon conference "*Basement membranes*", Il Giocco, Italy, 2007 (poster)

EMBO conference "*The complex life of RNA*", Heidelberg, Germany, 2010 (poster)

RNA society conference, Kyoto, Japan, 2011 (poster)

Versicherung

Ehrenwörtliche Versicherung

Ich versichere hiermit ehrenwörtlich, dass die vorgelegte Dissertation von mir selbständig und ohne unerlaubte Hilfe angefertigt ist.

München, 15.09.2011

Martina Schifferer-Waritschlager

Erklärung

Hiermit erkläre ich, dass die Dissertation nicht ganz oder in wesentlichen Teilen einer anderen Prüfungskommission vorgelegt worden ist und dass ich mich anderweitig einer Doktorprüfung ohne Erfolg nicht unterzogen habe.

München, 15.09.2011

Martina Schifferer-Waritschlager